PROCEEDING
OF 1ST INTERNATIONAL CONFERENCE
ON ENVIRONMENTAL PROTECTION
AND DISASTER RISKS

PART TWO

PROCEEDING
OF 1ST INTERNATIONAL CONFERENCE ON ENVIRONMENTAL PROTECTION AND DISASTER RISKS

PART TWO

Part Two of the proceeding book presents texts on the following topics: *Natural Hazards and Risks; Water Resources, Human Activities and Management.*

In Part One of the proceeding book were presented texts on the following topics: *Air Pollution, Climate and Health; Biodiversity; Informatics, Remote Sensing, High Performance Computing and GIS for Environmental Monitoring and Management.*

CONTENTS

NATURAL HAZARDS AND RISKS

THE WESTERN BLACK SEA WAVES 1980-2020 – STUDY BASED ON ERA5

Vasko Galabov

National Institute of Meteorology and Hydrology (NIMH)

Abstract: The study presents a reconstruction of the Western Black Sea wave climate based on a numerical hindcast using the SWAN wave model and ERA5 input data. While there are many wave hindcasts reconstructing the Black Sea wave climate, based on various atmospheric reanalysis projects, the present work is the first based on the state of art ERA5 reanalysis. We focus on the storminess affecting the Bulgarian coast. The storminess in the recent decade (2010-2019) was found to be the highest compared to the previous 3 decades covered by the reanalysis (while the previous 2000-2009 is with the lowest), but the trends in the storm proxies used in the study are not statistically significant. This confirms the conclusions of other studies that the wave climate of the Western Black Sea is steady.
Keywords: waves, wave climate, Black Sea, SWAN, ERA5

INTRODUCTION

The main hazards to the coasts are strong winds, high waves and storm surges. The extreme winds, waves and storm surges are associated with the severe sea storms. While the Black Sea is characterized with a lower frequency of the storms, the waves during the storms may reach heights that are similar to the wave heights in the oceans (Galabov et al, 2015). In the Black Sea long time series of operational measurements are missing and so are the studies of the wave climate based on them, with some exceptions for the Eastern Black Sea (Polonsky et al, 2014). Another exception based on measurements is the study of the wave energy for the Romanian coast (Tanase et al, 2018). Most of the studies of the wave climate are based on numerical modelling. The most used wave model in these studies is SWAN (Booij et al, 1999). The wind data usually is from atmospheric reanalysis, like ERA Interim (Dee et al, 2011), CFSR (Saha et al, 2010), NCEP reanalysis (Kalnay et al, 1996) or ERA Clim (Stickler et al, 2014). The first study based on numerical hindcast of the Western Black Sea waves is based on SWAN and REMO model atmospheric data (Valchev et al, 2010). Later Valchev continued with a study focused on the Western Black Sea storminess (Valchev et al, 2012). Arkhipkin et al studied the wave climate of the Black Sea

with a hindcast based on NCEP reanalysis (Arkhipkin et al, 2014). Divinsky and Kosyan studied the Black Sea wave climate using ERA Interim. Other authors use the CFSR reanalysis- (Akpinar and Bingolbali, 2016), (Akpinar et al, 2016), (Bingölbali et al, 2019), (Rusu et al, 2018). Some of the studies are focused on the wave energy instead of the storminess, such as (Rusu, 2019). Other works are focused on a specific region like the study of Zainescu et al, focused on the Danube delta (Zainescu et al, 2017). Recently Aydogan and Ayat (Aydogan and Ayat, 2018) studied the trends in the significant wave heights and found some small positive trends for the Western Black Sea of the 95th percentile of the significant wave height (SWH). Their study is based on ERA Interim. ERA Interim is replaced by the new state of art European reanalysis ERA5 (Herscbach et al, 2020). ERA5 is with significantly higher spatial and temporal resolution, so we decided to proceed with a wave hindcast based on ERA5 for the entire period of the reanalysis and to study again the storminess and the trends in the storm proxies for the Western Black Sea going from 1979 to 2020. As far as we know this is the first Black Sea wave hindcast based on ERA5. In the previous work of the author (Galabov & Chervenkov, 2018) the Western Black Sea storms are studied for a 110 years period, based on ERA Clim reanalysis. ERA Clim is available only until 2010, so the conclusions about the wave climate in the decade 2010-2019 are not possible. The present work fills the gap in this paper, going from 1980 to 2020 and therefore revealing the changes including the most recent decade and it is a continuation of some parts of (Galabov & Chervenkov, 2018). Later this year the ERA5 will be updated and will include the years from 1950 to 1978 and when it is available, we will update the wave hindcast from 1950.

METHODS AND DATA

The study is based on the SWAN wave model, as most of the other studies of the Western Black Sea wave climate. The reason is that SWAN is a state of art third generation wave model, that is an open source project and it is especially suitable for coastal regions and enclosed basins. It is also computationally cheap and very flexible wave model. For the purposes of the study SWAN was used in two domains- the big domain covers the entire Black Sea basin with a spatial resolution of 0.1° and provides the boundary conditions for a nested domain with a higher spatial resolution (1/30°) in the Western Black Sea.

The boundary of the nested domain is shown of figure 1. The model run covers the entire period 1979-2020 and the output of the computations is available for the entire nested domain with a temporal resolution of 3 hours, and for two locations- near the town Ahtopol and cape Shabla (representing the conditions at the southern and northern Bulgarian coast) with a temporal resolution of 1 hour. The computations are split in years and each year was set to start on 01 July and end on 30 June- for instance when we mention 1981 we mean the period 01.07.1980-30.06.1981. The reason is to include the entire stormy season (which in the Black
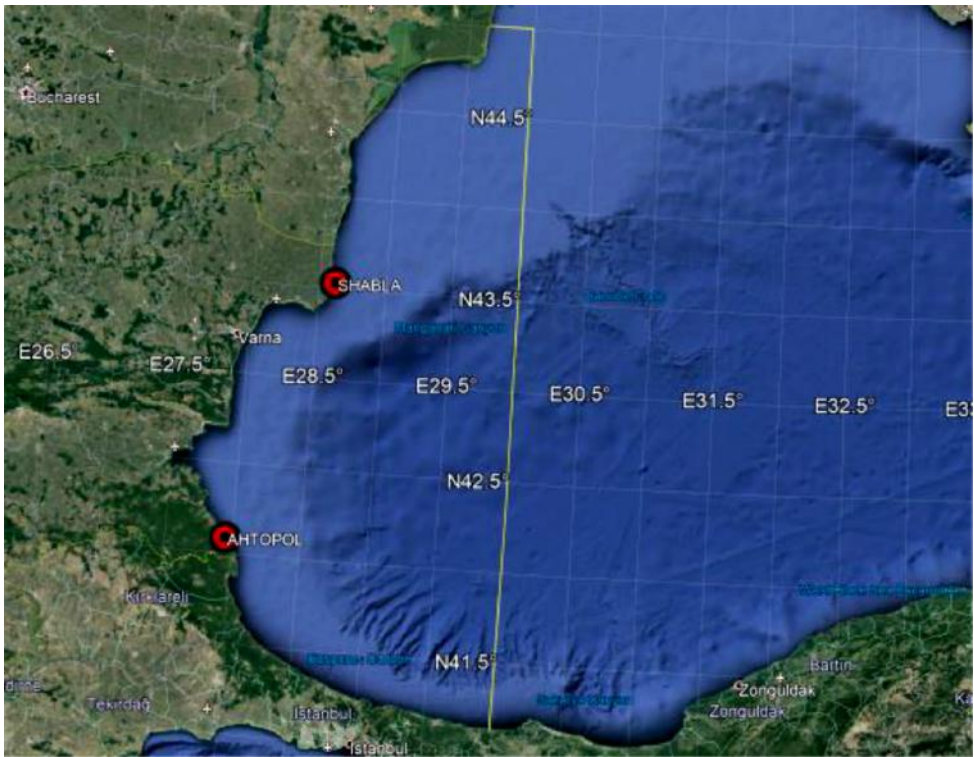
Figure 1. The yellow line shows the boundary of the nested domain.
The two locations (Ahtopol and Shabla) used in the study are also shown.

Sea is mainly the winter) in one computation i.e. to study stormy seasons instead of calendar years. The parameterizations of the SWAN model are based on the Komen parameterization scheme (Komen et al, 1984). The reason for the choice of the parameterization is that Komen scheme results in higher SWH than the other parameterizations (as shown in (Galabov et al, 2015)) and this way we partially compensate the underestimation of the wind speeds during storms, that is typical for the reanalyses. The time step of the model is 20 minutes. The computational grids are in spherical coordinates and the nested grid has 91x106 grid points.

The input data is the wind fields at 10m from the ERA5 reanalysis with a spatial resolution of 0.25° and temporal resolution of 1 hour. The bathymetry was obtained from ETOPO.

In order the study the wave climate and the storminess in the study we use some proxies of the storminess: the annual maximum SWH for the nested domain, or for the selected locations, the number of the storms per year (we identify as a storm

any event for which the SWH reach 2.5m or wave force 5 at WMO scale and if the SWH persists above 2.5m for at least 6 hours, and if the event is separated from the previous event by at least 48 hours interval). The number of the storms with a 2.5m SWH threshold is hereafter denoted as n25. We also use the number of the storms for which the SWH reach 4m (wave force 6 on WMO scale). These are the severe storms and their annual number is hereafter denoted as n40. In order to characterize the energy of the storms we use the total annual wave energy flux. The total wave energy flux is calculated using equation (1).

$$E = \frac{\rho g^2}{64\pi} TH^2 \approx \frac{1}{2} TH^2$$

1)

Where ρ is the water density, H is the significant wave height, T is the wave period (the so called wave energy period or T_{10} from the model output). The formula gives the wave power flux per 1m of the crest of the wave in kW/m. We calculate the total annual wave power flux only for the waves with SWH>2.5m and denote it E25 and use it to characterize the energy of all storms and also we calculate it only for the waves above 4m and denote it E40 to characterize separately the energetics of the severe storms.

In our study we also use as a storm proxy the so called Storm Power Index introduced by Dolan and Davis (Dolan and Davis, 1992) and denote it as SPI. SPI for a single storm is calculated multiplying the highest SWH during the storm by the duration of the storm in hours. After obtaining the SPI for each individual storm we add SPI for all storms within one year period and obtain the annual SPI.

RESULTS AND DISCUSSION

The first year period in our study is 1980, because ERA5 data is not available for the entire 1978/1979 stormy season. The last period is ending on 31.05.2020, however as an operational wave forecaster running operational version of SWAN the author did not observed any storms in the Western Black Sea during June 2020 and therefore the last one year period includes the entire stormy season 2019/2020.

On figure 2 the annual number of the storms above 2.5m SWH and above 4m SWH. As it may be seen, there is some weak positive trend of n25 for Ahtopol, however it is not statistically significant at p=0.05 when using the test of Mann and Kendall (Mann, 1946, Kendall and Stuart, 1976).

Next on figure 3 we show the evolution of the annual E25 and E40 for the selected locations. For both locations the trends are negligible and not significant. For Ahtopol E25 is reaching values above 8000 for 6 out of the 40 years, while for Shabla location it is above 8000 only in 2012 and for all other years it is below 6000. Overall the storminess of the location Shabla is lower that Ahtopol, showing that the storminess is significantly higher with more energetic storms at the southern
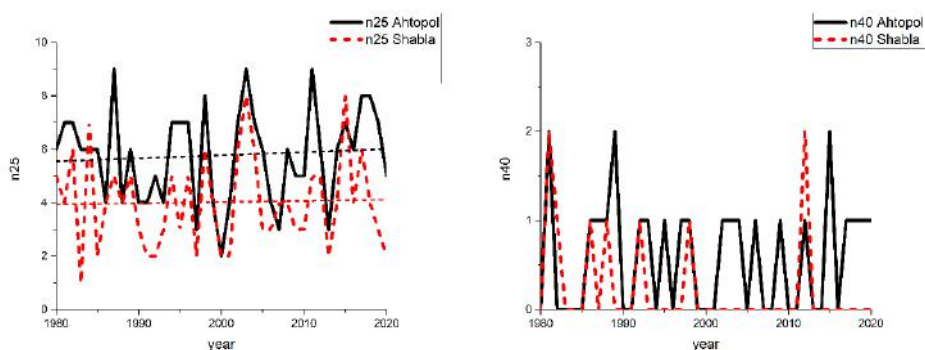
Figure 2. Left- the annual number of the storms above 2.5 SWH for Ahtopol and Shabla. Right- the annual number of storms above 4m SWH.

Bulgarian coast. Looking at fig.3 we can see that the year with the highest E40 at both locations is 2012 (which is exceptionally high for Shabla). For Ahtopol there is a negative trend in E40, however we cannot confirm it as statistically significant.

On figure 4 we show the anomalies of E25 and E40 (i.e. the annual value minus the mean value, divided by the standard deviation) for the entire nested computational domain in order to see the character of the storminess in the entire Western Black Sea. For E25 we have a very weak negative trend and for E40 weak positive trend (not statistically significant). The conclusion about the weak positive trend is in line with the findings of Aydogan and Ayat (Aydogan and Ayat, 2018). The year with the highest E25 in the Western Black Sea is 2015, while the year with the highest E40 (severe storminess) is 2012 followed by 1981 which is also with high E40 for both locations. Overall we cannot observe significant changes in the storminess in the Western Black Sea for the period 1980- 2020.
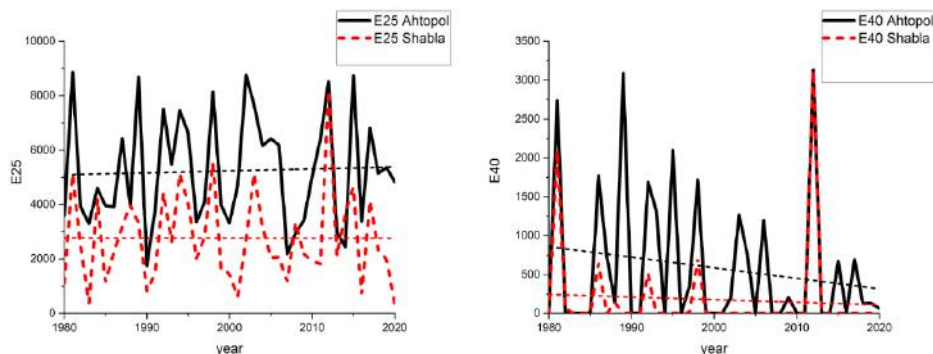
Figure 3. Left- E25 for Ahtopol and Shabla. Right- E40 for Ahtopol and Shabla.
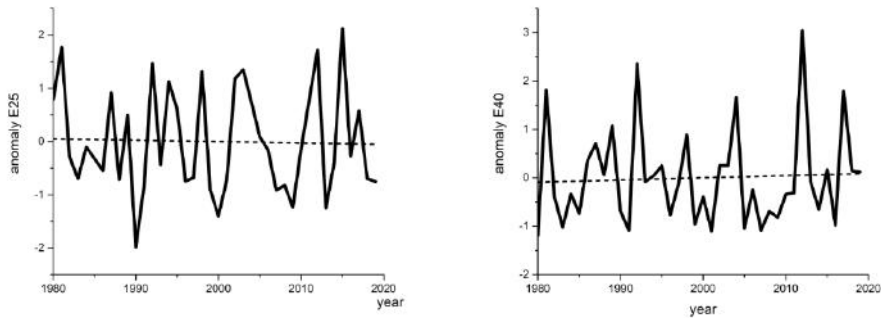
Figure 4. Left- E25 anomaly for the entire nested domain. Right- E40 anomaly for the entire nested domain.
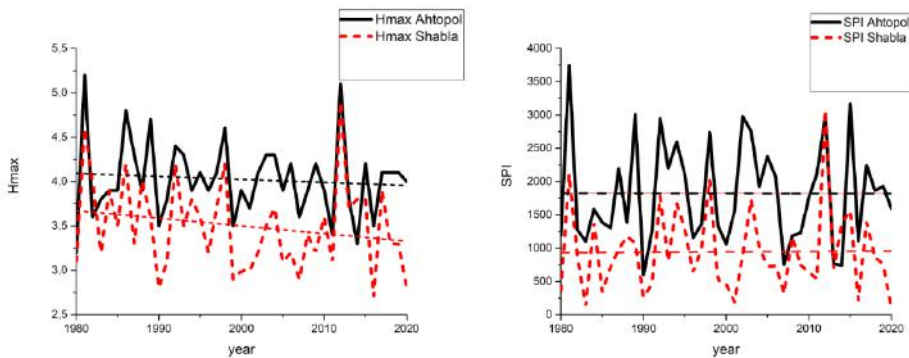
Figure 5. Left- the annual maximum SWH for Ahtopol and Shabla. Right- the storm power index (SPI) for Ahtopol and Shabla.

The annual maximum SWH (Hmax) and the storm power index (SPI) are shown on figure 5. The years with the highest wave heights above 5m for Ahtopol are 1981 (due to the storm of 8-10 January) and 2012 (due to the storm of 6-8 February). For Shabla the highest storm is the storm of 2012. The annual maximum for Shabla shows not significant negative trend. The SPI at both locations are steady and without noticeable trends. For Ahtopol the year with the highest SPI is 1981, while for Shabla it is 2012.

The annual maximum SWH is on figure 6. We observe a positive trend that again does not pass the significance test. Whether it is a significant trend as a result of the climate changes or not we cannot claim in the present work. We will evaluate it again after the inclusion of the period 1950-1978 (when it becomes possible).
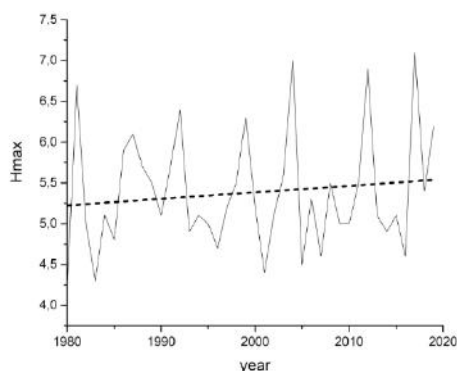
Figure 6. The annual maximum SWH for the entire nested
Western Black Sea domain.

Going on a decadal basis we observe that the decade 2010-2019 is the decade with the highest values of all storm proxies, while the decade 2000-2009 is with the lowest values i.e. with the lowest storminess. The values during the decade 2010-2019 are close to the values for the decades 1980-1989 and 1990- 1999, but a bit higher.

CONCLUSIONS
We presented a study of the Western Black Sea wave climate with a focus on the storminess and on the Bulgarian coast for the period 1980- 2020 based on a numerical simulation using SWAN Wave model. For the first time ERA5 was used to study the wave climate in the area. Generally we cannot confirm significant changes in the storminess in the area, but there are hints of some positive trends, that has to be clarified when it becomes possible to extend the period of the simulation.

REFERENCES
Akpinar, A., & Bingo¨lbali, B. (2016). Long-term variations of the wind and wave conditions in the coastal regions of the Black Sea. Natural Hazards, 84(1), 69–92.

Akpinar, A., Bingo¨lbali, B., & Van Vledder, G. P. (2016). Wind and wave characteristics in the Black Sea based on the SWAN wave model forced with the CFSR winds. Ocean Engineering, 126, 276–29

Arkhipkin, V. S., Gippius, F. N., Koltermann, K. P., & Surkova, G. V. (2014). Wind waves in the Black Sea: results of a hindcast study. Natural Hazards and Earth System Sciences, 14, 2883–2897.

Aydoğan, B., & Ayat, B. (2018). Spatial variability of long-term trends of significant wave heights in the Black Sea. *Applied Ocean Research*, *79*, 20-35.

Bingölbali, B., Akpınar, A., Jafali, H., & Van Vledder, G. P. (2019). Downscaling of wave climate in the western Black Sea. *Ocean Engineering*, *172*, 31-45.

Booij, N., Ris, R. C., & Holthuijsen, L. H. (1999). A third generation wave model for coastal regions: 1. Model description and validation. Journal of geophysical research: Oceans, 104, 7649–7666

Dee, D. P., Uppala, S. M., Simmons, A. J., Berrisford, P., Poli, P., Kobayashi, S., et al. (2011). The ERA-interim reanalysis: Configuration and performance of the data assimilation system. Quarterly Journal of the royal meteorological society, 137(656), 553–597.

Divinsky, B. V., & Kosyan, R. D. (2015). Observed wave climate trends in the offshore Black Sea from 1990 to 2014. Oceanology, 55, 837–843.

Divinsky, B. V., & Kosyan, R. D. (2017). Spatiotemporal variability of the Black Sea wave climate in the last 37 years. Continental Shelf Research, 136, 1–19.

Dolan, R., & Davis, R. E. (1992). An intensity scale for Atlantic coast northeast storms. *Journal of coastal research*, 8(4), 840-853.

Galabov, V., Kortcheva, A., Bogatchev, A., & Tsenova, B. (2015). Investigation Of The Hydro-Meteorological Hazards Along The Bulgarian Coast Of The Black Sea By Reconstructions Of Historical Storms. *Journal of Environmental Protection and Ecology*, *16*(3), 1005-1015.

Galabov, Vasko, and Hristo Chervenkov. "Study of the Western Black Sea Storms with a Focus on the Storms Caused by Cyclones of North African Origin." *Pure and Applied Geophysics* 175.11 (2018): 3779-3799.

Hersbach, H., Bell, B., Berrisford, P., Hirahara, S., Horányi, A., Muñoz-Sabater, J. ... & Simmons, A. (2020). The ERA5 global reanalysis. *Quarterly Journal of the Royal Meteorological Society*. (In in print).

Kalnay, E., Kanamitsu, M., Kistler, R., Collins, W., Deaven, D., Gandin, L., et al. (1996). The NCEP/NCAR 40-year reanalysis project. Bulletin of the American Meteorological Society, 77, 437–471.

Kendall, M. G., & Stuart, A. (1976). The Advanced theory of statistics: Distribution theory (Vol. I). London: Griffin

Komen, G. J., Hasselmann, S., & Hasselmann, K. (1984). On the existence of a fully developed wind sea spectrum. Journal of Physical Oceanography, 14, 1271–1285.

Mann, H. B. (1945). Nonparametric tests against trend. *Econometrica*, 13, 245–259.

Polonsky, A., Evstigneev, V., Naumova, V., & Voskresenskaya, E. (2014). Low-frequency variability of storms in the northern Black Sea and associated processes in the ocean–atmosphere system. *Regional environmental change*, *14*(5), 1861-1871.

Saha, S., Moorthi, S., Pan, H., Wu, X., Wang, J., & Coauthors, (2010). The NCEP climate forecast system reanalysis. Bulletin of the American Meteorological Society, 91, 1015–1057.

Stickler, A., Bro¨nnimann, S., Valente, M. A., Bethke, J., Sterin, A., Jourdain, S., et al. (2014). ERA-CLIM: historical surface and upper-air data for future reanalyses. Bulletin of the American Meteorological Society, 95, 1419–1430.

Tanase, V. M., Chiotoroiu, B. C., & Vatu, N. (2018). Wave energy along the Romanian Southern Black Sea coast. *JPhCS, 1122*(1), 012029.

Valchev, N., Davidan, I., Belberov, Z., Palazov, A., & Valcheva, N. (2010). Hindcasting and assessment of the western Black Sea wind and wave climate. Journal of Environmental Protection and Ecology, 11(3), 1001–1012.

Valchev, N. N., Trifonova, E. V., & Andreeva, N. K. (2012). Past and recent trends in the western Black Sea storminess. Natural Hazards and Earth System Sciences, 12(4), 961–977.

Rusu, L., Raileanu, A. B., & Onea, F. (2018). A comparative analysis of the wind and wave climate in the Black Sea along the shipping routes. *Water*, *10*(7), 924.

Rusu, L. (2019). The wave and wind power potential in the western Black Sea. *Renewable Energy*, *139*, 1146-1158.

Zainescu, F. I., Tatui, F., Valchev, N., & Vespremeanu-Stroe, A. (2017). Storm climate on the Danube delta coast: evidence of recent storminess change and links with large-scale teleconnection patterns. Natural Hazards, 87(2), 599–621.

✉ **Vasko Galabov**
http://orcid.org/0000-0003-3269-1486
National Institute of Meteorology and Hydrology
Sofia, Bulgaria
E-mail: vasko.galabov@meteo.bg

STORM SURGES AFFECTING THE BULGARIAN COAST - STUDY BASED ON 41 YEARS NUMERICAL HINDCAST

Vasko Galabov

National Institute of Meteorology and Hydrology (NIMH)

Abstract: We present the results of the numerical hindcast of the storm surges affecting the Bulgarian Black Sea coast during the period 1979-2020, using atmospheric data from the ERA5 reanalysis. The aim of the study is to evaluate the changes in the surge intensity and frequency during the period. The highest identified surges in the hindcast output are the surges of February 1979, January 1981 and February 2012- the surge of 2012 is the highest, while the surge of 1979 was found to be the longest and the most energetic event. We found no statistically significant inter annual change in the number, total duration and the introduced index characterizing the total energy of the surges above 60cm or 80cm was found. The total annual number of events above 40cm is with increasing trend which is statistically significant, but the total duration of events above 40cm does not show statistically significant trend- we observe more frequent but shorter events in the range 40-60cm during the last decade.

Keywords: storm surges, Black Sea, surge hindcast*,* sea level

INTRODUCTION

The storm surges in the Black Sea are less frequent than in the other seas and oceans, but they do have the potential to cause significant damages, because they cause a sea level variations that are 8 times greater (or more) than the other level variations (Mungov and Daniel, 2000). Some of the historical storm surge events such as the surges of February 1979 (Andreeva et al, 2011) and January 1981 caused damages and a coastal flooding including inundation of the town Pomorie in the Burgas Bay (South-eastern Bulgaria). Despite the fact that measurements from tide gauges are available since 1928, systematic studies of the storm surge climatology are missing for the Bulgarian coast. Approach based on numerical modelling was used in the studies of (Mungov and Daniel, 2000) of some specific cases, of the future storm surge climate (Krestenitis et al, 2012) or reconstructions of historical storms together with the waves (2018). At present there are no studies based on a longer periods (more than 30 years) of hindcasts or measurement processing. The

goal of the present work is to fill the gap and show the results of a long numerical hindcast of the surges affecting the Bulgarian coast and to estimate the changes in the frequency and magnitude of the storm surges during a few decades.

METHODS AND DATA

For the purposes of the study we performed a numerical hindcast of the storm surges. The numerical model that we use is the storm surge model of METEO FRANCE (Daniel, 1997). This model was adapted to the Black Sea more than 20 years ago (Mungov and Daniel, 2000). The model is two dimensional depth integrated working in spherical coordinates. The equations of the model and more details are presented in (Galabov, 2016) in this paper the version of the model that is in operational use in the National Institute of Meteorology and Hydrology (NIMH). In this study we used the same model setup as the mentioned operational model. The spatial resolution is 1/30° and the temporal resolution of the output is 1 hour (which is equivalent with the temporal resolution of the input meteorological fields). The computational domain covers the entire Black Sea. The hindcast was computed for the period 01.01.1979 to 31.05.2020 (the entire range of the availability of ERA5 input data). The computations are split in one year periods and each one year period starts from 01 July of the previous year and ends on 30 June on the year (i.e. for instance 2012 means 01.07.2011 to 30.06.2012). The reason for such an approach is to include the entire stormy season (which is in the cold part of the year in the Black Sea).

The input data for the model is the wind fields at 10m and the mean sea level pressure. These fields are obtained from the ERA5 atmospheric reanalysis (Hersbach et al, 2020). The spatial resolution of the data is 0.25° and the temporal resolution is 1 hour.

In the present study the location of the output data is selected to be a shallow water location (the depth of the point in the computational grid is 5m) nearby port Burgas. The shallow Burgas Bay is usually the most affected area by the storm surges (the town Pomorie that was inundated more than once is located in this bay), which was the reason why the Burgas bay has been selected.

To study the changes of the storm surge characteristics we used the highest annual surge height and some cumulative characteristics such as the total annual number of events and total annual duration of events above a certain threshold (40cm, 60cm and 80cm- low, moderate and high surges taking into account the specifics of the local storm surges). The numbers of events are denoted as n>40, n>60 and n>80 and the total duration of events h>40, h>60 and h>80 where the number is the threshold in cm. In order to characterise the energetics of the storm surge event we introduced an index which we call storm surge index that is calculated multiplying the squared highest height of an event multiplied by the duration of the event above a threshold value (in the present study we used 60cm as a threshold for being selected as a threshold of the moderate events, based on our experience with the operational surge prediction). The reason to introduce the index in such form is analogously to

the Storm Power Index introduced for the sea waves by Dolan and Davies (Dolan and Davis, 1992) which is the squared maximum significant wave height during the storm (which is proportional to the wave energy) multiplied by the duration above a threshold wave height. The storm surge is a long wave and therefore a similar approach to Dolan and Davies is reasonable to characterise the power of a single storm surge event and the cumulative annual value to characterize a storm season. Hereafter we denote the storm surge power index as nhh (n-duration, h- height).

RESULTS AND DISCUSSION

For the studied location within the Burgas Bay for the entire period 01.01.1979 to 31.05.2020 after processing of the results of the surge hindcast we identified 282 events with sea level rise above 40cm, 113 events above 60cm (moderate and significant events), and 30 events above 80cm (i.e. one or zero events per year, that we will classify as signicant events) and 7 events above 1m (events that potentially can lead to catastrophic consequences) of which two events are above 1.2m (1981 and 2012). For the event of February 1979 it is mentioned in the literature (Andreeva et al, 2011) that the surge was above 1.4m in the Burgas Bay, however it seems that the numerical model underestimates this event. Underestimation of the most extreme events is a limitation of the study and it is caused most likely due to underestimation of the extreme winds in the reanalysis that may be reduced by downscaling of the reanalysis- the approach used in (Bresson et al, 2018) and (Galabov et al, 2015). The underestimation may also be explained partially by the relatively low spatial resolution of the storm surge model. In (Galabov et al, 2015) a significant underestimation was observed- maximum surge less than 1m while using ERA Interim, while with the usage of ERA5 the maximum surge level is 1,16. While the use of ERA5 obviously still leads to some underestimation of extreme events but our goal here is to study the inter-annual changes instead of obtaining accurate values for single extreme events.

The characteristics of the three highest surges are given in table 1. The highest surge is the surge of 2012, while the surge of the 1979 is the longest (notice however, that the phase of the event that is above 1m is the longest for the event of 2012). If we set the threshold for calculating the storm surge index at 60cm, we obtain that the surge of 1979 is the most powerful, but the one in 2012 is close. The same conclusion of the surge of 1979 as being the most powerful is valid if we set the threshold at 40 or 80 cm. Further in the study we are going to use the value of 60cm as a threshold in order to select powerful enough events to calculate the storm surge index, but also to set it lower enough to be able to calculate it for each year (i.e. to avoid zero values). The temporal evolution of these three events is given on figure 1.

The total annual duration and number of events above a threshold (40, 60 and 80cm) is shown of figure 2. Notice that 1979 is not included, because ERA5 is not available for the entire winter season of 1978/179.

As it may be seen, the duration and number of events above 80cm does not show signs of a trend- trends are tested for statistical significance using the Mann and Kendall test (Mann, 1946), (Kendall, 1976). The winter season with the highest duration above 80cm is 2011/2012. The number and duration of events above 60cm does show some positive trend that is not statistically significant. The number and duration of events above 40cm show also a positive trend that is stronger for the number of events. The duration above 40cm is without statistically significant trend, while the trend in the number of events is the only trend of a storm surge indicator in this study that is statistically significant. This means that while there is no change in the total annual duration and number of the storm surges above 80cm, we do observe some increase in the number of low storm surge events (in the range 40-60cm), while their total duration does not changes that much- we observe more but shorter events in the lower range. The conclusion that there is no change in the number and duration of events above 80cm is showing us that there are no signs of changes in the frequency of the significant and catastrophic events that may cause damages and significant coastal flooding.
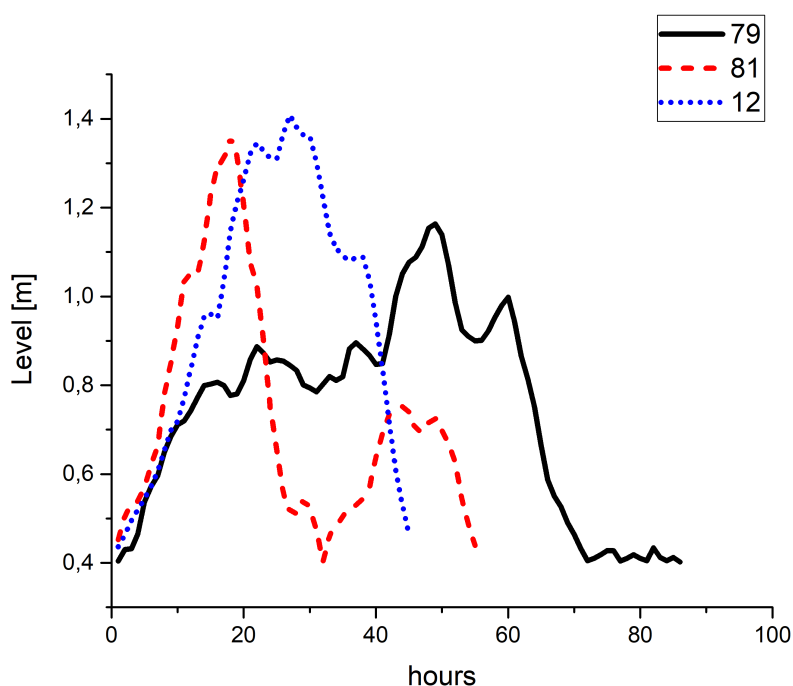
Figure 1. The temporal evolution of the three highest and most powerful surges during the period 1979-2020 according to the numerical hindcast.
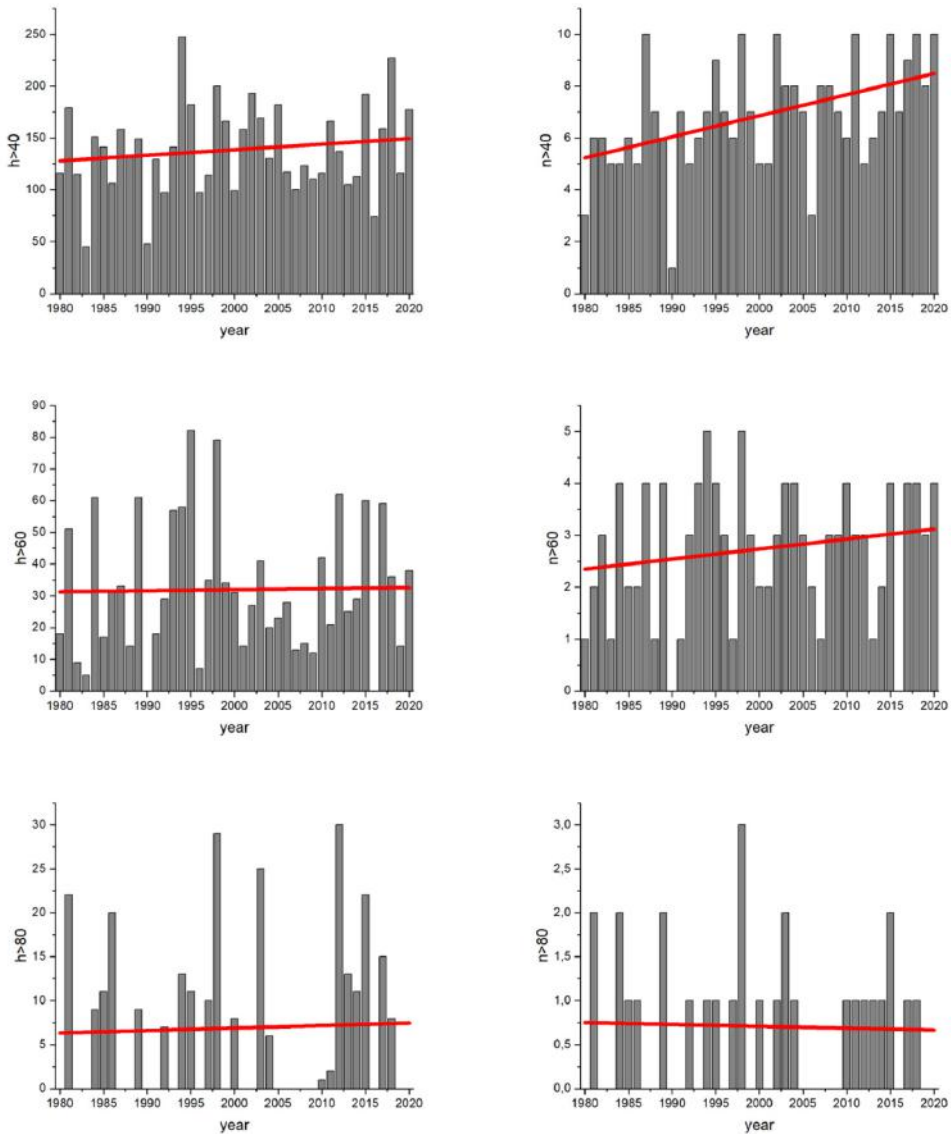
Figure 2. On the left side: total annual duration in hours of the events above a threshold (above 40cm- upper picture, above 60cm- middle row picture, above 80cm – lower row picture). On the right side: total annual number of events (storms) above a threshold (40cm- upper row, 60cm- middle row, 80cm- lower row)

Table 1. Characteristics of the three most significant surges in the period
1979–2020. The storm surge index was calculated using 60cm as a threshold.

Date	Duration above 40cm (h)	Duration above 60cm (h)	Duration above 80cm (h)	Duration above 1m (h)	Maximal surge (m)	Storm Surge Index (m2h)
17-20.02.1979	86	57	46	9	1.16	77
8-10.01.1981	55	20	15	12	1.36	37
6-8.02.2012	45	37	30	23	1.41	74

The annual maximum surge level and the storm surge index are shown on figure 3. As it may be seen, 1981 and 2012 are with the highest values of the surge level and also with the highest values of the storm surge index (and 2012 is with the highest value). For both indicators there is no statistically significant trend for the selected period, which strengthens the conclusion, that we do not observe changes in the frequency of the moderate and significant surges and no significant changes in the magnitude of the storm surges in terms of total annual maximum and storm surge index (characteristic of the total power). Of course the study has some limitations- the period is relatively short. Our further plans include an extension of the present study to the period 1950-2020 when ERA5 becomes available for the period 1950-1978.

We also used a spectral analysis of the studied indicators in order to search for signs of intra-decadal oscillations. For all of the mentioned indicators we found signs of an oscillation with a period of about 2.5 years. An oscillation with a similar period for the Black Sea level at the Bulgarian tide gauges was found by Pashova
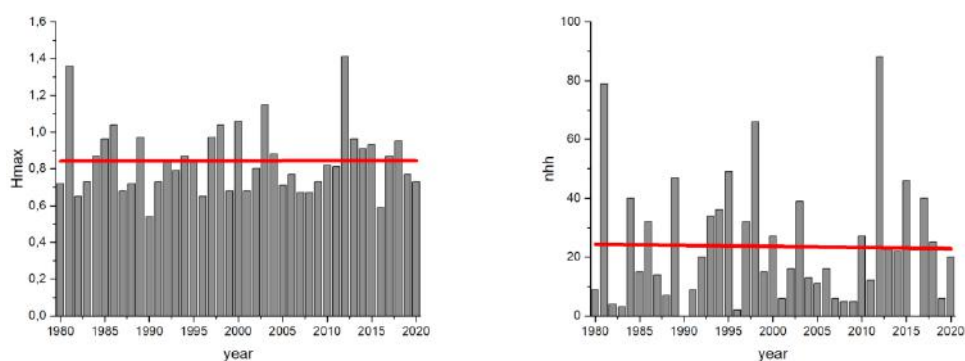
Figure 3. On the left side- the annual maximum surge (m). On the right side- the total annual storm surge index nhh (m²h) for the period 1980-2020

(Pashova, 2012). Such period of 2.4 years is characteristic of the North Atlantic Oscillation (NAO) as it was found by (Gámiz-Fortis et al, 2002). Another period of about 8 years was found for the storm surge index. Such period of an oscillation may also be explained by a relation between the Western Black Sea storm surges and the 8 years oscillation of NAO see (Pozo-Vázquez et al, 2000).

CONCLUSIONS

In this study we presented the characteristics of the storm surges affecting the Bulgarian Black Sea coast for the period 1979- 2020, based on a numerical modelling using the storm surge model of METEO FRANCE, modified for an use in the Black Sea. The input atmospheric data was obtained from the European atmospheric reanalysis ERA5. The highest surge in the model output was the surge of February 2012, while the longest and most energetic was the surge of February 1979. We studied the total annual number and duration of the surges above different threshold sea levels and also the annual maximum and the total annual value of the introduced in the study storm surge power index. We found no evidence of a trend in the frequency and magnitude of the surges affecting the Bulgarian coast, except for the lower events in the range of 40-60cm which are with increasing frequency, but without such practical importance as the moderate and high surges, which shows no signs of increasing frequency and intensity. We also found that the intra- decadal oscillations of the storm surge indicators may be explained by the corresponding oscillations of NAO. Our plans include an extension of the study to the period 1950- 2020 when ERA5 becomes available for the years before 1979.

REFERENCES

Andreeva, N., Valchev, N., Trifonova, E., Eftimova, P., Kirilova, D., & Georgieva, M. (2011). Literary review of historical storm events in the western Black Sea. Proc. of Union of Scientists–Varna, Marine Sciences, 105-112.

Bresson, É., Arbogast, P., Aouf, L., Paradis, D., Kortcheva, A., Bogatchev, A., ... & Tsenova, B. (2018). On the improvement of wave and storm surge hindcasts by downscaled atmospheric forcing: application to historical storms. *Natural Hazards & Earth System Sciences*, *18*(4).

Daniel, P. (1997). Forecasting tropical cyclones storm surges at Meteo-France. *WIT Transactions on The Built Environment*, *30*, 119-138.

Dolan, R., & Davis, R. E. (1992). An intensity scale for Atlantic coast northeast storms. *Journal of coastal research*, 8(4), 840-853.

Galabov, V., Kortcheva, A., Bogatchev, A., & Tsenova, B. (2015). Investigation Of The Hydro-Meteorological Hazards Along The Bulgarian Coast Of The Black Sea By Reconstructions Of Historical Storms. *Journal of Environmental Protection and Ecology*, *16*(3), 1005-1015.

Galabov, V. (2018) Operational storm surge modelling in the Western Black Sea: one way coupling with a wave model. *Bulgarian Journal of Meteorology and Hydrology*, 21, 1-2, 10-23.

Gámiz-Fortis, S. R., Pozo-Vázquez, D., Esteban-Parra, M. J., & Castro-Díez, Y. (2002). Spectral characteristics and predictability of the NAO assessed through singular spectral analysis. *Journal of Geophysical Research: Atmospheres*, *107*(D23), ACL-11.

Hersbach, H., Bell, B., Berrisford, P., Hirahara, S., Horányi, A., Muñoz-Sabater, J. ... & Simmons, A. (2020). The ERA5 global reanalysis. *Quarterly Journal of the Royal Meteorological Society*. (In in print).

Kendall, M. G., & Stuart, A. (1976). The Advanced theory of statistics: Distribution theory (Vol. I). London: Griffin

Krestenitis, Y. N., Androulidakis, Y., & Kombiadou, K. (2012). Storm surge modelling in the Black Sea. *Proceeding of protection and restoration of the environment XI, At Thessaloniki, Greece*, 786-795.

Mann, H. B. (1945). Nonparametric tests against trend. *Econometrica*, 13, 245–259.

Mungov, G., & Daniel, P. (2000). Storm surges in the western Black Sea. Operational forecasting. *Mediterranean Marine Science*, *1*(1), 45-50.

Pashova, L. (2012). Assessment of the sea level change on different timescales from Varna and Burgas tide gauge data. *CR Acad Bulg Sci, 65 (2)*. 193-202.

Pozo-Vázquez, D., Esteban-Parra, M. J., Rodrigo, F. S., & Castro-Díez, Y. (2000). An analysis of the variability of the North Atlantic Oscillation in the time and the frequency domains. *International Journal of Climatology: A Journal of the Royal Meteorological Society*, *20*(14), 1675-1692.

✉ **Vasko Galabov**
http://orcid.org/0000-0003-3269-1486
National Institute of Meteorology and Hydrology
Sofia, Bulgaria
E-mail: vasko.galabov@meteo.bg

SEISMOLOGICAL ANALYSIS
OF THE 2006 KARDZHALI EARTHQUAKE

Plamena Raykova, Dimcho Solakov, Stela Simeonova
*National Institute of Geophysics, Geodesy and Geography –
Bulgarian Academy of Sciences (NIGGG-BAS)*

Abstract: Studying of the space-time distribution of earthquakes is very important for understanding the physics of the earthquake generation process. The 2006 M_w4.7 KARDZHALI earthquake was followed by an intensive aftershock activity. We analyze the space-temporal pattern of earthquake distribution in the aftershock sequence of the main event. We find that both space and temporal distribution of aftershocks shows non-random features.

In this study P- and S-wave spectra for earthquakes from the seismic cluster (main earthquake - aftershocks) are generated. Earthquake parameters: seismic moment, source radius, stress drop are estimated applying Brune model for the M_w4.7 quake and five aftershocks with magnitude M_w in the interval 3.3 ÷ 3.7. The estimated stress drop value for the main event is within the expected range for moderate earthquakes (43 bars for the P-wave and approximately 65 bars for the S – wave).

Keywords: aftershocks, P and S-waves spectra, stress drop, seismic moment, seismic moment magnitude

INTRODUCTION

The spatial and temporal clustering of aftershocks is a dominant non-random element of the seismicity, so when the clusters are removed, the remaining activity can be modelled (as first approximation) as a Poisson process (Gardner and Knopoff, 1974). A formal definition of seismic clusters is still lacking despite of the conception that the earthquake clustering is an essential aspect of seismicity that provides key information on earthquake dynamics (Zaliapin and Ben-Zion, 2013).

Aftershocks are defined as seismicity above the background activity following a main shock. Aftershocks occur after the main event and their frequency decays over time, typically following a pattern known as the Omori's law, which later is modified by Utsu (1969) and is known as modified Omori's law. The power-low decay represented by the modified Omori relation is an example of temporal self-similarity of the earthquake source process.

The manifold purpose of our study is first to examine spatial and temporal pattern of aftershock distribution in the epicentral zone of the 2006 KARDZHALI M_w4.7 earthquake (M_w is estimated using relations $M_w=M_w(Md)$ presented in Solakov et al., 2018), then to test different statistical models for aftershock occurrence based on the transformation of the time scale t to a frequency-linearized time scale τ. Finally, the Akaike Information Criterion (Akaike, 1974) is used to select the best statistical model for aftershock occurrence.

Spectral analysis of seismic waves is one of the most important origin of information for the earthquake sources. In our study spectra of P- and S-waves for earthquakes from the seismic cluster (main earthquake - aftershock) of the 2006 KARDZHALI earthquake are generated. Earthquake parameters: seismic moment, source radius, and stress drop are estimated applying Brune model.

METHOD AND DATA
Methodology
For the aftershock data, we used the model obeying the modified Omori's law (Utsu, 1969):

$$n(t) = K(t+c)^{-p},$$
(1)

where $n(t)$ is frequency of aftershocks at time t; t is the elapsed time since the occurrence of the main shock, and K, p, c are constants.

Based on the assumption that aftershocks are distributed as a non-stationary Poisson process, Ogata (1983) proposed to use the maximum likelihood method for estimating the parameters K, c and p in the modified Omori formula.

The intensity function of the Poisson process (t) is defined by the relation:

$$\lambda(t) = \lim_{\Delta \to 0} Prob\{an\ event\ in\ [t,t+\Delta t]\} / \Delta t$$
(2)

Then the likelihood function of the aftershock sequence can be as follows:

$$f(t_1,t_2,t_n,\theta) = \prod_{i=1}^{N} \lambda(t_i;\theta) exp(\int_{S}^{T} \lambda(t;\theta)dt),$$
(3)

where the t_i {i=1,2, ... ,N} are the occurrence times of the events in the available period of observation [S, T] and the corresponding vector θ is $\theta =(K, p, c)$.

Using the modified Omori formula, the intensity function becomes:

$$\lambda(t,\theta) = K\ (t\ +\ c)^{-p}$$
(4)

The maximum likelihood estimates (MLE) of the parameters are those, which maximize function (4) with the corresponding vector θ (Ogata, 1983).

An integration of the intensity function $\lambda(t)$ gives a transformation from the time scale t to a frequency-linearized time scale τ (Ogata and Shimazaki, 1984). On this

time axis the occurrence of aftershocks becomes the standard stationary Poisson process if the choice of the intensity function $\lambda(t)$ (i.e. the parameters K, c and p) is correct.

The frequency-linearized time for an aftershock sequence can be defined as:

$$\tau = \Lambda(t) = \int_0^t \lambda(s)ds$$

(5)

A linear dependence between the observed cumulative numbers of aftershocks N and τ should be observed if an appropriate model has been selected. Anomalies in the aftershock activity are more evident on the $N(\tau)$ plot than on $n(t)$.

In order to select which model fits the observations better, the Akaike Information Criterion (AIC) (Akaike, 1974) is used. This is a measure of which model most frequently reproduces features similar to the given observations, and is defined by:

$$AIC = (-2)\,Max\,(ln-likelihood) + 2\,(Number\ of\ the\ used\ parameters)$$

(6)

Spectral analysis of seismic waves is one of the most important origins of information for the earthquake sources. The Brune model is the most common seismic source model extensively used for spectral characteristics. The source parameters of the events are computed following Brune's theory by using the corner frequency and the low frequency asymptote. The Brune model predicts the source displacement spectrum S(f), which depends on M_0 - the seismic moment, ρ - density, v - velocity at the source (P or S-velocity depending on spectrum), and f_0 - corner frequency.

The seismic moment M_0 is the most objective static measure of earthquake size. The scalar seismic moment M_0 is defined by the equation:

$$M_0 = \mu SD,$$

(7)

where μ is the shear modulus of the rocks (in pascals (Pa), i.e. newton per square meter), S – is the area of the rupture along the geologic fault (in square meters), and D is the average slip (displacement offset between the two sides of the fault).

Stress drop σ is the average difference between initial and final stress along a fault after an earthquake. For large, shallow earthquakes, $\Delta\sigma$ vary from about 1 to 10 MPa or from 10 to 100 bars with M_0 variations from 10^{18} to 10^{23} Nm. It has been observed that earthquakes near plate boundaries (interplate events) generally have lower stress drops than those that occur in the interior of plates (intraplate events) (e.g. Kanamori and Allen, 1986). In average $\Delta\sigma$ for interplate quakes is about 3 MPa (30 bars), while for intraplate events it is about 6 MPa (60 bars) (Allmann and Shearer, 2007).

For a circular fault in a whole space, Eshelby (1957) obtained:

$$\Delta\sigma = \frac{7}{16}\frac{M_0}{r^3},$$

(8)

where r is the fault radius and M_0 is seismic moment.

The first quantitative model for estimating stress drop was derived by Brune (1970), who assumed a simple kinematic model for a circular fault with effectively infinite rupture velocity and showed that the expected high-frequency spectral falloff rate is ω^{-2} and that the corner frequency is inversely proportional to the source radius. This result predicts that the fault radius varies as:

$$r = \frac{k\beta}{f_c},$$

(9)

where r is the fault radius, f_c is the observed corner frequency and k is a constant that depends upon the specific theoretical model.

The parameters M_0, $\Delta\sigma$ and r are calculated using the following relationships.

The seismic moment for P-wave (M_{0n}) is calculated as:

$$M_{0p} = \frac{\rho.4\pi.\Omega_p.R.v_p^2}{R_{\theta\varphi}(P)}$$

(10)

where ρ – density in g/cm³, Ω_p – spectral level in nm, v_p – velocity of P-wave, R – distance in km, $R_{\theta\varphi}(P)$ – radiation pattern.

The average correction for radiation pattern varies between 0.55 and 0.85. According to Aki and Richards, the average is 0.52 and 0.63 for P and S-waves, respectively (Aki and Richards, 2002).

The seismic moment for S-wave (M_{0s}) is calculated as:

$$M_{0s} = \frac{\rho.4\pi.\Omega_p.R.v_s^2}{R_{\theta\varphi}(S)}$$

(11)

where ρ – density in g/cm³, Ω_s – spectral level in nm, which is determined by the spectra of wave, and its value is determined by Z, N, E – components, $R_{\theta\varphi}(S)$ – radiation pattern, which for seismic moment for S-wave is 0.63, and v_s is velocity of S-wave.

The following formulas are used to determine the source radius and stress drop:

$$R_p = \frac{v_p.3.36}{2\pi f_0},$$

(12)

where v_p is P-wave velocity, and f_0 is corner frequency in Hz.

For S-wave, the source radius is determined in an identical approach:

$$R_s = \frac{v_s.2.34}{2\pi f_0},$$

(13)

where v_s is S-wave velocity, and f_0 is corner frequency in Hz.

The stress drop for P- and S-waves are calculated using the following relationships (Eshelby, 1957):

$$\Delta\sigma_p = \frac{7}{16}\frac{M_{0p}}{R_p^3}$$ (14)

$$\Delta\sigma_s = \frac{7}{16}\frac{M_{0s}}{R_s^3}\ ,$$ (15)

where R_p and R_s are the radius for P- and S-waves.

To meet the objectives of the present study a set of data including all events recorded by NOTSSI that are located in the vicinity of the inferred rupture zone of the 2006 $M_W 4.7$ KARDZHALI earthquake is compiled.

We accept that aftershocks satisfy the space-time criteria introduced by Gardner and Knopoff (1974) and modified by Christoskov and Lazarov (1981) for the Central Balkans:

$$log\ R_a(M_m)\ =\ 0.9696\ +\ 0.1243\ M_m$$

$$log\ T_a(M_m)\ =\ -0.62\ +\ 0.56\ M_m \qquad (M_m < 6.0)$$ (16)

$$log\ T_a(M_m)\ =\ -5.25\ +\ 2.15\ M_m\ -\ 0.137\ M_m^2 \quad (M_m \geq 6.0),$$

where M_m is the surface-wave magnitude of the main event, R_a is the largest distance between the main event and an aftershock, and T_a is the greatest elapsed time since the occurrence of the main shock.

RESULTS

The results of the present study are presented in Figs. 1-5 and Tables 1-2. The spatial distribution of earthquakes in the considered sequence is shown in Fig. 1. The temporal distribution of aftershocks is presented in Fig. 2-3, and Table 1. Results of spectral analysis is presented in Figs. 4-5 and Table 2.

Spatial distribution

Figure 1 illustrates spatial distribution of 130 aftershocks observed after the 2006 ($M_W 4.7$) earthquake that is located near the city of Kardzhali (seismogenic zone Eastern Rhodopes).

Figure shows the following characteristics: 1) the main shock and aftershock activity are clustering in an area, that is not associated with the defined fault structures; 2) a well-expressed tendency of aftershock area expansion in time and with decrease of magnitude is observed; 3) the aftershocks with magnitude $M_p < 3.0$ are dispersed in space and spread over large area.
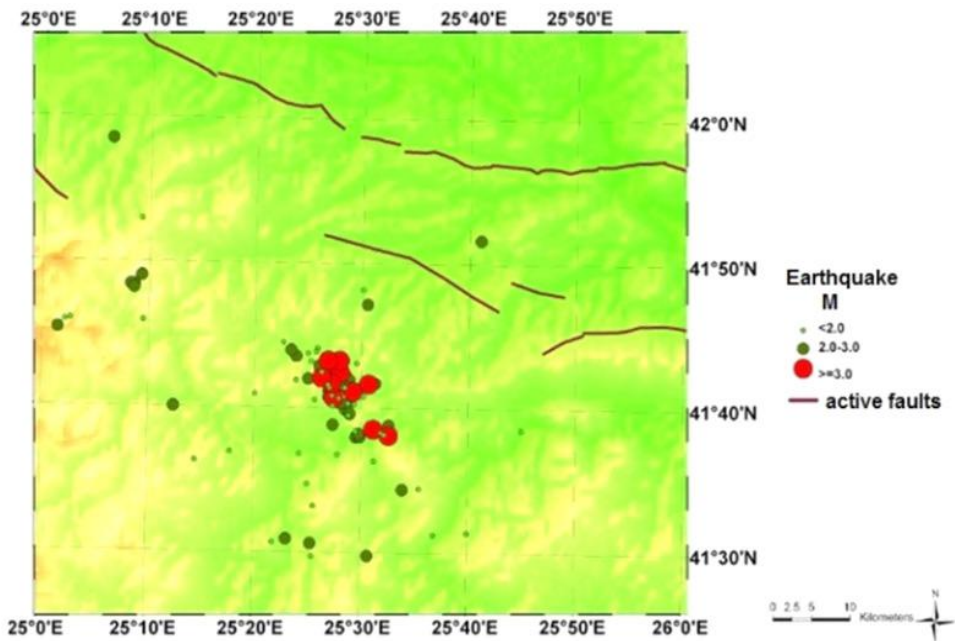
Figure 1. Epicentral map of the 2006 earthquake (M_W4.7) aftershocks.
The identified faults (modified from Report of Geoph.Inst.-BAS, 2008)
are denoted by dark red lines.

Temporal distribution

We analyze the aftershock sequence from 0 to T_a=50 days after the main earthquake. The time interval T_a is the calculated value of the greatest elapsed time since the occurrence of the main shock using equation (16). In the study two sets of data are analyzed – the first includes all aftershocks, the second data set covers all events with magnitude M_p≥2.0, located inside the area of interest.

The parameters K, c and p in the modified Omori formula (equation 1) are estimated using the maximum likelihood method. The estimated values for these parameters are presented in Tab. 1. The frequency-time distributions of earthquakes are presented in Fig. 3.

The cumulative number of events is plotted against the frequency-linearized time (as defined in eq. 5) using the estimated parameters K, p, c (Fig. 3). The observed distribution is compared to the theoretical distribution, based on the selected model (in this case, the model is the modified Omori formula). If the modeling of the sequence is appropriate, the cumulative number of events will increase linearly with τ. There is a relatively good correlation between the theoretical and the observed distribution for both analyzed cases.

The results (Fig. 3 and Tab.1) show that the model with an ordinary aftershock sequence, without threshold magnitude describes best the aftershock sequence of the 2006 earthquake.

Figure 3 shows that a nearly - linear trend of aftershock decay continues up to 53 days. About 53 days after the main shock the cumulative number of aftershocks increases rapidly with τ, showing a significant deviation from the prior trend. No large earthquake occurred in the region at that time. Therefore, this change in slope could be treated as a transition from aftershock activity to background seismicity. It should be noted that the predicted (by eq.16) duration of the aftershock activity is 42 days (by eq.16), which is approximately the same as observed duration.

a)   b)
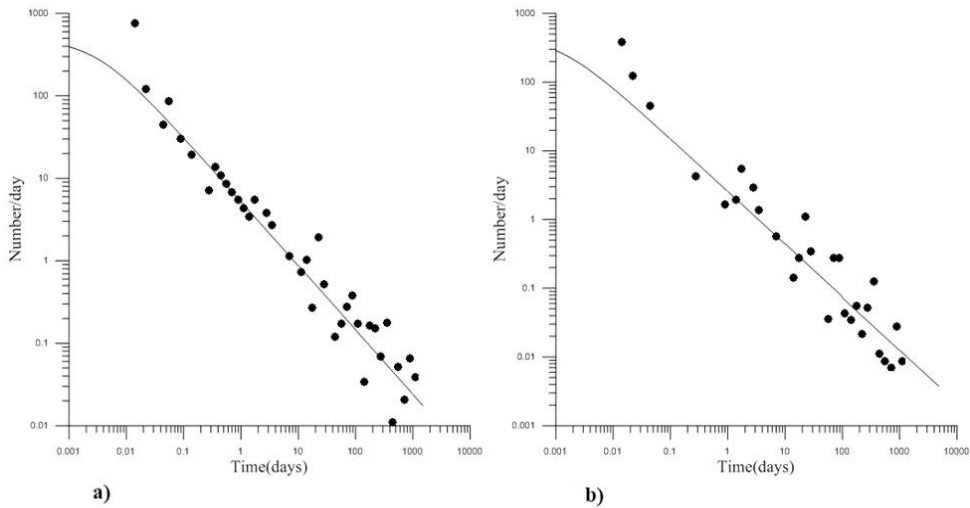
Figure 2. Frequency-time distributions of aftershocks; a) for a set of data including all aftershocks; b) aftershocks with magnitude, $M_p \geq 2.0$

Table 1. MLE's of the Omori formula parameters and corresponding AIC

Model	K	P	c	K_1	p_1	c_1	AIC
An ordinary aftershock sequence, without threshold magnitude	7.282	0.780	0.003				-8.564
An ordinary aftershock sequence, with threshold magnitude $M_a = 2$	2.554	0.768	0.001				31.198

The *p* value estimated for the aftershock sequence is in the middle of *p* value range obtained for aftershock sequences in Bulgaria and surroundings, (*p* $\in$ [0.71;1.17]) (Simeonova, Solakov, 1999).

a)

b)
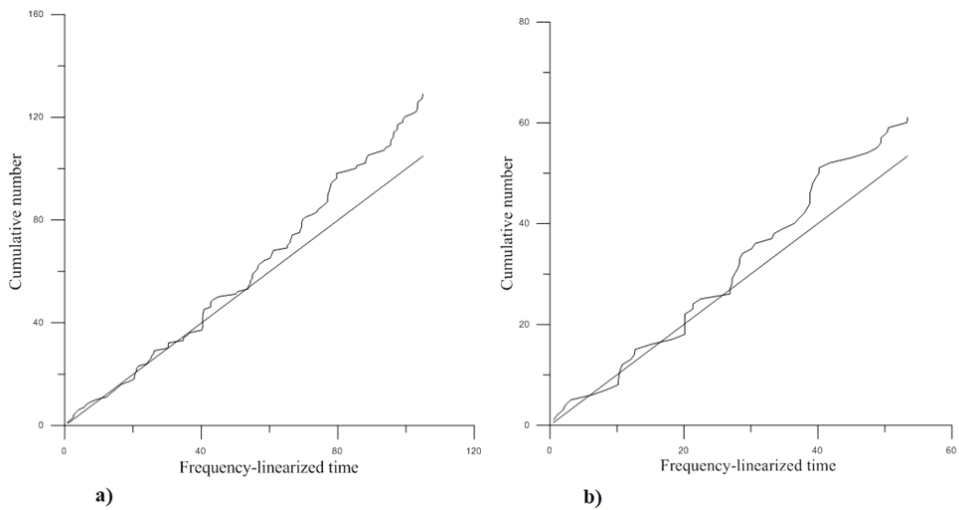
Figure 3. Plot of the cumulative number of events versus frequency-linearized time: a) all aftershocks; b) aftershocks with magnitude, $M_p \geq 2.0$

Spectral characteristics

Displacement spectra for P- and S- waves are generated for the seismic cluster occurred in 2006 in the Southern Bulgaria (seismogenic zone Eastern Rhodopes). The source parameters are estimated for 6 earthquakes: the M_W4.7 main event and five aftershocks with M_W in the range 3.3 ÷ 3.7.

The main event spectra are generated on the base of records at 7 stations (35 displacement spectra). Displacement spectra for P and S waves based on records at 3 stations are presented in the Fig.4. In the figure 5 are presented spectra for five of the strongest aftershocks. In the table 2 are shown source parameters of the events in the 2006 seismic cluster (the main shock and 5 aftershocks).

Table 2. Seismic source parameters of the earthquakes in the2006 seismic cluster that is located near the city of Kardzhali (seismogenic zone Eastern Rhodopes).

Date	φ(°)/ λ(°)	H (км)	M_W	Station	M_{0p} (Nm$_p$)	σ_p (bar)	S_r (км)	M_{0s} (Nm)	σ_s (bar)	S_r (км)
20.02.2006	41.69/25.48	13	4.7	7	1.69E+16	43.46	1.24	8.68E+16	65.29	1.72
20.02.2006	41.68/25.46	13	3.4	5	1.54E+13	25.64	0.18	1.94E+13	51.18	0.14
24.02.2006	41.72/25.47	20	3.3	5	7.57E+13	39.10	0.25	1.04E+14	63.54	0.20
24.02.2006	41.69/25.49	17	3.4	5	7.5E+13	11.02	0.35	1.02E+14	19.00	0.28
14.03.2006	41.70/25.45	12	3.7	5	2.24E+14	18.10	0.43	3.53E+14	39.36	0.33
14.03.2006	41.72/25.45	10	3.5	5	1.71E+14	7.94	0.52	2.02E+14	25.28	0.32

The results (based on P - wave and S - wave spectra) show that the stress drop for the main event is within the expected range for a moderate earthquake - about 43 bars for the P-wave and approximately 65 bars for the S - wave. The strongest aftershocks are characterized with lower than the main event stress drop values - varying between 7.94 - 39.1 bar for P wave; and 19.0 - 63.54 bar for S wave. Source radius for the main event is approximately 1.7 km. The results for the source radius for aftershocks are from 0.2 km to 0.5 km. The seismic moments for aftershocks in the range $1.54*10^{13} \leq M_0 \leq 3.53*10^{14}$ (Nm) and the corresponding moment magnitudes, M_W (estimated by displacement spectra), are in the interval $2.7 \leq M_W \leq 3.5$.
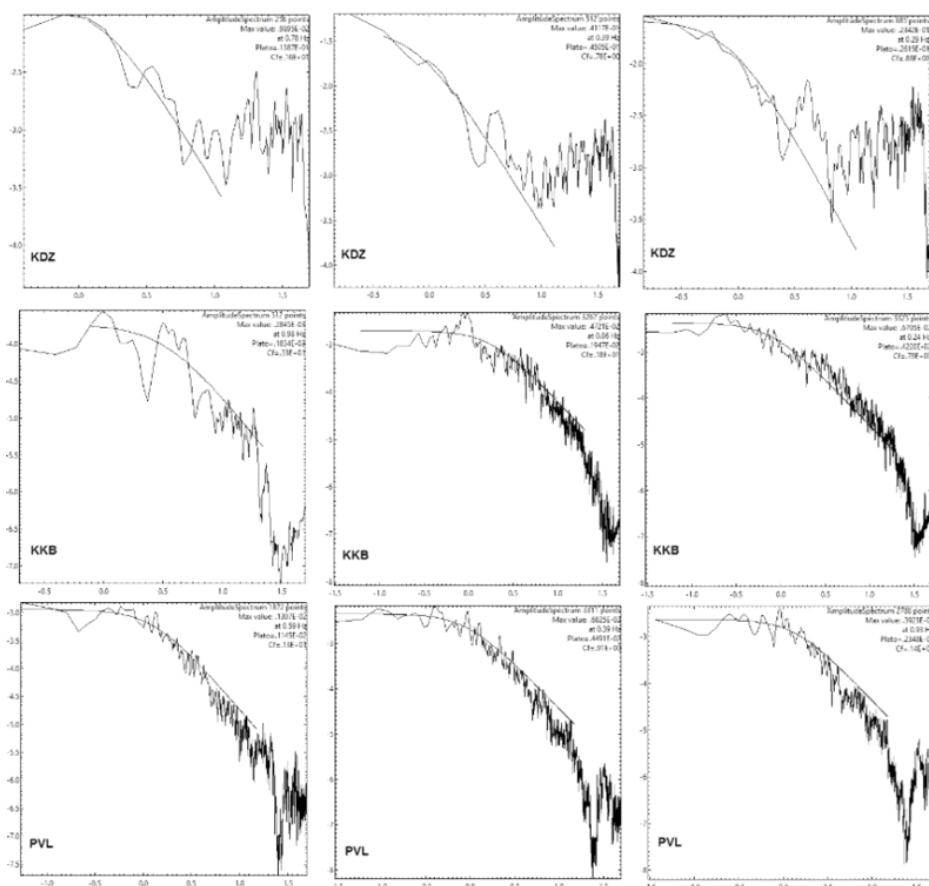
Figure 4. Displacement spectra for P (the most left column) and S waves for main event
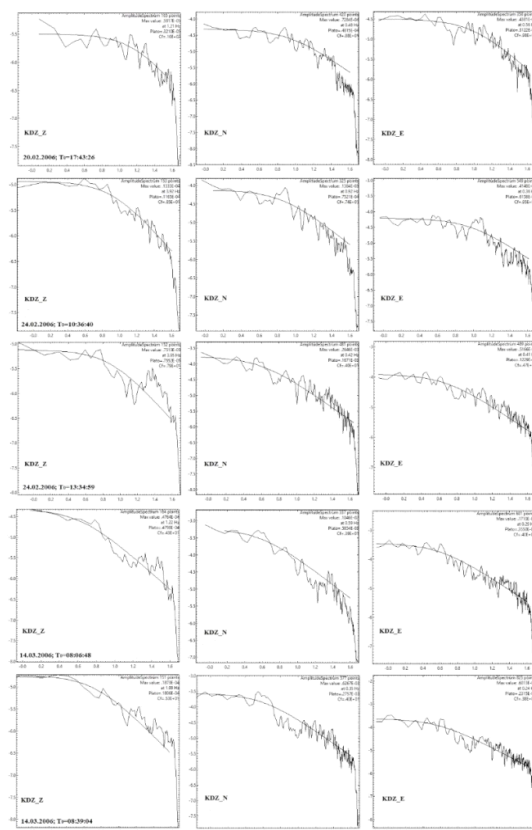
Figure 5. Displacement spectra for P (the most left column) and S waves
for the strongest aftershocks of the 2006, Southern Bulgaria, earthquake

CONCLUSIONS

The spatial distribution of earthquakes is not uniform before and after the main shock on February 20, 2006. Larger events tend to be more clustered than smaller ones.

Temporal distribution of events in aftershock sequence is well described by the modified Omori formula. The *p* value estimated for the aftershock sequence is in the middle of *p* value range obtained for aftershock sequences in Bulgaria and surroundings. Transition from aftershock activity to background seismicity is observed about 53 days after the main shock.

The estimated stress drop values for the main event is within the expected range for moderate earthquakes. The strongest aftershocks are characterized with lower than the main event stress drop values.

ACKNOWLEDGMENTS

REFERENCES

Akaike, H. (1974). A new look at the statistical model identification. *IEEE Trans. Autom. Control AC*-19, 716-723.
Such a source is cited in the main text as (Akaike, 1974)
Aki, K., P.G. Richards. (2002). *Quantitative seismology*. Second Edition, ISBN 0-935702-96-2, University Science Books, Sausalito, 704 pp.
Such a source is cited in the main text as (Aki and Richards, 2002)
Allmann, B. P., Shearer P.M. (2007). Spatial and temporal stress drop variations in small earthquakes near Parkfield, California. *J. Geophys. Res,* VOL. 112, B04305, doi:10.1029/2006JB004395
Such a source is cited in the main text as (Allmann and Shearer, 2007)
Brune, J. (1970). Tectonic stress and the spectra of seismic shear waves from earthquakes. *J. Geophys. Res.*, 75, 4997–5009.
Such a source is cited in the main text as (Brune, 1970)
Christoskov, L., Lazarov R. (1981). General considerations on the representativeness of the seismological catalogues with a view to the seismostatistical investigations. *Bulg.Geoph. J.*, 3, 58-72 (in Bulgarian).
Such a source is cited in the main text as Christoskov and Lazarov (1981)
Eshelby, J. D. (1957). *The determination of the elastic field of an ellipsoidal inclusion and related problems*. In: Proc. R. Soc. Lond. A 241, 376–396.
Such a source is cited in the main text as (Eshelby, 1957)
Gardner, J. K. and Knopoff L. (1974). Is the sequence of earthquakes in Southern California, with aftershocks removed Possionian? *Bull. Seis. Soc. Am.*, 64(5) 1363-1367.
Such a source is cited in the main text as (Gardner and Knopoff, 1974)
Kanamori, H., and Allen C. (1986). Earthquake repeat time and average stress drop, in Earthquake Source Mechanics*, Geophys. Monogr*. Ser., vol. 37, edited by S. Das, J. Boatwright, and C. H. Scholz, pp. 227– 2352, AGU, Washington, D.C
Such a source is cited in the main text as (Kanamori and Allen, 1986)
Ogata, Y., Shimazaki K. (1984). Transition from aftershock to normal activity: the Rat Islands earthquake aftershock sequence. *Bull. Seism. Soc. Am.*, 74, 1757-1765.
Such a source is cited in the main text as (Ogata and Shimazaki, 1984)

Ogata, Y. (1983). Estimation of the parameters in the modified Omori formula for aftershock sequences by the maximum likelihood procedure. *J. Phys. Earth*, 31, 115-124.
Such a source is cited in the main text as (Ogata, 1983)
Report Geoph. Ist. – BAS, (2008). *Part 6: Geology*. Sofia, fund of NIGGG, 80-113 (in Bulgarian).
Such a source is cited in the main text as (Report of Geoph.Inst.-BAS, 2008)
Simeonova, S. and Solakov D. (1999). Temporal characteristics of some aftershock sequences in Bulgaria. *Annali di Geofisica*, 42, 5, 821-83.
Such a source is cited in the main text as (Simeonova, Solakov, 1999)
Solakov D., Simeonova S., Raykova P., Aleksandrova I. (2018). Empirical rlations converting Md and Mp magnitudes applied in Bulgarian seismological routine practice to moment magnitude. Comptes rendus de l'Acad´emie bulgare des Sciences, 71, 8, 2018, DOI:10.7546/ CRABS.2018.08.09, 1076-1085.
Such a source is cited in the main text as (Solakov et al., 2018)
Utsu, T. (1969). Aftershocks and earthquake statistics (I) - Some parameters which characterize an aftershock sequence and their interaction. *J. Fac. Sc., Hokaido Univ., Ser. VII(Geophys.)*, 3, 129-195.
Such a source is cited in the main text as (Utsu, 1969)
Zaliapin I. and Ben-Zion Y. (2013). Earthquake clusters in Southern California I: Identification and Stability. *J.GEOPHYS. RES., Solid Earth*, 118, 6, 2847-2864.
Such a source is cited in the main text as (Zaliapin and Ben-Zion, 2013)

✉ **Plamena Raykova**
https://orcid.org/0000-0001-7060-0296
National Institute of Geophysics, Geodesy and Geography
Bulgarian Academy of Sciences
Sofia, Bulgaria
E-mail: plamena.raikova@gmail.com

✉ **Dimcho Solakov**
http://orcid.org/0000-0003-4148-0525
National Institute of Geophysics, Geodesy and Geography
Bulgarian Academy of Sciences
Sofia, Bulgaria
E-mail: dimos@geophys.bas.bg

✉ **Stela Simeonova**
National Institute of Geophysics, Geodesy and Geography
Bulgarian Academy of Sciences
Sofia, Bulgaria
E-mail: stelas@geophys.bas.bg

SEISMICITY PATTERNS ASSOCIATED WITH EARTHQUAKES ON THE BALKAN PENINSULA

Emil Oynakov, Dimcho Solakov, Irena Aleksandrova, Yordan Milkov
*National Institute of Geophysics, Geodesy and Geography –
Bulgarian Academy of Sciences (NIGGG-BAS)*

Abstract: Statistical analysis was performed, which revealed statistical parameters of the seismic setting before the earthquake in the region of Crete (01.04.2011 with coordinates 26.56oE, 35.64oN; Ml = 6.2, h = 63 km and T_0 = 13: 29: 10.5). For this purpose, the spatial and temporal changes in the b-value and the value of the Z-seismic lull were estimated. The temporary change in the b-value shows that the average value of b decreased from 1.75 ± 0.02 between 1985 and 2002 to 1.4 ± 0.02 between 2003 and 2011. A significant decrease in the b-value and clear anomalies of calm in the Z-value in early 2011 were also observed in several neighboring areas. The epicenter of the earthquake falls in an area with a relatively low value of the a-parameter estimated for the entire previous period. In the study area, the abnormal decreasing trend of the b-value may be an indicator of increased stress, and the increasing trend of the Z-value may indicate areas of calm before the studied earthquake.
Keywords: earthquake, recurrence graph, seismic hush

INTRODUCTION

The slope value of the repeatability graph (b-value) shows the distribution of the number of earthquakes by their magnitude and is widely used as a characteristic of the seismic process. An interesting property of the slope of the repeatability graph is its change over time. In addition, as noted in a number of publications, time variations (anomalous decrease in the value of b) may indicate a future earthquake (Rani, Srivastava, Srinagesh, Dimri, 2011; Stiphout, Schorlemmer, Wiemer, 2011; Wyss, Sobolev, Clippard, 2004; Wyss, Pacchiani, Deschamps, Patau, 2008). The magnitude-frequency distribution (1) determines the relationship between the frequency of occurrence and the strength of earthquakes (Gutenberg, Richter, 1944):

$$\log N(M) = a + bM, \tag{1}$$

where N (M) is the number of earthquakes with magnitudes greater than or equal to M; a - parameter characterizing the seismic activity; b- parameter describing the relative distribution of the force of events (Bridges, Gao, 2006). Spatial variations in the value of b characterize the seismicity in a given region (Tsukakoshi, Shimazaki, 2008). Usually, at a value of b ≥ 1, heterogeneity of the earth's crust and low voltage are assumed, while at b <1.0, volumes with homogeneity of the earth's crust and high voltage are assumed (Bridges, Gao, 2006). Studies have shown that a decrease in the value of b in the studied seismogenic region may be associated with an increase in stress before major earthquakes (Nuannin, Kulha ´nek, Persson, 2005; Stiphout, Schorlemmer, Wiemer, 2011; Wiemer, Wyss, 1997; Wyss, Stefansson, 2006; Wu, Chang, Zhao, Teng, & Nakamura, 2008).

In addition to variations in the values of b, changes in seismic activity and seismic lull can also be indicators of an impending earthquake. Changes in the rate of seismicity may be related to the physical properties of the earth's crust, for example, changes in the state of stress (Schorlemmer, Neri, Wiemer, Mostaccio, 2003; Urbancic, Trifu, Long, Toung, 1992). A noticeable decrease in seismic activity over months or years around the epicenter of an impending moderate or strong earthquake is considered a seismic lull (Chouliaras, 2009; Rudolf-Navarro, 2010; Wyss, Habermann, 1988). A suitable approach to study changes in seismic rate and seismic activity is the Z-test, used in many studies (Katsumata, 2011; Maeda, Wiemer, 1999; Stiphout, Schorlemmer, Wiemer, 2011).

The present work is aimed at studying the spatial zones around the epicenters of relatively strong earthquakes that occurred on the Balkan Peninsula, for anomalous values of the slope of the recurrence graph and other statistical parameters before the seismic event of 01.04.2011. with epicentral coordinates: 26.56oE, 35.64oN, magnitude Ml = 6.2 and depth h = 63 km.

METHODLOGY
Considering the exponential distribution of earthquakes by magnitude (Gutenberg, Richter, 1944), the value of the slope of the recurrence graph is estimated by the method of maximum likelihood (Utsu, 1965).

$$b = \frac{\log e}{M_{mean} - M_{min}}, \qquad (2)$$

where Mmean - average value of magnitude in the sample, M_{min} - is the minimum magnitude of the sample and is calculated as: M_{min}=Mc-ΔM/2, where ΔM - takes into account the rounding of magnitude and here is selected ΔM = 0.1 (Schorlemmer, Wiemer, Wyss, 2004), and Mc - the magnitude of the completeness of the sample. The root mean square error of the estimate is:

$$\sigma_b = \frac{b}{\sqrt{N}}. \qquad (3)$$

In this study, the spatial distribution of the b-value was calculated using the ZMAP software (Wiemer, 2001; Wiemer, Wyss, 1994), using the maximum likelihood methods and the least squared regression method. According to (Aki, 1965), the maximum likelihood method gives a more solid estimate than the least squared regression method. The first step in analyzing b-values is to determine the magnitude of Mc's completeness and its error. MS is defined as the lowest magnitude at which 100% of events in a given space and time are detected (Wiemer, Wyss, 2000; Wiemer, Wyss, 2002). Values lower than Mc are considered heterogeneous and incomplete.

The Z-test method is based on the research of Wyss and Habermann and (Wiemer, Wyss, 2002; Habermann, 1987), and is focused on the determination of spatiotemporal blocks in the seismically active zone with a significant change in the intensity of the seismic flow of events in the selected energy range. The analysis is based on the statistical function of the Z-test. To determine the seismic calm, the study area is covered with a grid with a fixed pitch. For each network node at a given point in time, the function is calculated

$$Z(t) = \frac{R_1 - R_2}{\sqrt{\frac{\sigma_1^2}{n_1} + \frac{\sigma_2^2}{n_2}}},$$ (4)

where R1 and R2 are the mean values of the earthquake flow velocity, respectively (number of earthquakes in a time window of 30 days) for two time intervals (one lasting at least a year and tied to the test date, the other including all other time); σ1 and σ2 - standard deviations of R1 and R2 respectively for the first and second time interval, and n1 and n2 - number of earthquakes for the respective period. For each node of the network, earthquakes with a depth of the hypocenter up to 70 km are considered. The high ones (positive) values of Z indicate a decrease in the seismicity rate flow and low values indicate an increase (Maeda, Wiemer, 1999). For all nodes of the network with a value of Z> 3 corresponds to 99% reliability of seismic attenuation determination (Wiemer, 2001; Wiemer, Wyss, 1994). The calculated values in the nodes of the network are combined on the principle of spatio-temporal neighborhood and determine the areas with seismic lull.

ZMAP software (Wiemer, 2001) was used for all calculations.

DATA

The present study analyzes a catalog of earthquakes for the period 1964 - 2020.05.18, (University of Athens-http: //dggsl.geol.uoa.gr/en_index.html). The catalog covers data in a spatial window 320 - 440 N and 100 - 300 E with a total number of earthquakes 295029, with depths $0 \leq h \leq 70$ km (Fig. 2, b) and with a magnitude Ml. The catalog is declustered using the Zmap program

(selected parameters: min for UNclustered events [day] = 1; max for clustered events [day] = 10; confidence level = 0.95; XK factor = 0.5; efective min mag cutoff = 1.5; interaction radius factor = 10; epicenter error = 5km; Depht errer = 10km). The program also evaluates Mc ≥ 3.5 (Fig. 2, a), after which the catalog is considered complete. The events below this magnitude threshold are removed, after which 24750 earthquakes remain (Fig. 1). Figure 3 shows a map of the spatial distribution of Ms.
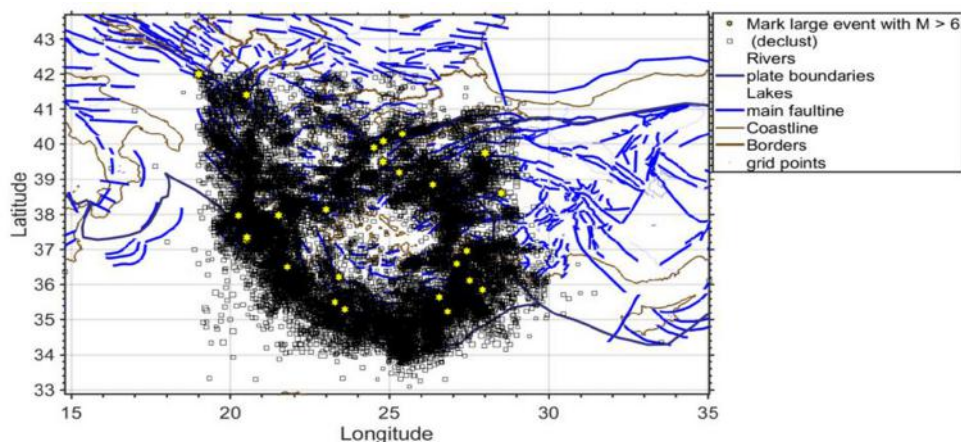
Figure 1. Map of earthquake epicenters with Mc≥3.5
after declustering of the catalog.
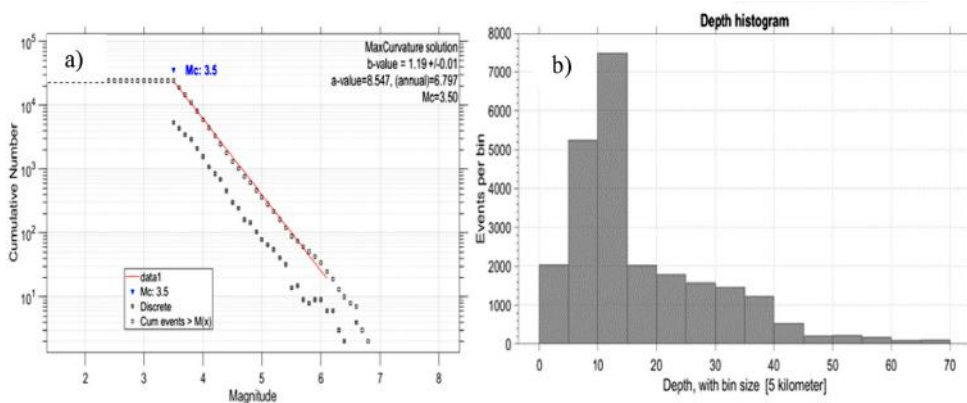
Figure 2. a) graph of the magnitude-frequency distribution Mc> 3.5;
b) histogram of the distribution of the hypocenters of the earthquakes in depth.
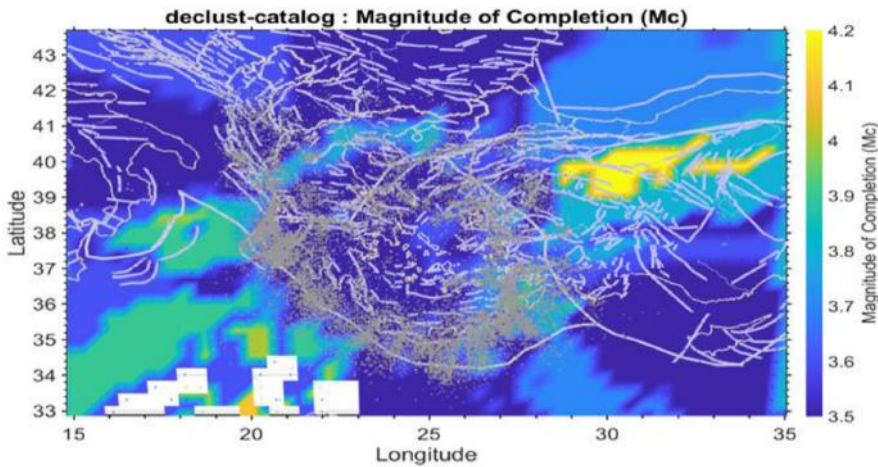
Figure 3. Spatial distribution of the magnitude threshold Mc.

**RESULTS OBTAINED FOR THE EARTHQUAKE FROM 01.04.2011.
WITH COORDINATES 26.56 ° E, 35.64 ° N; M1 = 6.2, H = 63 KM
AND T_0 = 13: 29: 10.5**

A spatial circle with a radius of 100 km and the center of the epicenter of the studied event (26.56 ° E, 35.64 ° N) presented in fig. 4a, containing 2602 events with Mc> 3.5 (Fig. 2b).
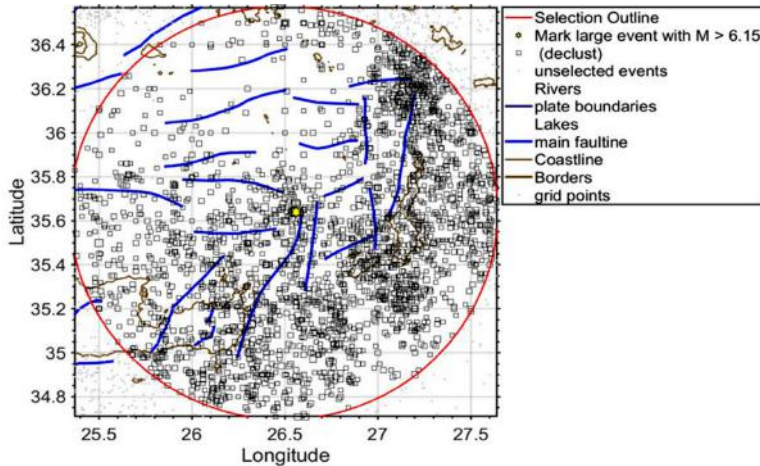
Figure 4. a) Map of the selected spatial circle of research;
b) spatial distribution of MS in the selected circle.

Figure 5 shows the graph of the time change of the b-value in the studied spatial window. The following parameters are set for the construction in the Zmap program: metod-Max Curvature; sample window size = 500; min of events = 50; window overlap (%) = 4; bootstraps = 200; smot plot = 5.
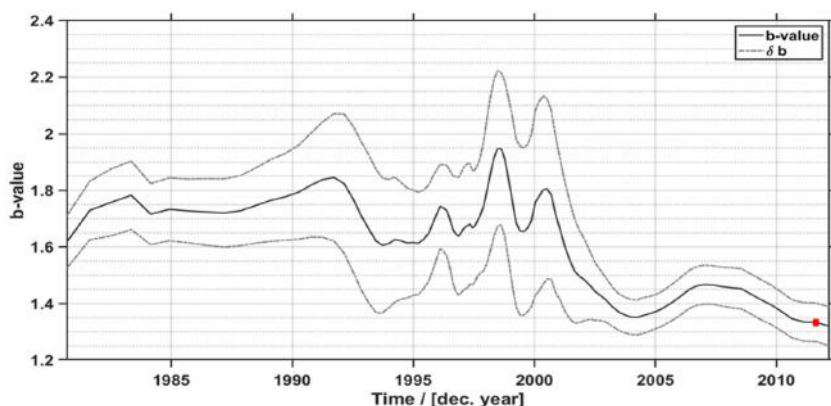
Figure 5. Time change of the b - value of earthquakes with Ml> 3.5 within the studied area;■ - moment of occurrence of the investigated event.

The graph of the value of b (Fig. 5) shows a maximum (b = 1.95) around 1998, which suggests increased heterogeneity and reduced voltages (Görgün Zang, Bohnhoff, Milkereit & Dresen, 2009). Since 2000 The b-value decreases continuously and in 2003 reaches a minimum of b = 1.35. The studied earthquake occurs in a period of decreasing value of b. A significant decrease in the value of b may be associated with an increasing effective level of stress before major earthquakes (Schorlemmer, Wiemer, Wyss, 2004; Wu, Chang, Zhao, Teng & Nakamura, 2008). In addition to the temporal change of the parameter b, the spatial changes in the researches are also analysed spatial circle (Fig. 6), calculated by the method of maximum likelihood (Fig. 6, a) and the method of least squares (Fig. 6, b). The spatial fluctuations of b for the studied landfill were estimated for the period from 1964 to 30.03.2011. hours before the earthquake on 01.04.2011 In the figure in ascending order are marked by low to high values of the b-parameter. Spatial differences in the value of b illustrate variability in plan, and relatively low values can determine the places where an earthquake would most likely occur (Schorlemmer, Neri, Wiemer, Mostaccio, 2003; Westerhaus, Wyss, Yilmaz, Zschau, 2002). The zones with relatively low values of b (0.9 - 1.2) are clearly delineated and the epicenter of the earthquake falls into them. According to (Schorlemmer, Wiemer, Wyss, 2004) and (Motaghi, Hessami, Tatar, 2010) low
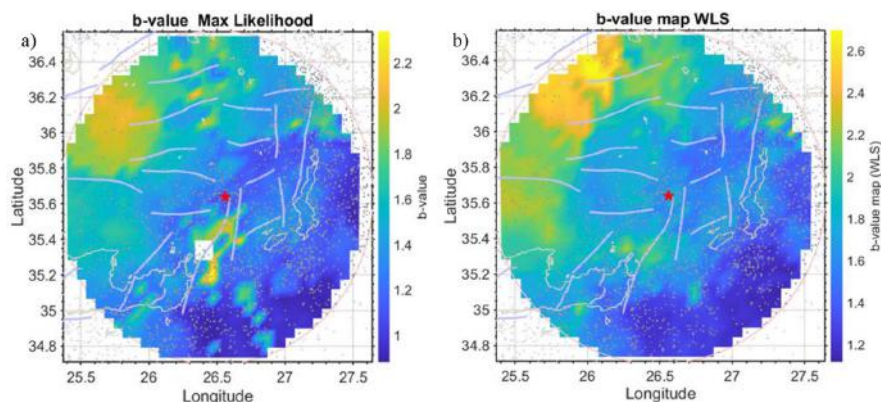
Figure 6. Spatial distribution of the b-parameter, calculated by the methods: a) maximum likelihood; (b) least squares; ⭐ - epicenter of the earthquake from 01.04.2011

values of b indicate that fault stresses accumulate in these zones until the main event is activated. Note that the least squares method gives better results. The spatial distribution of the a-parameter characterizing the seismic activity before the earthquake showed (estimated for the period from 1964 to 30.11.2011) that the epicenter falls in an area with relatively low seismic activity (a = 6-7), but which is close to the zone with relatively high activity (north of the epicenter, a = 9-10) (Fig. 7).

The spatial distribution of the Z-parameter before the earthquake of 01.04.2011 (Fig. 8) is calculated for the same landfill, comparing two time periods: 1st period from 30.03.1997 to 30.03.2005 and 2nd period from 30.03.2005 until 30.03.2011.

The high (positive) Z-values of the maps can be interpreted as a decrease in the flow rate of seismic events (seismic lull) compared to the first period, and the low (negative) Z-values represent an increase in seismicity rate. Earthquake density and distribution is a critical factor in interpreting Z-value variations. Large areas of constant value could show the same density of earthquakes for different periods of time, ie. may show a homogeneous degree of seismicity in this area.

And in the figure (Fig. 8a), the epicenter falls in an area with relatively high values of the Z-value (4-5), which means that the selected period (30.03.2005 to 30.03.2011) before the earthquake is a period of relative seismic lull. The relatively high values of Z = 4 - 5 show 99% reliability of the result. High values of Z = 5-6 are also observed in the northwestern part of the landfill, which may be due to the low density of earthquakes in this part of the landfill. To check, the Z-value was calculated in a polygon excluding the northwestern part. In this case, the epicenter falls exactly in the zone of relative seismic lull (Fig. 8, b - Z ≈ 4.
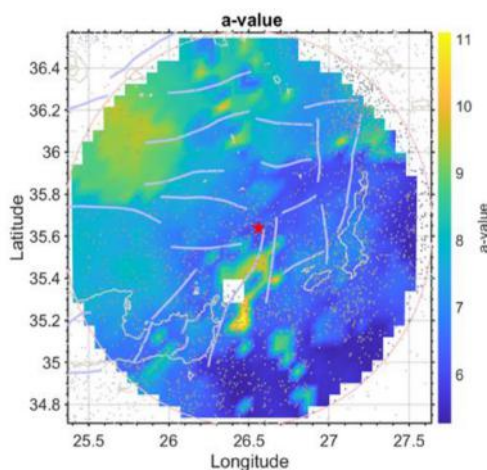
Figure 7. Spatial distribution of the a-parameter for the period 1964-30.03.2011; ★- epicenter of the earthquake from 01.04.2011.
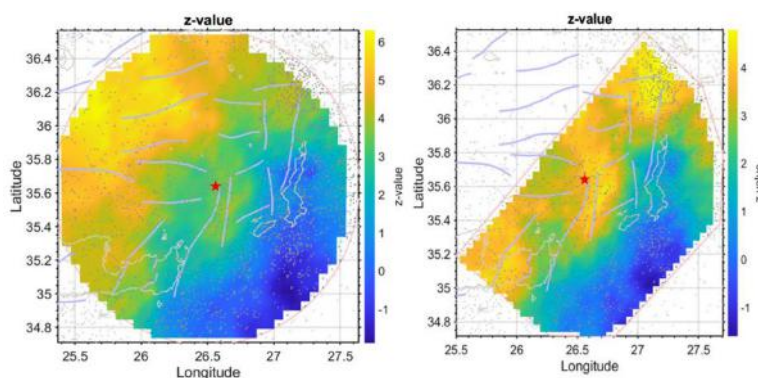
Figure 8. Z-statistics for the studied area a) in a circle with radius R = 100 km, center of the epicenter of the earthquake from 01.04.2011; (b) excluding the northwestern zone with low epicenter density; ★ - epicenter of the earthquake.

CONCLUSIONS

The temporary change in the b-value for the period 1964 - 2020 shows a minimum in the value of b (b = 1.35), preceding the earthquake of April 1, 2011 (Ml = 6.2) by about 7 years.

Large decreases in the value of b possibly associated with increasing effective levels of stress before major earthquakes. These significant decreases in the value of b can lead to an increase in effective stress before major events. An increase in

the b-value after these earthquakes may mean an increase in the heterogeneity of the earth's crust and a decrease in shear stress.

The change in the spatial distribution of the b value before the earthquake shows that the area with an abnormally low value of b covers the epicenter of the studied earthquake. These low values of b can be interpreted as a potentially locked or high-stress zone before major earthquakes.

The epicenters of the earthquakes are located in areas of relatively high value of the parameter Z≈4,2, which indicates a statistically reliable determination of an area with relatively seismic "calm" before the earthquake.

Therefore, a decrease in the value of b and seismic attenuation anomalies can be an indicator of strong stress release and these changes can be interpreted as predictors of strong seismic events.

REFERENCES

Rani VS, Srivastava K, Srinagesh D, Dimri VP (2011) Spatial and temporal variations of b-value and fractal analysis for the Makran region. Mar Geodesy 34:77–82 Reasenberg PA (1985) Second-order moment of Central California Seismicity. *J Geophys Res* 90:5479

Stiphout T, Schorlemmer D, Wiemer S (2011) The effect of uncertainties on estimates of background seismicity rate. *Bull Seismol Soc* Am 101(2): 482–494. doi:10.1785/0120090143

Wyss M, Sobolev G, Clippard JD (2004) Seismic quiescence precursors to two M7 earthquakes on Sakhalin Island, measured by two methods. *Earth Planets Space* 56:725–740

Wyss M, Pacchiani F, Deschamps A, Patau G (2008) Mean magnitude variations of earthquakes as a function of depth: different crustal stress distribution depending on tectonic setting. *Geophys Res Lett* 35:L01307. doi:10.1029/2007GL031057

Gutenberg B, Richter CF (1944) Frequency of earthquakes in California. *Bull Seismol Soc* Am 34:185–188

Bridges DL, Gao SS (2006) Spatial variation of seismic b-values beneath Makushin Volcano, Unalaska Island, Alaska. *Earth Planet Sci Lett* 245: 408–415

Tsukakoshi Y, Shimazaki K (2008) Decreased b-value prior to the M 6.2 Northern Miyagi, Japan, earthquake of 26 July 2003. *Earth Planets Space* 60:915–924.

Nuannin P, Kulha´nek O, Persson L (2005) Spatial and temporal b-value anomalies preceding the devastating off coast of NW Sumatra earthquake of December 26, 2004. *Geophys Res Lett* 32:L11307. doi:10.1029/2005GL022679

Wiemer S, Wyss M (1997) Mapping the frequency-magnitude distribution in asperities: an improved technique to calculate recurrence times? *J Geophys Res* 102(15):115–128

Wyss M, Stefansson R (2006) Nucleation points of recent main shocks in southern Iceland mapped by b-values. *Bull Seismol Soc* Am 96:599–608. doi:10.1785/0120040056

Wu, Y. M., Chang, C. H., Zhao, L., Teng, T. L., & Nakamura, M. (2008). A comprehensive relocation of earthquakes in Taiwan from 1991 to 2005. *Bulletin of the Seismological Society of America*, 98(3), 1471-1481.

Schorlemmer D, Neri G, Wiemer S, Mostaccio A (2003) Stability and significance tests for b-value anomalies: example from the Tyrrhenian Sea. *Geophys Res Lett* 30(16):1835. doi:10.1029/ 2003GL017335

Urbancic TI, Trifu CI, Long JM, Toung RP (1992) Space–time correlations of b values with stress release. *Pure Appl Geophys* 139:449–462

Chouliaras G (2009) Seismicity anomalies prior to 8 June 2008, Mw = 6.4 earthquake in Western Greece. *Nat Hazards Earth Syst Sci* 9:327–335

Rudolf-Navarro, A. H. (2010). Seismic quiescence patterns as possible precursors of great earthquakes in Mexico. *International Journal of Physical Sciences*, 5(6), 651-670.

Wyss M, Habermann RE (1988) Precursory seismic quiescence. *Pure Appl Geophys* 126:319–332

Katsumata K (2011) Long term seismic quiescence started 23 years before the 2011 off the Pacific coast of Tohoku earthquake (M = 9.0). *Earth Planets Space* 63:709–712

Maeda K, Wiemer S (1999) Significance test for seismicity rate changes before the 1987 Chiba-toho-oki earthquake (M6.7), *Japan. Ann Geofis* 42(5):833–850

Utsu, T. (1965). *A method for determining the value of b in the formula log n a bM showing the magnitude-frequency relation for earthquakes*, Geophys. Bull. Hokkaido Univ. 13, 99–103 (in Japanese with English summary).

Schorlemmer D, Wiemer S, Wyss M (2004) Earthquake statistics at Parkfield, Stationarity of b values. *J Geophys Res* 109:B12307. doi:10.1029/2004JB003234

Wiemer S (2001) A program to analyse seismicity: ZMAP. *Geophys Res Lett* 72:373–382

Wiemer S, Wyss M (1994) Seismic quiescence before the landers (M = 7.5) and big bear (M = 6.5), 1992 earthquakes. *Bull Seismol Soc* Am 84(3):900–916

Aki, K. (1965). *Maximum likelihood estimate of b in the formula log N= a-bM and its confidence limits*. Bull. Earthq. Res. Inst., Tokyo Univ., 43, 237-239.

Wiemer S, Wyss M (2000) Minimum magnitude of completeness in earthquake catalogs: examples from Alaska, the western United States, and Japan. *Bull Seismol Soc* Am 90(4):859–869

Wiemer S, Wyss M (2002) Mapping spatial variability of the frequency–magnitude distribution of earthquakes. Adv Geophys 45:259–302 Wu YM, Chiao LY (2006) *Seismic quiescence before the 1999*

Habermann RE (1987) Man-made changes of seismicity rates. *Bull Seism Soc* Am 77:141–159

University of Athens- http://dggsl.geol.uoa.gr/en_index.html

Görgün, E., Zang, A., Bohnhoff, M., Milkereit, C., & Dresen, G. (2009). Analysis of Izmit aftershocks 25 days before the November 12th 1999 Düzce earthquake, Turkey. *Tectonophysics*, 474(3-4), 507-515.

Westerhaus M, Wyss M, Yilmaz R, Zschau J (2002) Correlating variations of b values and crustal deformation during the 1990's may have pinpointed the rupture initiation of the Mw = 7.4 Izmit earthquake of 1999 August 17. *Geophys J Int* 148:139–152

Motaghi K, Hessami K, Tatar M (2010) Pattern recognition of major asperities using local recurrence time in Alborz Mountains, Northern Iran. *J Seismol* 14:787–802. doi:10.1007/s10950-0109201-z

✉ **Emil Oynakov**
National Institute of Geophysics, Geodesy and Geography
Bulgarian Academy of Sciences
Sofia, Bulgaria
E-mail: emil.ilievmg@gmail.com

✉ **Dimcho Solakov**
http://orcid.org/0000-0003-4148-0525
National Institute of Geophysics, Geodesy and Geography
Bulgarian Academy of Sciences
Sofia, Bulgaria
E-mail: dsolakov@geophys.bas.bg

✉ **Irena Aleksandrova**
National Institute of Geophysics, Geodesy and Geography
Bulgarian Academy of Sciences
Sofia, Bulgaria
E-mail: i.alex@abv.bg

✉ **Yordan Milkov**
National Institute of Geophysics, Geodesy and Geography
Bulgarian Academy of Sciences
Sofia, Bulgaria
E-mail: jori@abv.bg

SEISMIC STATIONS SITE-EFFECT FOR THE NATIONAL OPERATIVE TELEMETRIC SYSTEM FOR SEISMOLOGICAL INFORMATION (NOTSSI) NETWORK CALCULATED ON THE BASIS OF MICROSEISMIC NOISE

Emil Oynakov, Dimcho Solakov, Irena Aleksandrova
*National Institute of Geophysics, Geodesy and Geography –
Bulgarian Academy of Sciences (NIGGG-BAS)*

Abstract. The present study investigates the characteristics of seismic sites of some of the NOTSSI monitoring network stations, based on microseismic noise. Nakamura's method of the spectral ratio of the horizontal to the vertical components of the seismic noise (H / V), directly related to the S-wave velocity of distribution (Vs) at the observed site was used for calculating the station repairs. The spectral H / V ratio of the seismic noise for 11 seismic stations is calculated, combined with geological data bellow each station. The values of A_0 - site-effect, f_0 - resonance frequency and h - depth of reference at the most contrasting resonance boundary were obtained. Attention is paid to seismic instruments and sensors
Keywords: earthquake; site-effect; microseismic noise

INTRODUCTION

From a contemporary Plate-Tectonic aspect, the territory of Bulgaria belongs to the southern outskirts of the Eurasian plate. The geodynamics of the region are determined mainly by the subduction of the African Plate in the Aegean zone and the collision of the Arab Plate with the Eurasian one. The territory of southern Bulgaria falls within the northernmost border region with a predominantly extensional character of the cortex movements, defined as the "South Balkan Extension Zone" (Bindi, Parolai, Spallarossa, Catteneo, 2000). The pace of the horizontal movements of the Earth's crust for southern Bulgaria by GPS data do not exceed 3 – 5 mm / year and are usually in the range of 1 – 2 mm / year. The direction of movement towards Eurasia is south-southeast, which causes extensions in the north-south direction and the formation of structures in the east-west direction, for example the Sofia graben and others (Nakov, Kotzev, Burchfiel, King, 2005).

Seismicity

From a seismological point of view, the Bulgarian lands are part of the Alps-Himalayan seismic belt, characterized by a high level of seismic activity. Over the past centuries, Bulgaria has been subjected to strong earthquakes. The first written records of an earthquake in the country date back to the 1st century BC. At the beginning of the 20th century, a series of destructive seismic events took place on the territory of Bulgaria (5 earthquakes with magnitude greater than or equal to 7). High and intense is the seismic activity in SW Bulgaria during the period 1904 – 1906. This seismic series began on April 4, 1904 with the realization of two catastrophic earthquakes (magnitude greater than 7.0) in an interval of 23 minutes. In 1928, a series of three major earthquakes occurred along the Maritza River valley (in central southern Bulgaria). Since 1928, no other catastrophic earthquakes have occurred on the territory of Bulgaria. The most significant event in the 20th century, after 1928, was the 1986 earthquake with magnitude $M_S5.7$, which occurred in central northern Bulgaria (near the town of Strazhitsa).

At present, the National Seismic Network – NOTSSI, established in 1980, is a major part of NIGGG – BAS. The network was upgraded in 2005 and consists of 17 seismic stations and 2 local networks. The main task of the network is to monitor the seismicity realized on the territory of Bulgaria and the surrounding lands. NOTSSI is currently a world-class digital network that determines real-time earthquake parameters. The Network provides reliable seismological information, related to seismic risk reduction, both for the expansion of the research activities and for the work of the institutions. The methodology for analysis, assessment and mapping of the seismic risk in Bulgaria and the new assessment of seismic hazard for Bulgaria created in recent years, are based on the high-quality information from the NOTSSI.

Dynamic parameters and methodology of calculation

One of the important indicators for estimating tensions in the Earth's crust is the level of released tensions, which can be determined by analysing the dynamic parameters of the earthquakes. An important element in the calculation of the dynamic parameters is the transition from station spectrum to spectrum in the epicentre, by which the angular frequency (f_0) and the spectral density (Ω_0) are determined. Such transition must take into account the influence of the environment and the site-effect below the station ("amplification") along the path of the seismic beam. There are various methods for determining site-effects, described in various articles (Lemzikov, Lemzikov, 2010; Makagon, Sycheva, 1994; Panteleeva, 2013). One of the most promising and economical methods for determining site-effect under the station is based on the analysis of seismic noise using the Nakamura method.

At the centre of the method is the notion that the influence of the thin layer (not a large layer of the earth's crust, just below the seismic station) on the studied object, greatly amplifies the transverse waves (S-waves) and practically does not change the longitudinal (P-waves). Then the ratio of the spectral characteristics of the two horizontal components to the spectrum of the vertical component will characterize the so-called preliminary function, which depends on the thin layer below the object under consideration. As is known, the seismic sensors measure movements of the earth's crust in three directions: north-south (N), west-east (E), and vertically (Z). Essentially, the method determines the ratio of the spectrum of the horizontal components (H) to the spectrum of the vertical component (V). The H component is calculated as the average square of the spectra of the E and N components and V corresponds to the spectrum of the component Z:

$$H(f) = \frac{\sqrt{N^2(f)+E^2(f)}}{2}, \tag{1}$$

then directly is calculated the H / V ratio:

$$\frac{H}{V}(f) = \frac{H(f)}{V(f)} \tag{2}$$

In order to obtain the average characteristic of the ratio for one station, it is necessary to consider N time windows from seismic noise. Thus, for the N-interval of the station record, N ratios H / V are calculated, and their average is determined:

$$\frac{H}{V}(f)average = \frac{\sum \frac{H}{V}(f)}{N} \tag{3}$$

In the study of seismic noise, the time window (interval) of the recording should be from 30 to 60s (Parolai, et al., 2004; Picozzi, et. al., 2008; Nakamura, 1989), the choice depends on the characteristics of the seismic sensor. From the selected section of the record the linear trend is removed and, to prevent distortions at the ends of the spectrum, is smoothed out with the help of a 5% cosinusoidal window:

$$c(t) = \begin{cases} \frac{1}{2}(1 - cos\frac{\pi}{a}t, & 0 \le t \le a \\ 1, & a \le t \le (1-a) \\ \frac{1}{2}\left(1 - cos\frac{\pi}{a}(1-t)\right), & (1-a) \le t \le 1 \end{cases}, \tag{4}$$

where *t* is time; *a*-percent constituting *(a = 5%)*.

An error correction of the instrument measurements is applied to the resulting line and the spectrum is calculated using the Fast Fourier Transform:

$$X(k) = \sum x(j)e^{\frac{2\pi N}{(j-1)(k-1)}} \tag{5}$$

Then it is smoothed with the help of the Horse-Omachi method:

$$\left(\frac{\sin(b\log_{10}(\frac{f}{f_c})}{b\log_{10}(\frac{f}{f_c})}\right)^4, \tag{6}$$

Determination of the amplitude-frequency composition of the microseismic oscillations Microseismic oscillation spectra and H / V ratio were obtained with the help of the GEOPSY program. In order to avoid accidental errors (technogenic noises, transport, earthquakes, explosions, meteorological conditions, etc.), seismic records were taken from the stations with a duration of 24 hours, i.e. one day, from the seismically calm days (30.01.2019) and consistent with previous studies of seismic noise from stations (Dimitrova, Nikolova, 2011) . For this section of the seismic record, several hundred time windows were selected (60 seconds in duration) so that no random noise recordings would fall into the analysed sections.

Generalized H / V-ratio curves and corresponding standard deviation values were obtained by averaging the individual H / V-ratios for all time windows. As a result, for 11 seismic stations (Table 1) on the territory of Bulgaria, H / V curves were obtained characterizing the amplitude-frequency composition of the background microseismic oscillations (Figure 1 to Figure 7).

Table 1. Coordinates and equipment of the analysed seismic stations.

Station code	Digitizer	G. width (Nº)	G. longitude (Eº)	Altitude (m)	Seismometer
KDZ	DAS 9887	25,3396	41,6303	343	GURALP CMG 3ESPC/120
PLD	DAS 9905	24,7475	42,1469	195	GURALP CMG 40T
PGB	DAS 9908	24,1735	42,5137	569	GURALP CMG 40T
MMB	DAS A940	23,7496	41,547	618	STS-2
KKB	DAS A914	23,1287	41,8417	451	GURALP CMG 3ESPC/60
PSN	DAS A646	28,1359	43,6376	182	KS 2000/60s
SZH	DAS 990C	25,9762	43,2653	329	GURALP CMG 3ESPC/60
VTS1	DAS 9877	23,2342	42,6143	1387	GURALP CMG 3ESPC/120
PLN	DAS 98C5	23,4254	43,4762	1236	GURALP CMG 3ESPC/120
TRAN	DAS 98C5	22,6512	42,8345	421	GURALP CMG 3ESPC/120
PRD	DAS 990A	27,4099	43,1602	128	GURALP CMG 40T

According to the type of obtained curves of the H / V ratio, the studied seismic stations in the territory of Bulgaria can be divided into two groups (Figures 1 to 11). The first group includes seismic stations with steady amplitude frequency.

Characteristics of the microseismic signal

This group includes the stations Kardzhali (KDZ), Krupnik (KKB), Musomishte (MMB), Plana (PLN), Plovdiv (PLD), Preselentsi (PSN) and Vitosha (VTS) (Figures 1 to 7). In general, the H / V spectral curves for the stations in the first group are curves complicated slightly by small amplitude extrema. For some of the curves the level rises in the high frequency range. These types are H / V ratio curves for KDZ and MMB stations. This type of H / V ratio curve is typical for stations located directly at the outcrops of the root rocks of the surface foundation. Theoretically, for such stations, the H / V spectral curve should be straight parallel to the abscissa with an amplitude of about 1. The obtained H / V spectral curves for the stations in the first group satisfy this condition. For MMB, PLD, PSN and VTS1 stations we can notice smooth low frequency extremes and for KKB medium frequency stations.

The second group includes stations PRD, SZH, PGB and TRAN (Figs. 8-11). For three of the seismic stations (TRAN, SZH and PRD), the presence of narrow extremes of the H / V curves localized at frequencies of 4 – 10 Hz is observed. All four seismic stations in the second group are located at the outcrops of the root rocks on the surface, so that the presence of extremes cannot be explained by local soil conditions. The study of fracture zones by the low frequency microseismic sounding method shows that such extrema are observed close to the areas of high cracking and fragmentation with signs of Pliocene activation. Also, these types of extremes can be caused by the passage of a seismic signal through large structural inhomogeneities.
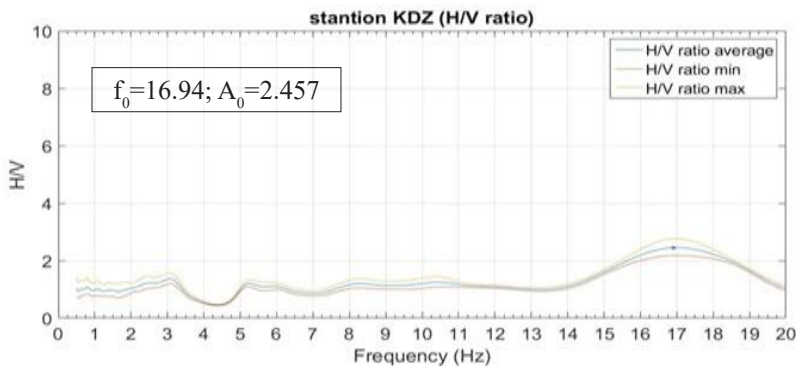
Figure 1. Graphs of: spectral ratio H / V of Kardzhali station (KDZ)
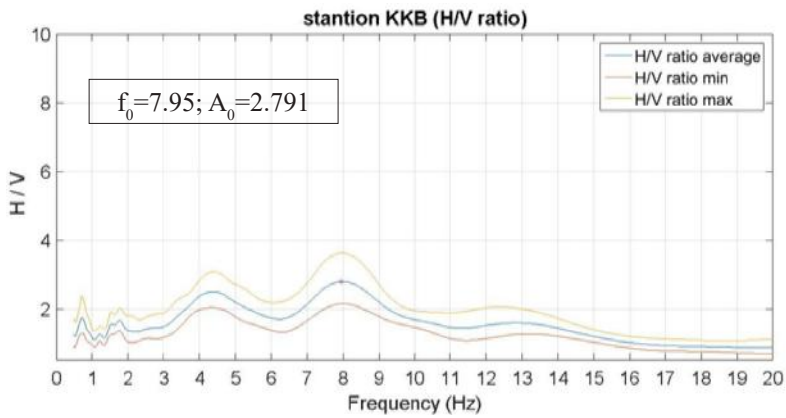
Figure 2. Graphs of: spectral ratio H / V of Krupnik Station (KKB)

Table 2 shows the calculated station corrections (amplification factor), the resonance frequency f_0 and the depth of reference of the most contrasting resonance boundary h, calculated by the formula:

$$h = \frac{V_S}{4 f_0},$$ (7)

where, Vs is the transverse wave speed taken from "Physical constants and modules of some rocks and minerals" (Christoskov, 2007) depending on the substrate on which the seismic station is deposited.
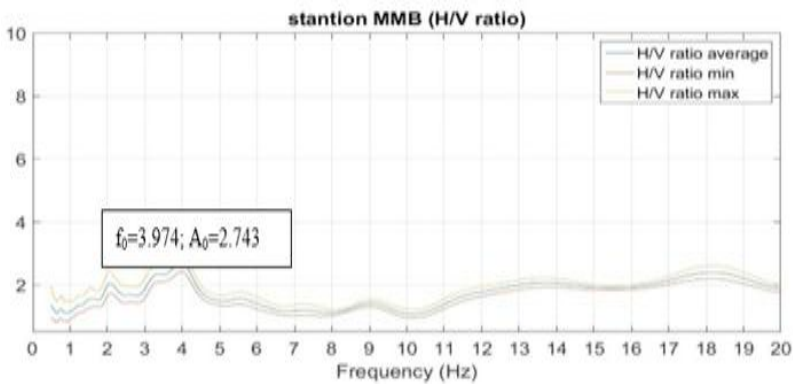
Figure 3. Graphs of: spectral ratio H / V of Musomishte Station (MMB)
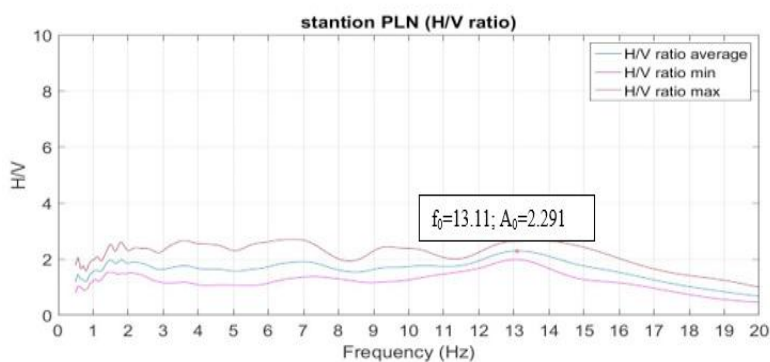
Figure 4. Graphs of: spectral ratio H / V of Plana station (PLN)
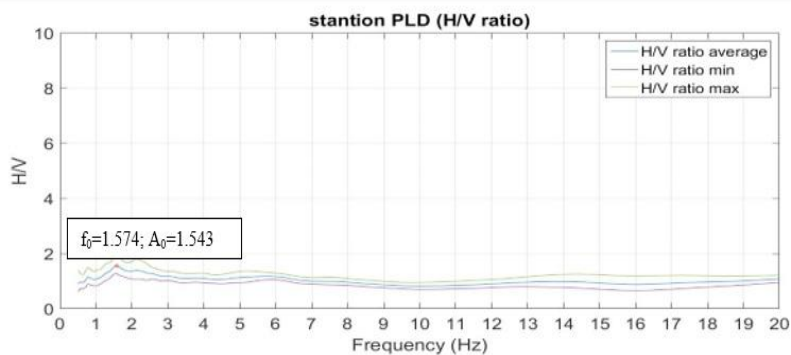
Figure 5. Graphs of: H / V spectral ratio of Plovdiv station (PLD)
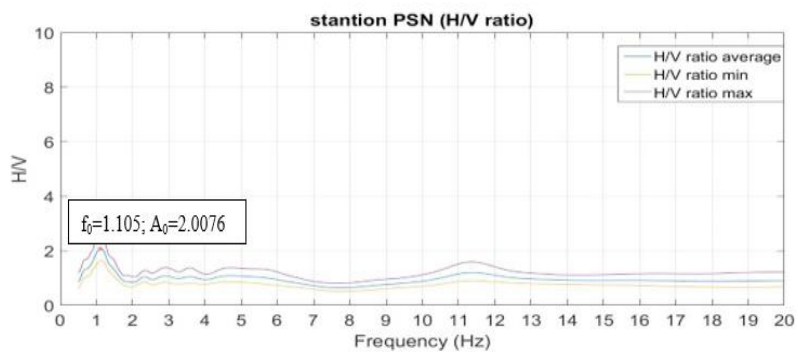
Figure 6. Graphs of: H / V spectral ratio of Preselentsi Station (PSN)
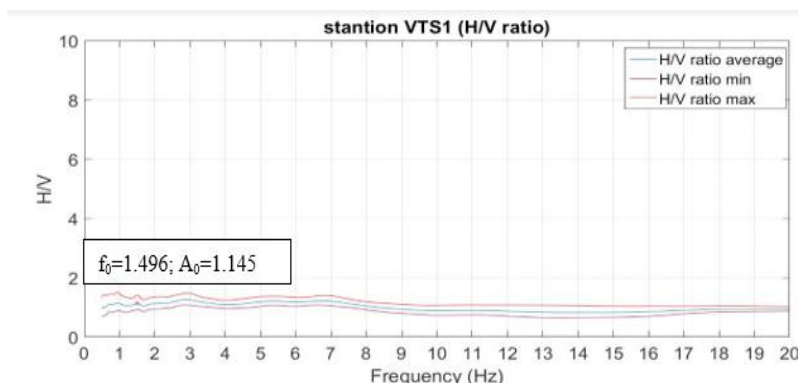
Figure 7. Graphs of: spectral ratio H / V of Vitosha Station (VTS)
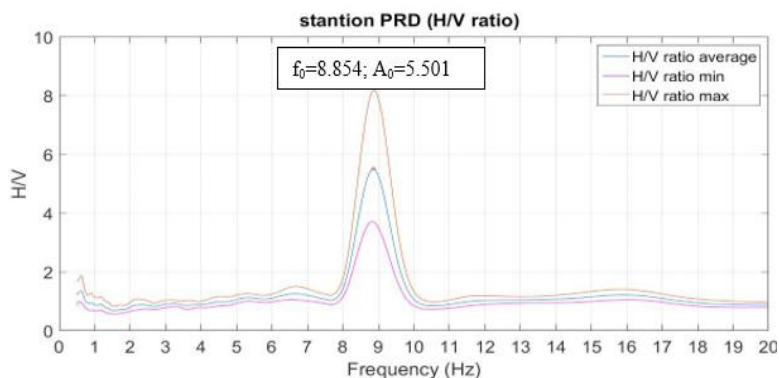
Figure 8. Graphs of: spectral ratio H / V of Provadia Station (PRD)
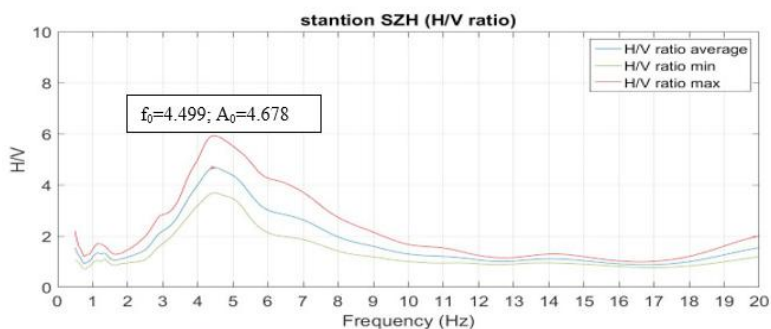
Figure 9. Graphs of: H / V spectral ratio of Strazhica Station (SZH)
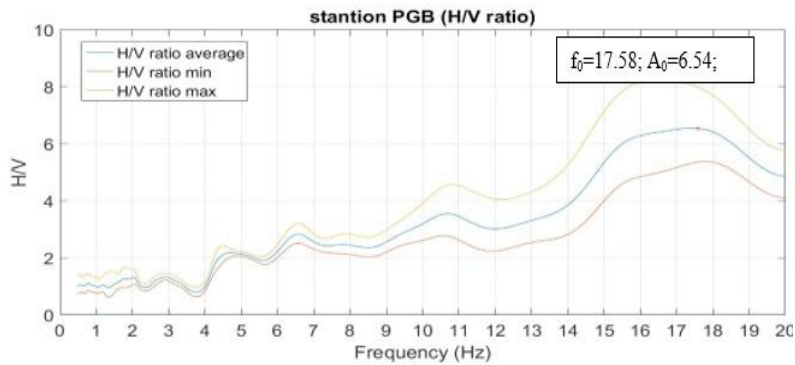
Figure 10. Graphs of: H / V spectral ratio; power spectra of the E, N and Z components of Panagyurishte Station (PGB)
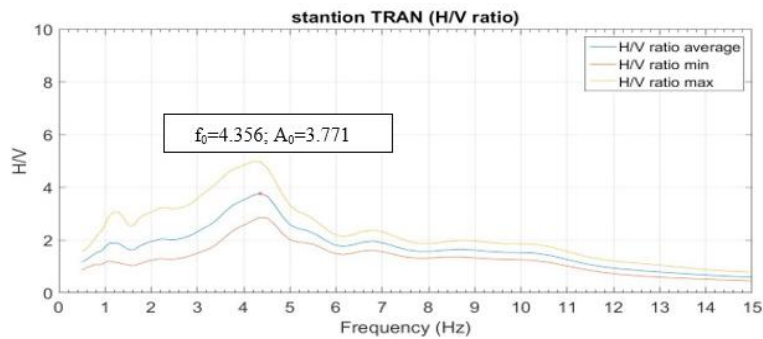
Figure 11. Graphs of: spectral ratio H / V of Tran Station (TRAN)

Table 2. Amplification factor for 18 seismic stations calculated by Nakamura method.

Station code	longitude	latitude	elevation, m	f_0	A_0	h, m
KDZ	25,3396	41,6303	343	16.94	2.457	36 - 44
PLD	24,7475	42,1469	195	1.574	1.543	397 - 460
PGB	24,1735	42,5137	569	17.58	6.54	34 - 39
MMB	23,7496	41,547	618	3.974	2.743	157 - 188
KKB	23,1287	41,8417	451	7.956	2.791	105-160
PSN	28,1359	43,6376	182	1.105	2.076	45 - 226
SZH	25,9762	43,2653	329	4.499	4.678	11 - 55
VTS1	23,2342	42,6143	1387	1.496	1.145	484 - 584
PLN	23,4254	43,4762	1236	13.11	2.291	72 - 129

TRAN	22,6512	42,8345	421	4.356	3.771	192-200
PRD	27,4099	43,1602	128	8.854	5.501	28 - 56

From Table 2 it can be summarized: the amplification value varies from 1.2 to 6.5 with resonance frequencies varying from 1.1 to 17 Hz.

CONCLUSION

Site-effects have been made using the Nakamura method applied to seismic noise recordings. The resulting site-effect for the stations from the NOTSSI network can be used in the transition from station spectra to the source spectrum.

REFERENCES

Bindi D., Parolai S., Spallarossa D., Catteneo M. 2000. Site effects by H/V ratio: Comparison of two different procedures / D. Bindi, S. Parolai, D. Spallarossa, M. Catteneo// *Journ. of Earthquake Engin*. Vol. 4. № 1. P. 97 – 113. 3.

Nakov, R., V. Kotzev, C. Burchfiel, R. King, 2005. Ten years of GPS Studies on the Active Tectonics of Bulgaria: an Overview and basic results. In: *Proc.of B.G.S. Int.Conf.*, eds., Y. Yanev, R. Nedialkov, 46-49.

Lemzikov V.K, Lemzikov M.V, 2010. *Features of attenuation of seismic waves in volcanic environments of Kamchatka*, Institute of Volcanology and Seismology, Far East Branch of the Russian Academy of Sciences, Petropavlovsk-Kamchatsky. 176 – 185.

Makagon M. Yu., Sycheva N. A. Kiev, 1994. Software complex for calculating station corrections (site effect) of stations based on seismic noise, *Vestnik KRSU*. 2013. Volume 13. No. 7, 90 – 96.

Panteleeva T.A., 2013 Spectra and focal parameters of earthquakes in Crimea and their spatial-temporal features, Abstract, 52 p. *Bulletin of the KRSU* . Volume 13. No. 7, 90 – 96 p. 3.

Dimitrova L., Nikolova, S., 2011. AMBIENT SEISMIC NOISE AT BROADBAND SEISMIC STATIONS OF BULGARIAN NATIONAL DIGITAL SEISMIC NETWORK (BNDSN) *Bulgarian Geophysical Journal*, Vol. 37, p. 48-61.

Parolai S., et al., 2004. Comparison of Different Site Response Estimation Techniques Using aftershocks of the 1999 Izmit Earthquake / S. Parolai,

D. Bindi, M. Baumbach, H. Grosser, C. Milkereit, S. Karakisa, S. Z unbul // *Bulletin of the Seismological Societyof Amer.* June. Vol. 94. № 3. P. 1096 – 1108. 2.

Picozzi M., et. Al., 2008. Site characterization by seismic noise in Istanbul, Turkey J. Z schau, M. Erdik// Soil Dynamics and Earthquake Engineering.. P. 2 – 6. 4. Nakamura Y., 1989. A method for dynamic characteristics estimation of subsurface usingmicrotremor on the ground surface / Y. Nakamura // *QR Railw. Tech. Res. Inst.* 30..P. 25 – 33.

Christoskov L., 2007. *Seismology Part 2. Earthquake sources and wave field in the Earth.* University Publishing House "St. Kl. Ohridski ", Sofia.

✉ **Emil Oynakov**
National Institute of Geophysics, Geodesy and Geography
Bulgarian Academy of Sciences
Sofia, Bulgaria
E-mail: emil.ilievmg@gmail.com

✉ **Dimcho Solakov**
http://orcid.org/0000-0003-4148-0525
National Institute of Geophysics, Geodesy and Geography
Bulgarian Academy of Sciences
Sofia, Bulgaria
E-mail: dsolakov@geophys.bas.bg

✉ **Irena Aleksandrova**
National Institute of Geophysics, Geodesy and Geography
Bulgarian Academy of Sciences
Sofia, Bulgaria
E-mail: i.alex@abv.bg

PARAMETERS OF THE SEISMIC RISK FOR BLAGOEVGRAD REGION, BULGARIA

**Petya Trifonova[1], Dimcho Solakov[1],
Stela Simeonova[1], Metodi Metodiev[1],
Stefan Florin Balan[2]**

[1]*National Institute of Geophysics, Geodesy and Geography –
Bulgarian Academy of Sciences (NIGGG-BAS)*
[2] *National Institute for Research and Development
for Earth Physics (NIEP), Romania*

Abstract: Exposure means people, property, systems, or other elements present in hazard zones that are thereby subject to potential losses. Present research analyses the human exposure at one of the most dangerous earthquake zones in Bulgaria-Blagoevgrad region as one of the main parameters of the seismic risk. Seismic hazard is modelled using GIS and overlaid with one square kilometre grid of population distribution in order to determine the population exposure. We define a parameter called "population exposure index" (PEI) which has five classes: Minor, Low, Moderate, High and Major. As was expected, the seismic hazard levels of Blagoevgrad region are in the upper part of the classification scale. The Krupnik-Kresna area is fully covered with the highest 5th level and the remaining part falls within the interval limits of level 4. The total population in the Blagoevgrad region (NUTS II) is around 138 000 people. Results show that more than 45 000 people are exposed to the highest level of seismic hazard. More than 50 settlements (towns and villages) are classified with Major (5) PEI.

Keywords: seismic risk, population exposure, Blagoevgrad, Bulgaria**.**

INTRODUCTION

The evaluated seismic hazard for Bulgaria in terms of Peak Ground Acceleration (PGA) calculated for a 475 years return period (Solakov et al, 2019a) shows that the highest ground motion levels are predicted for Blagoevgrad (Krupnik-Kresna) region, where the calculated PGA values exceeds 0.2g and in some places 0.3g (Fig. 1).

The Krupnik-Kresna area which occupies the north-western part of the investigated region is considered to be one of the most dangerous earthquake zones in Bulgaria and the Mediterranean as well. The high seismic activity in this area is
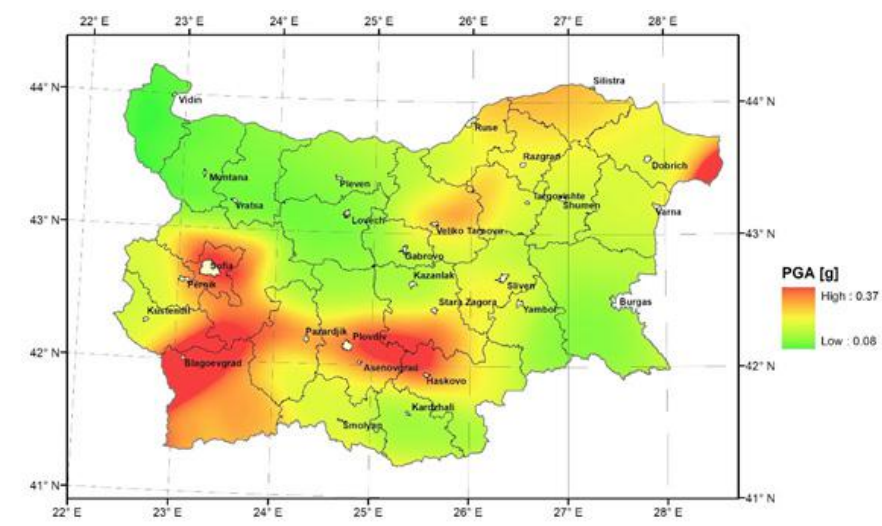
Figure 1. Seismic hazard map in PGA for Bulgaria for a 475 years return period (modified from Solakov et al., 2019a)

associated with the Struma fault system. Two of the strongest earthquakes in Europe in the twentieth century occurred in this area - the earthquakes of April 4, 1904 (M_S = 7.1 and M_S = 7.8). The second earthquake was felt even in Budapest. Krupnik, Brezhane, Simitli, Kresna and many other settlements were severely affected. Traces of the earthquake can be seen today in the Kresna valley. The earthquake activated a fault line with a sub-parallel direction. There were also huge cracks in the neighbouring Brezhanski graben. The subsidence at the Struma River was about 1.5-2 m, where a big step was formed. From the left bank of the Struma River the rupture was about 2 m high. In this region, where the thickness of the earth's crust is significant (below the western part of the Rhodope massif it reaches a depth of 40-50 km), originate the deepest earthquakes in Bulgaria.

In this research, the term risk follows the definition by the United Nations (UNDRO) and refers to the expected losses from a particular hazard to a specified element at risk in a particular future time period. Losses may be estimated in terms of human lives, buildings destroyed or in financial terms" (Burton, Kates&White, 1993). In our case, as far as we analyse the population exposure to earthquakes, risk is connected with potential human losses (casualties) resulting from seismic hazard. One of the main parameters needed for calculating the casualties is the population exposure. It refers to the human occupancy of hazard zones, or the population present within the hazard area that would be potentially directly affected by an event (Freire and Aubrecht, 2012).

METHODOLOGY

Mathematically, the risk is a function of hazard occurrence probability, element at risk (population) and vulnerability. We accept the hypothesis that the three factors explaining the risk are multiplying each other (Dao and Peduzzi, 2003) which means that if the hazard is 0 (null), then the risk is 0 (null). Theoretically, the risk is also null if nobody lives in an area exposed to hazard and if the population is invulnerable. In the present research we use the census-based resident population (i.e. night-time) and do not account for spatio-temporal variation of population distribution in urban areas.

Population exposure is modelled by crossing the seismic hazard and population living in the potentially affected area. We determine a parameter called "population exposure index" (PEI) which has five classes: Minor, Low, Moderate, High and Major.

The input data are: 1) seismic hazard for the territory of Bulgaria (Solakov et al., 2019a) re-calculated according to the USGS global Vs30 model (the time-averaged shear-wave velocity to 30 m depth) (https://earthquake.usgs.gov/data/vs30/) and 2) one sq. km. population grid of the Republic of Bulgaria resulted from the census performed in 2011(https://www.nsi.bg/en/content/12309/population-grid-1-sqkm-census-2011). Using the population grid rather than total number of population allows direct comparison between big cities and small villages (less populated towns have the same weight as more populated ones).

Similar analysis is performed by Solakov et al. (2019b) but they use as input data the population density in Bulgaria which is calculated for each settlement using the total number of population living there and the area of the village/town/city. In this way, the population is artificially distributed over the entire area on the one hand and on the other hand the settlements that occupy a large area artificially reduce the value of the calculated density.

First, both variables are classified in five levels using equal interval classification schemes (Table 1 and Table 2):

Table 1. Population density levels

Population density value [pers./sq.km]	Population density levels
0	1
1-100	2
101 - 1000	3
1001 -10 000	4
> 10 000	5

Table 2. Seismic hazard levels

Seismic hazard & Soil conditions PGA[g]*Vs30	Seismic hazard levels
≤ 0.10	1
0.1 – 0.14	2
0.141 – 0.18	3
0.181 – 0.25	4
≥0.26	5

The number of levels and method for classifying the resultant map were chosen according to several criteria such as the optimum number of levels for visual representation or the number and level of errors between them.

The combination of both seismic hazard and population density provides the population exposure as an element of risk. A hypothesis is made that similar to the risk it follows the multiplicative formula that could be simplified as Eq. (1):

$$PopExp^E = H^E \cdot Pop^E \tag{1}$$

where:

$PopExp^E$ is the population exposure for the single spatial element E, one square kilometer in size.

H^E is the seismic hazard class for the single spatial element E determined accord. to Table 1.

Pop^E is the population density class for the single spatial element E determined accord. to Table 2.

As was expected, the seismic hazard levels of Blagoevgrad region are in the upper part of the classification scale (Fig. 2). The Krupnik-Kresna area is fully covered with the highest 5th level and the remaining part falls within level 4 interval limits. Only several small region in the south-east direction can be classified as having moderate level 3 values.
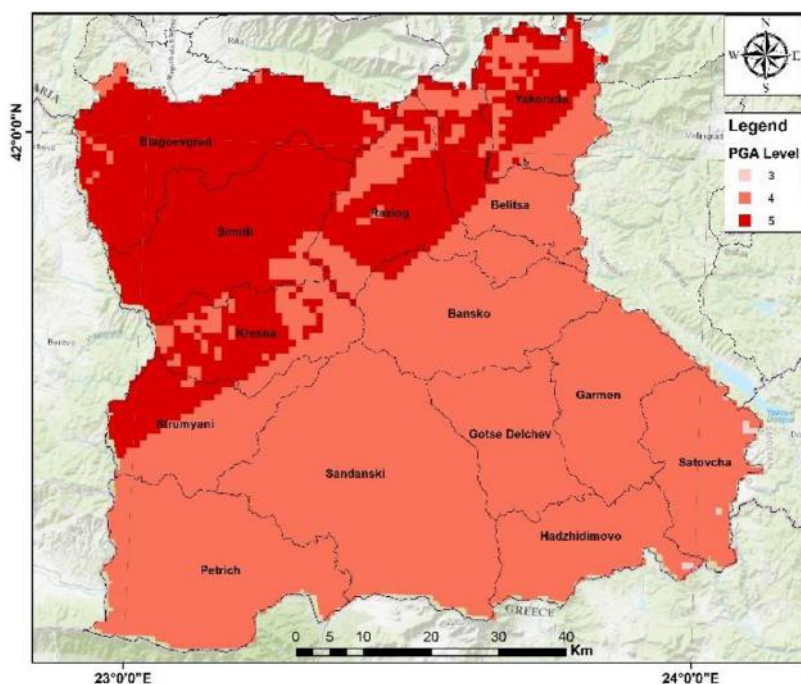
Figure 2. Levels of the seismic hazard obtained for Blagoevgrad region according to classification scheme in Table 2.

RESULTS

Calculation of the population which is exposed to seismic hazard is performed in a gridded spatial network with a single element *E* with dimensions 1x1 km. To determine the population exposure index (PEI) results obtained using Eq. 1 are also classified in five classes from 1 to 5: Minor, Low, Moderate, High and Major. Results, obtained for Bulgaria are given in the map of Figure 3.

According to those results, Sofia, Plovdiv and Blagoevgrad are the Top 3 municipalities with the major PEI level in Bulgaria. In the three districts live around 1.8 million people. A detailed breakdown for Blagoevgrad region (NUTS II classification) is given in Table 3 and Table 4.

Table 3. Settlements with Major PEI level in Blagoevgrad region

	Settlement		Total population	max PEI
	name	type		
1	Blagoevgrad	town	15925	5
2	Sandanski	town	11021	5
3	Simitli	town	5538	5
4	Izgrev	village	1025	5
5	Yakoruda	town	1700	5
6	Belitsa	town	1570	5
7	Razlog	town	4598	5
8	Bachevo	village	1016	5
9	Krupnik	village	1708	5
10	Kresna	town	2023	5

Table 4. Settlements with largest population in Blagoevgrad region

	Settlement		Total population	max PEI
	name	type		
1	Blagoevgrad	town	15925	5
2	Sandanski	town	11021	5
3	Gotse Delchev	town	6240	4
4	Petrich	town	6066	4
5	Razlog	town	4381	5
6	Bansko	town	3523	4
7	Parvomay	village	2501	4
8	Kresna	town	2023	5
9	Kochan	village	1971	4
10	Breznitsa	village	1905	4
11	Simitli	town	5538	5
12	Krupnik	village	1708	5
13	Yakoruda	town	1700	5
14	Belitsa	town	1570	5
15	Mikrevo	village	1522	4

More than 45 000 people are exposed to the highest level of seismic hazard in the region. In the list of Table 3 are four of the major towns in this area. Spatial distribution of the results is displayed in the Figure 4.

Results obtained by Dao and Peduzzi (2002) assessing global exposure and vulnerability towards natural hazards reveal that human vulnerability is mostly linked with country development level and environmental quality. Country development combines different indicators and parameters, but in the case of an
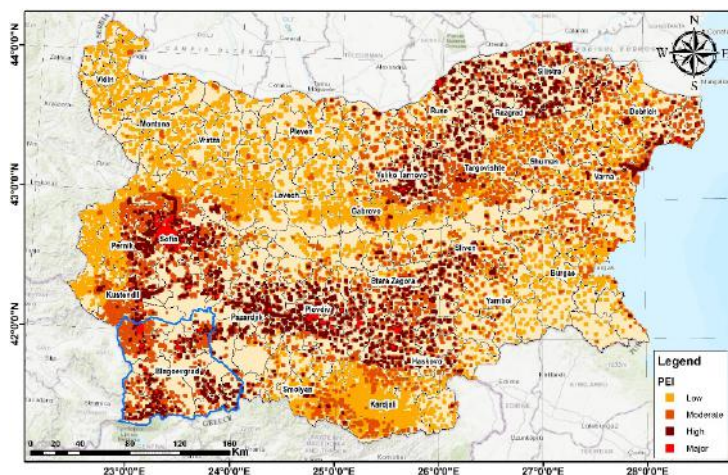
Figure 3. Spatial distribution of the population exposure index obtained for the territory of Bulgaria
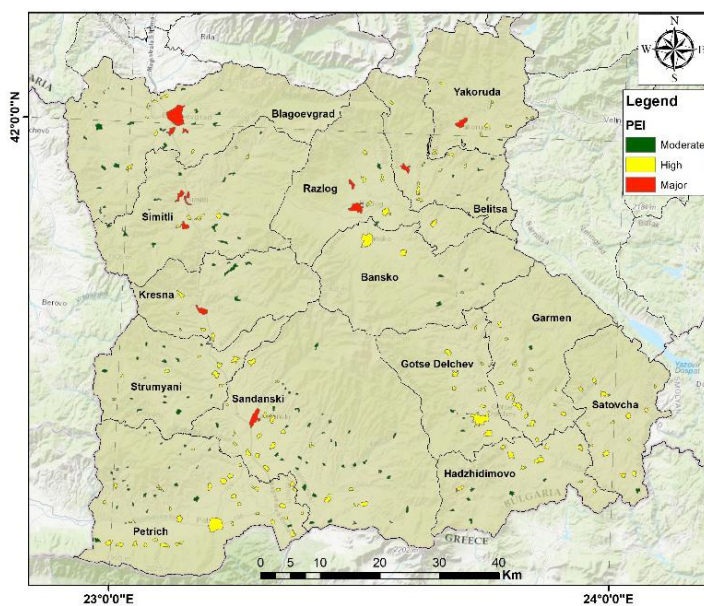
Figure 4. Spatial distribution of the population exposure index (PEI) obtained for Blagoevgrad region. Each settlement is colored according to the maximum value of PEI calculated for its inner elements according to Eq. 1. Displayed are the names of municipalities

earthquake the most important is the state of the norms for design and control over constructionл The first building code in Bulgaria defining regulations and associated standards intended to control aspects of the design, construction, materials, etc. that are necessary to ensure human safety and welfare (including resistance to collapse and damage) is from 1956. It was updated several times and now Bulgaria has adopted modern standards according to the requirements of Eurocode 8.

CONCLUSION

Determination of the population exposure index (PEI) in one of the most seismically active zone in Bulgaria – Blagoevgrad region shows that less than 30 percent of the settlements are characterised with Moderate (3) values of PEI. These are 85 small villages where the population is between 2 and 99 people. For all 14 towns where 60 000 people live, the obtained PEI values are High (4) and Major (5).

Purpose of the calculated population exposure index (PEI) is to give a qualitative information about the size of negative consequences which may occur in case of a strong earthquake. For quantitative analysis, measures of the exposure should be combined with the specific vulnerability of the exposed elements to seismic hazard, to estimate the quantitative risks and to determine the potential loses.

For the purposes of planning and analysis of measures for earthquake preparedness and disaster management in Blagoevgrad region the obtained map of PEI values would be a valuable tool as a base level information.

REFERENCES

Burton, I., Kates, R.W. and White, G.F. (1993) *The Environment as Hazard*, Second Edition. New York/London: Guilford Press, 290 pp.

Dao, H. and Peduzzi, P. (2003) *Global Risk And Vulnerability Index Trends per Year (GRAVITY), Phase IV: Technical annex and multiple risk integration*, UNDP/BCPR, Geneva, Tech. Rep., 31 pp.,

Freire S. and C. Aubrecht, (2012) Integrating population dynamics into mapping human exposure to seismic hazard, *Nat. Haz. Earth Syst. Sci.*, 12, 3533–3543, doi:10.5194/nhess-12-3533-2012.

Solakov et al. (2019a) *Seismic risk management for buildings*. Sofia. Acad. Publ. house "Prof. M. Drinov, pp 195. ISBN:978-954-322-988-8

Solakov D., M. Metodiev, S. Simeonova and P. Trifonova (2019b) Population exposure index – an element of seismic risk assessment, *10th Congress of the Balkan Geophysical Society*, Sofia, 2019, DOI: 10.3997/2214-4609.201902659

✉ **Petya Trifonova**
http://orcid.org/0000-0002-9728-9984
National Institute of Geophysics, Geodesy and Geography
Bulgarian Academy of Sciences
Sofia, Bulgaria
E-mail: p.trifonova@abv.bg

✉ **Dimcho Solakov**
http://orcid.org/0000-0003-4148-0525
National Institute of Geophysics, Geodesy and Geography
Bulgarian Academy of Sciences
Sofia, Bulgaria

✉ **Stela Simeonova**
National Institute of Geophysics, Geodesy and Geography
Bulgarian Academy of Sciences
Sofia, Bulgaria

✉ **Metodi Metodiev**
http://orcid.org/0000-0002-2950-9105
National Institute of Geophysics, Geodesy and Geography
Bulgarian Academy of Sciences
Sofia, Bulgaria

✉ **Stefan Florin Balan**
https://orcid.org/0000-0002-2308-7001
National Institute for Research and Development for Earth Physics
Măgurele, Romania
E-mail: sbalan@infp.ro

GEOARCHAEOLOGICAL RESEARCH IN THE AREA OF THE CAPE SHABLA USING UNMANNED AERIAL VEHICLES, NORTH BULGARIAN BLACK SEA COAST

Preslav Peev, Bogdan Prodanov
Institute of Oceanology - Bulgarian Academy of Sciences (IO-BAS)

Abstract. This paper aims to set out the role of using aerial remote sensing and marine hazard can play in informing responses to global challenges of coastal cultural heritage and enhancing the sustainable development of coastal zones. Aerial remote sensing and photogrammetric approaches are an integral part of modern archaeological research. In the last two decades of the century, a significant change in approaches to archaeological research has taken place: from direct fieldwork and excavation to remote sensing. In Bulgaria, this scientific discipline is quite new and it is in its infancy. However, during the last few years, the Institute of Oceanology – BAS conducted such types of investigations and a lot of new data have been collected. For this initial survey has been chosen a heritage site on the Bulgarian seashore. The studied area is the archaeological site Caron Limen/Caria at the Cape Shabla and it is determined as highly hazardous to coastal erosion. A systematic archaeological study of the topographic evolution of the coast in association with the functionality of case study area and other coastal facilities during Late Antiquity and Medieval Ages provides new data on the development of coastal life and especially the nature of sea exploitation in the context of maritime commerce.

Keywords: archaeology; unmanned aerial vehicles (UAVs); aerial photogrammetry; coastal erosion

INTRODUCTION

Aerial remote sensing is an integral part of modern archaeological research. In the last two decades of the century, a significant change in approaches to archaeological research has taken place: from direct fieldwork to remote sensing (Skrypitsyna et al. 2019). A brief overview of using UAV technology for surveying the Bulgarian coast shows, that possibilities of data acquisition in the field of coastal geomorphological and landscape mapping have been improved (Prodanov et al., 2020). The very high spatial resolution (2-10 cm) of the UAV datasets is a property that facilitates the three-dimensional (3D) landscape-scale change detection and

analyses of the coastal environment. Along the Bulgarian shores, UAV imagery has been used for derivation of digital surface models (DSMs), orthomosaic (OMs) and 3D Tiled models for subsequent analyses of the terrestrial and submarine morphology (Prodanov et al., 2019a, 2019b), mapping and determination of the conservation Status of natural habitats and species (Dimitrov & Savova, 2019), and archaeological research, etc.

GEOLOGICAL BACKGROUND

The investigated area includes the easternmost part of one of the main morphotectonic units in Bulgaria – the Moesian Epiplatform Plain (Kotzev et al., 2017). It is the eastern part of the Dobrudzha plateau, which is one of the major geological structures on the Balkans – the Moesian (Danubian) Platform (fig. 1). The geological formations occurring in the shoreline are complex and varied. The structure and the evolution of the area are controlled by extremely complex processes and factors, including fluctuations in relative sea level, fluvial inputs, marine dynamics, morphology, and tectonics.

The Moesian (Danubian) Platform occupies the northern part of the Bulgarian Black Sea coast. Its lithostratigraphic compositions are dominated by Miocene sedimentary strata, e.g., sandy limestones, sandstones, marls, clays, etc. (Peychev & Peev, 2006). A distinctive lithological feature of the shore in this area is the Quaternary loess (Kotzev et al., 2017). The thickness is between 9 to 19 m (Peychev & Peev, 2006).

The erosion shores are common in the northern extremity between Cape Sivriburun and Cape Shabla, being represented by Sarmatian limestones (the Karvuna Formation) in the base, being represented by loess type deposits (Peychev & Peev, 2006). At Cape Shabla, the cliff shore has a generally eastern exposure, and that is why the withdrawal rate is increased approximately $0.30_{m/year}$ (Peychev, Peev & Stanchev, 2006).

Since ancient times, the coastal area of Cape Shabla is settled by humans from the Prehistory and it is rich of archaeological sites and artifacts. In the area of Cape Shabla are known three sites which are important for both geography and archaeology: the submerged Prehistoric necropolis, the reef of the Lake Shablenska Tuzla and the ancient fortress Caron limen/Caria (Peev, 2008). The area is rich of heritage sites, but those of them, which are situated on the seashore, are exposed to natural hazards. The objective is to streamline the process of creating elevation data and contours lines, orthomosaics for survey detection, documentation, and monitoring of coastal archaeological sites.

CASE STUDY

The archaeological site is located at Cape Shabla, built on the coastal cliff. The remains of the site are today visible on the cliff and underwater. The most

Figure 1. The location of the archaeological sites Caron limen/Caria

significant architectural remains come from the time of the Late Antiquity (Tor-batov, 2002).

The port at the Cape Shabla is mentioned by Pomponius Mela (P. Mela 2, 22) (Baudet, 1843) and Flavius Arriuanus (Ar. PPE 35)(Müller, 1855), repeated by Anonymous Periplus, also (Ann. PPE 75)(Diller, 1952), as a port of Carians, situated between Kallatis (modern Mangalia, Romania) and Cape Kaliakra. The first narrative sources mentioned the site under the toponym Caron limen or Portus Caria. According to Anonymous periplus „Now *cariae* are called c*areae*" (Ann. PPE 75). The note refers to the locals and it should think that there is a change in the name of the settlement as Caria passes into Carea. Furthermore, Procopius (Procopius, De Aedificiis, IV. 11) mentioned Creas, a toponym which can be associated with Carea.

The first regular excavations took place during 1976 and 1979, directed by R. Boshnakov and Iv. Vasilchin (Torbatov, 2002). Underwater surveys were carried

out during 1962, 1974, 1979, and 1980 years by M. Lazarov and Bulgarian – Polish expeditions (Toncheva, 1964; Lazarov, 1988). The first authors who draw attention to Caron limen are N. Tsitsov (Tsitsov, 1909) and L. Bozhkov (Bozhkov, 1925). G. Toncheva (Toncheva, 1964) and, in particular, M. Lazarov (Lazarov, 1988) discussed this issue in more detail. There is a published map of the underwater reef (Lazarov, 1975). The last significant study of this site was done by S. Torbatov (Torbatov, 2002), who summarized almost all the available information on the archaeology and historical development of the region of Cape Shabla.

The oldest archaeological materials get back to the Late Bronze Age (1500–1200/1100 BC) (Peev, 2008). To the north of the reef, five stone anchors with holes were found at a depth between 1.5 up to 3.5 m (Lazarov, 1988; Orachev, Oracheva, 1988). The oldest amphorae have an origin of the Chios Islands in the Aegean and dated to the second and third quarters of the 5th century BC (Lazarov, 1988). The most widespread pottery found in the settlement da back to the 5th – 6th century AD (Torbatov, 2002).

METHODOLOGY/DATA AND METHODS/ DATA ACQUISITION

A DJI Phantom 4 Pro Quadcopter was used to photograph the archaeological site Caria and reconstruct the components' topography. Figure 2 presents the used workflow of conducted UAV survey, which is differentiated into five stages:

Stage 1. Planning of surveys. It is necessary to obtain a Flight permit by the Directorate General "Civil Aviation Administration" at the Ministry of Transport, Information Technology and Communications of the Republic of Bulgaria.

Stage 2. Cleaning of the Archaeological sites.

Stage 3. Preliminary on-site activities. Twenty-nine ground control points (GCPs) were systematically placed in the archeological sites. Geodetic control measurements were made with a GPS (HiTarget V90Plus), providing a millimeter accuracy. The overland control points are with 2 cm horizontal and 3 cm vertical accuracy.

Stage 4. Flight plan and image collection. The survey was conducted in the period October 15-16, 2019, under appropriate meteorological conditions. The flight altitude was 50 m at 1.45 cm ground sampling distance (GSD). For better details, some elements were captured at 25 m altitude with 0.75 cm GSD (Fig. 3).

Stage 5. Structure-from-motion data processing. UAV data processing of imagery was made by Agisoft Photoscan Professional and Pix4Dmapper (Fig. 3). Using this software usually requires up to eight main steps: (1) Masking of the images (optional) – in case that any of the photos include sky or other unwanted elements; (2) image alignment; (3) generation of the initial dense point cloud; (4) georeferencing of the model; (5) optimizing the image alignment using the ground control points; (6) generation of a high-resolution dense point cloud and generation of the DSM/DEM, OM and 3D TM (Fig.4).

Figure 2. A Workflow for 3D reconstruction of the Caron limen/Caria site
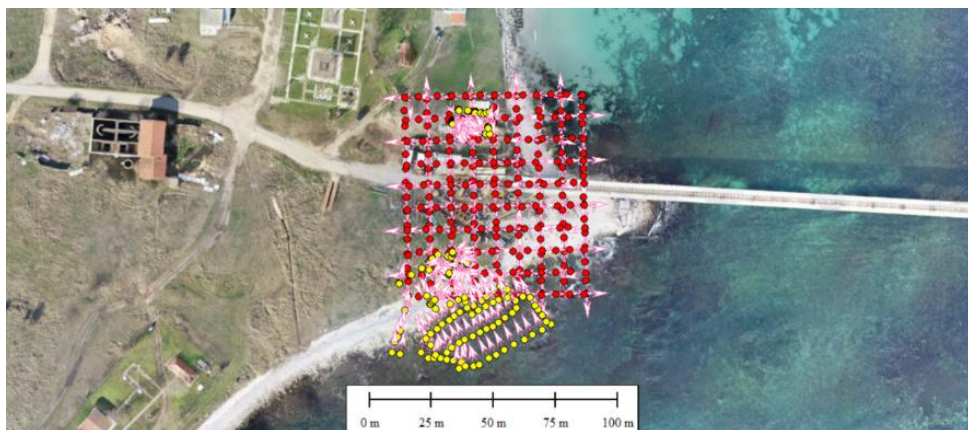
Figure 3. Location of the UAV imagery (red points: flight altitude –
50 m; yellow points: manual mode)

DIGITAL RECONSTRUCTION OF REMAINS
OF THE EARLY BYZANTIUM FORRTRESSSITE

From the information gathered so far, it can be concluded that in the area of Cape Shabla existed a harbour very well protected from the northern and eastern winds. In the results of various underwater investigations, the reconstruction of the port basin of the ancient settlement Caron limen/Caria is presented (Toncheva, 1964; Lazarov, 1988; Orachev, Oracheva, 1988). It is one of the safest ports on the Western Black Sea during the Late Bronze Age and Antiquity. It is possible that the antique harbour has had an artificial origin, considering the terminus *limen* (Angelova, 1985).

At the Cape Shabla, an underwater reef is known, which was a natural breakwater of the ancient settlement at the time of the lower Black Sea level. The first investigators of the history of the case study area testify that the reefs were once with artificial superstructure (Tsitsov, 1909). This coincides totally with the stated assumption by S. Torbatov (Torbatov, 2002), as well as with the toponym Caron limen/Portus Caria. During the underwater archaeological expeditions is determined that the site has a length of about 400 m and depth up to 4 m (Lazarov, 1988). A trestle was erected on it, which was destroyed during a storm in the winter of 2002 and it is currently under reconstruction. If we picture the situation before 3500 years with the Black Sea level about 3 – 5 m below present, we will see that the reef was above the water surface and it was protected the ancient bay (Peev, 2008). This explains the presence of a settlement and a harbour basin in the area, which is unsuitable for mooring nowadays. The absence of pottery material later

A) Digital surface model of (10 cm resolution)	B) Very high resolution orthomosaic (0.5 mm/pix)

C) 3D Tiled model
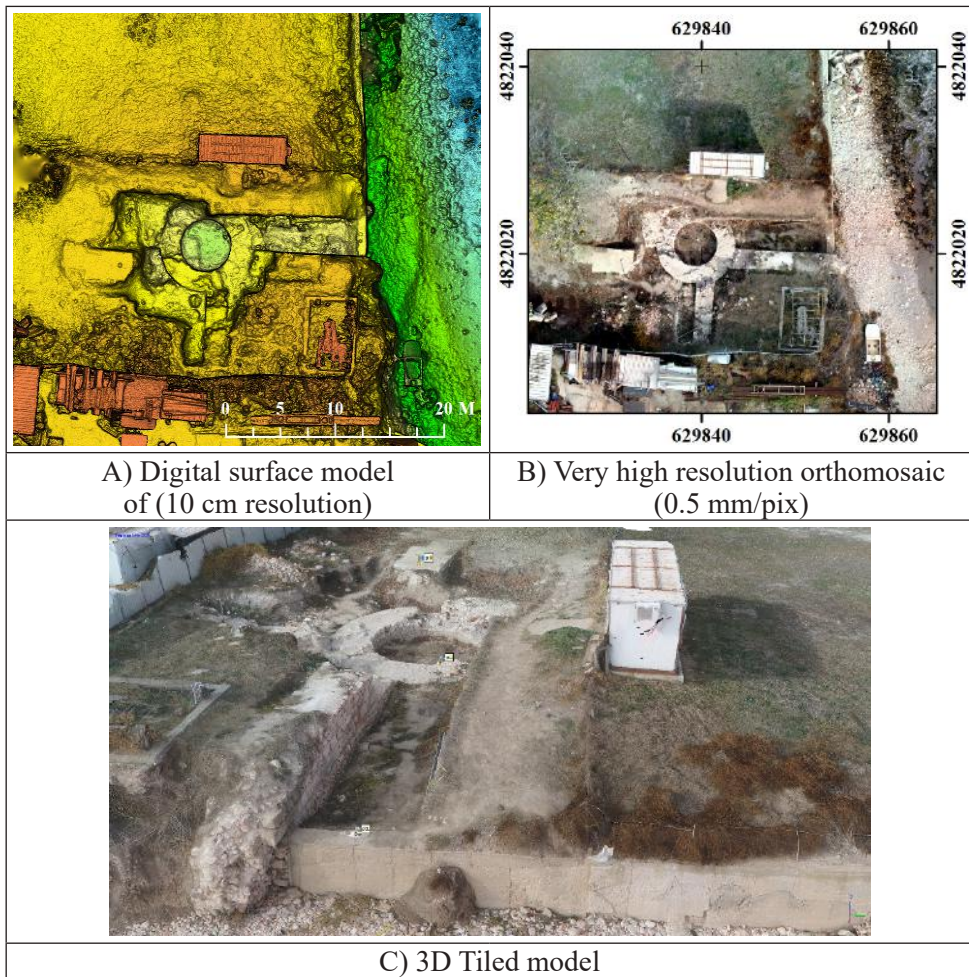
Figure 4. Remains of the site Caron limen/Caria (photo: authors)

than the end of the 6th century suggests that about 1400 years ago, there was a flood of the Nymphean transgression. The antique harbour basin itself is located south of the reef. The four lead stocks (type IV) of iron anchors were found to the east of the stone anchors at a depth of 10 – 11 m.

The preserved parts of Carea include northern city wall, tower, and a quarter of the southern part of this site (Fig. 4).

Meanwhile, various hydrological and geomorphological changes have modified the configuration of the coastline and palaeogeographic conditions in the Antique

landscape significantly. The changes become more noticeable after the 3rd-4th century AD when the rate of the Black sea level rising (the Nymphean transgression) increased, and as a result, the destruction of the coast (Peychev & Peev, 2006). This has not gone unnoticed by the author of The Anonymous Periplus where it is mentioned that "καὶ ἡ γῆ ἐν κύκλῳ τοῦ λιμένος κατακλύζεται" which means "now the land near the port is flooded" (Ann. PPE 75). The date of historical source's compilation is very important due to it may be the first known information about the sinking of the ancient port. C. Müller evidenced dating in the 5th century AD (Müller, 1855) and this opinion is accepted by most scientists. All of this does not allow us to restore the exact plan and view of the settlement during the different historical periods and the colossal changes in the configuration of the coast.

In the present day, the coastline is different from the Antiquity. A significant part of the port city has been destroyed irrevocably as a result of the Black sea level rising and increasing of the coastal erosion and possible seismic activities in the region. At the beginning of the 20th century, the eastern part of the settlement had already been completely lost. It is necessary to mention that damages of Carea have also caused by construction work (using materials from the fortress during the building of the Shabla lighthouse, disturbance of the cultural layers during the construction of military objects, etc.) and oil extraction activities.

CONCLUSION

The archaeological and historical heritage of the area is significant. This survey aims to develop methods for mapping and detection of coastal archaeological sites using technologies such as Autonomous Unmanned Aerial Vehicles (UAVs or drones), that have recently become affordable.

The results of the work carried out allowed us to correct and supplement the existing data, as well as to prepare the basis for creating a common geo-information space of the Bulgarian Black Sea region in the archaeological context.

The general impression is that the site is subjected to stress by a variety of factors and influences – natural hazards (coastal erosion, sea level rising), human activities (building works, tourist stress), etc. It is necessary the careful studying, including underwater, of the preserved parts of the settlement and the suggestion of emergency measures for its strengthening and conservation. What is now required are the resources on a scale to match the demands of this new and challenging agenda.

The archeological sites were photographed through Quadcopter Phantom 4 RTK, acquired under the project "Mapping and monitoring of depositional areas along the North Bulgarian Black Sea coast using Unmanned Aerial Vehicles" (Agreement № КП-06-COST-12/06.08.2019), funded by the National Science Fund at the Ministry of Education and Sciences of the Republic of Bulgaria.

REFERENCES

Angelova, H. (1985). About the uses of όρμος and λιμήν in Arrian's Περίπλους τού Πόντου Ευξείνον from the IInd C.A.D. *Thracia Pontica,* II, 8 – 11.

Baudet, L. (1843). *Géographie de Pomponius Mela.* Paris

Bozhkov, L. (1925). Gde se e namiralo antichnoto pristanishte Karia. *Bulgarian engineering – architectural society*, 25.8, 118 – 123 (in Bulgarian).

Diller, A. (1952). *The tradition of the minor Greek geographers.* Lancaster – Oxford: Lancaster Press/Blackwell .

Dimitrov, St. & Savova, V. (2019). UAS-based rapid mapping and assessment of sand dunes along the Bulgarian Black Sea coast: The Case of Coral Beach, Bulgaria. *Proceedings. of International Scientific Conference Geobalcanica`2019*, 567 – 572.

Kotzev, I., Stanchev, H., Stancheva, M., Filipova-Marinova, M., Yankova, M., Peev, P., Peychev, V., Krastev, A., Palazov, A. & Pavlov, D. (2017). *Sensitivity mapping and analysis of the Bulgarian Black Sea coastal zone.* Sofia: Total E&P Bulgaria B.V.

Lazarov, M. (1975). *The sunken fleet.* Varna: Georgi Bakalov (in Bulgarian).

Lazarov, M. (1988). Zagadachnoto kariysko pristanishte. *FAR'88*, 33 – 42 (in Bulgarian).

Müller, C. (1855). *Geographi Graeci Minores.* Paris: Instituti Franciae Typographi.

Orachev, At., Oracheva, I. (1988). Reconstruction of stone anchors from the Shabla museum collection. *Archaeology*, 1, 18 – 29 (in Bulgarian).

Peev, P. (2008). Underwater sites in the area of Cape Shabla (North-East Bulgaria). In: *Geoarchaeology and Archaeomineralogy (Eds. R.I. Kostov, B. Gaydarska, M. Gurova), Proceedings of the International Conference, 29-30 October 2008 Sofia, Bulgaria*, 303 – 304.

Peychev, V. & Peev, P. (2006). *Evolution of the Bulgarian Black Sea coast after the Early Holocene.* Varna: Slavena (in Bulgarian).

Peychev, V., Peev, P. & Stanchev, H. (2005). New data about coastal erosion rate along the Bulgarian Black Sea coast. *Proceedings of the Institute of Oceanology*, 5, 170 – 180 (in Bulgarian).

Prodanov, B., Lambev, T., Bekova, R. & Kotsev, I. (2019a). Applying Unmanned Aerial Vehicles for high-resolution geomorphological mapping of the Ahtopol coastal sector (Bulgarian Black Sea coast). *SGEM Conference Proceedings*,19 (2.2), 465 – 472.

Prodanov, B., Kotsev, I., Lambev, T., Dimitrov, L., Bekova, R. & Dechev, D. (2019b). Drone-based geomorphological and landscape mapping of Bolata Cove, Bulgarian coast. *Sustainable Development and Innovations in Marine Technologies*, Taylor & Francis Group, 592 – 598.

Prodanov, B., Kotsev, I., Lambev, T. & Bekova, R. (2020). Unmanned Aerial Vehicles for surveying the Bulgarian Black Sea Coast. *Comptes rendus de l'Academie Bulgarie des Sciences*, 73(5), 666 – 672.

Skrypitsyna, T.N., Kobzev, A.A., Kurkov, V.M. & Zhuravlev, D.V. (2019). Remote sensing data as a geospatial basis for archaeological research. *Engineering survey,* 13.3, 18 – 26 (in Russian).

Toncheva, G. (1964). *The sunken harbours.* Varna: Darzhavno izdatelstvo Varna (in Bulgarian).

Torbatov, S. (2002). *The defense system of the Late Roman province Scythia (the end of the 3rd – the 7th century AD).* Veliko Tarnovo: Faber (in Bulgarian).

Tsitsov, N. (1909). Starini v Shablensko (Balchishko). *Izvestiya na varnenskoto arheologichesko druzhestvo,* II, 78 – 79 (in Bulgarian).

✉ **Preslav Peev**
https://orcid.org/0000-0002-7841-548x
Institute of Oceanology
Bulgarian Academy of Sciences
Varna, Bulgaria
E-mail: peev@io-bas.bg

✉ **Bogdan Prodanov**
https://orcid.org/0000-0002-8118-3034
Institute of Oceanology
Bulgarian Academy of Sciences
Varna, Bulgaria
E-mail: bogdanprodanov@gmail.com

EARTHQUAKE SCENARIOS
FOR THE CITY OF RUSE

**Dimcho Solakov[1], Stela Simeonova[1], Plamena Raykova[1],
Boyko Rangelov[2], Constantin Ionescu[3]**
*[1]National Institute of Geophysics, Geodesy and Geography –
Bulgarian Academy of Sciences (NIGGG-BAS)
[2]University of Mining and Geology – Sofia, Bulgaria
[3]National Institute of Research and Development for Earth Physics, Romania*

Abstract: Earthquakes are the deadliest natural disasters affecting the human environment. Global seismic risk and vulnerability to earthquakes are increasing steadily as urbanization and development occupy more areas that a prone to effects of strong earthquakes. Furthermore, uncontrolled growth of mega cities in highly seismic areas in the world is often associated with the construction of buildings and infrastructure, inconsistent with the regional seismo-tectonic features and seismic hazard. The assessment of seismic hazard and generation of earthquake scenarios is the first link in the prevention chain and the first step in the evaluation of the seismic risk.

In the present study a deterministic earthquake scenario (expressed in macroseismic intensity MSK) for the city of Ruse is generated. The study is guided by the perception that usable and realistic, based on both local seismic history and tectonic conditions, ground motion maps have to be produced for urban areas. The scenario maps account soil amplification effects using the geotechnical zonation of the considered urban area.

Keywords: deterministic scenarios, intermediate depth earthquakes, Vrancea seismic source, Romania, Bulgaria

INTRODUCTION

By deterministic scenario it is mined a representation of the severity of ground shaking over an urban area, using one or more hazard descriptors. Such representation can be obtained either from the assumption of a "reference earthquake" specified by a magnitude or an epicentral intensity, associated to a particular earthquake source (e.g. a fault, a point, a crustal volume), or, directly, showing values of local macroseimic intensity, or of instrumentally measured parameters (if available), generated by a damaging, real earthquake of the past.

In the first case, the local ground shaking levels typically need to be evaluated through attenuation relations for the selected parameters. In the second case, the

most common situation is that of a single or few intensity values that concisely describes the severity of the effects on the built environment caused by the historical earthquake selected as representative.

Perhaps the single most important feature of the approach is that the deterministic scenario must be consistent with the seismic history of the city and with known active faults close to the city. Thus, the reference event could be either the "true" maximum historical earthquake that affected the city or destructive event close to the city complaint with known active faults.

A deterministic scenario for Ruse – one of the largest earthquake-prone cities in Bulgaria was developed. Ruse is the fifth-largest city in Bulgaria, with a population of near 160 000. Ruse is situated in the northeastern part of the country, on the right bank of the Danube in the mouth of Rusenski Lom River. It is the most significant Bulgarian river port. The city is an administrative, transport and tourism center of Bulgaria, Ruse is known for its 19th and 20th century Neo-Baroque and Neo-Rococo architecture.

In the present study, the deterministic earthquake scenarios (in terms of macroseismic intensity) that are consistent with the seismic history of the city of Ruse are generated. The seismic hazard for the city of Ruse is controlled by the Vrancea intermediate-depth source in Romania that is located at about 150 km to the N-NW from the city. (Simeonova et. al., 2006 and Solakov et al., 2009). The scenario earthquake ground motion fields in Ruse are derived postulating strong intermediate depth earthquakes in Vrancea.

METHODOLOGY

The approaches adopted for developing earthquake scenarios include the following stages:

1. Compilation of regional seismotectonic data base (region surrounding the considered urban area); 2. Analysis of regional seismotectonics (identification of active faults capable of generating earthquakes); 3. Evaluation of the seismic potential of the active structures (maximum expected magnitude); 4. Geotechnical characterization of the studied area; 5. Selection and weighting of appropriate GMPE's, consistent with the seismotectonic features of the region; 6. Selection of the scenario event (magnitude and hypocentral distace); 7. Evaluation of the ground motion parameters.

SEISMOTECTONICS

The tectonic situation in the Eastern Mediterranean is dominated by the collision of the Arabian and African plates with the Eurasian. The African continental plate is moving in north direction relative to Eurasia with velocity of about 20-25 mm/y (Solakov et al., 2019a). The leading edge of the African plate is subducted on the Greek arc under the Eurasian plate.

The recent tectonics of Bulgaria is determined by the geotectonic of the region in which dominate the processes of extension with general direction north-south. Analysis of the obtained horizontal velocities of the permanent GNSS stations and geodynamic networks shows that the horizontal velocities increase from 2 mm/y in the region of Northern and Eastern Bulgaria till 10 mm/y in the region of the Chalkidiki Peninsula. On the territory of Northern Bulgaria, the horizontal velocities are practically negligible which confirms that this region belongs to the Eurasian plate while Central Western and Southwestern Bulgaria belong to the so-called South Balkan Extensional Region – a transition zone between Eurasian continental plate and Aegean micro-plate (Solakov et al., 2019a).

The Vrancea seismogenic zone of Romania is a very peculiar seismic source, often described as unique in the world, and it represents a major concern for most of the northern part of Bulgaria. The events generated in this seismogenic zone are characterized by relatively deep hypocentres and wide area of macroseismic impact. In this area strong intermediate focused earthquakes are being realized with depth 90-230 km. The strongest known events, occurred in the Vrancea seismogenic zone are the following earthquakes: the 1802 quake with magnitude $M_W 7.9$ (ROMPLUS catalogue- Oncescu, et al. 1999), the 1940 $M_W 7.7$ (ROMPLUS catalogue available at https://web.infp.ro/#/romplus), and the 1977 quake, $M_W 7.5$ (according GCMT catalogue - Dziewonski, et al., 1981; Ekström, et al. 2012). Situated at distances larger than 200 km from the Vrancea zone, several cities in the northern Bulgaria suffered many damages due to high energy Vrancea intermediate-depth earthquakes (as illustrated in Fig.1).

Figure 1. Damages in Northern Bulgaria caused by the 1977 ($M_W 7.5$) Vrancea earthquake

SOIL PROPERTIES

The city of Ruse is situated in a flat area. Hills with an altitude of 120-140 m are located in the southeastern part of the city. The area is characterized by a high level of groundwater. Under dynamic loads of different intensity, the soil base can be subjected to liquefaction, sand volcanism and local landslides. These should be considered in seismic risk assessment of the city of Ruse.

The representation of the soil properties of the city was defined by the engineering parameter V_{s30} - average shear-wave velocity in the upper 30 m of the soil/rock profile. The V_{s30} values for the city of Ruse, presented in Fig. 2 are based on the results derived in the frame of the project "Environmental Protection and Reduction of Risks of Adverse Events and Natural Disasters". Figure 2 shows that the values of V_{s30} slightly vary throughout the territory of the city of Ruse. Four blocks with different properties are outlined throughout the city.

The most widespread soil (marked with Block 1) is quaternary loess with thickness over 30 m.
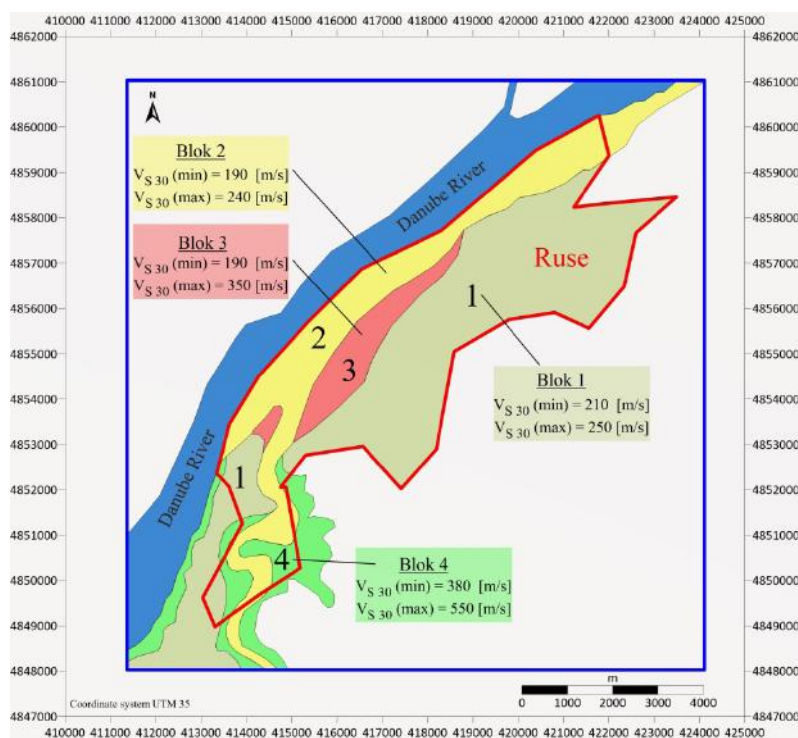
Figure 2. Average shear-wave velocity in the upper 30 m
of the soil/rock profile for the city of Ruse

Block 2 - These are alluvial formations on the flood terraces of the Danube and Rusenski Lom rivers. Water-saturated sands and cohesionless gravels up to 10 m thick characterized by a manifestation of liquefaction they lie everywhere over the fuzzy and karstic limestones from the Ruse Formation. Its thickness is over 50 m.

Bock 3 - cohesionless sands with thickness of 10-12 meters that are characterized by a pronounced liquefaction property.

Block 4 - organogenic and oolite limestones from the Ruse Formation. Cut deep from the Rusenski Lom. River. That is relatively the strongest soil base.

GROUND MOTION ATTENUATION (GMPE' S)

An essential element in seismic hazard analyses is the ability to estimate strong ground motion from a specified set of seismological parameters. This estimation is carried out using a Ground Motion Prediction Equation, or what is also referred to as an attenuation relation. A GMPE is a mathematical equation that relates a given strong-motion parameter to one or more parameters of the earthquake rupture, wave propagation path and local site conditions, referred to as seismological parameters. GMPE's are essential in seismic hazard studies, which are a key step for the evaluation of seismic risk and loss estimation for a region.

The selection process of adequate GMPE's started from a comprehensive list of available ground motion models to which a set of exclusion criteria was applied according to the similarity of the tectonic environment, clarity of the underlying datasets, frequency ranges of the predictive equations, the regression model, the definition of the prediction variables, international recognition, etc. The following three attenuation relationships were selected for intermediate depth earthquakes on the base of general criteria (Solakov at al., 2019b): BC Hydro – Abrahamson et al., 2016; Y97- Youngs et al., 1997; VAC-Vacareanu et al. 2015). These equations were tested against the actually recorded ground motion data for 8 moderate to large intermediate depth Vrancea earthquakes.

The method introduced by Scherbaum et al. (2009) is chosen for testing the models against the observational data. Scherbaum et al. (2009) provides a ranking criterion based on information theory. This technique is based on the probability for an observed ground motion to be realized under the hypothesis that a model is true.

It provides one value, the negative average log-likelihood LLH that reflects the fit between data and model:

$$LLH = -\frac{1}{N}\sum_{i=1}^{N}\log_2(g(x_i))\qquad(1)$$

with N the number of observations x_i, and g the probability density function predicted by the GMPE's (normal distribution).

A small LLH indicates that the candidate model is close to the model that has generated the data, while a large LLH corresponds to a model that is less likely of

having generated the data. The selected models provide low LLH values, less than 2.0 implying a good fit predicted values and observational data (as seen from Table 1). The GMPE VAC (Vacareanu et al. 2015) is the best fit to observations for strong Vrancea earthquakes - the lowest LLH value of 1.073. Therefore, the relation VAC (Vacareanu et al. 2015) is applied in all the following analysis.

Table 1. The LLH values corresponding to the selected three attenuation models for intermediate depth earthquakes

Law	All magnitudes - 173 observations		Mw>6 - 97 observations	
	Mean ln(obs)-ln(pred)	LLH	Mean ln(obs)-ln(pred)	LLH
BCHydro	0.021	1.307	0.15	1.272
Y97	-0.115	1.423	0.125	1.252
VAC	-0.24	1.343	-0.029	1.073

DETERMINISTIC EARTHQUAKE SCENARIOS FOR THE CITY OF RUSE IN TERMS OF INTENSITY

A deterministic earthquake scenario in macroseismic intensity is generated for the city of Ruse. The scenario is based on both local seismic history of the city and tectonic environment. The scenario earthquake is $M_W 7.5$ Vrancea quake at depth 94 km and hypocentral distance of 240 km.

The ground motions in PGA are calculated using the GMPE VAC (Vacareanu et al., 2015). The estimated peak ground accelerations are converted into intensity applying the following relations (Ardeleanu et al, 2020):

$$I = 3.146\log(PGA^{\max}) + 0.375 \tag{2}$$

$$I = 3.058\log(PGA^{gm}) + 0.731 \tag{3}$$

where PGA^{max} is the maximum of two horizontal components, PGA^{gm} is the geometric mean of two horizontal components in cm/s.

Seismic history of Ruse shows that the hazard for the city is mainly influenced by the intermediate depth quakes occurred in the region of Vrancea (Romania). Several Vrancea earthquakes have affected the city of Ruse since 1900.

Vrancea earthquakes that affected the city of Ruse with an intensity of 5 and higher are presented in Table 2. In the Table are presented the predicted PGA^{gm}, predicted and observed intensity I (in MSK), the available observed horizontal accelerations at a Ruse site and difference between observed and predicted values.

The data presented in Table 2 show a good agreement between observed and predicted intensities. The predicted intensity based on the observed peak ground

acceleration for 30.8.1986 earthquake overestimate the observed intensity.

Figure 3 illustrates earthquake scenario in macroseismic intensity (MSK) for the city of Ruse for Vrancea earthquake with M_W7.5 at depth 94 km and hypocentral distance 240 km.

Table 2. Observed and predicted ground motions for Ruse from intermediate depth Vrancea earthquakes

Date	M_w	Iobs[*]	PGA^{gm} pr	PGA^{max} obs[**]/Ipr	PGA^{gm} Obs[**]/Ipr	I pr	Iobs-Ipr
13.9.1903	6.3	5	29.4			5.2	-0.2
6.10.1908	7.1	5	72.5			6.4	-1.4
22.10.1940	6.5	5	29.7			5.2	-0.2
10.11.1940	7.7	7	94.9			6.8	0.2
4.3.1977	7.5	7	103.2			6.9	0.1
30.8.1986	7.23	6	79.9	75.5/6.3		6.5	-0.5
30.5.1990	6.95	6	53.3	114.5/6.9	100.1/6.8	6.0	0.0

[*] - from Simeonova S. et al. (2009) and Aleksandrova I. (2015), [**] - from Report GPhI, 2007.
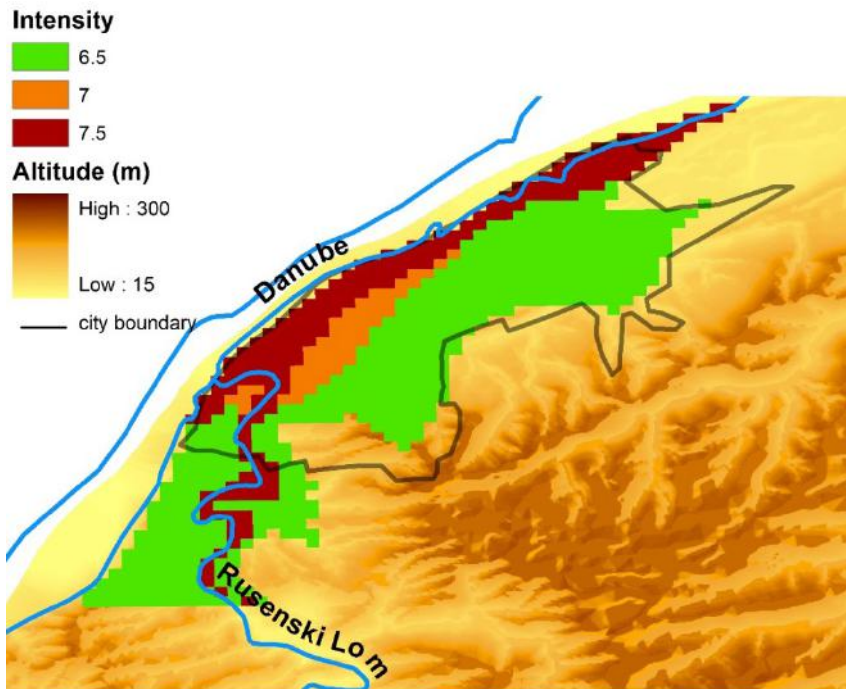
Figure 3. Deterministic earthquake scenario for the city of Ruse in intensity

In deterministic scenario (Fig.3) the predicted intensity is assigned to Block 3 (see Fig. 2). Intensity for Block 2 (Fig. 2) is increased with 0.5 because of the high ground water level. The intensity for Blocks 1 and 4 (Fig. 2) are decreased with 0.5 because of the observed impact of 1977 earthquake for Block 1 and for comparatively high Vs30 values for Block 4 (Fig.2).

The generated scenario earthquake is consistent with the conclusion reached after the 1977 Vrancea earthquake - the consequences decrease with distance from the Danube River (Brankov et al, 1983, Solakov et al., 2009).

It should be noted that the intensities in deterministic earthquake scenario for the city of Ruse (Fig.3) will increased with half intensity unit for the M_w8 Vrancea earthquake with depth 150 km and at a hypocentral distance of 256 km.

CONCLUSION

The main conclusions from this study can be summarized as follows:

A deterministic earthquake scenario in macroseismic intensity (MSK) is developed for the city of Ruse. The work on scenarios was guided by the perception that usable and realistic (also in the sense of being compatible with seismic histories of city that are often several centuries long) ground motion map had to be produced for the urban area The intensity values vary between 6.5 and 7.5 throughout the city of Ruse;

It should be emphasized that the GMPE that is presented in Vacareanu et al. (2015) and the conversion relations in Ardeleanu et al. (2020), are useful tool for seismic hazard assessment and deterministic earthquake scenario generation;

Estimation of deterministic earthquake scenarios for a city is one of the most important challenges in the field of seismology. Moreover, it is a key step for the evaluation of seismic risk and loss estimation for a city. The generated scenario map is reliable and can be used for developing risk scenario, for engineering decisions, and in infrastructure planning and insurance;

The earthquake scenarios are intended as a basic input for developing detailed earthquake damage scenarios for the city and can be used in earthquake-safe town and infrastructure planning;

The consideration of the earthquake scenarios into the policies for seismic risk reduction will allow focusing on the prevention of earthquake effects rather than on the activities following the disasters.

REFERENCES

Abrahamson, N., Gregor N., and K. Addo (2016). BC Hydro Ground Motion Prediction Equations for Subduction Earthquakes. *Earth. Spectra*: February 2016, Vol. 32, No. 1, pp. 23-44

Alexandrova, I., (2015). *Macroseismic field modelling for the territory of Bulgaria*. PhD thesis, 77 p. (in Bulgarian)

Ardeleanu, L., Neagoe C., Ionescu C., (2020). Empirical relationships between macroseimic intensity and instrumental ground motion parameters for the intermediate-depth earthquakes of Vrancea region. Romania *Natural Hazards, DOI: 10.1007/s11069-020-04070-0*

Brankov, G, Bonchev E., Ignatiev N., Boncheva H., Christoskov L., Paskaleva I., (1983). *Vrancea earthquake in 1977. Its after-effects in the People's republic of Bulgaria.* Publ. House of Bulg. Acad. Of Sci., Sofia, 428 p. (in Bulgarian)

Dziewonski, A., T. Chou and J. Woodhouse, (1981). Determination of earthquake source parameters from waveform data for studies of global and regional seismicity, *J. Geophys. Res*., 86, 2825-2852, 1981. doi:10.1029/JB086iB04p02825

Ekström, G., Nettles M., and Dziewonski A. M., (2012). The global CMT project 2004-2010: Centroid-moment tensors for 13,017 earthquakes, *Phys. Earth Planet. Inter*., 200-201, 1-9, doi:10.1016/j.pepi.2012.04.002

Oncescu M C., Mârza V I., Rizescu M., Popa M., (1999) The Romanian earthquake catalogue between 6 984–1996. In: Wenzel F, Lungu D, Novak O (eds.) Vrancea earthquakes: tectonics, hazard and 7 risk mitigation, *Kluwer Academic Publishers*, Dordrecht, pp 43-49

Report GPhI, (2007). *Seismic zoning of the Republic of Bulgaria, in accordance with the requirements of Eurocode 8* (interim report), pp 207 (in Bulgarian)

Simeonova S., Aleksandrova I., Solakov D., Popova I., Georgieva G., (2006). Observed macroseismic effects from intermediate Vrancea, Romania earthquakes (1940, 1977) on the territory of the town of Rousse. *Proc. Geosciences,* Sofia, 323-326.

Solakov D., Simeonova S., Aleksandrova I., Popova I., Georgieva G., (2009). Earthquake Scenarios: cases study for the cities of Ruse and Vratsa. *Conf. Proc. 5th Congress of Balkan Geophys. Soc.– Belgrade, Serbia10–16 May 2009, cp-126-00083, DOI: 10.3997/2214-4609-pdb.126.6497*.

Solakov D., Simeonova S., Trifonova P., Georgiev I., Raykova P., Metodiev M., Aleksandrova I., (2019a). *Building Seismic Risk Management, Part 2: Regional seismotectonic model and model of seismic sources*. BAS Publ. House, S., 21-45, 2019 (in Bulgarian).

Solakov D., Simeonova S., Raykova P., Oynakov E., Aleksandrova I., (2019b). GMPEs used in seismic hazard assessment for Bulgaria-selection and testing in Bulgaria. *Conf. Proc., 10th Congress of the Balkan Geophys. Soc., Sep 2019, 1–5, DOI: https://doi.org/10.3997/2214-4609.201902658*

Vacareanu R., Radulian M., Iancovici M., Pavel F., and Neagu C., (2015). Fore-arc and back-arc ground motion prediction model for Vrancea intermediate depth seismic source, *J. of Earthq. Eng.,* 19(3): 535-562.

Youngs R. R., Chiou S.J., Silva W. J., and J. R. Humphrey, (1997). Strong ground motion attenuation relationships for subduction zone earthquakes, *Seism. Res. Letters*, 68(1):58-73.

✉ **Dimcho Solakov**
http://orcid.org/0000-0003-4148-0525
National Institute of Geophysics, Geodesy and Geography
Bulgarian Academy of Sciences
Sofia, Bulgaria
E-mail: dimos@geophys.bas.bg

✉ **Stela Simeonova**
National Institute of Geophysics, Geodesy and Geography
Bulgarian Academy of Sciences
Sofia, Bulgaria
E-mail: stelas@geophys.bas.bg

✉ **Plamena Raykova**
https://orcid.org/0000-0001-7060-0296
National Institute of Geophysics, Geodesy and Geography
Bulgarian Academy of Sciences
Sofia, Bulgaria
E-mail: plamena.raikova@gmail.com

✉ **Boyko Rangelov**
University of Mining and Geology
Sofia, Bulgaria

✉ **Constantin Ionescu**
National Institute of Research and Development for Earth Physics
Magurele, Romania
E-mail: viorel2k@yahoo.com

COMPLEX ASSESSMENT
OF THE URBAN EARTHQUAKE RISK

Dimitar Stefanov
*National Institute of Geophysics, Geodesy and Geography –
Bulgarian Academy of Sciences (NIGGG – BAS)*

Abstract. The impact of earthquakes in urban areas is a complex problem compounded by multi-hazard and consequential risk issues, enormous inventory of vulnerable physical elements and the attendant socio-economic problems. An approach for assessment of urban earthquake risk is presented. Rational urban risk predictions and expected losses from major earthquakes in the future serve the basis and also provide strong reasons for the pro-active risk mitigation activities. The proposed approach is based on a combination of numerical values for the determined levels of consequences in the three considered areas (social consequences, material consequences, economic losses).

Keywords: earthquake; seismic risk; consequences; building stock

INTRODUCTION

In recent decades, earthquake disaster risks in cities have increased mainly due to a high rate of urbanization, faulty land-use planning and construction, inadequate infrastructure and services, and environmental degradation. Thus for urban centres under possible exposure to large earthquakes, it is imperative that certain preparedness and emergency procedures be contrived in the event of and prior to an earthquake, which in turn requires quantification of the effects of the earthquake on the physical and social environment. The main element of such quantification is the building losses, which is directly related to casualties, planning of emergency response, first aid and emergency shelter needs. A seismic risk analysis addressed to earthquake emergency management and protection strategies planning, requires vulnerability and damage evaluation performed at territorial scale. The results provided by a seismic risk analysis could be regarded as helpful guidelines on respect to all the phases of the risk management: during normal periods, during crisis periods, as well as in the recovery and post-emergency periods. During normal periods, a seismic risk analysis can provide a support to formulate general strategies for earthquake mitigation and disaster

response planning. The casualty evaluation allows judging whether medical care and emergency response essential facilities are sufficient compared to the estimated consequences. In the post emergency period a seismic risk analysis allows identifying the most effective solutions to rebuilt, choosing interventions that may represent an improvement for the future.

METHODOLOGY FOR SEISMIC RISK ASSESSMENT

The present study is based on the "Methodology for Analysis, Evaluation and Mapping of the Seismic Risk of the Republic of Bulgaria", developed by the NIGGG – BAS for Ministry of Regional Development and Public Works, approved by the Minister and having the force of a normative document (Methodology, 2018). The first step is to identify the regions with equal macroseismic intensity referring to the seismic intensity map. Then each building is assigned to a relevant vulnerability class following a procedure based on EMS: The buildings are grouped according to their vulnerability class: from A to F. To each group of buildings, the number of those that reach certain damage grade is calculated directly using the values of the DPM (damage probability matrix) for the vulnerability class and depending on the seismic intensity for the location of the building. The buildings with equal damage grade are selected among all the buildings in the region with equal intensity and belonging to the same vulnerability class. In that way the number of the damaged building is determined. Subsequently the area of the damaged buildings according the damage grades is also calculated from the GIS database for the region. That area is used to assess the monetary loss and the human casualties. The approach is applied to each elementary cell of the GIS representation of the region (the cell is usually 400x400m).

CASE STUDY 1 – TOWN OF SEVLIEVO

The town of Sevlievo is located in central north Bulgaria. The seismic risk assessment is made for three scenarios, corresponding to three levels of seismic input (Solakov, 2019):

• Seismic intensity 7 degree – indicative base for a relatively weak earthquake;
• Seismic intensity 7,5 degree – corresponds to seismic excitation with a return period of 475 years;
• Seismic intensity 8 degree – corresponds to seismic excitation with a return period of 1000 years.

The population is 20 898 people, according to data from the National Statistical Institute. The results are obtained in two variants depending on when the seismic impact occurs – day or night. Table 1 summarizes the social losses – the distribution of the affected people – injured and victims, for the three scenarios considered. Table 2 presents a detailed distribution of the injured by category. The number of people left without shelter (need for accommodation) is given in Table 3.

Table 1. Distribution of the affected people –
injured and victims (day and night)

Intensity (degrees)	Injured - by day (pcs.)	Victims - by day (pcs.)	Injured - by night (pcs.)	Victims - by night (pcs.)
7	17 – 22	5 – 6	29 – 33	8 – 10
7,5	70 – 86	20 – 24	92 – 112	26 – 31
8	147 – 210	40 – 49	201 – 247	56 – 68

Table 2. Distribution of the injured by category (day and night)

Intensity (degrees)	S1-day (pcs.)	S2-day (pcs.)	S3-day (pcs.)	S1-night (pcs.)	S2-night (pcs.)	S3-night (pcs.)
7	6 – 8	5 – 6	6 – 8	10 – 11	9 – 11	10 – 11
7,5	25 – 31	22 – 27	23 – 28	32 – 39	30 – 36	30 – 37
8	52 – 93	48 – 59	47 – 58	71 – 87	66 – 81	64 – 79

Designations: S1 – Minor injuries ; S2 – In need of hospital treatment ; S3 – Severely injured

Table 3. Number of homeless people (need for accommodation)

Intensity (degrees)	people without shelter (pcs.)
7	310
7,5	618
8	1013

The distribution of the buildings, respectively by number and by total floor area (TFA, m^2), in the different levels of damage is systematized in Tables 4 and 5. Table 6 shows the distribution of buildings by area in percentages of the total number.

Table 4. Distribution of buildings (by number) in different damage levels

	Intensity (degrees)		
Damage levels	7	7.5	8
No damage	3837	2901	1964
Slight	2758	2666	2573
Medium	1303	1666	2028
Heavy	484	864	1243
Very heavy	121	344	571
Destruction	13	75	137

Table 5. Distribution of buildings by TFA (m²) in different damage levels

Damage levels	Intensity (degrees)		
	7	7.5	8
No damage	1083978	873211	662744
Slight	511750	561696	611065
Medium	152189	242972	333948
Heavy	35673	85089	134588
Very heavy	6109	23496	40884
Destruction	506	3741	6976

Table 6. Distribution of buildings by area (in %) in different damage levels

Damage levels	Intensity (degrees)		
	7	7.5	8
No damage	60,6	48,8	37,0
Slight	28,6	31,4	34,1
Medium	8,5	13,6	18,7
Heavy	2,0	4,8	7,5
Very heavy	0,3	1,3	2,3
Destruction	0,03	0,2	0,4

The economic losses are calculated on the basis of the results obtained for the damages and destructions of the three main groups of buildings. The results are summarized in Table 7.

Table 7. Economic losses (thousands of BGN) in the main groups of buildings

Intensity (degrees)	Residential	Industrial and administrative	Special	Total
7	23180	6735	1115	31030
7,5	32466	22242	2587	57295
8	49574	23618	4059	77251

CASE STUDY 2 – TOWN OF BLAGOEVGRAD

The town of Blagoevgrad is located in southwestern Bulgaria. The seismic risk analysis is performed for a deterministic scenario in terms of macro seismic intensity (Stefanov, 2020). The intensity map is based on the seismic scenario in terms of peak ground acceleration (PGA) and velocity (PGV) for an earthquake with magnitude M_W=6.5 with rupture under the city. The territory of the city is divided into cells with a size of 400/400 m. The intensity is calculated for each cell separately

based on the data from the engineering-geological studies. The mean value for the intensity (of all cells) is I_{mean} = 8,65.

The population is 70 881 people, according to data from the National Statistical Institute. The results for social losses are available in two variants, depending on when the earthquake occurs – day or night. Table 8 summarizes the social losses – the distribution of the affected people – injured and victims. Table 9 presents a detailed distribution of the injured by category. The number of people who remain without shelter (need for accommodation) is in the range 4219 – 4688 people.

Table 8. Distribution of the affected people –
injured and victims (day and night)

Injured - by day (pcs.)	Victims - by day (pcs.)	Injured - by night (pcs.)	Victims - by night (pcs.)
1056 – 1174	292 – 325	1116 – 1242	323 – 352

Table 9. Distribution of the injured by category (day and night)

S1-day (pcs.)	S2-day (pcs.)	S3-day (pcs.)	S1-night (pcs.)	S2-night (pcs.)	S3-night (pcs.)
368 – 409	347 – 386	341 – 379	388 – 432	362 – 403	366 – 407

Designations: S1 – Minor injuries ; S2 – In need of hospital treatment ; S3 – Severely injured

The distribution of buildings, by number and total floor area – TFA (m²), in the different levels of damage is summarized in Table 10. The same table shows the distribution of buildings as a percentage of total built-up area.

Table 10. Distribution of buildings (by TFA)
in different levels of damage

Damage grade/	No damage	Slight	Medium	Heavy	Very heavy	Destruction
Total floor area (m²)	1396335	1515121	1015920	509862	189660	41058
Total floor area (%)	29,9	32,5	21,8	10,9	4,1	0,9

The economic losses are calculated on the basis of the results obtained for the damages and destructions of the three main groups of buildings. The results are summarized in Table 11.

Table 11. Economic losses in the main groups of buildings

	Residential	**Industrial and administrative**	**Special**	**Total**
Economic losses (thousands of BGN)	178102	107469	18805	304376

COMPLEX ASSESSMENT OF THE URBAN SEISMIC RISK

One task facing the state authorities is mapping the seismic risk for the territory of Republic of Bulgaria. Seismic risk mapping can be done in different ways, depending on which authorities will use the information and for what purposes. The first stage of the work includes a quantitative assessment of losses – social, material and economic. In the second stage, it is necessary to apply an approach for calculating a complex numerical risk assessment, which will allow comparison of data for different regions, cities, etc. In the present work, an approach for calculating a complex assessment of the urban seismic risk is applied.

The proposed approach is based on the normative document (Guidelines, 2017) which is applied by all structures of the General Directorate "Fire Safety and Protection of the Population" in Bulgaria. All disaster response plans are developed on its basis and this makes it important for the overall seismic risk management process.

For seismic risk, the potential adverse effects are determined in the following areas:

– Social consequences (C) – consequences for people and disruption of normal social function – the potential number of dead, seriously injured or injured, as well as the number of people directly affected – evacuated / displaced and temporarily accommodated persons;

– Material consequences (M) – damage to buildings, facilities;

– Economic losses (E) – the total losses in BGN for all categories, including the costs for immediate or long-term recovery measures.

The overall approach is based on consequences assessment. For the purpose the consequences are divided into 5 levels (from minor to catastrophic) and each level is assessed with the corresponding number of points – Table 12. A detailed description of the impact consequences criteria is given in the same table.

Table 12. Criteria for consequences

Level	Description	Detailed description	Points
1	Minor	No injuries, little or no damage, small financial losses.	1
2	Small	Need for first aid, minor damage to buildings, medium financial losses.	2
3	Moderate	Need for medical treatment of the victims, moderate damage to buildings, high financial losses.	3

4	Severe	Significant injuries, high level of damage to buildings and infrastructure, large financial losses.	4
5	Catastrophic	Deaths, most buildings and infrastructure were severely damaged, huge financial losses.	5

There are three options for assessing social consequences. The first is according to the potential death toll. The results are given in Table 13. For the town of Sevlievo the consequences are catastrophic for all three cases of seismic impact. The criterion is more than 1 death per 10000 inhabitants. For the city of Blagoevgrad, the assessment is also a catastrophic level of consequences.

Table 13. Social consequences - potential death toll

	By day (pcs.)	By night (pcs.)	Coefficient "k"	Consequences
Sevlievo I=7	6	10	k = 20848 / 10000 =2,08	Catastrophic - potential number of deaths directly caused by the dangerous event (disaster): > 1 per 10 000 population of the city
Sevlievo I=7,5	24	31	k = 2,08	Catastrophic
Sevlievo I=8	49	68	k = 2,08	Catastrophic
Blagoevgrad I_{mean} = 8,65	325	352	k = 70881 / 10000 =7,08	Catastrophic

The second option is according to the number of seriously injured people – Table 14. The criterion is similar – more than 1 seriously injured per 10000 inhabitants. For Sevlievo the result is k = 2.08 and for Blagoevgrad k = 7.08. In both cases, the level of consequences is catastrophic.

Table 14. Social consequences – Potential number seriously injured

	By day (pcs.)	By night (pcs.)	Coefficient "k"	Consequences
Sevlievo I=7	8	11	k = 20848 / 10000 =2,08	Catastrophic – potential number of severely injured: > 1 per 10 000 population of the city
Sevlievo I=7,5	28	37	k = 2,08	Catastrophic
Sevlievo I=8	58	79	k = 2,08	Catastrophic
Blagoevgrad I_{mean} = 8,65	379	407	k = 70881 / 10000 =7,08	Catastrophic

The third option is according to the potential number of people directly affected by the earthquake - Table 15. For the town of Sevlievo at the first two levels of seismic excitation (I = 7, I = 7.5) the level of consequences is severe. The criterion is between 100 and 1000 people evacuated, relocated or temporarily accommodated. At the highest level of seismic impact (I = 8) the result is a catastrophic level of consequences – the criterion is more than 1000 evacuated or relocated people. For the city of Blagoevgrad, the level of consequences is also catastrophic, as the number of people affected is 4688.

Table 15. Social consequences - Potential number of the people affected immediately from the earthquake

	Without shelter (pcs.)	Consequences
Sevlievo I=7	310	Severe – between 100 and 1000 evacuated / moved and temporarily accommodated persons.
Sevlievo I=7,5	618	Severe
Sevlievo I=8	1013	Catastrophic – more than 1000 evacuated / moved and temporarily accommodated persons.
Blagoevgrad $I_{mean} = 8,65$	4688	Catastrophic

The material consequences are determined on the basis of the distribution of damages (the percentage distribution of the unfolded built-up area). The five levels of consequences correspond to the damage levels. Only the catastrophic level corresponding to the levels of damage very heavy and destruction – Table 16. Multiplying the area by the parameter β (points at each level of consequences) gives the numerical value for each level (TFA * β). After summing these values, the final numerical estimate for the material consequences is obtained – the last column of Table 16. The obtained values vary from 1,529 for Sevlievo (I = 7) to 2,289 for Blagoevgrad (I_{mean} = 8,65). In practice, this is a weighted assessment of the impact of each individual damage level on the overall assessment of the material consequences.

Table 16. Material damages – level of consequences

Level	1		2		3		4		5		
Description	Minor: β=1		Small: β=2		Moderate: β=3		Severe: β=4		Catastrophic: β=5		Total Σ
	TFA,%	TFA*β	TFA,%	TFA*β	TFA,%	TFA*β	TFA,%	TFA*β	TFA,%	TFA*β	
Sevlievo I=7	60,6	0,606	28,6	0,572	8,5	0,255	2	0,08	0,33	0,0165	1,529
Sevlievo I=7,5	48,8	0,488	31,4	0,628	13,6	0,408	4,8	0,192	1,5	0,075	1,791

Sevlievo I=8	37	0,37	34,1	0,682	18,7	0,561	7,5	0,3	2,7	0,135	2,048
Blagoevgrad I_{mean} = 8,65	29,9	0,299	32,5	0,65	21,8	0,654	10,9	0,436	5	0,25	2,289

The assessment of the economic consequences is based on a comparison of the value of monetary losses with a part of the gross domestic product (GDP) of the region (city). For both cities, the assessment of the economic consequences is catastrophic – Table 17. The criterion is losses greater than 3% of gross domestic product. The losses for Sevlievo are in the range from 31030 to 77251 thousand BGN while the value of 3% GDP = 8470 thousand BGN. The losses for Blagoevgrad are 304376 thousand BGN while the value of 3% GDP = 20703 thousand BGN.

Table 17. Economic losses – monetary loss activity and / or value of assets

	Losses thousand BGN	**GDP thousand BGN**	**Consequences**
Sevlievo I=7	31030	282332 3% = 8470	Catastrophic - economic losses of assets > 3% of gross domestic product (GDP) in the district or city concerned.
Sevlievo I=7,5	57295		Catastrophic
Sevlievo I=8	77251		Catastrophic
Blagoevgrad Imean = 8,65	304376	690097 3% = 20703	Catastrophic

The level of potential harmful consequences for seismic risk is formed by three factors (social consequences, material consequences, economic losses), which have different relative weight. The percentage distribution of the severity of each of the three factors in calculating the level of consequences is determined as follows:

– Social consequences (S) – 50% weight due to the high priority of protection of human life and security, as well as community preparedness, response and recovery;

– Material consequences (M) – 30% weight due to the importance of the protection of buildings and infrastructure in terms of social care;

– Economic losses (E) – 20% weight, reflecting the secondary priority and the fact that usually most of the economic losses is damage to the urban area.

The final numerical value is obtained by multiplying the numerical values for the determined levels of consequences in the three areas (social consequences, material consequences, economic losses) by the respective weighting factors and summing them – Table 18.

Table 18. Complex risk assessment

Consequences	weighting factor %	Sevlievo I=7	Sevlievo I=7,5	Sevlievo I=8	Blagoevgrad I_{mean} = 8,65
Social	50	2,5	2,5	2,5	2,5
Material – building stock	30	0,45	0,54	0,63	0,69
Economic	20	1	1	1	1
Overall assessment "R"		**3,95**	**4,04**	**4,13**	**4,19**

The overall assessment for earthquake risk varies from 3,95 for the city of Sevlievo (I = 7) to 4.13 (I = 8), while for Blagoevgrad (I_{mean} = 8.65) it is 4.19.

CONCLUSION

The assessment of the consequences of earthquakes is based on procedures for integrating seismic hazard with the seismic vulnerability of building structures. A detailed quantitative assessment of the consequences in the form of losses includes:

• Assessment of direct damages and destructions of the building stock. This fact is important and should be taken into account when planning the necessary resources (building materials and labor) to recover the damaged building stock.

• Assessment of social losses – injured people and victims. The assessment of casualties and injuries is based on parameters that take into account the specific conditions in the study area, such as type of construction system, building density, time of the event, etc. The number of people who remain without shelter (need for accommodation) is determined.

• Estimation of economic losses due to direct physical damage and destruction of the building stock. These amounts can be used to develop disaster response plans and plan the need for financial resources to rebuild the building.

Based on the results of the detailed seismic risk assessment for two Bulgarian cities, an approach for complex risk assessment is proposed, which will allow direct comparison of the numerical values for different cities, municipalities or districts. The approach can be applied in practice in the forthcoming seismic risk mapping for the Republic of Bulgaria.

the framework of the Contract No D01-161/28.08.2018 (Project "National Geoinformation Center (NGIC)" financed by the National Roadmap for Scientific Infrastructure 2017 – 2023.

REFERENCES

Guidelines for the development and preparedness for the implementation of disaster protection plans (2017). Disaster Risk Reduction Council at the Council of Ministers of the Republic of Bulgaria (in Bulgarian).

Methodology for analysis, evaluation and mapping of seismic risk of the Republic of Bulgaria, (2018). Ministry of Regional Development and Public Works, Construction and Architecture, Issue no. 5, ISSN 0324-0711 (in Bulgarian).

Stefanov, D., Solakov, D., Milkov, J. (2020) Assessment of the effects of strong earthquakes on the city of Blagoevgrad**,** XXth Int. Multidiscip. Sci. GeoConf. Surveying, Geology and Mining, Ecology and Management – SGEM 2020 (in print).

Solakov, D., Stefanov, D. and team (2019). *Building seismic risk management.* Sofia: Prof. Marin Drinov Publishing House of Bulgarian Academy of Sciences (in Bulgarian).

✉ **Dimitar Stefanov**
National Institute of Geophysics, Geodesy and Geography
Bulgarian Academy of Sciences
Sofia, Bulgaria
E-mail: dstefanov@geophys.bas.bg

ASSESSMENT OF LANDSLIDE SUSCEPTIBILITY AND HAZARD ALONG THE NORTHERN BULGARIAN BLACK SEA COAST

Plamen Ivanov[1], Rosen Nankin[1], Vladislav Zaalishvili[2]

[1]Geological Institute –
Bulgarian Academy of Sciences (GI-BAS)
[2]Geophysical Institute of Vladikavkaz Scientific Centre,
Russian Academy of Sciences – Vladikavkaz

Abstract: The Black Sea coast is one of the regions of Bulgaria with distribution of a significant part of the Bulgarian landslides. The analysis of the factors influencing the stability of the coastal slopes shows that they have a higher concentration and more intensive total impact on the northern part of the Bulgarian Black Sea coast, where most of the larger landslides are located. In this study, the Mora and Vahrson method was applied to estimate the landslide susceptibility along the northern Bulgarian Black Sea coast. This method is based on evaluation of various local factors for slope instability which are estimated using a Geographic Information System. The purpose of the study is to produce a landslide susceptibility map and to locate landslide-prone areas for this region.

Keywords: landslide, slope stability, Mora and Vahrson method, Black Sea coast

INTRODUCTION

The aim of these studies is to identify areas prone to landslides along the northern Bulgarian Black Sea coast (Fig. 1). For this purpose, the method of Mora and Vahrson was used, which was applied in compiling the Map of landslide susceptibility for the region. This method has already been successfully applied in Bulgaria for the region of the Sofia valley (Berov & Frangov, 1997) as well as for the Bulgarian Black Sea coast (Dobrev et al., 2014; Berov et al., 2016; Berov et al., 2020). This publication attempts to apply the method to a part of this area where there is a concentration of landslides. The geological structure and the special lithological varieties in this area have an impact on the landslide susceptibility along the coast.

Figure 1. Location of the studied area

The territorial distribution of landslides along the northern Bulgarian Black Sea coast is considered on the basis of field studies conducted in 2018 and 2019 for the region from Varna to Shabla – Varna, Balchik and Kamen Bryag Landslide areas (Nankin & Ivanov, 2019). Much of the northern Black Sea coast is covered by old, conditionally stabilized or active landslides (Varbanov, Frangov & Evstatiev, 1997; Frangov et al., 1998; Berov et al., 2002, 2013; Lakov, Stoynev & Konstantinov, 2002; Evlogiev & Evstatiev, 2013, 2016; Evstatiev, Evlogiev & Nedelcheva, 2017; Frangov & Krastanov, 2015; Atanasova & Nikolov, 2019; Atanasova-Zlatareva et al., 2019). They originated in Sarmatian sediments composed of limestone, diatomaceous clays, aragonite clays and sandstones due to fluctuations in sea level during the Pleistocene and seismic impacts. In the regions along the Varna and Balchik coasts there are two types of landslides - circus for the Varna landslide region and linear-stepped (package) for the Balchik landslide region and the landslide region Kamen Bryag. Of these old landslides in the area of the resorts near Varna, only the coastal part is usually active under the action of sea abrasion, in contrast to Balchik, where a large part of the landslide slope is unstable (Kamenov et al., 1972).

CONDITIONS AND FACTORS FOR THE OCCURRENCE OF LANDSLIDE PROCESSES

The northern, platform part of the Bulgarian Black Sea coast is built of almost horizontally lying sedimentary rocks of Tertiary and Quaternary age. The terrain in the coastal part of the Varna Depression has a plateau-like character. In the section North of Varna there are 2 plateaux – Frangya and Dobrudzha, separated by the valley of the Batova River. The valley of the Batova River is cut 200-250 m into the Miocene sediments, has a flat bottom and relatively steep valley slopes. The altitude at the edge of the plateau decreases in a northerly direction.

The **Varna landslide area** includes the coast of the city of Varna to the valley of the Batova River near the village of Kranevo. Landslide complexes (circus type) are manifested on the eastern slope of the Frangya Plateau – from the edge to the

beach. The area is composed of Miocene sediments, represented by several formations: Galata Formation (gN_1^{t-s}) – sands and clays, Euxinograd Formation (evN_1^{kg-s}) – sandstones, diatomaceous clays, Frangya Formation (frN_1^s) – water-saturated sands and Odurtsi Formation (odN_1^s) – mainly from limestone (Evlogiev, Evstatiev, 2016). The formation of deep landslides in this area is mainly due to sea abrasion.

The Black Sea coast, northeast of the Batova River to the west of the town of Kavarna (**Balchik landslide area**), is covered by old and recent landslides (Evlogiev, Evstatiev, 2013; Evstatiev et al., 2017). The landslide strip has an average width of 400–500 m, and in some places near the plateau it ends with a steep 40–50 m slope. Landslide bodies are usually formed by 3-4 visible linearly oriented steps and hills (landslide packages) of different heights. The depths of the old landslides reach 40-60 m, in some places even more. The sediments affected by the landslide processes belong to the Karvuna (kvN1s), Topola (toN1s) and Euxinograd Formations (evN1s). The sediments of the Topola Formation, composed of aragonite sediments (classified as sandy and silty clays) with layers of strong limestone (Koleva-Rekalova, 1994; Nankin & Krastanov, 2017) are of the greatest importance for landslide activity.

Landslide area Kamen Bryag includes two landslides (Taukliman and Yailata), which are stepped, linearly elongated, lateral ejection type. Both landslides are probably caused by strong earthquakes, the main prerequisite being the geological structure, represented by two radically different in terms of engineering geological properties sediments. The upper part is made of limestones of the Odurtsi Formation (odN1s) with an average thickness of 30–40 m, and below them Oligocene clays with a thickness of more than 100 m (Avramova-Tacheva, Kostak & Dobrev, 1998).

Of the endogenous processes, the most significant for landslides are the slow vertical movements of the earth's crust and earthquakes. The vertical rise of this part of the coast, related to geohistorical time (Dobrev & Stanoev, 1985), is an important factor for the formation of high and steep slopes and for the occurrence of large landslides on them. Earthquakes have a more significant impact on the landslide processes along the Varna and Dobrudzha coasts, with strong earthquakes in the area of Shabla-Kaliakra (Iliev, 1973; Konstantinov, 1991; Konstantinov et al., 1992; Dimitrov, Parlichev & Dobrev, 2017). The main exogenous processes influencing landslide activity are abrasion, the impact of surface and groundwater and man-made factors.

ASSESSMENT OF LANDSLIDE SUSCEPTIBILITY ALONG THE NORTHERN BULGARIAN BLACK SEA COAST USING THE MORA AND VAHRSON METHOD

In the present study, the Mora and Vahrson method (Mora & Vahrson, 1994) is applied to assess the landslide susceptibility along the northern Black Sea coast, which is severely affected by landslides. The method is based on the weight as-

sessment of various adverse conditions and destabilizing factors on slope stability. A modified method proposed for the region of the Bulgarian Black Sea coast with an additional triggering factor "abrasion / erosion" was used to assess the susceptibility to landslides (Dobrev et al., 2014; Berov et al., 2016). The landslide hazard is expressed by the following equation using a free and open source Geographic Information System (https://www.qgis.org/en/site/):

$$H = (Sr * Sl * Sh) * (Ts + Tp + Te) \qquad (1)$$

where
Sr – slope factor.
Sl – lithology factor.
Sh – soil moisture (humidity) factor.
Ts – seismic intensity triggering factor.
Tp – precipitation intensity triggering factor.
Te – erosion/abrasion triggering factor.

The description of the factors involved in the assessment of susceptibility is taken from tables with setpoints (points) proposed by the authors of the method (Mora & Vahrson, 1994).

The slope factor *Sr* takes into account the displacement of the terrain per unit area. Digital elevation model (DEM) was used for the zoning of this factor (Fig. 2).

The lithology factor *Sl* is determined depending on the engineering geological properties of the lithological varieties that make up the study area. In the original approach proposed by Mora & Varhson (1994), this indicator varies from 1 to 5, with 1 point given for the strongest varieties and 5 points for the weakest. In the present study, an adaptation of the method was made according to the engineering geological conditions typical for the northern Bulgarian Black Sea coast (Table 1). Four categories are selected, which are shown in Table 1 and in Fig. 2.

Table 1. Lithology factor criteria characteristic for the northern
Bulgarian Black Sea coast, classification and scores

Lithology	Qualification	Value of Sl
Rock formations: sedimentary rocks (Neogene, Paleogene, etc.) limestones with sandy and clayey layers - Odurtsi Formation odN_1^s	Moderate	2
porous, often shelled limestones with layers of clay - Karvuna Formation kvN_1^s	Medium	3
Alternating sedimentary rocks - (Paleogene). Weathered rocks clays, some sands and clayey sandstones - Ruslar Formation $(rPg_2^3\text{-}Pg_3)$ marls with thin layers of sandstone - Avren Formation $(avPg_2^{2\text{-}3})$	High	4

| Deluvial and alluvial deposits; clay sediments of Quaternary, Neogene and Paleogene age Alluvial formations - sands, gravels and less clays (aQh) modern beach sands (mQh) - marine terraces clayey loess (eQp$^{2-3}$) unlitified, unconsolidated aragonite sediments - Topola Formation (toN$_1^s$) oligomictic sands, rarely with sandstone lenses and interlayers - Frangya Formation (frN$_1^s$) calcareous clays, often diatomaceous, with thin layers of diatoms - Euxinograd Formation evN$_1^{kg-s}$ sands with layers of clays, sandstones and rarely conglomerates – Galata Formation (gN$_1^{t-s}$) | Very High | 5 |

The weakest and respectively most susceptible to landslide processes are the youngest lithological formations (Neogene and Quaternary) - mainly clayey and cohesionless soils. Of particular importance for the development of landslides are the aragonite sediments of the Topola Formation (distributed from the village of Kranevo to the town of Kavarna). Recent data show that these sediments are composed of unlitified, unconsolidated aragonite sediments (Koleva-Rekalova, 1994, 1998; Nankin & Krastanov, 2017; Ivanov, Nankin & Krastanov, 2019; Koleva-Rekalova & Dobrev, 2019; Yaneva et al., 2019), white, cream to beige in color. In terms of texture, they are massive and less often laminated. In the sections usually established strong, mostly micritic limestones with a thickness of 7 to 25 cm, which layer the aragonite sediments.

The Euxinograd Formation (evN$_1^{kg-s}$) is represented by gray, calcareous clays, often diatomaceous, with thin layers of diatoms. There are also very thin detrital lenses and layers of crushed shells of mollusks, and sometimes fine sand. The Frangya Formation (frN$_1^s$) is composed of yellowish, whitish oligomictic sands, rarely with sandstone lenses and interlayers.

The Galata Formation (gN$_1^{t-s}$) is characterized by a predominance of yellowish and whitish sands, but they often contain layers of gray and greenish clays and sandy clays, less often lentils and layers of sandstones, sandy and detrital limestones and rarely conglomerates, mainly at the base. The Odurtsi Formation (odN$_1^s$) is represented by 5-6 to 40-50 meters of white and yellowish detrital, shell and oolite limestones with sandy and clayey layers. The Karvuna Formation (kvN$_1^s$) is composed of porous, often shelled limestones with layers of clay and/or striped clay-carbonate materials. Eolian formations (eQ$_p^{2-3}$) are represented by clayey loess, yellow to brownish. Alluvial formations (aQ$_h$) are distributed along the current riverbed and floodplains of the rivers Provadiyska and Batova, as they are represented by gravels, sands and less clays. Recent sea formations (mQ$_h$) are composed of beach sands, which are distributed in major resorts - Golden Sands, Kranevo and Albena. The last two formations have a limited distribution in the
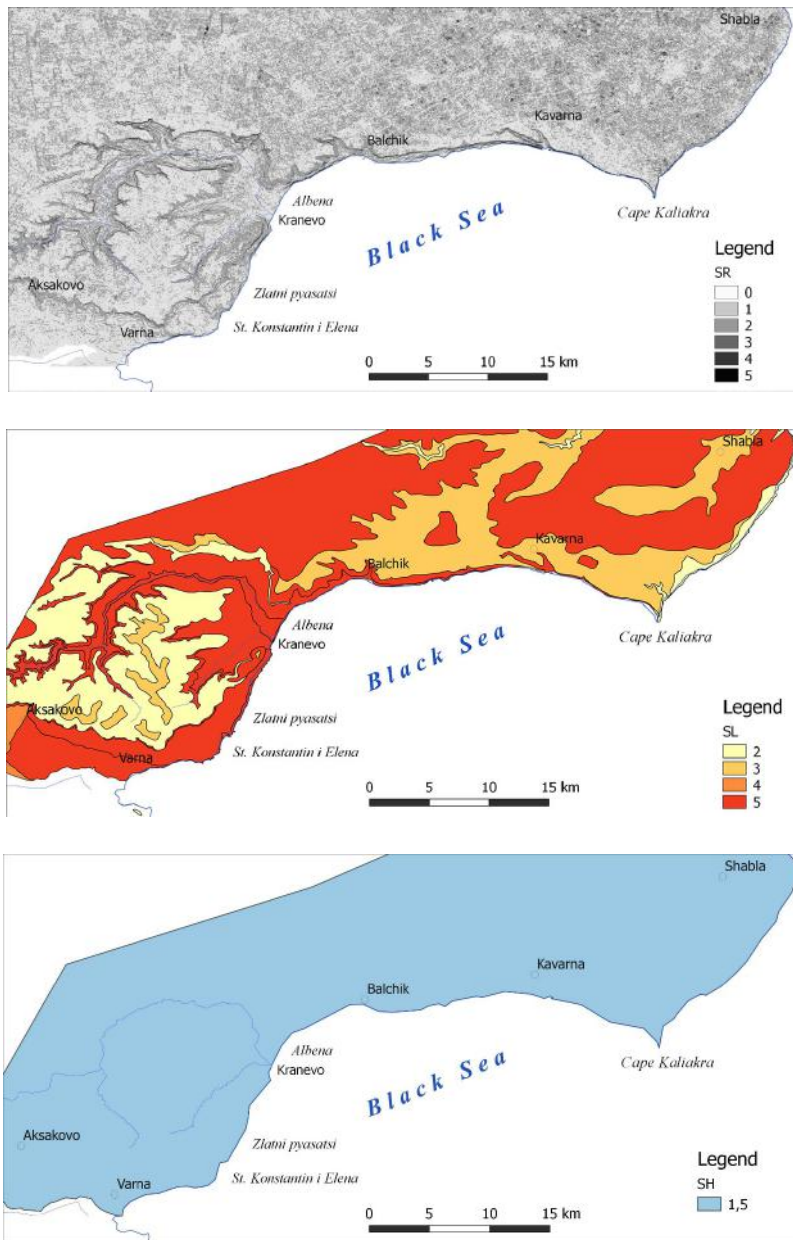
Figure 2. Susceptibility factors of the northern Black Sea coast: *Sr* – slope factor, *Sl* – lithology factor, *Sh* – soil moisture (humidity) factor
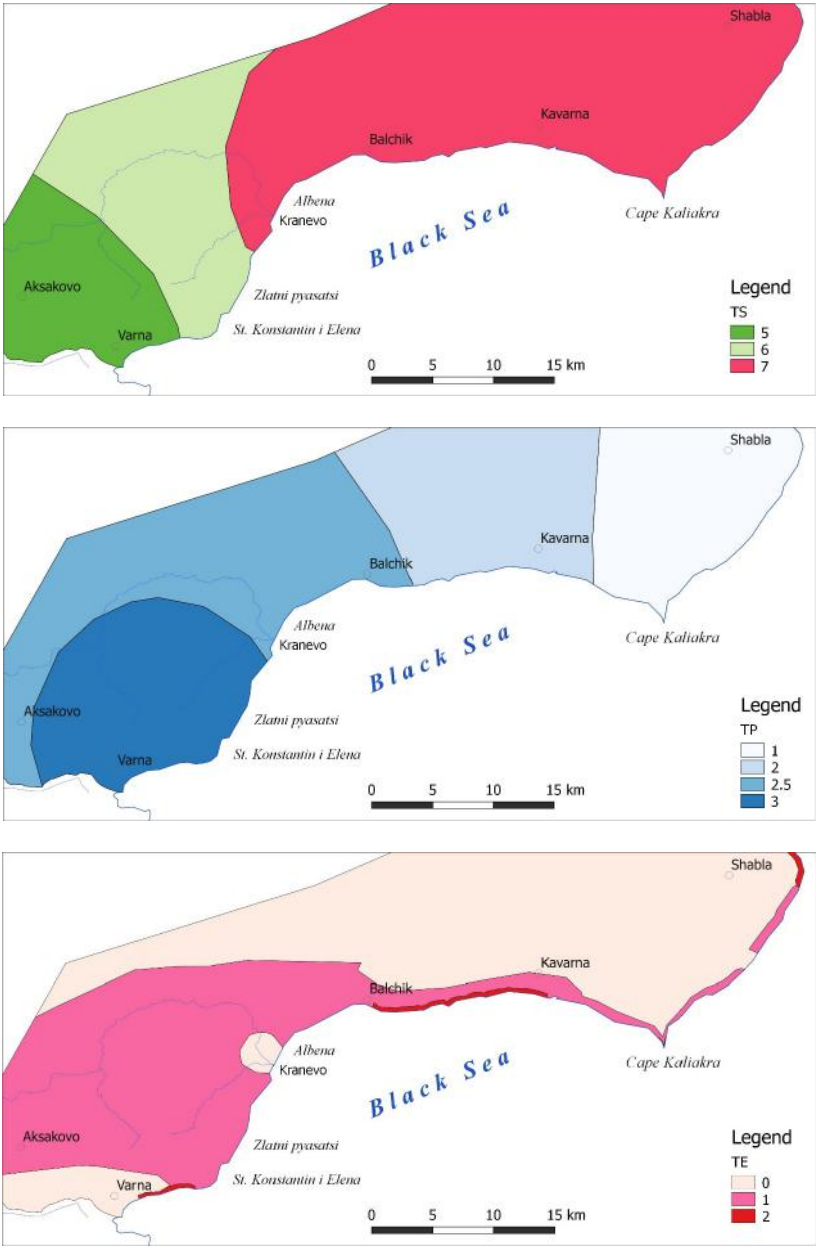
Figure 3. Triggering factors of the northern Black Sea coast: *Ts* – seismic intensity factor, *Tp* – precipitation intensity factor, *Te* – erosion/abrasion factor

study area. The Avren Formation ($avPg_2^{2-3}$) is represented by light gray to creamy yellowish marls with well-pronounced layered sandstone on the southwestern slopes of the Varna plateau. The Ruslar Formation (rPg_2^3-Pg_3) forms varying in width stripes on the slopes of the Varna plateau and is composed of light gray to beige, weakly bonded, calcareous to slightly calcareous, clayey-sandy siltstones, among which are embedded siltstone-spongolite clays.

The soil moisture factor *Sh* is determined in accordance with the accumulated value of the precipitation index, varying from 1 to 5. For the country, however, its maximum value is about 3, and for the coast it is below 1.5 (Fig. 2). In the present study, the soil moisture factor Sh was determined on the basis of data published by Koleva & Peneva (1990) (Dobrev et al., 2014; Berov et al., 2016; Chapanov et al., 2019; Berov et al., 2020).

The data needed to determine the precipitation triggering (destabilizing) factor *Tp* were taken from the same source (Koleva & Peneva, 1990) (Fig. 3).

According to the seismic zoning of the country which is referred for a 1000 year period (Ordinance № RD-02-20-2 of 27 January 2012 on design of buildings and structures in earthquake areas), the seismic intensity factor *Ts* for the northern Bulgarian Black Sea coast varies from 5 (VII degree according to MSK-64) to 7 (IX degree according to MSK-64), and in the seismically active region near Shabla-Kaliakra it has a value Ts = 7 (Fig. 3).

For the zoning by erosion-abrasion hazard the Map of the geological hazards in Bulgaria (Iliev-Bruchev, ed., 1994) was used, and for the coast - data from Shuiskij & Simeonova, (1982) and from the project *Elaboration of analysis, evaluation and mapping of geological risk* (http://gis.mrrb.government.bg/KGR/). The following results for the erosion and abrasion factor *Te* are presented in Fig. 3.

MAP OF LANDSLIDE SUSCEPTIBILITY AND HAZARD

Landslide susceptibility is calculated according to formula 1 (Table 2) and is shown in fig. 4, using a classification scheme in 5 classes. The results show the terrains where we can most likely expect manifestation of landslides. The location of the landslides in the area is also shown.

Table 2. Classification of the landslide susceptibility (hazard)
or the northern Bulgarian Black Sea coast

Value from equation (1) *H*	Class	Classification of landslide susceptibility
0-6	I	Negligible
7-32	II	Low
33-162	III	Moderate
163-225	IV	Medium
226-345	V	High
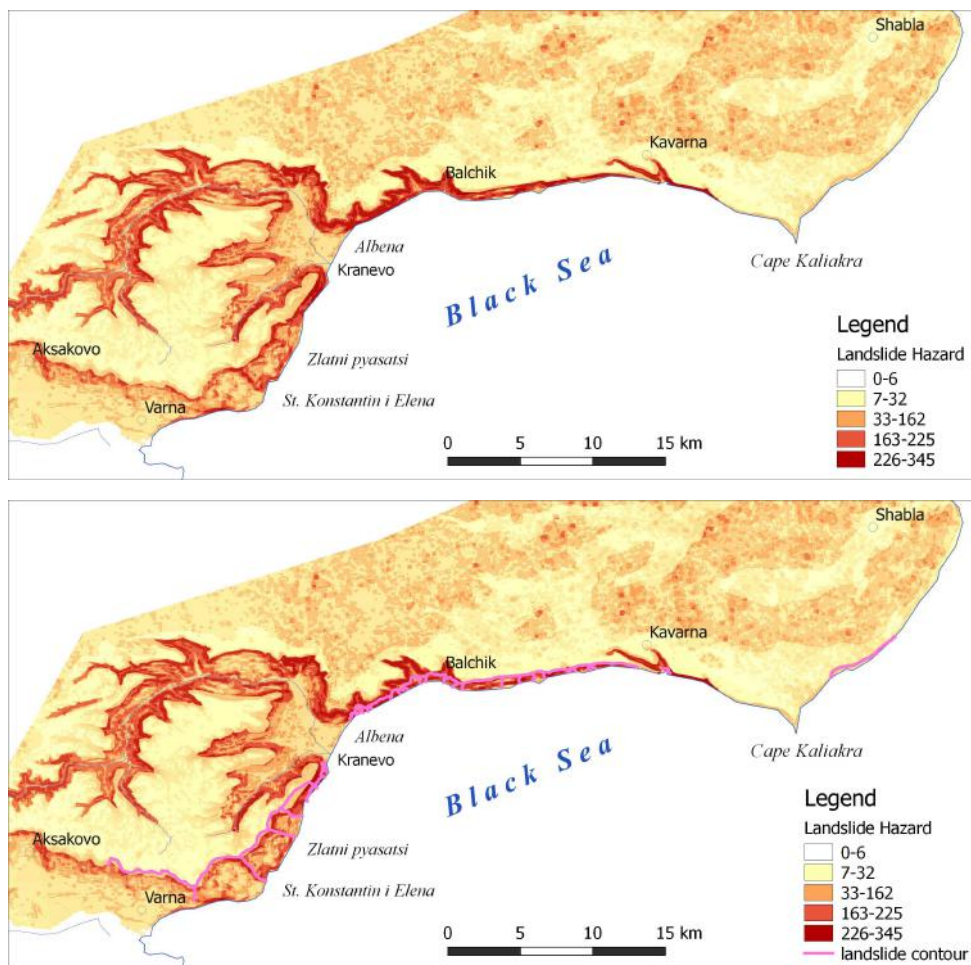
Figure 4. Landslide Susceptibility and Hazard along the northern Black Sea coast

CONCLUSION

The analysis of the factors influencing the stability of the coastal slopes shows that they have a higher concentration and more intensive total impact on the northern part of the Bulgarian Black Sea coast, where most of the larger landslides occur. Particular attention is paid to the special lithological varieties in this area (SL) influencing the landslide susceptibility. The compiled landslide distribution maps are the first step to subsequent assessments and landslide hazard and risk maps. As can be seen from the result expressed on the Susceptibility Map (Fig. 4), the maximum number of points obtained in the assessment of the northern Bulgarian

Black Sea coast is 345. This corresponds to a medium degree of hazard according to the original methodology of Mora & Vahrson (1994). The slopes along the Varna and Balchik coasts are most susceptible to landslides with H > 226 points. Deep landslides with periodic activation of parts of them prevail. The majority of the study area is characterized by moderate and low degree of landslide hazard.

ACKNOWLEDGMENTS

REFERENCES

Atanasova, M. & Nikolov, H. (2019). Studying the coastal landslides processes by InSAR. – In: *Proceedings SPIE 11156, Earth Resources and Environmental Remote Sensing/GIS Applications X*, 1115619, 10 p.

Atanasova-Zlatareva, M., Nikolov, H., Georgiev, I., Ivanov, A. & Dimitrov, N. (2019). Monitoring of landslide processes at the NE Bulgaria by joint use of GNSS and InSAR. – In: *10th Congress of Balkan Geophysical Society, BGS 2019*.

Avramova-Tacheva, E., Kostak, B. & Dobrev, N. (1998). Present dynamics of a landslide process in the Black sea coast region N of Varna (Bulgaria). – *Acta Montana IRSM AS CR, Series A, No.12 (107)*, 5–15.

Berov, B. & Frangov, G. (1997). Zoning of Sofia valley according to degree of potential landslide hazard. *4-th National Scientific and Practical Conference on Scientific support of Prevention activities and Protection of the population in case of emergency*. The Permanent Committee for Monitoring Disasters and Accidents. Sofia, 5–6 November 1997, Vol. 5, pp. 207–215. (in Bulgarian).

Berov, B., Dobrev, N., Brouchev, I. & Fukuzono, T. (2002). Landslides in Bulgaria. – *Journal of the Japan Landslide Society* 38 (4), 334–343.

Berov, B., Ivanov, P., Dobrev, N., Nankin, R. & Krastanov, M. (2013). State of the art for landslides along the North Bulgarian Black Sea coast. – In: Margotti, C., P. Canuti, K. Sassa (eds.). *Landslide Science and Practice*, *5, Complex Environment.* Berlin, Heidelberg, Springer, 97–102.

Berov, B., Ivanov, P., Dobrev, N. & Krastanov, M. (2016). Addition to the method of Mora & Vahrson for landslide susceptibility along the Bulgarian Black Sea coast. – In: *12th International Symposium on Landslides, Napoli, Italy,* 12-19 June 2016, CRC Press, A Balkema book, vol. 2, 397–403.

Berov, B., Nikolova, N., Ivanov, P., Dobrev, N., Krastanov, M. & Nankin, R. (2020). Landslide susceptibility mapping using GIS: A case study along Bulgarian Black Sea coast. – In: *Proceedings Vol. 1, 8th International Conference on Cartography and GIS*, 2020, Nessebar, Bulgaria, 287–296.

Chapanov, Y., Atanasova, M., Orehova, T., Nikolov, H. (2019). Rainfalls and groundwater influences on landslides in Northeast Bulgaria. – In: *Proceeding of the 10th Congress of the Balkan Geophysical Society,* 18-22 September 2019, Albena Resort, Bulgaria.

Dimitrov, O., Parlichev, D. & Dobrev, N. (2017). Seismic and precursory aspect information about topography and tectonics of Bulgarian Black Sea coast. *Engineering Geology and Hydrogeology* 31, 13–23 (in Bulgarian with English abstract).

Dobrev, T. & Stanoev, I. (1985). Isostasy and vertical movements of the earth's crust in the territory of Bulgaria. *Geologica Balcanica* 15 (2), 75–96 (in Russian with English Abstract).

Dobrev, N., Ivanov, P., Berov, B. & Krastanov, M. (2014). Landslide susceptibility assessment of Bulgarian Black Sea coast with using of Mora and Vahrson method. *Engineeging Geology and Hydrogeology,* 28, 69–82 (in Bulgarian with English abstract).

Evlogiev, Y. & Evstatiev, D. (2013). Landslides near the Topola village (Northern Black Sea coast). *Engineering Geology and Hydrogeology* 27, 13–69 (in Bulgarian, with English abstract).

Evlogiev, Y. & Evstatiev, D. (2016). Landslides in the area of Varna city – Golden Sands resort (Black Sea Coast). – *Eng. Geol. and Hydrogeol.*, *30*, 49–114 (in Bulgarian with English abstract).

Evstatiev, D., Evlogiev, Y. & Nedelcheva, M. (2017). The landslides Zapadni Karamanlii and Momchilski Rid – Balchik Black Sea Coast. – *Rev. of the Bulgarian Geological Society, 78,* 1–3, 3–23 (in Bulgarian with English abstract).

Frangov, G. & Krastanov, M. (2015). Evaluation of the possibilities for construction on ancient landslide. – In: *Proceedings of the 12*th *International IAEG Congress "Engineering Geology for Society and Territory"*. Torino*, 267–271.

Frangov, G., Varbanov, R., Yordanova, J. & Stakev, M. (1998). Contemporary landslide activity along Varna and Balchik sea coast. – In: Marinski, J. (Ed.) *Protection and long-term Stabilization of the Slopes of the Black Sea Coast*. Sofia, BAS, Acad. Publ. House "Prof. Marin Drinov", 20–29 (in Bulgarian with English abstract).

Iliev, I. (1973). Effect of the earthquakes on the appearance and activation of landslides along the Dobrudja Black Sea Coast. *Review*

of the Bulgarian Geological Society 34 (1), 75–85 (in Bulgarian with English abstract).

Iliev-Broutchev, I., ed. (1994). *Geological hazards in Bulgaria – Map in scale 1:500 000 and explanatory text.* Military Topographic Service, Troyan/Publishing House of BAS, Sofia, 143 p. (in Bulgarian with English abstract).

Ivanov, P., Nankin, R. & Krastanov, M. (2019). Cliff erosion – mapping, causes and effects in coastal zone near Cape Kaliakra (northern Bulgarian Black Sea). – *Geologica Balcanica* 48 (3), 35–41.

Kamenov, B., Demirev, A., Voutkov, V., Tsvetanov, S., Avramova, E., Iliev, I., Simeonova, G., Ilieva, L. & Milev. G. (1972). The landslides along the Balchik Black Sea coast. *Bulletin of the Geological Institute – Series Engineering Geology and Hydrogeology*, 5–31 (in Bulgarian with English abstract).

Koleva, E. & Peneva, R. (1990). *Climate guide. Precipitation in Bulgaria.* Institute of Meteorology and Hydrology, Bulgarian Academy of Sciences, Sofia, 169 p. (in Bulgarian).

Koleva-Rekalova, E. (1994). Sarmatian aragonite sediments in North-Eastern Bulgaria – origin and diagenesis. *Geologica Balcanica* 24 (5), 47–64.

Koleva-Rekalova, E. (1998). Formational conditions of the Sarmatian sedimentary rocks from the Balchik area, North-Eastern Bulgaria. *Review of the Bulgarian Geological Society* 59 (1), 69–74 (in Bulgarian with English abstract).

Koleva-Rekalova, E. & Dobrev, N. (2019). Sarmatian carbonate tempestites from Kaliakra Cape (NE Bulgaria): evidence for the existence of microbialites. C. R. Bulg. Sci., 72, 11, Academic Publishing House "Prof. M. Drinov", 1507–1514.

Konstantinov, B. 1991. Probable secondary seismic deformations along the Bulgarian Black Sea coast. – *Ann. of Mining and Geological Univ.*, 37, 3, 67–78 (in Bulgarian).

Konstantinov, B., Angelov, K., Lakov, A., Stojnev, S., Konstantinov, V. (1992). Landslides activization from earthquake motions. *Sixth International Symposium on Landslides (ISL 1992)*, 1181–1186.

Lakov, A., Stoynev, S. & Konstantinov, B. (2002). Geodynamic hazard and geodynamic risk along the Bulgarian Black Sea coast. *Proceedings of the 9th National Mine Surveying Conference with International Participation "Analysis, Modelling and Control of Geological Risk in Disturbed Territories"*, 263–268 (in Bulgarian).

Mora, S. & Vahrson, W-G. (1994). Macrozonation Methodology for Landslide Hazard Determination. *Bulletin of the Association of Engineering Geologists.* Vol. 31, No. 1, 49–58.

Nankin, R. & Krastanov, M. (2017). Geotechnical parameters of limestone from the Topola Formation in the area of Topola Village, Kavarna Municipality (NE Bulgaria). *Geologica Balcanica* 46 (2), 83–86.

Nankin, R. & Ivanov, P. (2019). Current state of the landslides affecting the Northern Bulgarian Black Sea Coast. *Review of the Bulgarian Geological Society*, vol. 80, part 3, 2019, p. 176–178 (in Bulgarian with English Abstract).

Shuiskij, J. & Simeonova, G. (1982). On the type of abrasion cliffs along the Bulgarian Black Sea Coast. *Engineering Geology and Hydrogeology* 12, 11–21 (in Bulgarian with English abstract).

Varbanov, R., Frangov, G. & Evstatiev, D. (1997). New destructive landslides northward from the town of Varna. *Journal Minno Delo i Geologia*. 5: 6–12 (in Bulgarian).

Yaneva, M., Koleva-Rekalova, E., Nikolov, P. & Ognjanova-Rumenova, N. (2019). Topola Formation, Northeastern Bulgaria – biostratigraphical and palaeoecological aspects. *Review of the Bulgarian Geological Society* 80 (3), 133–135.

✉ **Plamen Ivanov**
https://orcid.org/0000-0002-7139-7303
Geological Institute
Bulgarian Academy of Sciences
Sofia, Bulgaria
E-mail: plivanov62@geology.bas.bg

✉ **Rosen Nankin**
https://orcid.org/0000-0002-5314-0897
Geological Institute
Bulgarian Academy of Sciences
Sofia, Bulgaria
E-mail: nankin_r@abv.bg

✉ **Vladislav Zaalishvili**
https://orcid.org/0000-0002-0596-1148
Geophysical Institute of Vladikavkaz Scientific Centre
Russian Academy of Sciences
Vladikavkaz, Russia
E-mail: vzaal@mail.ru

ASSESSMENT OF EMPIRICAL RELATIONSHIPS BETWEEN BEACH-FACE SLOPES AND SEDIMENT SIZES USING FIELD DATA (BURGAS BAY CASE)

Petya Eftimova, Nikolay Valchev, Bogdan Prodanov,
Nataliya Andreeva, Todor Lambev, Liubomir Dimitrov
Institute of Oceanology – Bulgarian Academy of Sciences (IO-BAS)

Abstract: The study examines the relationships between the beach-face slopes and sediment sizes for several coastal stretches located in Burgas Bay using limited field data, and explores the applicability of a number of previously developed formulations for local geomorphic, lithologic and wave conditions. Knowledge on the clear dependence between considered parameters is of particular importance for many engineering applications such as calculation of maximum run-up, shoreline changes, beach berm erosion potential, and assessment of coastal flood and erosion hazards. The results have shown that none of the considered empirical relationships can be used straightforwardly, although some of them might be considered for future analysis. Hence, it is necessary to enrich the database with wider ranges of beach-face slopes, sediment sizes coming from areas with different wave exposure and morphodynamics state in order to elaborate a reliable native relationship suitable for local to regional specifics of the western Black Sea coast. This underpins the importance of regular coastal monitoring.

Keywords: Black Sea coast, sediment grain size, beach-face slope, empirical relationships

INTRODUCTION

Beach-face is the most dynamic part of the beach body. Its form evolves reflecting all changes in the wave and the tidal regime, from small waves during calm conditions or varying with the development and decaying of storms and surges. Different processes take place in this narrow area, where the sea meets the land, with different effect on beach morphodynamics – the wave uprush and backwash, processes of infiltration and exfiltration of water, the sediment sorting, the effects of ground water flows/levels on the sediment transport. Many researchers have studied this dynamic area and especially the beach-face slope and its dependence on the characteristics of beach sediments and wave action. One of the pioneer research was performed by Bascom (1951) who analysed

data from 40 Pacific coast sandy beaches of the USA, including different types of beaches (steep and flat ones), measured during winter and summer conditions. He analysed different factors that affect beach-face slopes, the distribution of median diameter of sediments along beach profiles, the sediment sorting. These are the effects of wave action, the wave steepness, the influence of engineering facilities, abundance of sediments, storm effects. He concluded that beach-face slope is controlled mainly by the size of the sand and the intensity of wave action and developed relationships between the beach-face slope and the median diameter for different conditions at a qualitative level.

Many other studies followed different approaches investigating the beach-face behaviour: beach-face sediment properties, sediment grain size and sorting, among which those of Turner (1995) and Wilson et al. (2008); effects of swash infiltration and exfiltration (e.g. Baldock & Hughes, 2006; Masselink & Puleo, 2006); behaviour of groundwater flow in the beach-face area (e.g. Li et al., 2002; Horn, 2006).

The beach-face slope ($tanβ$) is determined by the angle between the beach-face and mean sea level or as "the seaward slope of the beach between the low tide line and the upper limit of wave swash" (Schwartz, 2006), while sediments are represented by the medium grain size (D_{50}), which is the value of the particle diameter at 50% in the cumulative distribution. Both parameters are frequently used in many engineering applications, such as calculation of maximum run-up, shoreline erosion, beach berm erosion potential, assessment of coastal flood and erosion hazards.

Lack of sufficiently detailed data on beach slopes and sediments necessitates finding a relationship between the two parameters to enable useful predictions. Different empirical formulae have already been proposed to connect the beach-face slope to the median sediment size following different approaches. For example, Sunamura (1975, 1984), analysing laboratory and field data, elaborated such formulae to predict the beach-face slope, based on sediment sizes and wave parameters (breaking wave height and wave period). Similarly, Uda & Sakai (1985) used significant wave height based on field measurements. Reis & Gama (2010) developed a relationship between sand size, offshore wave height and beach-face slope by introducing the so-called Constructal law based on field data. Fleming (2011) suggested two relationships for dissipative and reflective beach states using only the sediment size. Based on analysis of laboratory data, Kim et al. (2014) proposed an equation including sediment size and wave period. Bujan et al. (2019) analysed large datasets of data pairs $tanβ$ - D_{50} and developed a formula covering wide range of sediments. McFall (2019) proposed three relationships depending on beach exposure for protected, moderately protected and exposed beaches.

Due to the existing variety of formulations for a wide range of conditions, it is difficult to choose the most suitable for application in the study area. Therefore, the

aim of the present study is to investigate the suitability of the existing formulations on the relationship between *tanβ* and D_{50} for conditions of the southern Bulgarian coast making use of the available field data.

DATA AND METHODS
Study site

The study site is situated on Burgas Bay coast (Fig. 1), the largest bay along Bulgarian coastline, located at the western Black Sea. It is distinguished with a complex orography, weak tides of about 8 cm and slight to moderate sea states (Rogev, 1975). Three coastal sites have been investigated– the large sandy Pomorie spit (1), a group of small beaches in the southern part of Burgas Bay near Kraymorie (2) and Chengene Skele (3) (Fig 1).
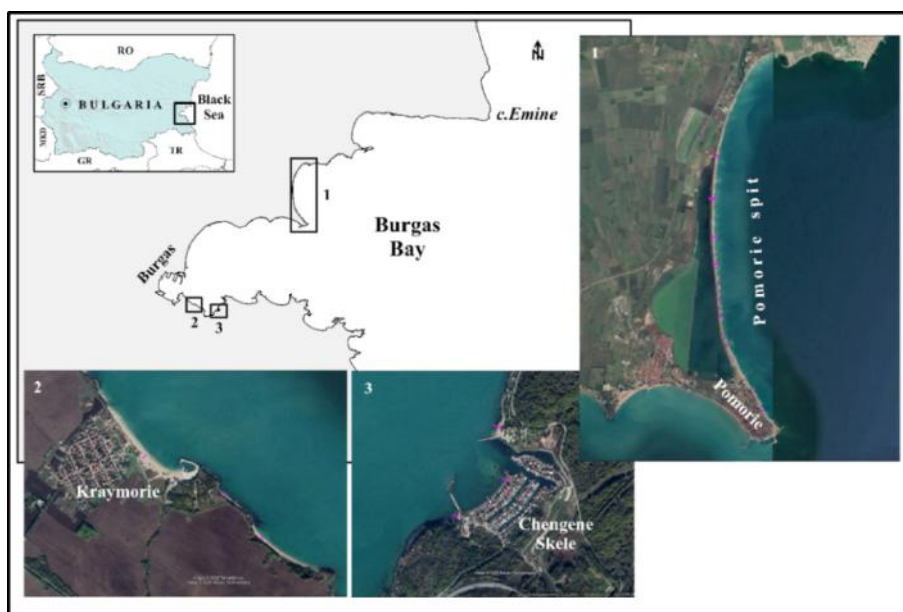
Figure 1. Location of the coastal stretches within the study site in Burgas Bay. Cross-shore profiles for which data pairs *tanβ* - D_{50} were extracted are illustrated with magenta lines

Pomorie sandy spit is located along the northern arm of Burgas Bay (Figs. 1, 2A) and encompasses the second longest (6.9 km) sandy beach along the Bulgarian coast (Popov & Mishev, 1974). The coastal area has eastern exposure. The northern part of the spit separates Pomorie Lake (a coastal lagoon) from the sea. Therein, the

A

B

C

Figure 2. Beaches and visualization of sand samples collected along
the coastal areas of: A) Pomorie sand spit, B) Kraymorie, C) Chengene Skele

beach is backed by a dune and a dyke, which stretch along the entire sandy spit. The southern part stretches in front of Pomorie town, as herein the coast is protected by seawalls and groynes. Kraymorie coastal area is located to the south of Burgas city and encompasses three natural sandy beaches backed by relatively low cliffs with NE exposure (Figs. 1, 2B). The longest of the three (~ 700 m) is situated in front of Kraymorie resort village. Its southern end is occupied by a marina, which accommodate a fisherman village. The other two beaches have natural origin with lengths of 200 m and 600 m, respectively. Chengene skele is situated further east from Kraymorie and is a heavily man-modified small bay of NW exposure (Figs. 1, 2C). The fisherman village at Chengene skele serves as Burgas fishing port. It is protected by coastal structures from both sides, while the inner part of the bay is constructed as parallel piers for boats mooring.

With respect to wave climate, values of significant wave height means and maxima of waves entering Burgas Bay are about 0.6 m and 6.0 m, respectively. Propagating towards the coast they are being transformed and near-shore values range within 0.3-0.5 m for means and 2.5-5.0 m for maxima. Peak wave period is uniform throughout the bay – 4-5 s for means and 10-11 s for maxima. According to climatic wave conditions estimated based on the wind fetch (Valchev et al., 2014) the area of Pomorie spit is classified as exposed to wave action, as the offshore significant wave heights are 0.5 m and 5.0 m, respectively. The other two sites (Kraymorie and Chengene Skele) are classified as moderately exposed and offshore significant wave heights are about 0.45 m and 4.0 m.

Sediments on Pomorie spit are of uniform grain size, well sorted and with high content of heavy fraction ranging within 43.5-79.3%. They are distinguished with their dark colour owing to the considerable concentration of the heavy magnetite fraction. Their carbonate content grows southward as the maximum is reached at Burgas beach (20%). Genesis of the magnetite sands is related to the inflow of alluvial material enriched with heavy minerals. In the southern part of Burgas, where Kraymorie and Chengene Skele are located, the sediments are predominantly poorly sorted quartz aleurite sands as the heavy fraction content diminishes eastward due to the prevailing coastal current direction. Their carbonate content is 27.2% in the western and 25.4% in the eastern part as the higher content is attributed to the contribution of shells (Popov & Mishev, 1974).

Beach-face slopes

Following the adopted methodology for UAV-based surveying of the Bulgarian Black Sea coastal zone (Prodanov et al., 2020), WingtraOne VTOL mapping drone and DJI Phantom 4 RTK Quadcopter were used to capture aerial images of the land-sea interface and reconstruct the topography of the studied coastal stretches. The high accuracy of the photogrammetric models was assured by carrying out of combined geodetic measurements. The ground control points (GCPs) were collected with a

HiTarget V90Plus GPS, along with a certified RTK network in Bulgaria, providing a high enough accuracy of the coordinate records. The GCPs were of 2 cm horizontal and 3 cm vertical accuracy. For better details of coastal landforms, the flight altitude was reduced under 100 m with 0.8 cm ground sampling distance, which allowed a generation of very high-resolution digital surface models (under 20 cm/pix) and orthophoto mosaics (2.5 cm/pix). 18 cross-shore profiles covering the beach-face slope area were extracted from the DSMs as follows: 13 at Pomorie spit, 3 at Kraymorie and 2 at Chengene skele (see magenta profiles in Fig. 1). The beach-face slopes were calculated taking into account the part of profile between mean sea level and upper limit of wave swash. *tanβ* are in following ranges: 0.054 – 0.259 (Pomorie spit), 0.112 – 0.173 (Kraymorie) and 0.087 – 0.130 (Chengene Skele).

Sediments

Sediment data were gathered simultaneously with the terrain data during two field surveys. The sediment samples were taken at the shoreline (lower part of the beach-face) from the upper 5 cm surface layer. The sediment sampling positions coincided with the profile data. The samples were processed through sieve analysis and their properties were calculated using the software GRADISTAT® package Version 8.00 (Blott & Pye, 2001). The median grain sizes (D_{50}) are found to be vary as follows: 0.19 - 0.80 mm (Pomorie spit), 0.22 - 0.67 mm (Kraymorie) and 0.17 - 0.25 mm (Chengene Skele); thus, the sediments vary from fine to coarse sands according to Wentworth size scale (Wentworth, 1922).

Wave data

Wave conditions were determined using wave hindcast data obtained by means of nested WAM-SWAN wave model train with a grid spacing of 1/30⁰ and covering 57-year period (1949-2006) (Valchev et al., 2010). The wave parameters - mean significant wave height 0.75 m and mean wave period 2.7 s - were extracted for point located in front of Burgas Bay at 48 m depth.

Formulations tested

Sunamura (1975 and 1984) proposed empirical formulae for prediction of the beach-face slope based on breaking wave height, acceleration due to gravity, median grain size and wave period using data from three field locations and twelve laboratory studies. The relationships were developed for $tanβ$ = 0.011 - 0.7 and D_{50} = 0.2 - 1.0 mm. The equations are suitable for use with field data, thus for Sunamura (1975):

$$tanβ = \frac{c_1 g^{0.5} D_{50}^{0.5} T}{H_b}, \quad c_1 = 0.1$$

(1)

while for Sunamura (1984):

$$tan\beta = c_1/(H_b/g^{0.5}D_{50}{}^{0.5}T)^{0.5}, \quad c_1 = 0.12 \tag{2}$$

The equation $H_b = 0.39g^{0.2}(TH_0^2)^{0.4}$, proposed by Komar and Gaughan (1972), is used for calculation of breaker wave height, where H_0 is deep water wave height.

Uda & Sakai (1985) suggested relationship between beach-face slope, sediment size and significant wave height based on field measurements:

$$tan\,\beta = c_1(D_{50}/1000\ H_s)^{c_2} \tag{3}$$

where $c_1 = 4.5, c_2 = 0.5$.

Reis & Gama (2010) formula connects sand size, offshore wave height and beach-face slope using data from two spots on the southwestern Portuguese coast. The slopes were in the range 0.03 - 0.18, while $D_{50} - 0.1$ - 1.9 mm. Thus the beach-face slope is calculated as:

$$tan\,\beta = c_1H_s{}^{c_2}D_{50}{}^{c_3} \tag{4}$$

$c_1 = 0.9; \quad c_2 = -10/3; \quad c_3 = 4/3$.

In Fleming (2011) the relationships between the two main parameters were developed for different beach states. He suggested using the surf scaling parameter (ε) (Guza & Inman, 1975) or the Dean parameter (Dean, 1973) to differentiate between morphodynamic states of the profiles. According to surf scaling parameter, the beach states are determined as: reflective: $\varepsilon < 3$, intermediate: $3 < \varepsilon \leq 33$, dissipative: $\varepsilon \geq 33$. According to the Dean parameter (B_s), the reflective beach state is reached when $B_s \leq 1$, while the dissipative state corresponds to $B_s \geq 6$. For $1 < B_s < 6$ intermediate state is indicated. The relationships proposed were modified after Flemming and Fricke (1983), and based on field measurements data of Bascom (1951) and Wiegel (1964) including 500 profiles and over 600 sand samples with $D_{50} = 0.17$ - 0.8 mm, and $tan\beta = 0.012$ - 0.25.

In order to find the beach slopes for the two types of beach states, the following equations are used:

$$\beta = 13.39\,e^{(-D_{50}/0.7954)} \tag{5}$$

for dissipative beach state
$$\beta = 0.057 + 33.5152\,e^{(-D_{50}/0.8517)} \tag{6}$$

for reflective beach state; where D_{50} is in phi and β - in degrees. For intermediate beach states, the values occupy positions between the reflective and dissipative domains.

The beach-face slope equation in Kim et al. (2014) is based on analysis of laboratory datasets defined by ranges – D_{50} = 0.2 - 0.7 mm, $tan\beta$ = 0.03 - 0.26 – and reads:

$$tan\beta = c_1 T^{c_2} D_{50}^{c_3},$$ (7)

where T is the deep water wave period; $c_1 = 0.332$; $c_2 = -0.416$; $c_3 = 0.122$.

Bujan et al. (2019) conducted a large-scale study of a very wide range of sediment sizes and beach-face slopes. They analyzed data of 2144 field measurements from 78 studies of different scale, covering grain populations with median sizes from 0.063 mm (very fine sand) to 4096 mm (boulders), and slopes ranging from 0.01 to 0.83. The proposed relationship is based only on sediment median size applicable to the range 0.125 – 770 mm:

$$tan\beta = a(D_{50} - 0.125)^b + c$$ (8)

where a = -0.154, b = -0.145 and c = 0.268.

McFall (2019) developed three relationships in dependence of wave exposure for protected, moderately protected and exposed beaches, based on grain size (D_{50} = 0.1 - 1.0 mm) and beach-face slope ($tan\beta$ = 0.007 - 0.25) data from 181 locations. The formulae for the three types of exposure, where $tan\beta$ is expressed through the horizontal distance X (1:X vertical : horizontal), are the following:

Protected: $\qquad\qquad\qquad X = 3.1d^{-1.1}$

Moderately protected: $\qquad X = 2.1d^{-1.8}$ (9)

Exposed: $\qquad\qquad\qquad X = 3.9d^{-1.85}$

Results and discussion

Behaviour of the available field data pairs $tan\beta$ - D_{50} is presented in Fig. 3. It can be seen that $tan\beta$ increases with the increase of D_{50}, which confirms the previously identified trends in literature. The beach-face slopes grow more rapidly (0.05 to 0.17) for fine sands (0.17-0.25 mm) and medium sands (up to D_{50} = 0.3 mm). Medium and coarse sands data points are more widely dispersed not showing any particular tendency. Three types of functions were tested to find out the best fit to describe the available field data pairs $tan\beta$ - D_{50} – linear, exponential and polynomial. The regression analysis reveals that the polynomial fit provides the best approximation. However, this result is not satisfactory enough due to relatively low value of R^2 = 0.45.

Polynomial
$y = 17.184x^2 - 2.9848x + 0.4076$
$R^2 = 0.4519$

Linear
$y = 1.9970x + 0.1298$
$R^2 = 0.3509$

Exponential
$y = e^{4.6516x} - 1.6878$
$R2 = 0.2851$

- in situ data
— Polynomial fit
– – Linear fit
······ Exponential fit
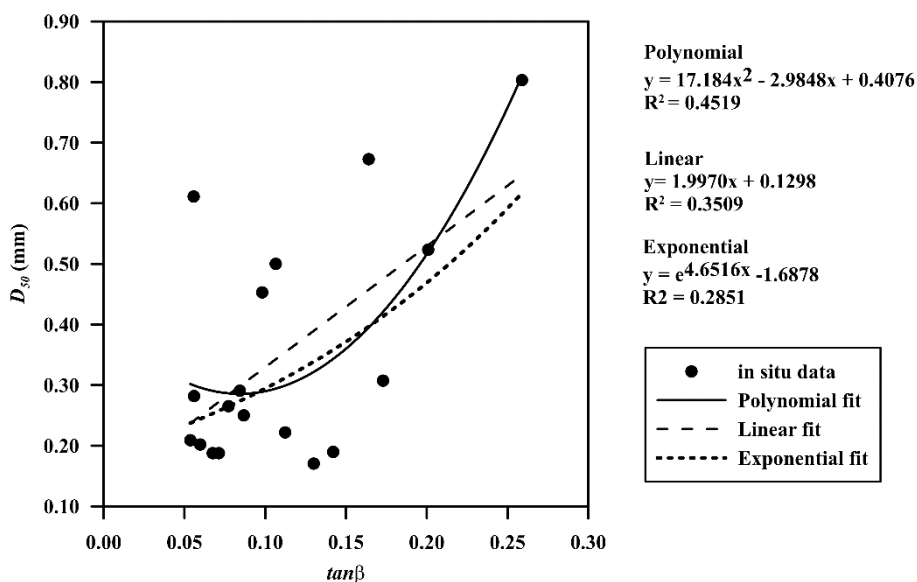
Figure 3. Distribution of field data pairs and fit functions

Due to the variety of data and conditions under which the formulae in question were derived, an initial assessment was needed to select the most appropriate for the local conditions. Therefore, the first step was to test the compatibility of in situ data (respectively the fit line) with the Eq.(1)-(9) applied for D_{50} from 0.1 mm to 1.0 mm, with increment of 0.1 mm. This range was selected as it covers the variability of D_{50} field data. In the formulae where wave data are required (i.e. Reis & Gama, Uda & Sakai, Kim et al. and Sunamura) we used the wave conditions mentioned in the previous section. The result is presented in Fig. 4.

Generally, it is observed that the measured data pairs fit relatively well in the prediction area prescribed according to McFall, Bujan et al., Flemming, Uda & Sakai, and Kim et al., showing similar behaviour of $tan\beta$ with the increase of D_{50}, i.e. narrow range of beach-slopes corresponds to wider range of sediment sizes. On the other hand, the expressions of Reis & Gama and Sunamura deviate significantly illustrating the opposite dependence. This can be attributed to the fact that they are derived based on oceanic wave conditions deferring considerably from the local wave climate. For this reason, they have been discarded from further analysis. However, additional efforts might be considered to precise the type of wave statistics that would suite these formulations better.

Examining the available measurements as a single dataset does not give a possibility to take into account the specific types of coast. Therefore, in order to de-
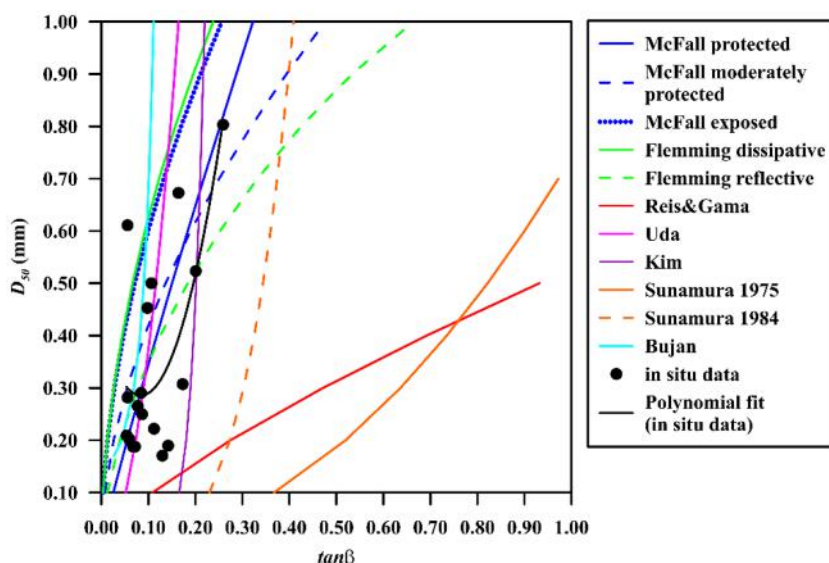
Figure 4. Representation of field data against all selected predicting formulations

tail the analysis, the tested formulae were divided into two groups depending on whether coastal types are considered or not. The first one deals with either wave exposure (after McFall) or morphodynamic beach state (after Flemming), while the second one takes into account only D_{50} (after Bujan et al.) possibly influenced by wave parameters (after Uda & Sakai and Kim et al.). Results are presented in Fig. 5.

The notion of wave exposure in the present study followed the wave exposure analysis of the Bulgarian coast made by Valchev et al. (2014) taking into account sites' geomorphic settings. Thus, the beach at Pomorie spit was deemed exposed, whereas the beaches at Kraymorie – moderately protected. The small beaches at Chengene Skele were considered protected due to presence of large number of shore defense structures (according to McFall, 2019). For exposed coasts McFall's formula predicts smaller beach-slopes for the same D_{50} compared to the measurements. Nevertheless, the correlation between predictions and field data appears to be strong (R = 0.71). Formulation valid for moderately protected coasts copes worse to represent the field data (R = 0.48) as larger deviation is observed for smaller sediment sizes (D_{50} = 0.05-0.1 mm). Data for protected coast type (Chengene Skele) are insufficient to establish any relationship (Fig. 5A).

Concerning the beach state concept across the studied coastal stretches, the northern end of Pomorie spit was established to be in intermediate state, which soon shifts to dissipative that dominates the larger part of it (10 out of 13 profiles). This finds expression in alongshore sediment size variability, which decrease
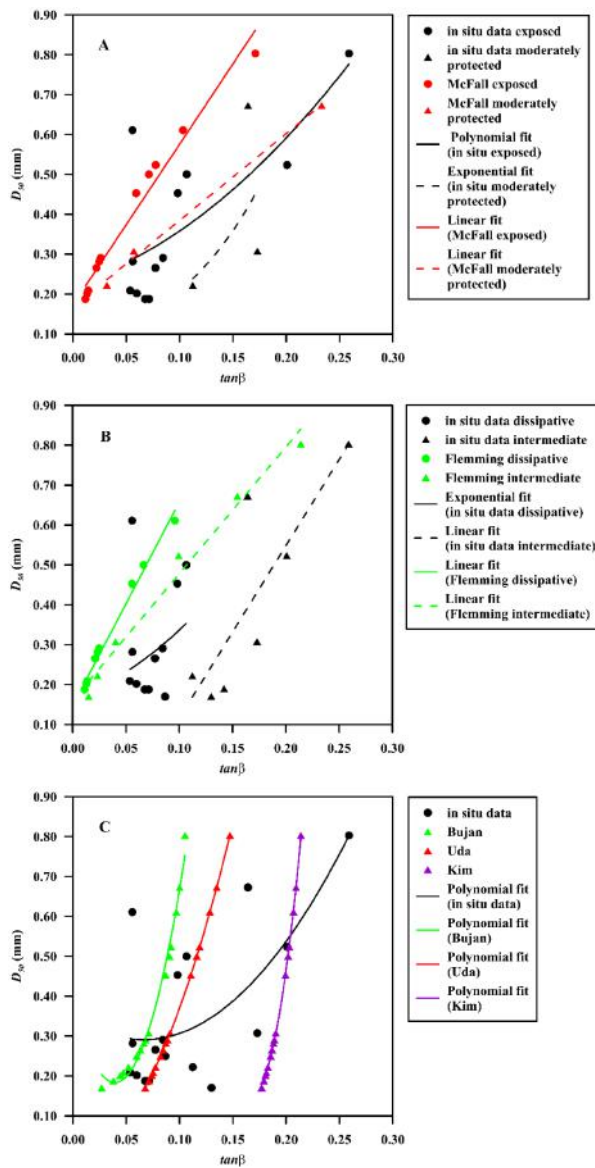
Figure 5. Representation of field data against predicting formulations according to consideration of coastal types (states): A) wave exposure, B) morphodynamic beach state and C) accounting only for D_{50} possibly influenced by wave parameters

southward from ~ 0.45 to 0.2 mm. The beach-face slopes follow the similar pattern. As for Kraymorie and Chengene Skele, the beaches are predominantly in intermediate state. Fig. 5B shows that profiles' slopes in dissipative state are concentrated in a quite narrow range 0.05-0.11, while predictions span over a two times wider range for the same D_{50}, which affects negatively the correlation between the series (R = 0.25). On the other hand, for the profiles in intermediate state this tendency is less discernable as Flemming's formula predicts smaller $tan\beta$ (Fig. 5B). In this case the stronger correlation is achieved, that is 0.84.

With respect to the second group of relationships, they predict beach-face slopes in very narrow ranges expressing the similar behaviour but Kim et al. calculates steeper slopes compared to the other two formulae (Fig. 5C). This is not the case with the field data as the measured slopes span over all empirical curves resulting in a more slanted polynomial fit. Nevertheless, moderate correlation can be reported – R is about 0.55 for all cases.

CONCLUSIONS

The presented study investigated the relationships between the beach-face slope and sediment size for several coastal stretches in Burgas Bay using field data and available formulations. An attempt was made to explore their applicability for local geomorphic, lithologic and wave conditions. Although the results are not unambiguous, several formulations can be considered deem for future exploration, as these are Fleming's Eqs. (5-6), McFall's Eq. (9) and partially Eqs. (3), (7) and (8). The major drawback consists in lack of sufficient field data pairs, which underpins the importance of regular coastal monitoring. The other reasons may be attributed to the presence of magnetite fraction in the local sediments, which alters their dynamic properties. In conclusion, it is to be considered elaboration of native relationships accounting for the local to regional specifics of the western Black Sea coast. Therefore, it is necessary to expand the database to cover wider ranges of beach-face slopes and sediment sizes coming from areas with different wave exposure and morphodynamics state.

REFERENCES

Baldock, T.E. &Hughes, M.G. (2006). Field observations of instantaneous water slopes and horizontal pressure gradients in the swash-zone. *Continental Shelf Research*, 26, 574–588.

Bascom, W.N. (1951). The relationship between sand size and beach-face slope. Eos. Trans. AGU 32 (6), 866–874.

Blott, S.J. & Pye, K. (2001). Gradistat: a grain size distribution and statistics package for the analysis of unconsolidated sediments. Technical communication. *Earth Surface Processes and Landforms*, 26, 1237–1248.

Bujan, N., Cox, R. & Masselink, G. (2019). From fine sand to boulders: Examining the relationship between beach-face slope and sediment size, *Marine Geology*, 417, 106012.

Flemming, B.W. & Fricke, A.H. (1983). Beach and nearshore habitats as a function of internal geometry, primary sedimentary structures and grain size. In: McLachlan, A., Ersamus, T. (Eds.), Sandy Beaches as Ecosystems. Dr. W. Junk Publishers, The Hague, 115–132.

Flemming, B.W. (2011). 3.02 - geology, morphology, and sedimentology of estuaries and coasts. In: Treatise on Estuarine and Coastal Science. Academic Press, Waltham, pp.7–38.

Guza, R.T. & Inman, D.L. (1975). Edge waves and beach cusps. *J. of Geophysical Research*, 80, 2997–3012.

Horn, D.P. (2006). Measurements and modeling of beach groundwater flow in the swash-zone: a review. *Continental Shelf Research*, 26, 622–652.

Johnson, J. W. (1949). Scale effects in hydraulic models involving wave motion, *Trans. Amer. Geophys. Union*, 30, 517 - 525.

Kim, H., Hall, K., Jin, J.-Y., Park, G.-S. & Lee, J. (2014). Empirical estimation of beach-faceslope and its use for warning of berm erosion. *J. of Measurements in Engineering*, 2, 1, 29–42.

Li, L., Barry, D.A., Pattiaratchi, C.B. & Masselink, G. (2002). BeachWin: modelling groundwater effects on swash sediment transport and beach profile changes. *Environmental Modelling and Software*, 17, 313–320.

Mangor, K.; Drnen, N.K.; Kærgaard, K.H. & Kristensen, S.E.2017. Shoreline Management Guidelines. Hrsholm, Denmark: DHI, 462p.

Mangor, K.; Drnen, N.K.; Kærgaard, K.H., and Kristensen, S.E. (2017). Shoreline Management Guidelines. Hrsholm, Denmark: DHI, 462p.

Masselink, G.& Puleo, J.A. (2006). Swash-zone morphodynamics. *Continental Shelf Research*, 26, 661–680.

McFall, B.C. (2019). The Relationship between Beach Grain Size and Intertidal Beach Face Slope. *J. of Coastal Research*, 35, 5, 1080-1086.

Popov V. & K. Mishev. (1974). Geomorphology of the Bulgarian Black Sea coast and shelf. Sofia: Publishing house of the Bulgarian Academy of Sciences. 267. (In Bulgarian)

Prodanov, B., Kotsev, I., Lambev, T. & Bekova, R. (2020). Unmanned Aerial Vehicles for surveying the Bulgarian Black Sea Coast, *Comptes rendus de l'Academie Bulgarie des Sciences*, 73, 5, 666-672.

Rector, R.L. (1954). Laboratory Study of Equilibrium Profiles of Beaches. Technical Memorandum. U.S. Army Corps of Engineers.

Reis, A.H. & Gama, C. (2010). Sand size versus beachface slope–an explanation based on the constructal law. *Geomorphology*, 114, 3, 276–283.

Rogev, B. (1975). Sea-level fluctuations in front of Burgas and Varna. *Communications of the State Geographical Institute*, Sofia (in Bulgarian)

Schwartz, M. (2006). Encyclopedia of Coastal Science. nov. Springer Science & BusinessMedia. https://link.springer.com/referenceworkentry/10.1007%2F1-4020-3880-1_140.

Sunamura, T. (1975). "Static" relationship among beach slope, sand size, and wave properties. *Geogr. Rev. Jpn*, 48, 7, 485–489.

Sunamura, T. (1984). Quantitative predictions of beach-face slopes. *GSA Bulletin*, 95, 2, 242–245.

Turner, I.L. (1995). Modelling the time-varying extend of groundwater seepage on tidal beaches. *Earth Surface Processes and Landforms*, 20, 833–843.

Uda, T. & Sakai, Y. (1985). Summarized data of beach profiles and wave observations at AjigauraBeach. Technical Memorandum of Public Works Research Institute, Ministry of Construction of Japan, No. 2294, 286.

Valchev, N., Davidan, I., Belberov, Z., Palazov, A. & Valcheva, N. (2010). Hindcasting and assessment of the western Black sea wind and wave climate, *J. of Environmental protection and ecology,* 11, 3, 1001-1012.

Valchev, N., Andreeva, N. & Prodanov, B. (2014). Study on wave exposure of Bulgarian Black Sea coast, *Proc. of 12th Int. Conference on Marine Science and Technology Black Sea 2014, Varna*, 175-182.

Wentworth, C.K. (1922). A scale of grade and class terms for clastic sediments. *J. of Geology*, 30, 377-392.

Wiegel, R.L. (1964). Oceanographic Engineering. Prentice Hall, Englewood Cliffs, NJ, 532.

Wilson, A.M., Huettel, M. & Klein, S. (2008). Grain size and depositional environment as predictors of permeability in coastal marine sands. *Estuarine, Coastal and Shelf Science*, 80, 193–199.

✉ **Petya Eftimova**
https://orcid.org/0000-0002-3805-1511
Institute of Oceanology
Bulgarian Academy of Sciences
Varna, Bulgaria
E-mail: eftimova@io-bas.bg

✉ **Nikolay Valchev**
https://orcid.org/0000-0002-3895-1683
Institute of Oceanology
Bulgarian Academy of Sciences
Varna, Bulgaria
E-mail: valchev@io-bas.bg,

✉ **Bogdan Prodanov**
https://orcid.org/0000-0002-8118-3034
Institute of Oceanology
Bulgarian Academy of Sciences
Varna, Bulgaria
E-mail: bogdanprodanov@gmail.com

✉ **Nataliya Andreeva**
https://orcid.org/0000-0003-4090-8016
Institute of Oceanology
Bulgarian Academy of Sciences
Varna, Bulgaria
E-mail: n.andreeva@io-bas.bg,

✉ **Todor Lambev**
Institute of Oceanology
Bulgarian Academy of Sciences
Varna, Bulgaria
E-mail: totolamb@abv.bg

✉ **Liubomir Dimitrov**
https://orcid.org/0000-0003-4252-8455
Institute of Oceanology
Bulgarian Academy of Sciences
Varna, Bulgaria
E-mail: geos@io-bas.bg,

ASSESSMENT OF DESTABILIZING FACTORS ON A POTENTIAL LANDSLIDE SLOPE IN SOFIA KETTLE – EXAMPLE FROM THE GERMAN VILLAGE AREA, BULGARIA

Miroslav Krastanov
Geological Institute – Bulgarian Academy of Sciences (GI-BAS)

Abstract. In the present study, a specific sample area has been selected, where an assessment model is made for the stability of a slope subjected to anthropogenic impacts. A slope from the foot of the Lozenska mountain in the periphery of the Sofia kettle has been chosen as such an exemplary area, as part of the dangers arising in the Trans-Balkan valleys. Landslide processes as a result of anthropogenic impact often occur on the territory of the Sofia valley. The increased construction, the development of hard-to-reach terrains with large slopes, their undermining, the seismic impact and the low values of the strength-deformation parameters of the geological varieties building the respective terrains contribute to their occurrence. The deforestation, the loads with heavy embankments, the hydration, the inhomogeneity of the layers of the earth base have a strong destabilizing effect. The terrain in question is located in the southeastern part of the village of German, at the base of a steep $35 \div 49°$ slope. The paper presents the results of field and laboratory studies, analyzes of slope stability by the method of Felenius. The severity of the impact of the various destabilizing factors was assessed.

Keywords: landslide, slope stability, factory of safety, Sofia kettle

INTRODUCTION

The Sofia kettle has been selected as one of the regions in the country where landslides often occur due to anthropogenic impact (Berov et al., 2002; Bruchev et al., 2006; Berov, 2008). The consequences are often associated with significant material damage – cracking and destruction of buildings and facilities, disruption of transport infrastructure, and sometimes human casualties.

Favorable conditions for the occurrence of landslides with anthropogenic character are the cutting of steep slopes, the diverse geological structure and the low values of the shear strength of the geological varieties (Frangov, 1990; Berov, 2002; Yaneva, Berov & Frangov, 2002, etc.). The stability of the slopes is most destabilized by heavy embankment loads, slope felling, dewatering of clay deposits, dynamic

impacts from vehicles, the correct choice of physical and mechanical properties of earth-based materials, deforestation of slopes and earthquakes. The considered terrain, which slope reaches 49º, is also potentially endangered by landslides. The studied terrain is located in the southeastern part of the village of German (Fig. 1).

Figure 1. Panoramic view of the investigated slope

GEOMORPHOLOGICAL, GEOLOGICAL
AND ENGINEERING GEOLOGICAL CONDITIONS

The Sofia kettle represents a complex, asymmetric graben of block structure in the West Srednogorie region. It is separated by the surrounding mountains (Sofia Balkan mountain to the north, by the Lozenska and Vitosha mountains to the south, by the Lyulin mountain and the Slivnitsa hills to the west and by the western parts of the Ihtiman Sredna Gora mountain – to the east) by a complex fault system. The boundaries are determined by the distribution of the Neogene and Quaternary depositions in the places where they come into contact with the older formations.

The Sofia kettle is filled with Upper Neogene lake sediments represented by loose and more or less compacted sediments – mainly sandy and silty clays, clays, sands, lignite coals, gravels, conglomerates (Yaneva, Berov & Frangov, 2002).

The uppermost part of the Neogene sediments is represented by the depositions of the Lozenec Formation (lzN_2). These deposits serve as a soil base for construction purposes on the territory of the town of Sofia and the greater part of the kettle itself. The sediments are represented to the depth of $25 - 30$ m by sands of various grain-size distribution (silty, fine, small- and medium-sized sands) and by silty or silty-sandy clays. The gravels among them are in the form of lenses or intercalations with clayey-sandy filler. The great variety in the lithological composition of

these depositions determines the diversity and the variation in a broad range of their physical and mechanical properties. The important feature of their granulometry is the high content of the silty fraction (42 – 82 %) which explains to a great degree the peculiarities in their physical and mechanical properties – low bulk density, high pore coefficient, high moisture content, plastic consistency (Bozhinova & Ilieva. 1990; Ivanov, 2001; Bozhinova-Haapanen & Uusinoka, 2014; Stoynev & Lakov, 2017). The decrease of the physical and mechanical parameters is almost parallel with the increase of the silty fraction.

The Neogene Sediments are covered by Quaternary sediments of irregular thickness represented by a culture layer, brown and black silty clays, alluvial gravel and sands building the river terraces, and deluvial and alluvial fan boulders, gravels and clays along the peripheral parts of the kettle. A characteristic feature of the sediments filling the kettle is their frequent facial variability, inconstancy of composition, thickness and properties both in vertical and horizontal direction. In general the Quaternary soils possess relatively high pore volume and low deformation module. That is the reason for the differences in their distribution, composition and properties, reflecting on the construction conditions and on the manifestation of various unfavorable processes and phenomena (Ivanov & Angelova, 1997; Ivanov, Frangov & Yaneva, 1998; Yaneva & Donkova, 2017).

The genesis of the lithological varieties determines to a great extent their properties and accounts for the origin and development of the different processes. The geodynamic processes and phenomena observed in the kettle are the landslides, dry shrinkage of clays, swelling of clays, marshlands, suffusion, sand liquefaction, seismicity, etc. (Iliev-Broutchev, ed., 1994; Berov, 1995; Berov & Ivanov, 1995; Frangov & Dobrev, 1991; Konstantinov et al., 1992; Ivanov, 1996, 1997, 2002; Berov & Frangov, 1997;Ivanov & Frangov, 2000; Berov et al., 2002). Engineering geological properties of the sediments in Sofia basin and their susceptibility to subsidence have been considered by a number of authors (Ivanov, 1996; Frangov, & Ivanov, 1999; Kostov&Bozhinova-Haapanen, 2015). Sofia valley district is a seismically active zone with several strong manifestations of earthquake during the last two centuries.

The area is characterized by a complex geological structure (Antonov et al., 2011). The studied terrain is represented by materials of proluvial and deluvial origin. Proluvial deposits cover the Neogene sediments or older rocks with an uneven, blurred boundary. They are represented by block-boulder unsorted, conglomerates, quartz sandstones and andesites.

The deluvial deposits fill the inter-cone depressions at the northern foot of the Lozenska mountain. They are made of coarse-grained deposits with a clayey or clayey-sandy matrix with ridged pieces up to 2 – 3 cm, mostly of quartz. The pieces are gravel and boulder in size. In some places there is a rough layering, emphasized by thin clay layers and the arrangement of small rock fragments. From an engineering geological point of view, the studied area is part of the foot of the Lozenska mountain

and is characterized by the manifestation of the so-called slow creep on the slopes. In case of unplanned technogenic intervention in such slope sections, the manifestation of active landslide processes with unpredictable consequences is possible. The manifestation of muddy-stone torrent in historical time in the area of the village of Lozen has been registered in the slopes of the Lozenska mountain. This leads to the conclusions that in case of careless anthropogenic interference and outpouring of water in the slopes, local flows in the proluvial-deluvial materials are possible.

Geomorphologically, the region is the northern periphery of the proluvial deposits at the foot of Lozenska Mountain.

The studied terrain is flat in 63% of its area, and in its other part it is steep with a slope from southeast to northwest. Average altitude in the flat part of the property is 590 – 591 m, and in its steepest part is 598-599 m. The height of the slope reaches 10 m (Fig. 2). The terrain morphology is additionally modelled by anthropogenic impact (embankments).

From the conducted researches three engineering geological varieties were established. Their spatial arrangement is shown in Fig.3
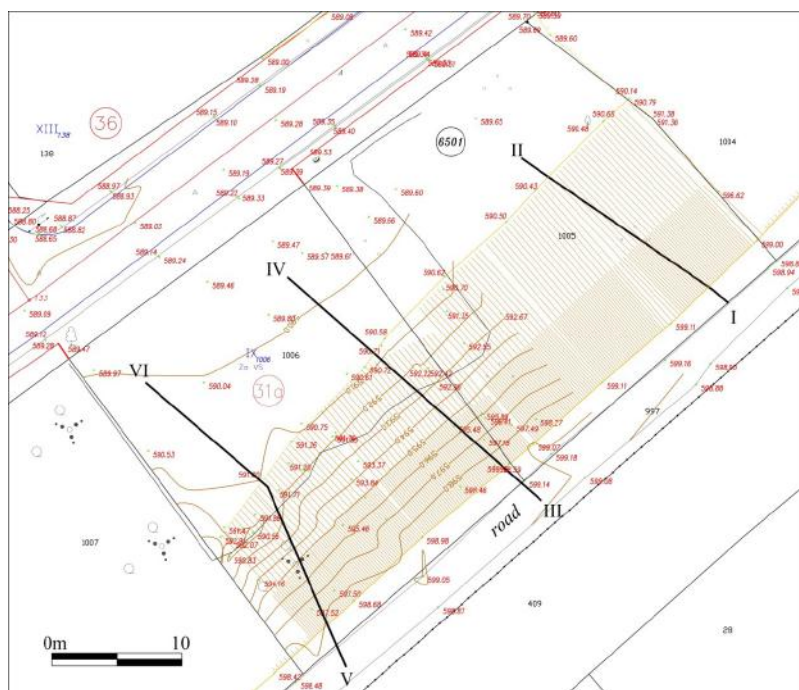

Figure 2. Topographic map of the terrain with the location of the engineering geological cross-section
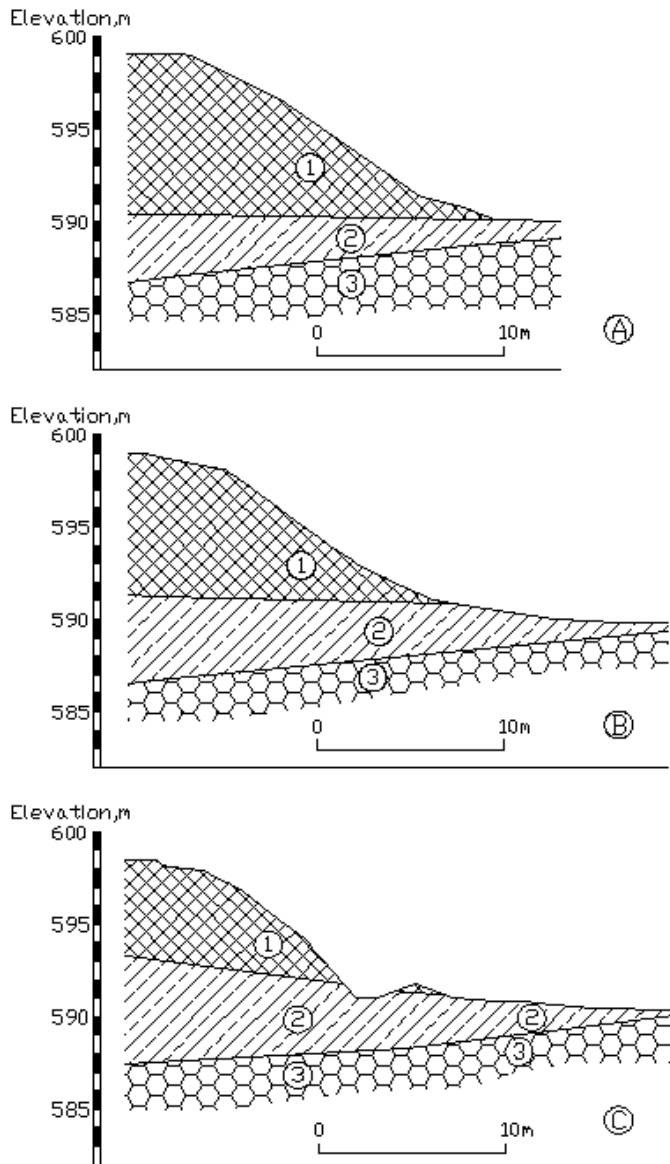
Figure 3. Cross-section: A – Cross-section I –II; B – Cross-section III – IV; C – Cross-section V – VI; natural geological setting: 1 – Embankment tQh; 2 – Clays to sandy clays pr-d Qh; 3 – Block-boulder conglomerates, quartz sandstones and andesites prN_2-Qp

GEOTECHNICAL CONDITIONS AND SLOPE STABILITY

Depending on the genesis, lithological features and physical and mechanical parameters of the varieties, three engineering geological layers are separated.

Layer 1 – Embankment. It is systematically laid and is represented from powdery clays to powdery sandy clays with small to medium gravels in places reaching boulders. The established thickness of the embankment is 0.30 ÷ 8.70 m.

Layer 2 – Quaternary clay. It is represented by brown powdery clay in medium to hard plastic consistency. Layer 2 is established jointly throughout the study area. Layer 2 lies under layer 1 at a depth of 0.30 to 8.70 m from the ground surface. The thickness of the layer is 0.80-0.90 ÷ 5.6 m from the modern level of the terrain.

Layer 3 – Block-boulder rock species. Layer 3 lies under layer 2 at a depth of 0.80 to 12.00 m from the ground surface. The layer is represented by block-boulder quartz sandstones, andesites, tuffs and conglomerates. Layer 3 is established everywhere on the studied terrain, as its thickness is over 2.50 m.

Shear strength parameters are obtained by the laboratory plane shear tests on undisturbed soil samples and from heavy-type penetrometer (DPH) penetration test (Table 1).

Table 1. Values of physical and mechanical parameters of different strata

Geological strata	Bulk density γ kN/m³	Angle of int. friction, f deg.	Cohesion, c kN/m²	Undrained cohesion, Cu kN/m²	Undrained cohesion, Cu* kN/m²
Layer 1	18,7	12,9	31,0	91	34
	17,9÷19,9	12,1÷22,8	26,3÷59,0	34÷154	13÷46
Layer 2	19,3	14,1	26,0	103	69
	18,3÷20,5	8,1÷21,4	28,3÷92,5	69÷154	35÷88
Layer 3	26,0	31,0	5960		
	26,0÷26,1	-	-		

Note: numerator – average value (samples); denominator – min ÷ max; * – undrained cohesion determined by field penetration test

During the study, groundwater at a depth of up to 13.00 m was not detected.

The current degree of stability of the slope is determined by three representative profiles (figures 2, 3 and 4). The Felenius method is applied. With this method (only valid for circular form slide surfaces) intra interface forces are ignored and thereby the unknowns are reduced to: n values of normal forces Ni; n values of shear forces Ti; Safety factor Fs (Fellenius, 1927).

When compiling the computational geomechanical model, the results of the engineering geological studies, the geomorphological features of the slope and the physical and mechanical indicators of the construction soils were taken into account. The slope analyzes were performed with the program "SLOPE" of the

xc = 13,29 yc = 601,62 Rc = 12,31 Fs=1,26
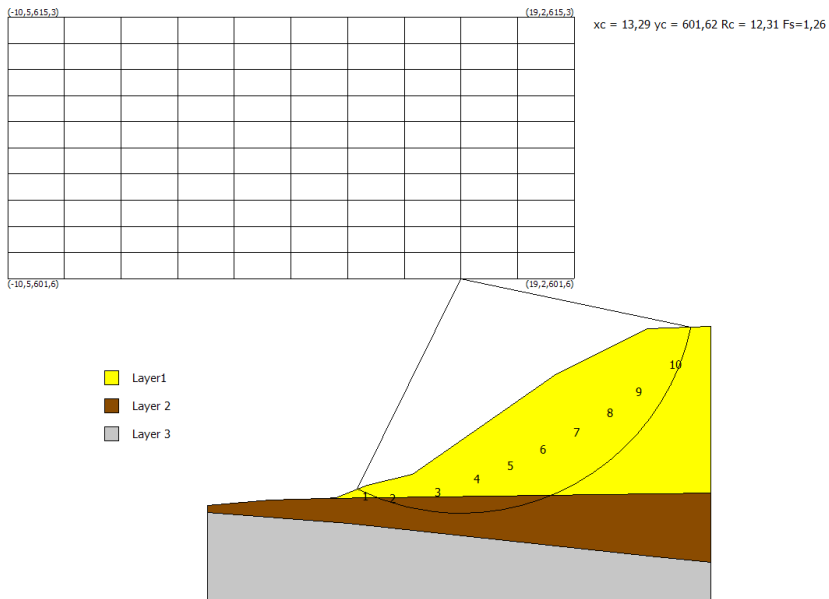
Figure 4. Calculation cross-section I – II for slope stability in natural state

xc = 16,43 yc = 599,88 Rc = 11,30 Fs=1,31
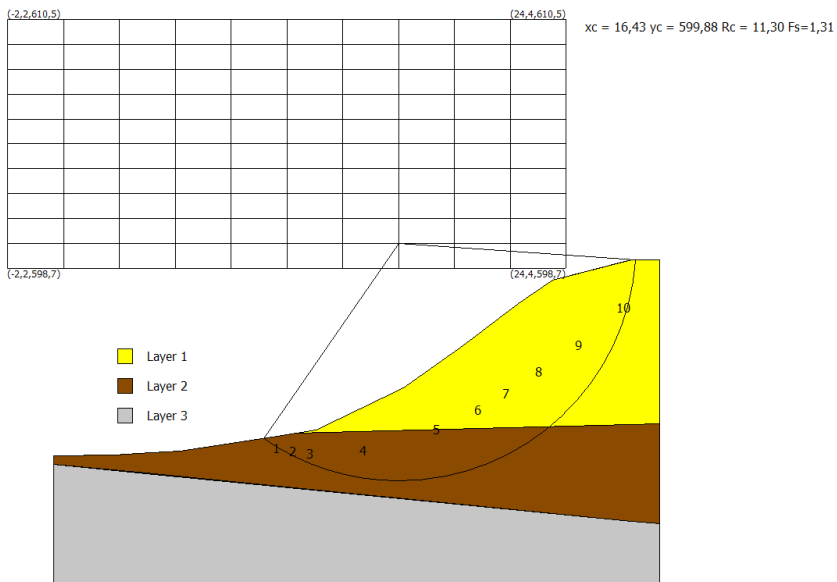
Figure 5. Computational cross-section III – IV for slope stability in natural state
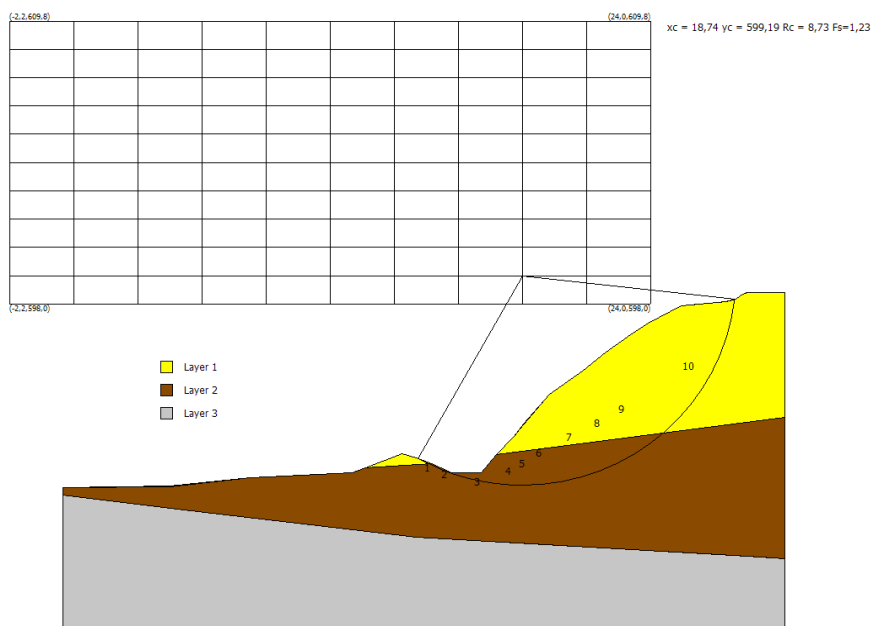
Figure 6. Calculation cross-section V– VI for slope stability in natural state

Italian company "GEOSTRU" Ltd. on 449 sliding surfaces. The following variants have been studied: stability of a slope in its natural state at a basic combination of loads, at a water-saturated slope, at a loaded slope and an earthquake of IX degree. The results of the stability analyzes are shown in Figures 4, 5 and 6. These figures show the contours of the sliding surfaces, on which the safety factors F_s for the different states are calculated, the number of lamellae and the network with the centers of equilibrium.

The values obtained for the coefficient of stability are given in Table 2.

Table 2. Results of slope stability

Slope condition	Cross-section	Safety factor F_s
Natural terrain		1.26
Water saturated terrain	I – II	1.26
Natural terrain with earthquake		0.97
Natural terrain with additional load		1.22
Natural terrain		1.31
Water saturated terrain	III – IV	1.31
Natural terrain with earthquake		0.97

Natural terrain with additional load		1.26
Natural terrain		1.23
Water saturated terrain	V – VI	1.23
Natural terrain with earthquake		1.00
Natural terrain with additional load		1.19

CONCLUSION

In the selected sample area of a slope section at the foot of Lozenska mountain, some peculiarities of the engineering-geological conditions in the periphery of the Sofia valley have been established, which would contribute to the careful assessment when undertaking technogenic intervention in such sections.

From the performed studies and analyzes of the slope stability the following conclusions can be made about the influence of the various factors on the stability of the studied slope :

• In the natural state the studied terrain on all three analyzed profiles is in a stable state, as the coefficient of resistance is in the range between Fs = 1.23 ÷ 1.31 depending on the natural slope and the varieties from the ground.

• The increase in the groundwater level has a weak effect on the stability of the slope. This is also due to the fact that the embankment has a role to retain water in the open channel, which is located next door and to protect neighboring areas from flooding.

• With an estimate for maximum earthquake of IX degree, the stability of the slope decreases to values Fs = 0.97 – 1.00, which characterizes it as unstable.

• When reporting a load at the top of the slope in the amount of a heavy truck, a negative impact is found on the coefficient of stability, which decreases to Fs = 1.19 – 1.26, but nevertheless the slope remains stable.

• The most adverse effect on the stability of the studied terrain has the seismic impact, as the coefficient of stability decreases by 23 to 35% of that in the natural state.

• In case of additional load on the considered slope, the coefficient of stability decreases by 3 ÷ 4%.

• In this case, the main trigger for the occurrence of landslides may be the seismic impact, as well as a combination of two or more anthropogenic factors.

REFERENCES

Antonov, M., Milovanov, P., Popov, A., Bonev, K., Dulgerov, M., Marinova, R. & Sarov, S. (2011). *Explanatory Note to the Geological Map of the Republic of Bulgaria. Scale 1:50 000. Map Sheet К-34-59-Б (Sofia-south)*. Sofia, Ministry of Environment and Water, Bulgarian Geological Survey, 51 p.

Berov B. (1995). Technogenic unfavorable ecogeological changes in the Sofia valley. *Collection of scientific papers by Nat. Conf. with International participation – "Automation and Informatics'95", "Ecological Engineering and Environmental Protection EEER'95"*, November 7 – 9, 1995, Sofia, 94 – 97 (in Bulgarian).

Berov, B. (2002). Some Anthropogenic Changes in the Geological Environment in Bulgaria. *Geologica Balcanica*, 32(2 – 4), Sofia, 107 – 111.

Berov, B. (2008). Zoning of Sofia valley according to the level of geological hazard. *Geologica Balcanica*, 37(1 – 2), Sofia, 73 – 78.

Berov, B. & Frangov, G. (1997). Zoning of Sofia valley according to degree of potential landslide hazard. *4-th National Scientific and Practical Conference on Scientific support of Prevention activities and Protection of the population in case of emergency*. The Permanent Committee for Monitoring Disasters and Accidents. Sofia, 5 – 6 November 1997, Vol. 5, 207 – 215 (in Bulgarian).

Berov, B. & Ivanov, P. **(**1995). Possible secondary seismogenic deformations in Sofia kettle. – In: *Proc. of the XV Congr. CBGA,* September 17 – 20, 1995, Athens, Greece, 965 – 969.

Berov, B., Dobrev, N., Brouchev, I. & Fukuzono, T. (2002). Landslides in Bulgaria. – *Journal of the Japan Landslide Society* 38 (4), 334 – 343.

Bozhinova, A., Ilieva. L. (1990). Structural and mechanical properties of Sofia clays. – In: *Proc.VI-th International Congress of Engineering Geology*, 6 – 10 August 1990, Amsterdam, Netherlands, 1809 – 1812.

Bozhinova-Haapanen, A. & Uusinoka, R. (2014). X-Ray Tests on the Mineral Composition of Sofia Clay Deposits. *Engineering Geology and Hydrogeology*, 28, 91 – 105.

Bruchev, Il., Varbanov, R., Frangov, G., Dobrev, N., Ivanov, P., Berov, B. & Diankov, Hr. (2006). Update landslide map of Bulgaria. *National Scientific and Technical Conference "State and Control of Landslide and Erosion Processes in Bulgaria"*, 30.XI – 1.XII 2006, Sofia, Prof. Marin Drinov Publishing House of BAS, 23 – 31 (in Bulgarian).

Fellenius, W. (1927). *Erdstatische Berechnungenmit Reibung und Kohäsion (Adhasion) und unter Annahme kreiszy lindrischer Gleitflachen*. Berlin: Ernst & Sohn.

Frangov, G. (1990). Main regularities in the distribution of technogenic landslides in Bulgaria. – *Rev. of the Bulgarian Geological Society*, vol. LI, part 3, 79 – 85 (in Bulgarian, with English abstract).

Frangov, G. & Dobrev, N. (1991). Distribution, features and activity of the landslides in the area of Bankya. – *Construction*, 9 – 10, 12 – 17.

Frangov, G. & Ivanov, P. (1999). Engineering geological modeling of the conditions in the Sofia graben and land subsidence prognoses. – In: *Proc. IV Working Group Meeting "Expert Assessment of Land Subsidence Related to Hydrogeological and Engineering Geological Conditions in the Regions of Sofia, Skopje and Tirana"*, Sofia, 03.12 – 06.12.1999, 7 – 13.

Iliev-Broutchev, I., ed. (1994). *Geological hazards in Bulgaria – Map in scale 1:500 000 and explanatory text.* Military Topographic Service, Troyan/Publishing House of BAS, Sofia, 143 p. (in Bulgarian, with English abstract).

Ivanov, P. (1996). Engineering geological properties of the sediments in Sofia basin and their susceptibility to subsidence. – In: *Proc. First Working Group Meeting "Expert Assessment of Land Subsidence Related to Hydrogeological and Engineering Geological Conditions in the Regions of Sofia, Skopje and Tirana"*, Sofia 31.10 – 3.11.1996, 36 – 41.

Ivanov, P. (1997). Assessment of the Geological Conditions in the Sofia Kettle under Seismic Impact. – *Proc. Intern. Symp. on Eng. Geol. and the Env., IAEG*, Athens, Greece 23 – 27 June 1997, BALKEMA, Rotterdam, 1265 – 1270.

Ivanov, P. (2001). Deformation Properties of the Neogene Sediments in Sofia kettle. – In: *Proc. "Expert Assessment of Land Subsidence Related to Hydrogeological and Engineering Geological Conditions in the Regions of Sofia, Skopje and Tirana" Final Conference*, Sofia (27 – 30.6.2001), 27 – 34.

Ivanov, P. (2002). Engineering Geological Conditions in the Sofia Kettle and Consequences from the Earthquakes. *Geologica Balcanica, 32*, 2 – 4, 117 – 122.

Ivanov, P. & Angelova, D. (1997). Geoecological Assessment of the Slope Surfaces in the Sofia Kettle. – In: *Proc. Intern. Symp. on Eng. Geol. and the Env., IAEG*, Athens, Greece 23 – 27 June 1997, BALKEMA, Rotterdam, 1271 – 1276.

Ivanov, P. & Frangov, G. (2000). Engineering-geological prerequisites for the seismic-hydrodynamic phenomena in the region of Gnilyane (Sofia District) during the Krupnik Earthquake in 1904. *Reports on Geodesy*, Warszawa, 4(49), 155 – 162.

Ivanov, P., Frangov, G. & Yaneva, M. (1998). Engineering geological characteristics of Quaternary sediments in Sofia graben. – In: *Proc. Third*

Working Group Meeting "Expert Assessment of Land Subsidence Related to Hydrogeological and Engineering Geological Conditions in the Regions of Sofia, Skopje and Tirana", Sofia, December 1998, 29 – 32.

Konstantinov, B., Angelov, K., Lakov, A., Stojnev, S. & Konstantinov, V. (1992). Landslides activization from earthquake motions. *Sixth International Symposium on Landslides (ISL 1992)*, 1181 – 1186.

Kostov, V. & Bozhinova-Haapanen, A. (2015). Settlement prediction for buildings founded on Pliocene clays from the territory of Sofia city. – *International Multidisciplinary Scientific Geo Conference Surveying Geology and Mining Ecology Management, SGEM*, 2(1), pp. 633 – 640.

Stoynev, S. & Lakov, A. (2017). Deformation properties of the Pliocene clays from the Sofia Basin. *Journal of mining and geological sciences*, vol. 60, part I, Geology and Geophysics, 128 – 131.

Yaneva, M., Berov, B. & Frangov, G. (2002). Evolution of Sofia Basin during the Neogene. *Geologica Balcanica*, 32(2 – 4), Sofia, 135 – 138.

Yaneva, M. & Donkova, Y. (2017). Quaternary deposits of the alluvial rivers in Sofia Basin. *Comptesrendus de l'Académiebulgare des Sciences*, 70 (1) 103 – 110.

✉ **Miroslav Krastanov**
https://orcid.org/0000-0002-0250-0346
Geological Institute
Bulgarian Academy of Sciences
Sofia, Bulgaria
E-mail: miro_k@geology.bas.bg,

AN EARTHQUAKE CATALOGUE FOR BULGARIA AND ADJACENT AREAS SINCE 1981

Dimcho Solakov, Stela Simeonova, Plamena Raikova, Irena Aleksandrova
National Institute of Geophysics, Geodesy and Geography –
Bulgarian Academy of Sciences (NIGGG-BAS)

Abstract. A homogeneous earthquake catalogue for Bulgaria and adjacent areas covering the period 1981–2019 is presented. The existing catalogues (including instrumental seismicity) for Bulgaria, covering the time period 1981–2000, were updated for the time period 2001-2019 using instrumentally determined focal earthquake parameters. In the present update catalogue, M_W is calculated for the entire period 1981–2019 applying the regression equations converting magnitude scales used in Bulgarian seismological routine practice (M_d and M_P) to the most reliable and widely used scale of magnitude, i.e. the seismic moment magnitude, M_W. Thus, a magnitude homogeneous catalogue concerning M_W scales is presented. The extended catalogue contains 645 independent events. The completeness test revealed that the catalogue is complete for moment magnitudes larger than or equal to 3.2 for the last 39 yr.

Keywords: earthquake catalogue, magnitude scales, homogeneous catalogue, completeness test, magnitude scales, Bulgaria

INTRODUCTION

Bulgaria is an earthquake prone country. Over the past centuries, Bulgaria has experienced strong earthquakes. The first well documented earthquake on the territory of Bulgaria is the 1st century BC quake occurred in the Black Sea near the town of Kavarna. Some of the Europe's strongest 20th century earthquakes occurred in Bulgaria (at the beginning of the 20th century from 1901 to 1928 on the territory of Bulgaria occur 5 earthquakes with magnitude larger than or equal to 7.0). Impressive seismic activity developed in the SW Bulgaria during 1904-1906. The seismic sequence started on 4 of April 1904 with two catastrophic earthquakes within 23 minutes (the first quake at $10^h 05^{min}$ with $M_W 6.8$ considered as a foreshock and the second one at $10^h 26^{min}$ with $M_W 7.6$ and $I_0=10$-the main shock). Along the Maritca valley, in 1928 a sequence of three destructive earthquakes occurred. The towns Plovdiv, Chirpan, Parvomay suffered great damage.

The beginning of Bulgarian seismology dates back to 1891. At that time Spas Watzof, the director of Central Meteorological Station in Sofia, organized network of correspondents for observation of the felt earthquakes in Bulgaria (Watzof, 1902). The period of Bulgarian historical era ends in 1905 when the seismograph of Omori-Boch type was installed in the first Seismological Station in the town of Sofia.

At present NIGGG-BAS runs the Bulgarian seismological network-NOTSSI (National Operative Telemetric System for Seismological Information). NOTSSI was founded at the end of 1980. The institute also operates two local seismic networks deployed around the Kozloduy Nuclear Power Plant and the town of Provadia in North-eastern Bulgaria. In 2005, the institute performed overall modernization of the NOTSSI. The upgraded Bulgarian Seismological Network consists of a National Data Centre and 25 stations equipped with RefTek High Resolution Broadband Seismic Recorders – model DAS 130-01/3. The configuration of NOTSSI is presented in Fig. 1.

Real-time data transfer from seismological stations to data centre was realized via Virtual Private Network (VPN) of the Bulgarian Telecommunication Company (BTC). Real-time data acquisition was performed using REFTEK's full duplex error-correction protocol RTPD. For data archiving two formats are used: PASSCAL and wildly used for seismological data mini SEED.

Currently, the Bulgarian seismological network allows reliable localization of low magnitude events $M_p > 1.5$ within the network, and $M_p \geq 3.0$ at regional distances. M_p is the magnitude scale that is presently used in Bulgarian seismological practice.
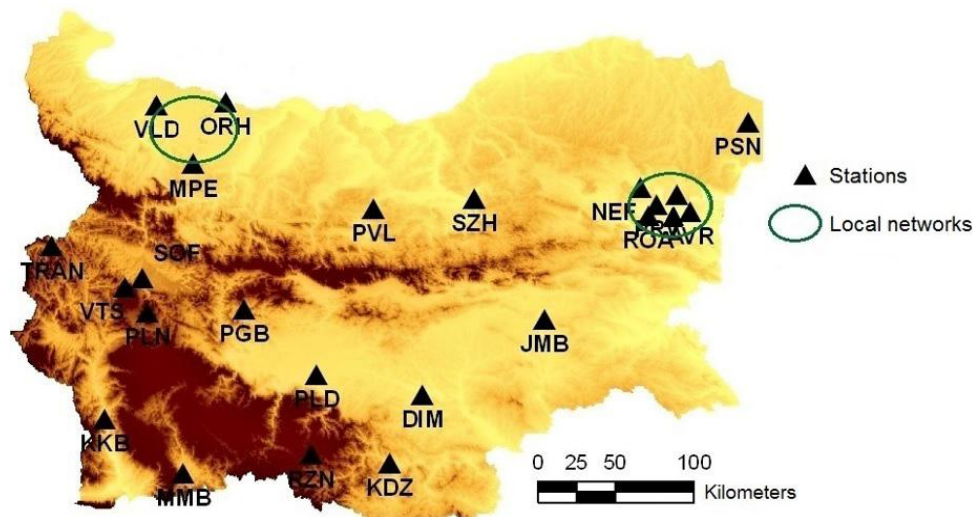

Figure 1. Bulgarian seismological network (NOTSSI)

It is defined by using the maximum amplitudes of body P waves recorded on the broadband seismographs.

Since 2005-2006, real-time data exchange between Bulgaria and Greece, Romania, Serbia, Macedonia, Slovakia, Slovenia, Austria and other regional and national seismological data centres was implemented.

The first Bulgarian earthquake catalogue covering instrumental seismicity for the period 1981–1990 was published by Solakov et al. (1993). The next catalogue for the period 1991-2000 was elaborated by Botev et al. (2010). Both catalogues contain recalculated earthquake parameters and M_d (duration magnitude scale) magnitude estimates

The catalogue presented in our study is processed in the sense that duplicated events and quarry blasts are removed. The seismic clusters for-aftershocks and swarms are identified. A space-time magnitude dependent window that is proposed by Christoskov and Lazarov (1981) for the Balkan region is used for for-aftershock identification. Thus, the earthquake catalogue presented here includes 1024 shallow earthquakes while the number of independent events is 645. Furthermore, the estimation of the moment magnitude for the whole instrumental period (1981–2019), which is considered as the most reliable magnitude scale, was another scope of the present study. A comprehensive assessment of catalogue completeness indicates that no earthquake with magnitude 3.2 or greater has been omitted in the whole instrumental period (1981–2019).

Earthquake parameters

Data for earthquake catalogue were collected from the Seismological Bulletins of the Bulgarian seismological network (NOTSSI) for the period 1981-2019. At present (since 1981) the Bulgarian seismological network ensures reliable registration and high-quality information for earthquakes occurred in Bulgaria and surroundings.

Each earthquake in the compiled catalogue is specified by space-temporal, and magnitude parameters: T_0, φ, λ, h, M.

To assure a consistency in the locations, a software based on Geiger's method that is a version of the HYPO 71 - called DHYPO (Solakov, Dobrev, 1987) which is used in the seismological practice of Bulgaria is applied in the computation of earthquake focal parameters.

Data (in the compiled catalogue) are unified and standardized in accordance with requirements of the international seismological centres. The catalogue is processed in the sense that duplicated events and quarry blasts are removed, the foreshocks and aftershocks are identified, and uniform magnitude measure is estimated for each earthquake.

The present catalogue version comprises 1024 events, for which the spatial distribution is shown in Fig. 2. It is obvious from Fig. 2 that earthquakes spread throughout Bulgaria, except north-western part of the territory.

Significant concentrations of epicentres are observed in the south-western Bulgaria. In the cases of aftershock sequences, such as the ones of Strazhitza 1986 (central part of Northern Bulgaria), Valandovo 2009 (in the Northern Macedonia, close to Bulgaria-Greece border), and Sofia 2012 (central part of western Bulgaria), the expressed events clustering is observed.
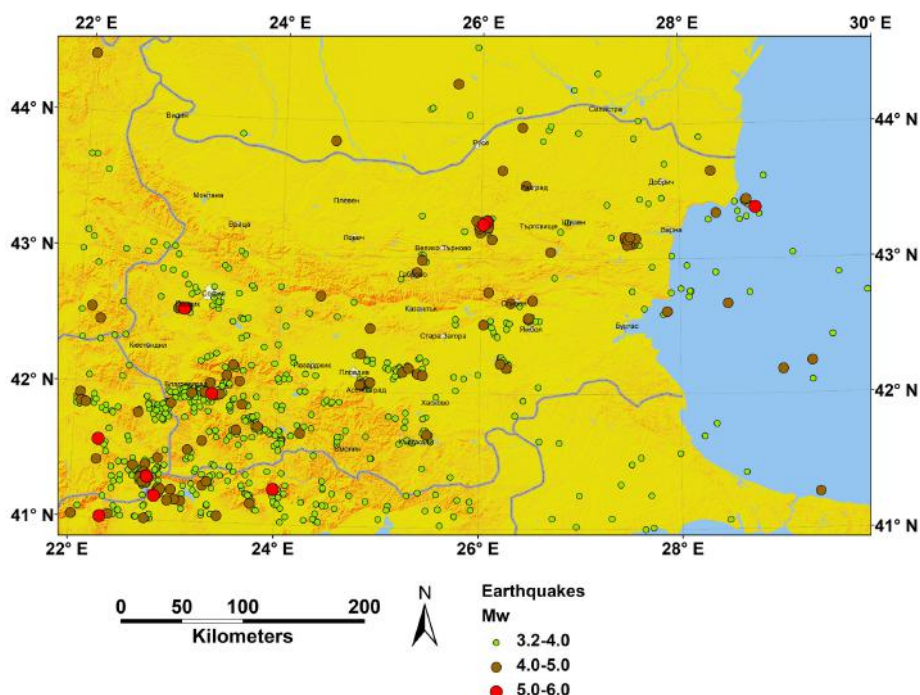
Figure 2. Spatial distribution of the epicentres of shallow earthquakes in Bulgaria and adjacent areas during the period 1981–2019

Frequency depth distribution of earthquakes is presented in Fig.3. The earthquakes in the considered region occurred in the Earth's crust up to 30 km. The hypocentres are mainly located in the upper crust (up to 20 km), and only a few events are related to the lower crust. The maximum density of seismicity involves the depth layer between 2 and 15 km. The strongest events are generated at the depth up to 15 km.

Harmonization of moment magnitude M_w
The moment magnitude M_w is considered by the worldwide seismological community to be the most reliable magnitude scale, since it is not saturated and

is not dependent on the frequency window. In order to obtain a homogeneous and reliable moment magnitude for the period 1981–2019, the M_w for events of the catalogue was calculated using empirical relations converting magnitudes expressed in magnitude scales (M_d and M_p) used in Bulgarian seismological routine practice to equivalent moment magnitudes (Solakov et al., 2018):

$$M_w = 1.09\,M_d - 0.05 \pm 0.26 \tag{1}$$
$$M_w = 0.93\,M_p + 0.31 \pm 0.19 \tag{2}$$

The catalogue presented in the present study was truncated at a moment magnitude of 3.2 in order to include as many small well-determined events as possible and thereby provide the best representation of the seismicity.
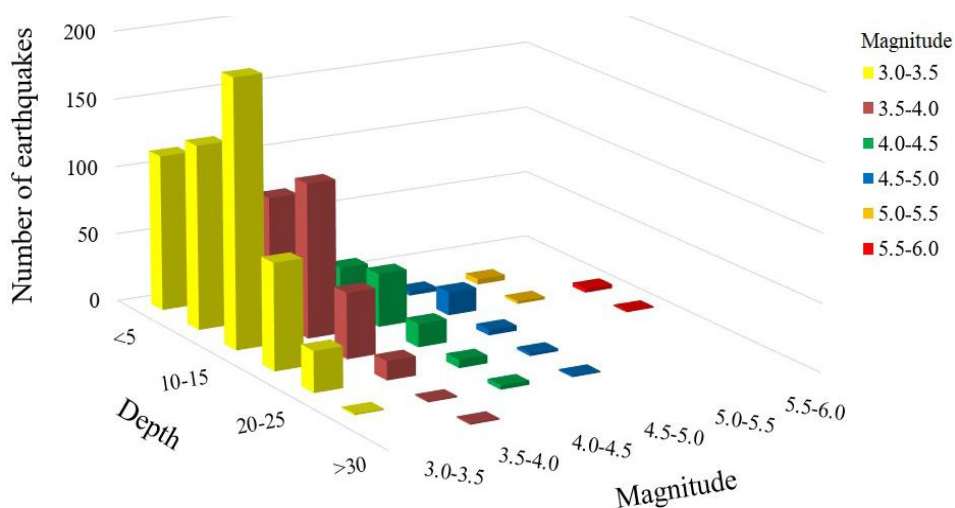
Figure3. Frequency depth distribution of shallow earthquakes occurred in Bulgaria and adjacent areas during the period 1981–2019

Completeness

A key requirement of any earthquake catalogue is to be as complete and homogenous as possible with respect to magnitude or other accepted earthquake parameter certainly down to a known threshold for a known time span. Data completeness and homogeneity is largely dependent upon availability and is governed by factors including the time interval in question, geographical region, and recording instrumentation used. Catalogue completeness is defined as the magnitude M_C above which is considered to be fully reported and is based on de clustered catalogue. Earthquake cluster identification within a catalogue involves separation of the independent background seismicity from dependent event sequences.

Window-based de clustering algorithm GKlb (Luen and Stark, 2012) is used in this study. The algorithm consists of the following: an event is in a given cluster if and only if it is in the window of at least one other event in the same cluster. In every cluster all events, except the largest, are removed. The Gardner and Knopoff (1974) space-time-magnitude window is applied. Additionally, earthquakes occurred far outside the network (e.g. in the Black sea at longitude more than 29° E) are excluded from the compiled data sample. The de clustered catalogue consists of 645 events.

Several methods exist that analyse catalogue completeness. The traditional method for estimation of the catalogue completeness uses the cumulative frequency-magnitude distribution of Gutenberg and Richter (1944, 1956). The *b*-value stability approach (MBS) presented in Woessner and Wiemer (2005) is applied for analysing the catalogue completeness. The magnitude M_C is defined as magnitude at which the following criteria are satisfied for the first time:

$$\Delta b(m) = | b_{ave} - b(m) | \leq \delta b(m) , \tag{3}$$

$$b_{ave} = \sum_{j=1}^{5} b(m + 0.1j)/5 , \tag{4}$$

$$\delta b(m) = 2.3 b(m)^2 \sqrt{\frac{\sum_{i=1}^{N}(M_i - \overline{M})^2}{N(N-1)}} , \tag{5}$$

where *b(m)* is *b*-value evaluation for magnitudes greater or equal to the cut-off magnitude *m*, N-number and $\overline{M}$ - mean magnitude of earthquakes with M ≥ m.

In Fig. 4 are presented the results that are obtained for the de clustered catalogue.
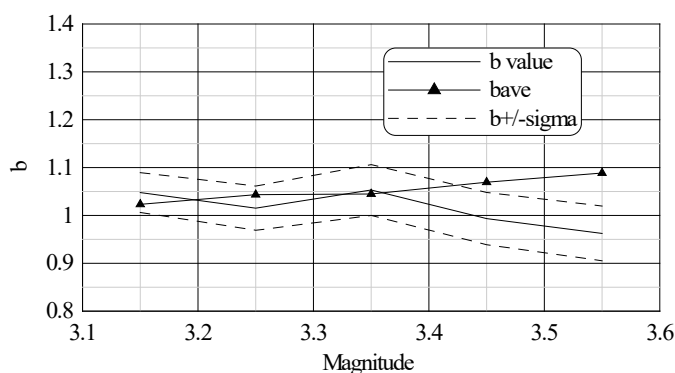
Figure 4. Plot of *b*, b_{ave} and the uncertainties δ*b* as a function of cut off magnitude *m* for the MBS approach

The results show that the catalogue could be considered complete for magnitude 3.2.

Poisson test of de clustered catalogues

Let a de clustered catalogue consist of n earthquakes in time interval *[0,T]* with origin times T_i {i=1,2,…,n}. If the earthquakes follow spatially inhomogeneous, temporally homogeneous Poisson process then the times T_i will be independent and identically distributed in time interval *[0,T]*. Two approaches are applied to test of the null hypothesis (H_0) that de clustered catalogue is a homogeneous temporal Poisson process realization: conditional chi-square test and Kolmogorov-Smirnov (KS) test (among others Luen and Stark, 2012).

Conditional Chi-square test

The time period of the catalogue is divided into 142 disjoint time intervals with length 100 days and the number of events in each interval is counted (Fig. 5). In Fig. 5 is shown the time of the strongest event in the catalogue.
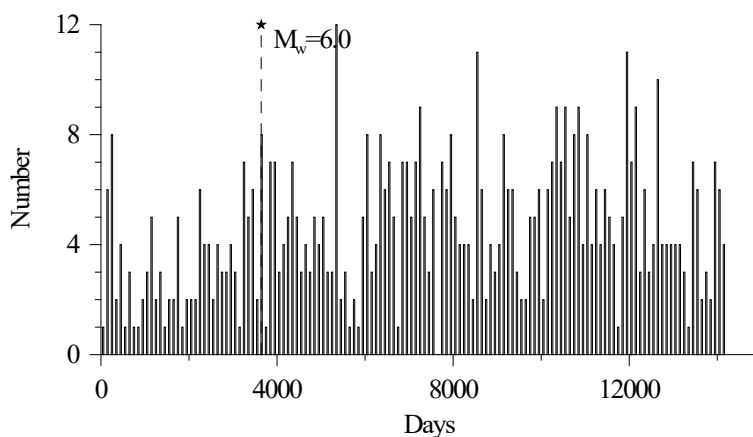
Figure 5. Earthquake number distribution in disjoint time intervals
with length 100 days

If the earthquakes follow Poisson process, then conditional on the number of events in the catalogue, the joint distribution of the numbers of events in the disjoint time windows will be multinomial with equal probabilities. The test statistic for our case is:

$$\chi_c^2 = \sum_{i=1}^{K} \frac{(N_i - \hat{\lambda})^2}{\hat{\lambda}},$$ (6)

where N_i is the number of events in the i-th time window, $\hat{\lambda}$ is theoretical rate of events per interval (estimated as n/K, K-number of intervals). If H_0 is true χ_c^2 will be approximately chi-square distributed with 141 degree of freedom. The Poisson hypothesis (H_0) is rejected for the whole catalogue. If we consider two sub catalogues (up to strongest event and after it) the Poisson hypothesis fail to reject - the probabilities of obtaining the sample result if the Poison hypothesis is true are 0.3 and 0.076 respectively. In Table 1 are presented the obtained results.

Table 1. Results for conditional chi-square test

Catalogue	Number of intervals	$\hat{\lambda}$	χ_c^2	Probability
Whole	142	4.53	185.83	0.007
Before the strongest event	36	3.14	38.96	0.300
After the strongest event	106	5	126.4	0.076

Kolmogorov-Smirnov test

The Kolmogorov–Smirnov test is a nonparametric goodness-of fit test and is used to determine whether two distributions differ. The Kolmogorov–Smirnov statistics quantifies a distance between the empirical distribution function of the sample and the cumulative distribution function of the reference distribution and is defined by:

$$D_n = \sup_t | \frac{\sum_{i=1}^{n} 1_{t_i \leq t}}{n} - \frac{t}{T} | \qquad (7)$$

where

$$1_{t_i \leq t} = \begin{cases} 1 & if \quad t_i \leq t \\ 0 & if \quad t_i > t \end{cases} \qquad (8)$$

The KS test rejects the H_0 if D_N is greater than or equal to a critical value $C(n,\alpha)$. In Table 2 are presented the obtained results.

Table 2. Results for KS test

Catalogue	Number of events	D_N	$C(n,0.01)$	$C(n,0.2)$
Whole	645	0.088	0.064	0.042
Before the strongest event	116	0.0939	0.15	0.01
After the strongest event	529	0.0369	0.071	0.047

The Poisson hypothesis (H_0) is rejected again for the whole catalogue while H_0 fail to reject for the two sub catalogues - $Dn<C(n,0.2)$.

Entries of the Bulgarian catalogue

The new earthquake catalogue for Bulgarian and adjacent areas that is here presented covers the instrumental period 1981–2019. The presented version of the catalogue comprises 1024 events, for which the spatial distribution is shown in Fig. 2 and Fig.3. After the data processing, selection, and harmonization check described above, the number independent tectonic earthquakes reduce to 645 events.

The Bulgarian catalogue (Solakov et al, 2020) is available at the home page of the National Institute of Geophysics, Geodesy and Geography [http://www.niggg.bas.bg] where the following information is given:

– Origin time in standardize GMT: Year, month, day, hour, minute and second;
– Epicentre coordinates: Latitude $\varphi°$ N and Longitude $\lambda°$ E;
– Focal depth in km;
– Estimated moment magnitude, M_W.
– Estimated epicentral/maximum intensity.

CONCLUSIONS

A new earthquake catalogue for the instrumental period has been compiled for Bulgaria and surroundings. The earthquake catalogue presented here includes 1024 shallow earthquakes while the number of independent events is 645.

The Bulgarian catalogue is processed in the sense that data have been filtered to remove duplicated events and quarry blasts within the catalogued region. Additionally, the clusters (fore-aftershocks and swarms) are identified.

Reported magnitudes for all 1024 events have been converted onto homogenized moment magnitude scale using magnitude conversion equations valid only for regional scale (Bulgaria and surroundings).

The completeness tests show that the catalogue is complete for moment magnitudes M_W larger than or equal to 3.2 for the last 39 yrs. and no earthquake with magnitude above 3.2 have been omitted in the whole instrumental period (1981-2019).

The hypothesis for temporally homogeneous Poisson process for the whole catalogue is rejected, while it fails to reject for the two sub catalogues (before and after the strongest event).

The new Bulgarian earthquake catalogue that is as accurate, homogeneous and complete as possible will be very useful for a more comprehensive assessment of seismic risk in the region

and Natural Disasters", approved by the Resolution of the Council of Ministers № 577/17.08.2018 supported by the Ministry of Education and Science of Bulgaria (Agreement № ДО-230/06-12-2018.

REFERENCES

Botev E., Glavcheva R., Babachkova B., Velichkova S., Tzoncheva I., Donkova K. (2010). Bulgaria Catalogue of Earthquakes 1981-1990. *Mining activity and Geology*, 5-6, 39-42, (in Bularian).

Christoskov, L., Lazarov R. (1981). General considerations on the representativeness of the seismological catalogues with a view to the seismostatistical investigations. *Bulg.Geoph. J.*, 3, 58-72 (in Bulgarian).

Gardner, J. K. and Knopoff L. (1974). Is the sequence of earthquakes in Southern California, with aftershocks removed Possionian? *Bull. Seis. Soc. Am.*, 64(5) 1363-1367.

Gutenberg, B. and Richter, C. (1944). Frequency of Earthquakes in California, *Bull. Seism. Soc. Am.*, 34, 185–188.

Gutenberg, B. and Richter, C (1956). Magnitude and energy of earthquakes, *Ann. Di. Geof.,* 9, 1–15.

Luen, B., Stark Ph. (2012). Poisson tests of declustered catalogues, *Geophys. J. Int.* 189, 691–700

Solakov D., Dobrev Tch., (1987). Program for earthquake parameters determination. *BGJ*, 13, 4 (in Bulgarian).

Solakov, D., Simeonova S. (Editors) (1993). Bulgaria Catalogue of Earthquakes 1981-1990, BAS, Geoph.Inst., Seism.Dep., Sofia, pp 39.

Solakov D., Simeonova S., Raykova P., Aleksandrova I. (2018). Empirical rlations converting Md and Mp magnitudes applied in Bulgarian seismological routine practice to moment magnitude. *Comptes rendus de l'Acad´emie bulgare des Sciences*, 71, 8, 2018, DOI:10.7546/CRABS.2018.08.09, 1076-1085.

Solakov D., Simeonova S., Raykova P., Aleksandrova I. (2020). Catalogue of the earthquakes in Bulgaria and surroundings since 1981, Funds NIGGG-BAS, https://doi.org/10.34975/ctlg-2020.v.1

Watzov Sp. (1902). *Earthdquakes in Bulgaria during XIX century*. Central Meteor. St., Imprimerie de L'Etat, Sofia, p. 93 (in Bulgarian and French)

Woessner, J., Wiemer St. (2005). Assessing the Quality of Earthquake Catalogues: Estimating the Magnitude of Completeness and Its Uncertainty. *Bulletin of the Seismological Society of America*, Vol. 95, No. 2, pp. 684–698.

✉ **Dimcho Solakov**
http://orcid.org/0000-0003-4148-0525
National Institute of Geophysics, Geodesy and Geography
Bulgarian Academy of Sciences
Sofia, Bulgaria
E-mail: dimos@geophys.bas.bg

✉ **Stela Simeonova**
National Institute of Geophysics, Geodesy and Geography
Bulgarian Academy of Sciences
Sofia, Bulgaria
E-mail: stelas@geophys.bas.bg

✉ **Plamena Raikova**
National Institute of Geophysics, Geodesy and Geography
Bulgarian Academy of Sciences
Sofia, Bulgaria
E-mail: plamena.raikova@gmail.com

✉ **Irena Aleksandrova**
National Institute of Geophysics, Geodesy and Geography
Bulgarian Academy of Sciences
Sofia, Bulgaria
E-mail: i.alex@abv.bg

Natural Hazards
and Risks

AGGREGATED TSUNAMI SCENARIO
FOR KARPATHOS ISLAND

Lyuba Dimova[1], Reneta Raykova[1], Alberto Armigliato[2],
Gianluca Pagnoni[2], Stefano Tinti[2]
[1]Department of Meteorology and Geophysics, Faculty of Physics,
"St. Kliment Ohridski" University of Sofia
[2]Sector of Geophysics, Department of Physics and Astronomy,
University of Bologna – Bologna, Italy

Abstract: Karpathos is the second largest of the Greek Dodecanese islands. Historical data such as the event of 9 February 1948, indicate that this area is prone to earthquakes and tsunamis. In this study we evaluate the tsunami hazard for the Karpathos Island by means of a scenario-based technique. We take into account tsunamis generated by three main seismic sources in agreement with local tectonics and historical records. The code UBO-TSUFD is used for all numerical simulations. Tsunamis are computed in several domains with different resolution for a better calculation of the maximum coastal wave height and tsunami inundation. Tsunami parameters for each individual scenario are used to construct a unique aggregated scenario, which help us to evaluate the inundation zone. The contribution of all scenarios along the coast of Karpathos is studied via synthetic mareograms. It is found that EHA dominates and that the southern Karpathos is more exposed to tsunamis.

Keywords: tsunami, scenario-based tsunami technique, seismic sources, UBO-TSUFD, Karpathos Island.

INTRODUCTION

The Aegean region include a large part of Greece and Turkey and is characterized by high seismic activity. The zone where subduction is predominant is the so-called Hellenic Arc, where the African Plate submerged beneath the Aegean microplate by approximately 10 mm/yr. In particular Karpathos Island is situated in the southern part of the Aegean Sea near the boundary of tectonic plates and volcanic arcs. This leads to a variety of the mechanism for the generation of tsunami: earthquakes, landslides and volcanic eruptions. Historically documented tsunamis in the region of the southern Aegean Sea and Karpathos Island are reviewed in the following papers (Dimova & Raykova, 2016; Papadopoulos et al., 2014). The region experienced devastating earthquakes and tsunamis throughout history like the events in 365

A.D., 1303 A.D. and more recently the earthquake in 1956, when tsunami initial waves are estimated in the range between 10 and 30 meters (Galanopoulos, 1957; Ambraseys, 1960). The earthquake and the followed tsunami in 1948 are not well studied yet. Ebeling et al., (2012) explored the hypothesis for combined generation mechanism – earthquake and underwater slide.

In this study we simulate tsunamis generated by seismic sources in the vicinity of Karpathos Island: one placed near Crete in the Eastern Hellenic Arc (EHA), with reference to the 1303 A.D., Mw=8.0 event), another near Rhodes (hypothetical scenario earthquake, Mw=7.3), and one near the coast of Karpathos, based on the 1948, Mw=7.3 earthquake. We are focused on the southern part of the island (Karpathos, Arkasa and the Airport) since the slopes to the north are very steep and inundations are not expected.

THE TSUNAMI SIMULATION METHOD AND RESULTS
Computational grids
Tsunami simulations are carried out in four grids with different resolution in order to evaluate the maximum wave elevation and the inundation zone. Characteristics of the computational grids are presented in Table 1. The outer grid (G1) includes the eastern part of Crete, the islands of Karpathos and Rhodes and the southeastern Aegean Sea. The smaller grid G2 covers the area of Karpathos Island. Grid 3 and Grid 4 are located in the southern part of Karpathos with focus on the city of Arkasa, the Airport and the city of Karpathos. Figure 1 illustrates the position of the grids. The bathymetry and topography data is compiled by different resolution data sets (GEBCO, SRTM, EMODNET).

Table 1. Characteristics of the used grids

Grids	Easting (m) (UTM 35 zone)	Northing (m) (UTM 35 zone)	Spatial resolution (m)	Time step (s)	Nodes in X direction (counts)	Nodes in Y direction (counts)	Total number of nodes (counts)
G1	314500-685500	3706500-4097000	500	1.0	743	782	581026
G2	470200-539700	3900200-3979700	100	0.2/0.25	696	796	554016
G3	505340-517340	3916240-3927840	20	0.1	601	581	349181
G4	517540-520740	3928940-3932840	20	0.125	161	196	31556

Generation of tsunamis
In order to model a tsunami generated by an earthquake, the displacement over the fault plane has to be transformed into deformation of the seafloor. Usually this

procedure can be done using the method proposed by Okada (Okada, 1985). Okada presents a complete set of solutions for each point source as well as for each finite rectangular fault for any depth and dip angle. The focal mechanism is the most important parameter by which the fault geometry is determined and by which we can draw conclusions about the stress regime in a given region. The geometry and the focal mechanisms of the modelled events are given in Table 2. The results from the Okada`s model are the initial conditions for the propagation of tsunami.

Table 2. Source parameters

	EHA (8 August 1303)	Karpathos (9 February 1948)	Rhodes (hypothetical)
L (km)	125	50	50
W (km)	50	23	23
Strike (°)	268	210	328
Dip (°)	48	60	73
Rake (°)	71	115	71
Slip (m)	6	3.2	3.2
UBD* (km)	4	2	3
UBMP**	(415550, 3819090)	(529004, 3934086)	(652446, 4029658)
Mw	8.0	7.3	7.3

*UBD – Upper Border Depth; **UBMP – Upper Border Middle Point (UTM 35 zone)

The initial sea surface elevations are plotted in Figure 1. The minimum and maximum values are in the range between -0.5 and 3.3 m. The fault models are taken to be in accordance with the results obtained in several papers (Dimova, 2018; Ebeling et al., 2012; Yolsal & Taymaz, 2012). The strike angle for Karpathos scenario is oriented to maximize the effects towards the island of Karpathos.

Propagation of tsunamis

UBO-TSUFD (University of Bologna – TSUnami Finite Difference) code is used to model the propagation of tsunamis and the interaction of waves with shores. The model was developed at the University of Bologna (Italy) by the working group of prof. Stefano Tinti (Tinti & Tonini, 2013). The theory of the propagation of tsunami waves is based on two equations: the continuity equation (mass conservation law) and the moment conservation equation, as well as appropriate boundary conditions. UBO-TSUFD resolves Navier-Stokes equations in approximation of shallow water theory by the finite difference technique through explicit leap-frog scheme. Discretization in space is in Cartesian coordinate system. After implementation of the model we get the propagation field; the field of maximum elevation; the maximum particle velocity field and the water column on land.

The tsunami propagation field from EHA source shows that in 12 minutes the waves reach Karpathos Island. The scenario referred to 1948 indicates that in case of tsunami due to this source the evacuation time for the eastern and southeastern coastal zone of Karpathos is less than 5 minutes. The first positive waves generated by Rhodes hypothetical source reach the eastern part of Karpathos after 20 minutes. Mainly the radiation pattern is focused between Rhodes Island and Turkey.

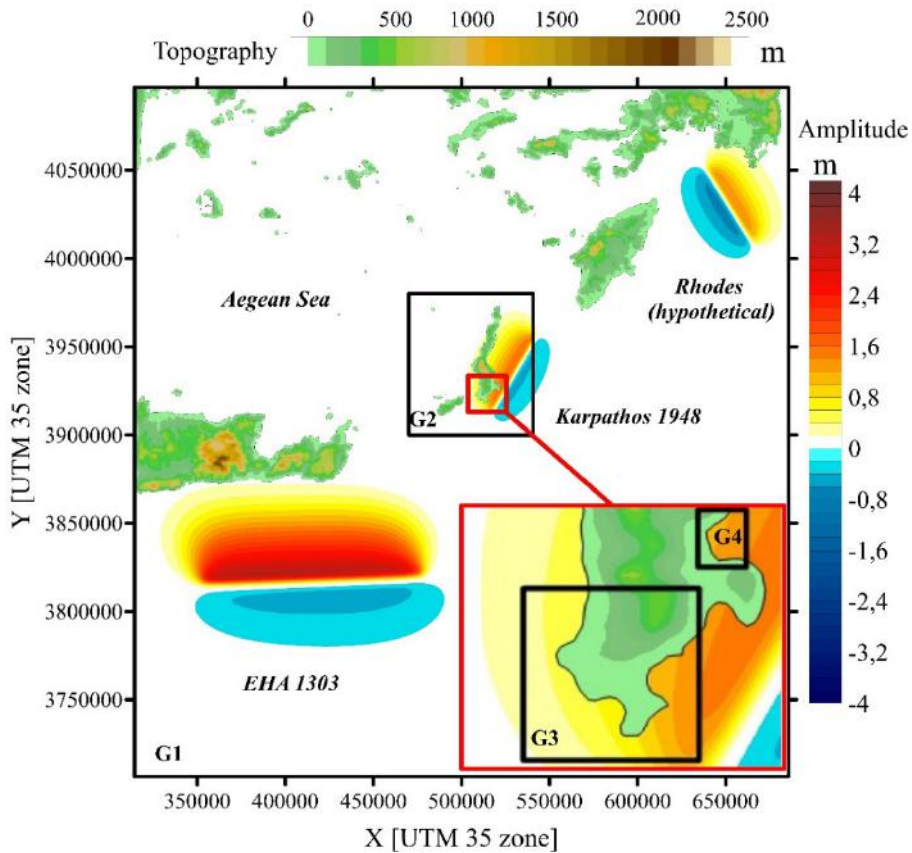**Figure 1.** Position of the grids and initial sea surface elevations for the three sources.

EHA scenario contributes mostly for the southwestern part of the island. The most affected areas from potential tsunami for this source are the city of Arkasa and the Airport. Large part of the tsunami energy is concentrated towards southeastern Crete. Karpathos tsunamigenic source distributes its maximum energy towards the

eastern and southeastern parts of the Karpathos Island. Potentially threatened areas due to tsunami are Karpathos (the capital), Lakki and the eastern side of the Airport. Both of the sources generates maximum elevations around 5 m. Rhodes hypothetical scenario has insignificant impact on the coasts of Karpathos with positive waves less than 2 m. Nevertheless, this source is located close to zones with high seismicity, therefore tsunamis are expected.

Synthetic mareograms

The evolution of the tsunami in time is clearly seen through synthetic mareograms. Figure 2 illustrates the first two hours of the amplitude dynamic of the tsunamis due the three sources. The position of the five mareograms is shown in Fig. 3b. For Arkasa and the Airport EHA source dominates with long period amplitudes between 5 and 10 minutes. Minimum and maximum elevations generated by Karpathos and Rhodes sources for these points vary in the range -1 and +1 meter. For Lakki, Karpathos (north) and Karpathos (south) the leading first positive wave is induced by Karpathos source and it is followed by a negative drop, around 5 m in particular at mareogram Karpathos (north). In addition
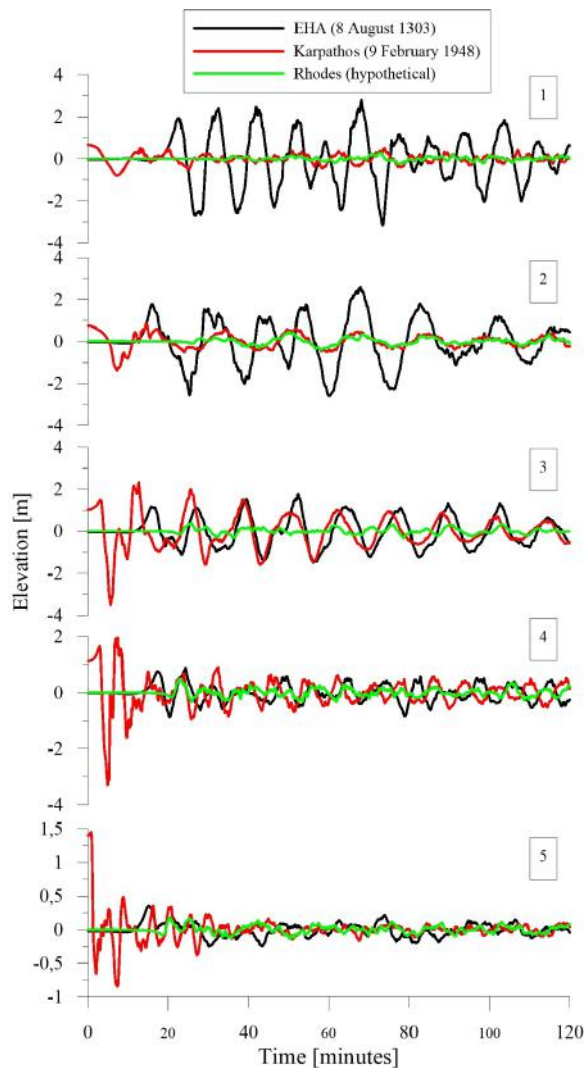

Figure 2. Synthetic Mareograms: 1. Arkasa; 2. Airport; 3. Lakki; 4. Karpathos (north); 5. Karpathos (south).
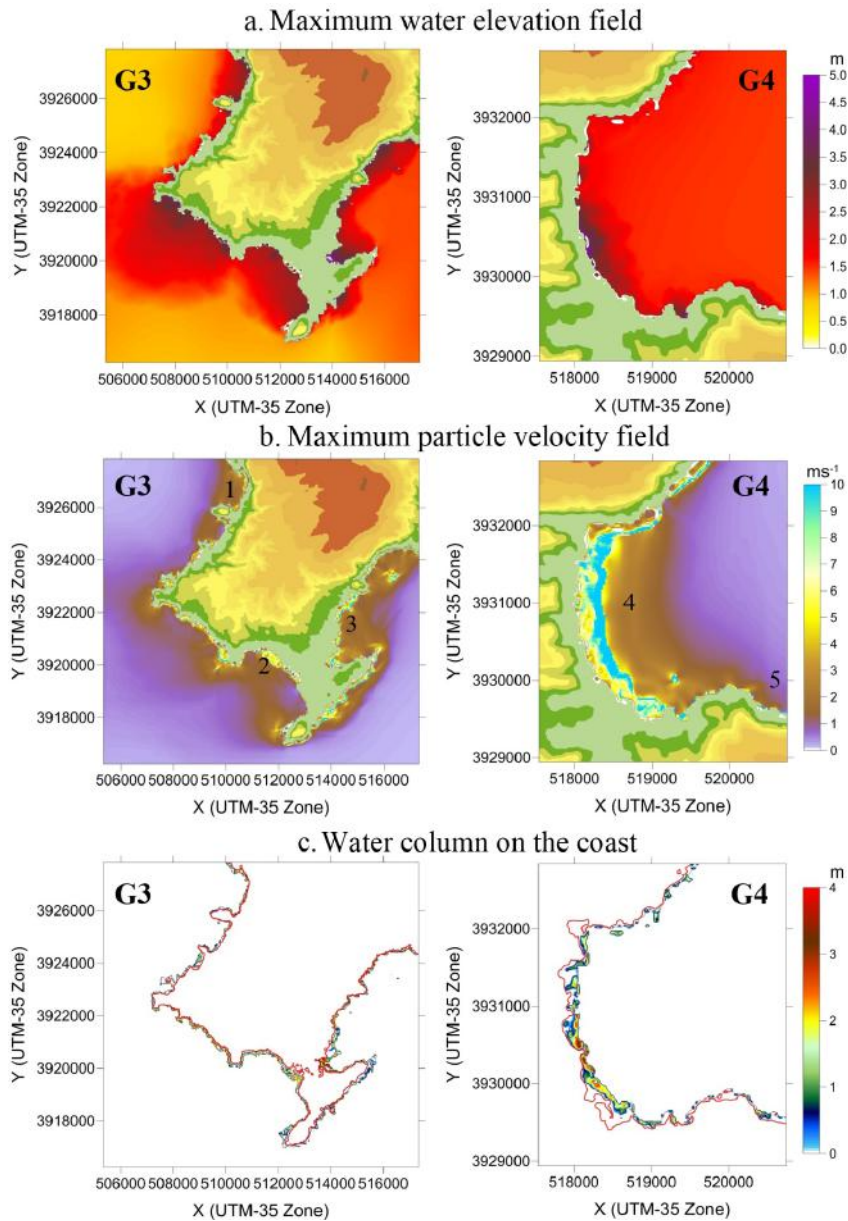
Figure 3. Aggregated tsunami scenario: a. Maximum elevation field;
b. Velocity field. Inserted numbers present the location of mareograms;
c. Water column on the coast.

the recession of the sea is seen around 5 to 10 minutes after the earthquake, which is confirmed by eyewitnesses (Papadopoulos et al., 2007). Rhodes hypothetical source creates insignificant sea disturbances compared to the other two sources. Due to the closeness of the tsunamigenic sources EHA and Karpathos, the time for evacuation of the population is extremely short.

AGGREGATED TSUNAMI SCENARIO

The results obtained for the three individual scenarios are combined in order to construct the procedure known as aggregated tsunami scenario. The extreme value reached in every single node of the grid is selected to build the maps presented in Figure 3. These values could be the highest or the lowest computed for an individual scenario.

The upper panel illustrates the aggregated maximum water elevation field zoomed for G3 and G4. The elevation varies between 2.5 m and 5 m. Higher values are expected near Arkasa, the Airport, Lakki and the capital. The steep cliffs on the western segment between Arkasa and the Airport act like a natural barrier for the waves. On the other hand the eastern part, where Karpathos is situated, is more exposed to tsunami, due to the planar beach. In addition, the bathymetry becomes shallower, evidently seen from the maximum particle velocity field depicted in Fig. 3b.

Zooming on the southern part of the island it is seen that the bay of Karpathos, Arkasa and the Airport are flooded while the northern and northwestern parts of the island remain unaffected by the tsunamis. The red line in Fig. 3c mark out the 5 meter isoline above the sea. The water column over Karpathos Airport is computed in the range between 1 m and 2 m. Tsunami waves penetrate in the capital of Karpathos to a maximum level around 4 m.

CONCLUSIONS

Destructive tsunamis in this area are not so frequent events, but their tsunamigenic potential is high, since the region lies between a subduction zone to the south and a volcanic arc to the north. Therefore, numerical simulations of tsunamis are extremely important to evaluate tsunami hazard, especially in areas where the historical information is insufficient. In this work we assess the tsunami hazard on the coasts of Karpathos by means of an aggregated scenario. The results show that the EHA source, referred to the 1303 AD event has a maximum tsunami impact on the southern part of the island, whereas the Karpathos source (reference event 1948) affects mostly the eastern coastline. Most of the numerical methods underestimates the observed tsunami waves. Nevertheless secondary effects like underwater landslides must not be excluded in the generation of tsunamis. Indeed such complex events could increase significantly the expected maximum tsunami heights.

REFERENCES
Ambraseys, N. (1960). The seismic sea-wave of July 1956 in the Greek archipelago. *Journal of Geophysical Research*, 65 (4), 1257–1265.

Dimova, L. (2018). Tsunami radiation pattern in the southern Aegean Sea. *Annual of Sofia University "St. Kliment Ohridski", Faculty of Physics*, v. 111, 23-40.

Dimova, L. & Raykova, R. (2016). Observations and modeling of tsunamis in the Eastern Mediterranean (review). *Annual of Sofia University "St. Kliment Ohridski", Faculty of Physics*, v. 109, 24-41.

Ebeling, C., Okal, E., Kalligeris, N. & Synolakis, C. (2012). Modern seismological reassessment and tsunami simulation of historical Hellenic Arc earthquakes. *Tectonophysics*, 530-531, 225-239.

Galanopoulos, A. (1957). The seismic sea-wave of 9 Iouliou 1956. *Praktika Academy Athens*, 32, 90–101 (in Greek with Engl. abstr.).

Okada, Y. (1985). Surface deformation due to shear and tensile faults in a half-space. *BSSA*, 75, 4, 1135-1154.

Papadopoulos, G., Dashkalaki, E., Fokaefs, A., Giraleas, N. (2007). Tsunami hazards in the Eastern Mediterranean: strong earthquakes and tsunamis in the east Hellenic Arc and trench system. *Nat. Hazards Earth Syst. Sci.*, 7, 57–64.

Papadopoulos, G.A., Gràcia, E., Urgeles, R., Sallares, V., De Martini, P.M., et al., (2014). Historical and pre-historical tsunamis in the Mediterranean and its connected seas: Geological signatures, generation mechanisms and coastal impacts. *Marine Geology*, 354, 81-109.

Tinti, S. & Tonini, R. (2013). The UBO-TSUFD tsunami inundation model: validation and application to a tsunami case study focused on the city of Catania, Italy. *Nat. Hazards Earth Syst. Sci.*, 13, 1759-1816.

Yolsal-Cevikbilen, S. & Taymaz, T. (2012). Earthquake source parameters along the Hellenic subduction zone and numerical simulations of historical tsunamis in the Eastern Mediterranean. *Tectonophysics*, 536-537, 61-100.

✉ **Lyuba Dimova**
https://publons.com/researcher/AAF-6356-2019/
Department of Meteorology and Geophysics
Faculty of Physics
"St. Kliment Ohridski" University of Sofia
Sofia, Bulgaria
E-mail: lyuba_dimova@phys.uni-sofia.bg

✉ **Reneta Raykova**
https://publons.com/researcher/ABC-4630-2020/
Department of Meteorology and Geophysics
Faculty of Physics
"St. Kliment Ohridski" University of Sofia
Sofia, Bulgaria

✉ **Alberto Armigliato**
https://publons.com/researcher/D-8817-2012/
Sector of Geophysics
Department of Physics and Astronomy
University of Bologna
Bologna, Italy
alberto.armigliato@unibo.it,

✉ **Gianluca Pagnoni**
https://publons.com/researcher/I-6497-2012/
Sector of Geophysics
Department of Physics and Astronomy
University of Bologna
Bologna, Italy

✉ **Stefano Tinti**
https://publons.com/researcher/E-2745-2014/
Sector of Geophysics
Department of Physics and Astronomy
University of Bologna
Bologna, Italy

STATISTICAL ASSESSMENT
OF ANNUAL MAXIMUM DAILY PRECIPITATION
OVER BULGARIA IN THE PERIOD 1892-2018

Krastina Malcheva, Tania Marinova, Lilia Bocheva
National Institute of Meteorology and Hydrology (NIMH)

Abstract: Annual maximum daily precipitation from 292 meteorological stations of the national meteorological network has been used to investigate the statistical properties of extreme precipitation in the period 1892-2018. The stationarity of time series has been examined for abrupt changes and slow variations by the non-parametric Pettitt and Mann-Kendall tests. The return levels of annual maximum daily precipitation for selected probabilities of exceedance have been assessed on the base of the best-fitted combination of probability distributions and parameters estimation methods for each of the time series.
Keywords: extreme precipitation, statistical modelling, return levels.

INTRODUCTION

The reliable assessment of the probabilities of extreme precipitation occurrence in the changing climate acquired great importance because of the significant and long-standing effect of these extremes on the ecological systems and many economic sectors. Annual maximum daily precipitation amount represents one of the most essential and comprehensible characteristics of extreme precipitation, frequently used in flood risk assessment (Field et al., 2012). The global analysis of instrumental records of this variable in recent decades is showing that at global or continental scales, extreme precipitation events are increasing in intensity and/or frequency in nearly two-thirds of meteorological stations (Westra et al., 2013).

Since the beginning of the 21st century, a significant number of extreme daily rainfall events have been registered in Bulgaria (especially in 2005 and 2014) that often led to considerable economic losses and human casualties. As a whole, the intra-annual variability of the maximum daily precipitation follows the peculiarities of the precipitation regime in the country. In the areas with a continental climate, the minimum of precipitation amounts occurs during the winter. The number of rainy days, as well as the cases of heavy rainfall, increase sharply in the second half of the

spring, with a clear peak of abundant rain in the early summer. In the second half of autumn, rainfalls are predominantly frontal. Precipitation totals increase with altitude, which is better expressed in the low and medium mountain parts and for north or northwest slopes. In the areas under a stronger Mediterranean influence, the maximum precipitation is observed in the second half of autumn and early winter, and daily quantities may exceed 100 mm. Although the precipitation amount and intensity decrease in the spring, there is a pronounced secondary rainfall maximum in early summer. Autumn is the rainiest season on the Black Sea coast.

The selection of suitable probability distribution functions and parameters estimation methods is essential in the at-site statistical analysis of extremes as the inappropriate choice could lead to significant error and bias in the estimated characteristic values, especially at lower exceedance probability (longer return periods). The aim of the present survey is to explore the available precipitation data from the beginning of meteorological observations in Bulgaria and determine the return levels of annual maximum daily precipitation for selected probabilities of exceedance, following a clear procedure of statistical processing. All statistical computations and scripts have been made using freely available R Software Version 3.6.2 (R Core Team, 2019) and RStudio Version 1.2.5033 (RStudio Team, 2019). The maps are created using the advanced tools for geostatistical analysis of ArcGIS 2.4 (Environmental Systems Research Institute, 2019).

DATA AND METHODS

Daily precipitation measurements in the meteorological network of the National Institute of Meteorology and Hydrology (NIMH) report the 24-hour precipitation amount from 7.30 h local time of the previous day to 7.30 h of the current day. All available historical daily precipitation data from the beginning of the respective measurements to the end of 2018 were inspected. Primary data control was performed, and the necessary corrections were done. The selection of stations for the present study was made in accordance with the common constraints for obtaining reliable statistical assessments: (1) at least 40 years of continuous observations, (2) no more of 10% missing data for the whole observational period, and (3) relatively evenly spatial distribution except mountainous areas where the meteorological network is sparse. Finally, 292 meteorological stations were selected (Fig. 1), and annual maximum daily precipitation amounts were determined for the whole observational period of each station.

The real length of time series (without gaps) varies between 40 and 127 years. Many of the statistical methods used in this study can be applied to incomplete data series provided that the gaps are randomly distributed and relatively small. Annual maximum daily precipitation time series (AMDP) that didn't satisfy these constraints were trimmed to the possibly longest observational period. The frequency distributions of AMPD length and maximum values are presented in
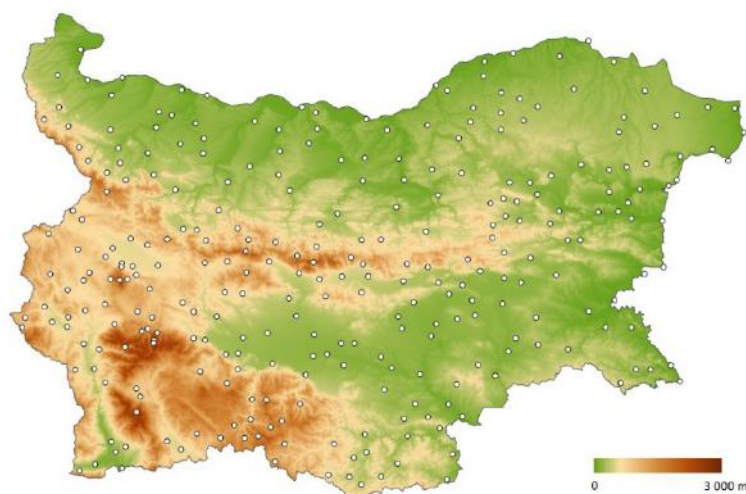
Figure 1. Spatial distributions of meteorological stations used in the study

Fig. 2. The absolute maximum of daily precipitation in the period 1892-2018 is 342 mm, measured in 1951 near Varna.
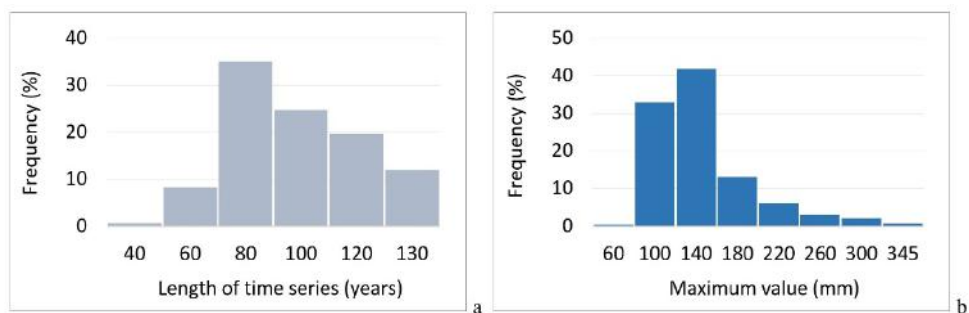
Figure 2. Frequency distributions of the length (a) and maximum values (b) of AMDP

Exploratory data analysis

Preliminary assessment of statistical behaviour of the annual maximum daily precipitation included detection of outliers and change points, calculation of descriptive statistics, and normality testing. Outliers are defined as values higher than $Q3 + 1.5IQR$, where $Q3$ and IQR are, respectively, the upper quartile and the interquartile range calculated for each time series. In Fig. 3 is shown the number of detected outliers on the background of the number of operating meteorological

stations by years. The increasing number of outliers since the end of 1990th is related to the climate variability of maximum daily precipitation in recent decades that confirmed the findings in Westra et al. (2013). Because outliers can severely influence the skewness and kurtosis of the samples, daily precipitation data were carefully examined to determine whether detected outliers are due to recording errors, or they are real observations.
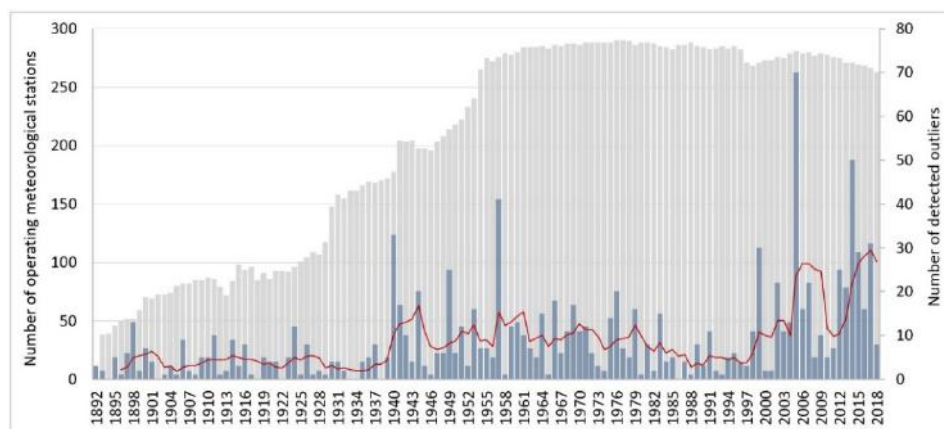
Figure 3. Number of detected outliers (grey columns) and 5-year moving average (red line) on the background of the number of operating meteorological stations (light grey columns) by years

Fig. 4 illustrates the frequency distributions of the basic statistics of AMDP. All time series are positively skewed (right-tailed towards the higher precipitation amounts) with kurtosis between –0.3 and over 50. About 5% of medians and 65% of Q3-values represent heavy, potentially dangerous, precipitation ($\geq$60 mm/24 h) as stated in Alpert et al. (2000) and Tsonevsky et al. (2010); a similar threshold also is used in the forecasting of dangerous weather events in NIMH according to the METEOALARM alerting protocol. The correlation between AMDP statistics and the altitude, latitude and longitude is not statistically significant. The AMDP quartiles show a common tendency to increase with altitude, as well as in the north-south and west-east directions.

Faragó & Katz (1990) underline that the sampling conditions (homogeneity, independence, sample size) affect the accuracy of approximations for extreme climate events based on extreme value theory, so this approach is most readily useable for large, homogeneous, stationary samples. If the patterns of long-term variation of AMDP, supposed to be independent, identically distributed (i.i.d.) random variables, have not changed substantially over the observational period,
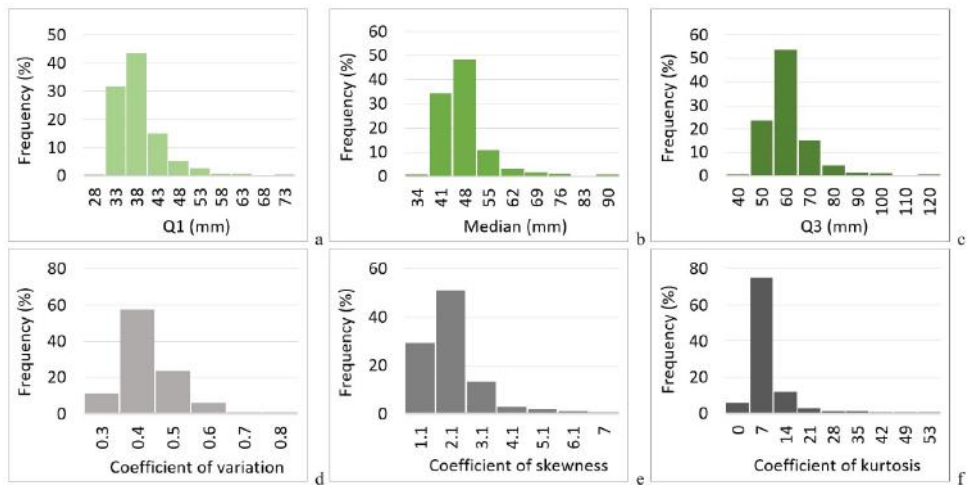
Figure 4. Frequency distribution of the first quartile Q1 (a), median
(b) and third quartile Q3 (c) values, coefficient of variation
(d), and coefficients of skewness (e) and kurtosis (f) of AMDP;
on the abscissa are shown values of the bins upper bound

the data were assumed as identically distributed and generated from independent observations. Homogeneity, stationarity, and independence of AMDP were tested using RHtestsV4 (Wang & Feng, 2013) and R packages' trend' (Thorsten, 2020) and 'stats' (R Core Team, 2020). Pettitt's test is commonly applied to detect abrupt change-points in time series. The test is considered to be powerful and sensitive to all possible conditions resulting in stochastic ordering (Serinaldi & Kilsby, 2016). In about 10% of the time series were detected change-points at a 5% significance level. The non-climatic abrupt changes were tested by using the RHtestsV4 software in the mode "with reference series", which can detect multiple change-points in data series that may have zero-trend or a linear trend throughout the whole period of record and first-order autoregressive errors (Wang, 2008). RHtestsV4 confirmed the results after the Pettitt's test only for 12 stations with a relatively long period of observation. In these cases, the representative periods for statistical modelling of the annual maximum daily precipitation were selected as the longest homogenous parts of the respective samples.

The non-parametric Mann-Kendall test (Kendall, 1975) is widely used to detect monotonic trends in climate and hydrological data. The test, applied to the AMDP at a 5% level of significance, revealed more neutral or increasing trends. About 9% of time series showed a significant increase, and about 5% – a significant decrease of annual maximum daily precipitation (predominantly for stations in South-West

Bulgaria and mountainous areas). Sen's slope estimates of trend magnitude (Sen, 1968) range from –8.2 to 3.7 mm/decade, but for 75% of stations, these values fall in the interval from –1 to 1 mm/decade. The lower values are related to the shorter time series (Fig. 5).

Ljung and Box's test for serial autocorrelation, as described in the R package 'stats', revealed that 5% of the analyzed AMDP have a weak lag-1 autocorrelation at 95% confidence level. As autocorrelation can influence the significance of results after the Mann-Kendall test, the trend analysis was repeated after prior removal of autocorrelation from the series by trend-free-pre-whitening (R package 'modifiedmk'; Patakamuri & O'Brien, 2019). So far as this approach didn't have a substantial effect on the results, it was accepted that the autocorrelation could be ignored.
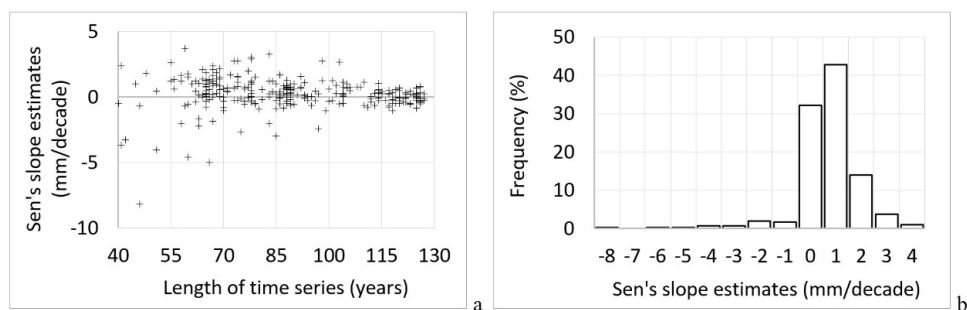
Figure 5. Scatter-plot of Sen's slope trend estimates against the length of time series (a) and frequency distribution of Sen's slope trend estimates (b)

Statistical modelling of annual maximum daily precipitation data

The empirical distribution functions allow the estimation of the probability of non-exceedance for each value of a given data sample, as well as the fitting of different theoretical distribution functions on the sample. If z_1, z_2, ..., z_m are the ordered block-maxima values, then the empirical distribution function evaluated at z_i can be established through Weibull plotting positions as:

$$\widetilde{G}(z_i) = \frac{i}{m+1}, \text{ where } i = 1, 2, ..., m \qquad (1)$$

This formula is known in the literature as unbiased regarding the probably exceedance of the plotting positions (Makkonen, 2006).

The generalized extreme value (GEV) distribution have been used as modelling frame to examine the extreme behaviour of annual maximum daily precipitation. It is the limiting distribution of normalized maxima of a sequence of independent and

identically distributed (i.i.d.) random variables (Coles, 2001) with the following cumulative distribution function:

$$G(z) = \exp\left\{-\left[1 + \xi\left(\frac{z-\mu}{\sigma}\right)\right]^{-1/\xi}\right\}, \tag{2}$$

where μ is the location parameter, σ is the scale parameter and ξ is the shape parameter. Different values of ξ lead to three types of extreme value distributions: (1) $\xi \to 0$ corresponds to the bounded Gumbel distribution, (2) $\xi > 0$ corresponds to the heavy-tailed Fréchet distribution, and (3) $\xi < 0$ corresponds to the light-tailed Weibull distribution. The flexibility of the GEV model makes it a key tool for a block-maxima method in the Extreme Values Analysis, including the cases of non-stationarity.

L-moments approach facilitates the estimation process in the analysis of extremes. L-moments are derived from Probability Weighted Moments (Hosking, 1989) and represent an alternative set of scale and shape parameters of a data sample or a probability distribution. They are less subject to bias in estimation and more robust to the presence of outliers in the data (Hosking, 1990). Asymptotic approximations to sampling distributions are better for L-moments than for ordinary moments. Let $X = \{x_1, x_2, \ldots, x_n\}$ be a given ordered sample. The unbiased estimator b_r is defined as a linear combination of ordered statistics:

$$b_r = \frac{1}{n}\sum_{i=1}^{n}\frac{(i-1)(i-2)\ldots(i-r)}{(n-1)(n-2)\ldots(n-r)}x_{i:n} \tag{3}$$

Unbiased sample estimators of the first four L-moments are obtained by:

$$\begin{aligned}
l_1 &= b_0 \\
l_2 &= 2b_1 - b_0 \\
l_3 &= 6b_2 - 6b_1 + b_0 \\
l_4 &= 20b_3 - 30b_2 + 12b_1 - b_0
\end{aligned} \tag{4}$$

L-coefficient of variation (L-Cv), skewness (L-Cs) and kurtosis (L-Ck) are defined as L-moments ratios t, t_3 and t_4 (Hosking, 1990):

$$\begin{aligned}
t &= l_2 / l_1 \\
t_3 &= l_3 / l_2 \\
t_4 &= l_4 / l_2
\end{aligned} \tag{5}$$

Selection of probability distributions and parameters estimation methods

L-moments ratio diagram provides a visual comparison of sample estimates of the dimensionless ratios L-Cs and L-Ck with their population equivalents, pre-

sented as lines for some widely used probability distributions (Hosking, 1990). Although this approach most often is used in the hydrological frequency analyses, there are many examples of its successful application in studies of climate extremes (e.g. Guttman, 1993; Dewar & Wallis, 1999; Khaliq et al., 2005). The inclusion of centred moving average of L-Ck against L-Cs in the diagram delineates a trace in the cloud of data-points that usually lies near to one of the theoretical distributions curves. Thus the common suitability of a given probability distribution can be easily assessed.

For evaluating the appropriateness of different probability distributions, the following goodness-of-fit tests were used: (1) Cramér-von Mises test (CVM), included in the R package 'lmomco' (Asquith, 2018) and (2) Akaike information criterion (AIC) – in the R package 'extRemes' (Gilleland & Katz, 2016). The R package 'gnFit' (Ali Saeb, 2018) was used to link the CVM test with the 'fevd' function in the R package 'extRemes' (instead of AIC) for achieving consistency with the test result from L-moments analysis. AIC test was applied for comparison of the suitability of stationary and non-stationary GEV models. Akaike (1973) has shown that choosing the model with the lowest expected information loss is asymptotically equivalent to choosing a model that has the lowest AIC value. Cramér-von Mises test is designed to assess the goodness of fit of a cumulative distribution function compared to a given empirical distribution function. For each time series, the best-fitted probability distribution was chosen based on the minimum values of CVM statistics (Laio, 2004). Many authors studied the power and robustness of Cramér-von Mises and Anderson–Darling statistics (e.g. Stephens, 1986; Choulakian & Stephens, 2001; Laio, 2004; Deidda & Puliga, 2006) when parameters of some widely used distributions are estimated by different methods, such as maximum likelihood and probability weighted moments.

Various Monte Carlo simulations to judge the performance of a certain combination of estimation method and probability distribution have been performed in Van Gelder (2000). The author points out that it is impossible to conclude which method (ordinary moments, L-moments, maximum likelihood, or Bayesian techniques) has the best performance, in general, and underlines the robustness of the L-moments method against "contaminated" data and its possibility defining selection criteria for a probability model. In the present survey, parameters of GEV distribution were estimated by using the methods of Maximum Likelihood (ML) and L-moments (LM), embedded in the respective R packages' extRemes' and 'lmomco'. Parameters of the other selected distributions were obtained by the LM method. The presence of significant non-stationarity in AMDP cannot be ignored when estimating characteristic values for long return periods (Milly, 2008). Following the concept described in Coles (2001), the recent version of R package 'extRemes' provides the possibility to set all three parameters of GEV distribution as time-dependent. In this study, the location parameter was assumed to be a linear function of time, while the scale and shape

parameters remain constant (i.e. the non-stationarity of daily precipitation extremes is represented only by the AMDP trend):

$$G(z_t) = \exp\left\{-\left[1 + \xi\left(\frac{z - \mu(t)}{\sigma}\right)\right]^{-1/\xi}\right\}, \quad \mu(t) = \mu_1 t + \mu_0 \tag{6}$$

where μ_0 is the initial threshold value, and μ_1 is the increment of the location parameter over time.

Several scripts (in R environment) were developed to facilitate the process of statistical modelling and determination of return levels with selected exceedance probabilities.

RESULTS

Among weather or climate variables, precipitation amount has the strongest evidence for a heavy tail, which can be evaluated by the likelihood ratio test for the shape parameter of the GEV distribution (Katz, 2002; Smith, 2001). The modelling of AMDP through the GEV distribution (using R package 'extRemes') showed that about 84% of the shape parameter (ξ) values fall in the interval 0.0-0.4 (with median 0.1), which set the focus of the study to the heavy-tailed distributions of exceedances and also is consistent with results in Serinaldi & Kilsby (2014).

The L-moments ratio diagram of all stationary AMDP allows a visual estimation of the range and variation of L-kurtosis and L-skewness (Fig. 6). The centred moving average of L-Cs vs L-Ck (with a window size of 21 points) outlined a trace close to the GEV distribution and partially to the GLO (generalized logistics) distribution. After assessing each of time series separately, it was found that PE3 (Pearson type 3) distribution shows a good fitting to the empirical data for a number of stations. Generally, GEV distribution is appropriate for modelling the statistical behaviour of AMDP because the bivariate median of the samples' skewness and kurtosis is consistent with the population equivalents of skewness and kurtosis of GEV distribution.

Cramér-von Mises goodness-of-fit test outlined the GEV distribution as suitable for statistical modelling of annual maximum daily precipitation in the highest number of stations (103 out of 292), the GLO distribution is the second (92 stations), and the PE3 distribution outperforms the other two in 53 cases. The non-stationary GEV model (with maximum likelihood estimation method) has been applied to 44 time series. The time span of the model was limited to the "immediate" future because it supposes the retention of a linear trend for μ outside the observational period. That can lead to a substantial prediction error, as far as the evolution of the climate system and precipitation regime, in particular, cannot be predicted unambiguously. As regard to stationary time series, the maximum likelihood method for estimating parameters of GEV distribution provided a better fit to the empirical data compared to the L-moments estimation method for 8 time series.
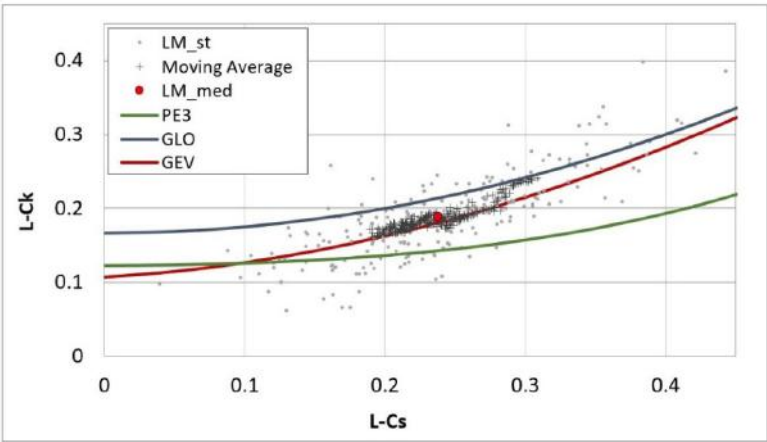
Figure 6. L-moments ratio diagram for all stationary AMDP (LM_st)
and the corresponding bivariate median (LM_med); GEV (Generalized
extreme value), GLO (Generalized logistic), and PE3 (Pearson type III)
distribution; Moving Average presents the averaging across LM_st by
a moving window with a size of 21 points.

The spatial distribution of the best-fitted combination of probability distributions
and parameters estimation methods for each AMDP is shown in Fig. 7. There
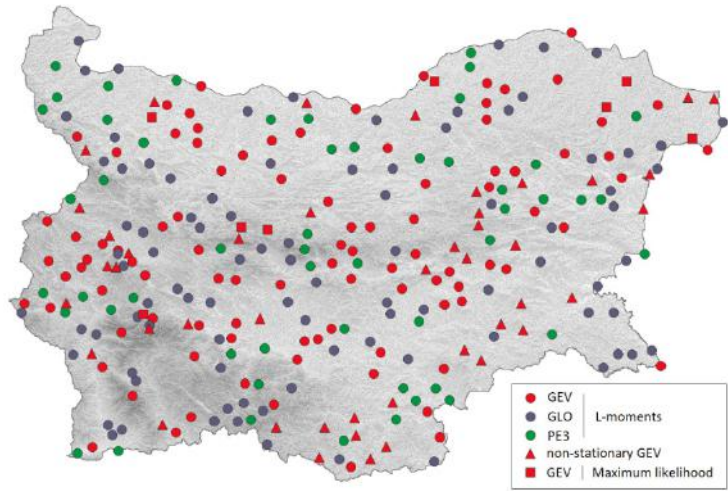
Figure 7. Spatial distribution of the best-fitted combination
of probability distributions and parameters estimation methods

is not observed strong dependence between the type of probability distributions and altitude, latitude, or longitude. The spatial patterns of GLO distribution or heavy-tailed GEV distribution can be associated with the large scale atmospheric circulation patterns over the Balkans, but also with local (spatially unevenly distributed) extremely high rainfall events. The non-stationary GEV distribution type occurred more frequently in Southern Bulgaria.

Fig. 8 displays the spatial distribution of 20-year and 100-year return levels of annual daily precipitation maxima, as well as the respective frequency distributions. The median of 20-year return level (or 5% probability of exceedance) is 79.5 mm, and for 100-year return levels (1% probability of exceedance) – 109.3 mm. The lower return level values prevailed in the central part of Western Bulgaria and upper part of Struma Valley, whereas the higher values are expected in the southern parts of the Rhodope Mountains, Strandzha region, the central part of Balkan Mountains, and the northern-most part of the Black Sea coastal region.
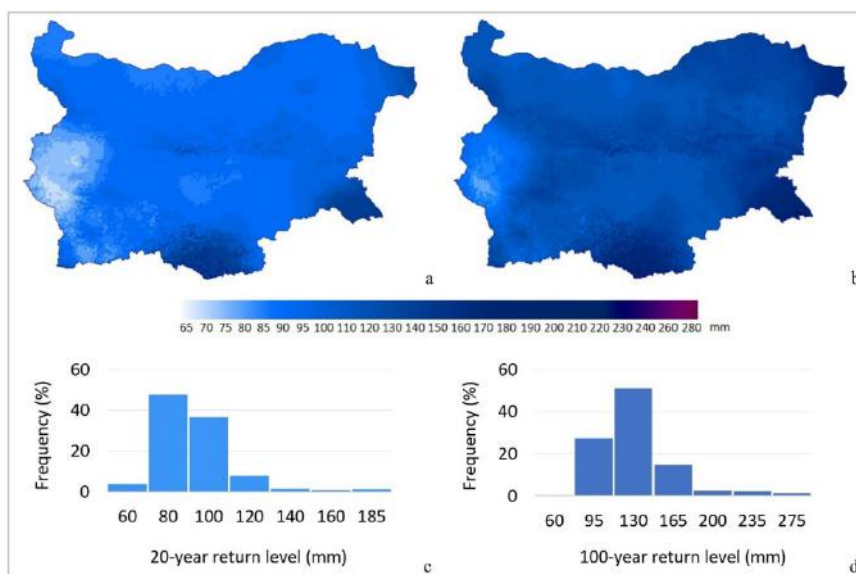
Figure 8. Spatial distribution of estimated 20-year (a) and 100-year (b) return levels of annual daily precipitation maxima, as well as the respective frequency distributions - (c) and (d)

CONCLUSIONS

A statistical assessment of annual maximum daily precipitation on the base of available historical precipitation data from the beginning of meteorological

observations in Bulgaria was made. After primary quality control and analysis of historical daily precipitation data, a total of 292 meteorological stations were selected. The analysis of annual maximum daily precipitation time series outlined some main statistical characteristics of extreme precipitation in the period 1892-2018.

• All time series are positively skewed. About 5% of medians and 65% of Q3-values represent potentially dangerous precipitation (≥60 mm/24 h).

• The increasing number of outliers since the end of 1990th is related to the climate variability of maximum daily precipitation in recent decades. In about 10% of the time series were detected change-points after Pettitt's test (at a 5% significance level).

• Mann-Kendall test revealed a significant increase (at a 5% level of significance) of annual maximum daily precipitation in about 9% of stations. A significant decreasing trend appeared in about 5% of stations, predominantly in South-West Bulgaria and mountainous areas.

• The presence of significant non-stationarity in AMDP cannot be ignored when estimating characteristic values for long return periods. The GEV distribution is very flexible for modelling different behaviour of extremes, including a non-stationarity.

• Modelling of annual maximum daily precipitation data through the GEV distribution showed that approximately 84% of the shape parameter (ξ) values fall in the interval 0.0-0.4 (with median 0.1), which corresponds to heavy-tailed distributions.

The spatial distribution of return levels of annual maximum daily precipitation with 1% and 5% probability of exceedance showed that lower values prevailed in the central part of Western Bulgaria and upper part of Struma Valley, whereas the higher values were expected for the southern parts of the Rhodope Mountains, Strandzha region, the central part of Balkan Mountains, and the northern-most part of the Black Sea coastal region.

REFERENCES

Akaike, H. (1973). Information theory and an extension of the maximum likelihood principle. In B. N. Petrov & F. Caski (Eds.), *Proceedings of the Second International Symposium on Information Theory*, 267-281.

Alpert P., Ben-gai T., Bahard A., Benjamini Y., Yekutieli D., Colacino M., Diorado L., Ramis C., Homar V., Romero R., Michaelides S. & Manes A. (2000). The paradoxical increase of Mediterranean extreme daily rainfall in spite of decrease in total values. *Geoph. Res. Letters*, 29 X-1- X-4

ArcGIS Pro Help (2019). *Environmental Systems Research Institute*. Red-lands, CA, https://pro.arcgis.com/en/pro-app/help/main/welcome-to-the-arcgis-pro-app-help.htm

Asquith, W.H. (2018). Package 'lmomco': L-moments, censored L-moments, trimmed L-moments, L-comoments, and many distributions. *Texas Tech University*, Lubbock, Texas, https://CRAN.R-project.org/package=lmomco

Choulakian, V., Stephens, M.A., 2001. Goodness-of-Fit Tests for the Generalized Pareto Distribution. *Technometrics*, 43, 478–484.

Coles, S. (2001). *An Introduction to Statistical Modelling of Extreme Values*. 2nd ed. Springer-Verlag, London.

Deidda, R. & Puliga, M. (2006). Sensitivity of goodness-of-fit statistics to rainfall data rounding off. *Physics and Chemistry of the Earth*, 31, 1240-1251.

Dewar, R. E. & Wallis, J. R. (1999). Geographical Patterning of Interannual Rainfall Variability in the Tropics and Near Tropics: An L-Moments Approach. *J. Climate*, 12, 3457–3466,

Faragó, T. & Katz, R. W. (1990). *Extremes and Design Values in Climatology*, Report No. WCAP-14, WMO/TD-No. 386, World Meteorological Organization, Geneva.

Field, C.B., Barros, V., Stocker, T.F., Qin, D., Dokken, D.J., Ebi, K.L., Mastrandrea, M.D., Mach, K.J., Plattner, G.-K., Allen, S.K., Tignor, M. & Midgley P.M., Eds. (2012). *Managing the Risks of Extreme Events and Disasters to Advance Climate Change Adaptation.* A Special Report of Working Groups I and II of the IPCC. Cambridge University Press, New York, NY, USA

Gilleland, E. & Katz R.W. (2016). extRemes 2.0: An Extreme Value Analysis Package in R. *Journal of Statistical Software*, 72(8), 1-39.

Guttman, N. B. (1993). The use of L-moments in the determination of regional precipitation climates. J. Climate, 6, 2309–2325

Hosking, J.R.M. (1989). *The Theory of Probability Weighted Moments*. Technical Report RC-12210, IBM Thomas J. Watson Research Center, Yorktown Heights, NY.

Hosking, J.R.M. (1990). L-moments: Analysis and Estimation of Distributions Using Linear Combinations of Order Statistics. *Journal of Royal Statistical Society (Series B)*, 52, 105–124.

Katz, R. W. (2002). Do weather or climate variables and their impacts have heavy-tailed distributions? 16th Conf. on Probability and Statistics in the Atmospheric Sciences, Orlando, FL, *Amer. Meteor. Soc.*, J3.5. [Available online at https://ams.confex.com/ams/annual2002/techprogram/paper_26949.htm.]

Kendall, M.G. (1975). *Rank Correlation Methods*. Charles Griffin: London, UK.

Khaliq, M.N., St-Hilaire, A., Ouarda, T.B.M.J. and Bobée, B. (2005). Frequency analysis and temporal pattern of occurrences of southern Quebec heatwaves. *Int. J. Climatol.*, 25: 485-504.

Laio, F. (2004). Cramer-von Mises and Anderson-Darling goodness of fit tests for extreme value distributions with unknown parameters. *Water Res. Res.*, 40, W09308.

Makkonen, L. (2006). Plotting positions in extreme value analysis. *J. Appl. Meteorol. Climatol*. 45, 334– 340.

Milly, P.C.D., Betancourt, J., Falkenmark, M., Hirsch, F.M., Kundzewicz, Z.W., Lettenmaier, D.R. & Stouffer R.J. (2008). Stationarity is dead: whither water management? *Science*, 319, 573–574

Min, S.K., Zhang, X., Zwiers, F.W., Friederichs, P. & Hense, A. (2009). Signal detectability in extreme precipitation changes assessed from twentieth century climate simulations. *Climate Dyn.*, 32, 95–111.

R Core Team (2019). R: A language and environment for statistical computing. *R Foundation for Statistical Computing*, Vienna, Austria. http://www.R-project.org/

RStudio Team (2019). RStudio: Integrated Development for R. *RStudio*, Inc., Boston, http://www.rstudio.com/

Patakamuri, S.K. & O'Brien, N. (2019). Package 'modifiedmk': Modified Versions of Mann Kendall and Spearman's Rho Trend Tests. https://CRAN.R-project.org/package=modifiedmk

Saeb, A. (2018). Package 'gnFit': Goodness of Fit Test for Continuous Distribution Functions. https://CRAN.R-project.org/package=gnFit

Sen, P.K. (1968). Estimates of the regression coefficient based on Kendall's tau. *Journal of the American Statistical Association*, 63, 1379–1389

Serinaldi, F. & Kilsby, C.G. (2014), Rainfall extremes: Toward reconciliation after the battle of distributions, *Water Resour. Res.*, 50, 336–352

Serinaldi, F. & Kilsby, C.G. (2016). The importance of prewhitening in change point analysis under persistence. *Stochastic Environmental Research and Risk Assessment*, 30(2), 763-777.

Smith, R.L. (2001). Extreme value statistics in meteorology and the environment. *Environmental Statistics*, Chapter 8, pp. 300–357.

Thorsten, P. (2020). Package 'trend': Non-Parametric Trend Tests and Change-Point Detection. R package version 1.1.2, https://CRAN.R-project.org/package=trend

Tsonevski I., Campins J., Genoves A. & Jansa A. (2010). Atmospheric patterns for heavy precipitation in Bulgaria. *Rom. Jour. of Meteor.*, 1, 1-12.

Van Gelder, P.H.A.J.M. (2000). *Statistical Methods for the Risk-Based Design of Civil Structures*, PhD thesis, Delft University of Technology

Wang, X.L. & Feng Y. (2013). RHtestsV4 User Manual. Climate Research Division, *Atmospheric Science and Technology Directorate*, Science and Technology Branch, Environment Canada. Available online at http://etccdi.pacificclimate.org/software.shtml

Wang, X.L. (2008). Accounting for autocorrelation in detecting mean-shifts in climate data series using the penalized maximal t or F test, *J. Appl. Meteor. Climatol.*, 47(9), 2423-2444.

Westra, S., Alexander, L.V. & Zwiers, F.W. (2013). Global Increasing Trends in Annual Maximum Daily Precipitation. *J. Climate*, 26, 3904–3918.

✉ **Krastina Malcheva**
https://orcid.org/0000-0003-0909-4237
National Institute of Meteorology and Hydrology
Sofia, Bulgaria
E-mail: krastina.malcheva@meteo.bg

✉ **Tania Marinova**
National Institute of Meteorology and Hydrology
Sofia, Bulgaria
E-mail: tania.marinova@meteo.bg

✉ **Lilia Bocheva**
National Institute of Meteorology and Hydrology
Sofia, Bulgaria
E-mail: lilia.bocheva@meteo.bg

EFFECT OF SAHARAN DUST INTRUSIONS ON PRECIPITATION CHEMISTRY IN BULGARIA

Emilia Georgieva, Elena Hristova, Blagorodka Veleva
National Institute of Meteorology and Hydrology (NIMH)

Abstract: The objective of this work is to investigate the influence of Saharan dust events on the chemical composition of rain samples collected at three sites in Bulgaria during 2017-2018. Saharan dust intrusions were identified through a combination of satellite retrieved aerosol data and results from dust forecasting models and from backward trajectory model. The chemical composition of the samples (acidity pH, conductivity EC, main ions and elements) is analysed in view of the direction of the approaching air masses – "direct" influence (south-west), and "indirect" influence from other directions and regions, already impacted by Saharan dust. All samples were characterised by elevated values of pH (max 7.4), EC (max 202 μS.cm^{-1}) and Si, Ca, Fe, Mg concentrations. For cases with direct influence Si and Ca values were up to 1.5 and 25 mg.l^{-1}. In most of the indirect cases increased concentrations of sulphate, nitrate and ammonium were observed (up to 39.5, 23.1 and 8.3 mg.l^{-1}).

Keywords: precipitation chemistry, Saharan dust, field campaigns, dust models, satellite AOD

INTRODUCTION

Sand and Dust Storms are recognized as hazardous meteorological events that impact the society in many ways – soil and agriculture, ecosystems, air quality and human health, aviation, visibility, solar power production and other socio-economical activities. These events present a unique form of natural hazard in that the source and the impact regions can be separated by great distances (Middleton et al., 2019). Mineral dust particles can be lifted by strong winds from bare dry soils into the atmosphere and being transported downwind affecting regions hundreds to thousand kilometers away. It is estimated that between 1000 and 3000 Tg of mineral dust is uplifted into the atmosphere annually, with Saharan desert being the largest global contributor (Prospero et al., 2002). The atmosphere of the Mediterranean Basin is highly influenced by the Sharan Dust intrusions, as two of the main transport paths of the emitted dust particles is northward to Europe, and eastward to Middle East (Goudie and Middleton, 2006).

The airborne dust particles are removed from the atmosphere by settlement (dry deposition) or are washed out by rains (wet deposition). The last mechanism is prevailing for fine grained particles and distances far-away from the source regions (Stuut et al., 2009). There are various effects of the deposited dust particles: they are capable of modifying the soil properties, can act as fertilizes in marine ecosystems (Maher et al., 2010) and can neutralize atmospheric acidity and reduce acid rains (Rogora e al., 2004).

Although Saharan dust events are detected with higher frequency in the Mediterranean countries and southern Europe, other northern and central parts of the continent are also influenced (Klein et al., 2010, Varga et al., 2013). The Balkans are not regarded as a dusty region, but the location in the so called D1B zone of the Saharan dust-fall map (Stuut et al., 2009) implies that Saharan dust can be incorporated in the soil system and change its structure.

The frequency of Saharan Dust outbreaks for Bulgaria is about 20% over annual days, as estimated by 10 years data for PM10 concentrations at the regional background station Rozhen (Pey et al., 2013). The maximum of Saharan outbreaks towards Bulgaria is in spring and autumn, as found in a recent study based on satellites data for the period 2005-2018 (Dimitrova et al., 2019). This study indicates that on average the days with Saharan outbreaks are 10-13 for the months March, April, May, and can be 20 and more for the same months in specific years. As in Bulgaria during spring also the precipitations are frequent, it could be expected that their chemical composition is influenced by Saharan dust. At the National Institute of Meteorology and Hydrology (NIMH) a monitoring network for acidity of precipitations has been established (Hristova, 2017). In the last years the chemical analysis of the rain water samples was extended (including main ions, macro and microelements) giving thus possibility to investigate also the characteristics of precipitation chemistry during Saharan dust outbreaks in the country.

The purpose of this study is to analyse the influence of Saharan dust on the chemical composition of rain samples collected at three sites in Bulgaria during field campaigns in 2017-2018. Another objective is to discuss precipitation chemistry in view of typical pathways of the dust loaded air masses.

METHODOLOGY

The procedures used for the collection of precipitation samples and their chemical analysis, as well as the methods applied for identification of Saharan dust intrusions are briefly outlined.

Precipitation samples and their chemical analysis

The collection of precipitation samples was organised during field campaigns in 2017-2018 at three meteorological stations located in different environment (Fig. 1). Two of the stations are in the western part of the country: urban one - Sofia-

NIMH (42.655 N, 23.384 E, 586 m asl), and a mountain one – peak Cherni Vruh (42.6167 N, 23.2667 E, 2286 m asl). The third station is rural one in southeast Bulgaria near the Black Sea coast - Ahtopol (42.084 N, 27.952 E, 26m asl). Daily precipitation samples in Sofia and Ahtopol were collected with an automatic wet only device (WADOS), at Cherni Vruh a passive bulk sampler was operated, made of polyethylene terephthalate funnel that was washed every day with deionized water to avoid dry deposition.

Figure 1. Geographical map of Bulgaria with sampling sites
(orange square – Sofia, blue triangle – Cherni vruh, red circle – Ahtopol)

The collected samples were further analysed for acidity-pH, conductivity-EC, main anions Cl^-, SO_4^{2-}, NO_3, cation NH_4^+ and elements Na, K, Mg, Ca, Fe, Si, Zn, Cu. More details and detection limits for the analysed elements are given in Hristova et al., 2020.

Identification of Saharan Dust intrusions

A combination of modelling results and observational data were used in order to identify the days characterised by Saharan dust outbreaks in Bulgaria in 2017 and 2018. For all the dates with available precipitation chemistry data at the three stations, an analysis was carried out, involving the following information:

a) Results for dust optical depth, dust surface concentrations, dust dry and wet depositions forecasted by the models at the Barcelona Supercomputing Centre (BSC) - BSC-DREAM8b (Basart et al., 2012) NMMB/BSC-Dust (Pérez et al., 2011), horizontal resolution 0.3° x 0.3°;

b) Results for aerosol optical depth and dust surface concentrations, forecasted by the ensemble model at the World Meteorological Organization Sand and Dust Storm Warning Advisory and Assessment System (WMO SDS-WAS) Regional Center for Northern Africa, Middle East and Europe on a grid with resolution 0.5° x 0.5°;

c) Results for the dust and total aerosol optical depth at 550nm, and PM10 concentrations forecasted by the global CAMS-ECMWF model (Benedetti et al., 2009), over Europe on a grid resolution 0.125° x 0.125°, available through the Copernicus Atmosphere Monitoring Service (CAMS);

d) Result for dust and PM10 over Europe by the CAMS regional air quality ensemble model, with horizontal resolution 0.1°x0.1° (Marécal et al., 2015);

e) Maps based on multi-model results at global scale with resolution 0.1°x0.1° at the Marine Meteorology Division of the Naval Research Laboratory, USA (NRL), (Xian P. et al., 2019);

f) HYSPLIT air mass backward-trajectories (Stein et al, 2015, Rolph et al., 2017) calculated at three arrival heights (500, 1500 and 3000m agl.) for 96 hours, using NCEP GDAS meteorological input with resolution 0.5° x 0.5°, and reanalysis data ;

g) Satellite data for AOD (level 3 MODIS Terra&Aqua globally on a grid 0.1° x 01°), for Aerosol absorbing index and Dust optical depth from MetOP satellites;

h) Observed particulate matter (PM10) concentrations at two background rural stations in mountain areas in BG – Kopitoto (BG0070A) and Rozhen (BG0053R).

RESULTS AND DISCUSSION
Selected dates and samples

The analysis of the origin of the dust loaded air masses indicated that the daily precipitation samples can be grouped into two main categories – with "direct" influence, i.e. approaching flow from southern directions, mainly from south-west, and with "indirect" influence, associated with other directions and respective regions, already impacted by Saharan dust. Table 1 presents details for the samples analysed in this study and the type of influence attributed to them.

Table 1. Date, location and type of influence for the precipitation samples used in this study, A- direct influence, B – indirect influence

No	Date	Sofia	ChVruh	Ahtopol	Type
1.	04.06.2017			+	A
2.	06.06.2017		+		A
3.	03.07.2017		+		B
4.	04.07.2017			+	B
5.	20.09.2017		+		A
6.	07.02.2018	+			A
7.	08.02.2018			+	A
8.	02.03.2018	+			A
9.	05.03.2018			+	A

10.	06.03.2018	+			A
11.	19.03.2018		+		A
12.	20.03.2018		+		A
13.	20.03.2018			+	A
14.	21.03.2018	+			A
15.	22.03.2018	+			A
16.	23.03.2018	+			B
17.	23.03.2018			+	B
18.	28.03.2018			+	A
19.	06.04.2018	+			A
20.	16.04.2018	+			A
21.	24.04.2018	+			B
22.	24.04.2018		+		B
23.	05.05.2018	+			B
24.	10.06.2018	+			B
25.	15.06.2018			+	B
26.	30.06. 2018		+		B

Examples for type A and type B of Saharan Dust outbreaks

Some of the analysed maps and precipitation chemistry data are shown as example for two cases for the types A and B influence of dust loaded air masses. The first case (16.04.2018) is characterized by Saharan flow from south-west (Fig. 2). The second case (30.06.2018) is a situation with north and north-westerly intrusion towards Bulgaria, but the regions in Central and Western Europe were impacted by Saharan dust few days before (Fig. 4). The chemical composition for precipitation samples for these cases is shown in Fig. 3 and Fig. 5.

a)   b)

c)   d)
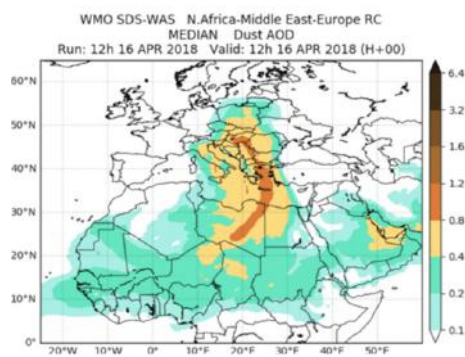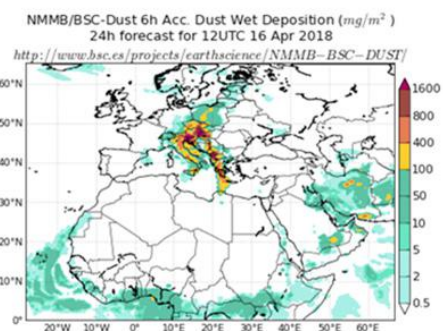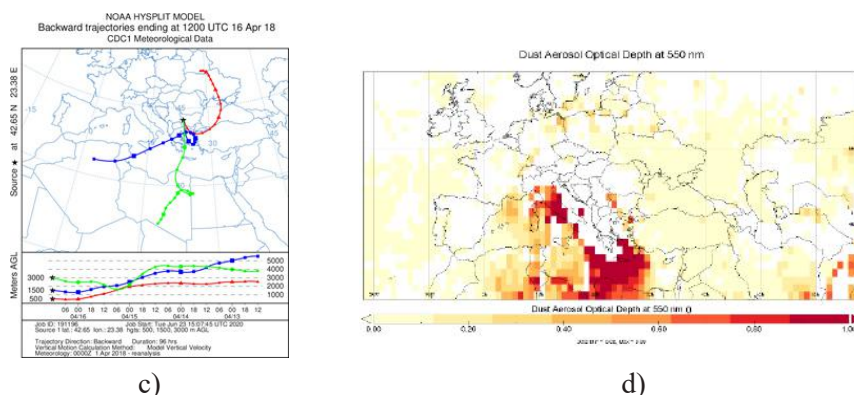
Figure 2. Case 16.04.2018 a) Dust AOD from SDS-WAS ensemble model;
b) Dust wet deposition from NMMB/BSC-Dust model; c) HYSPLIT back
trajectories, and d) Dust AOD a from IASI instrument on MetOpA
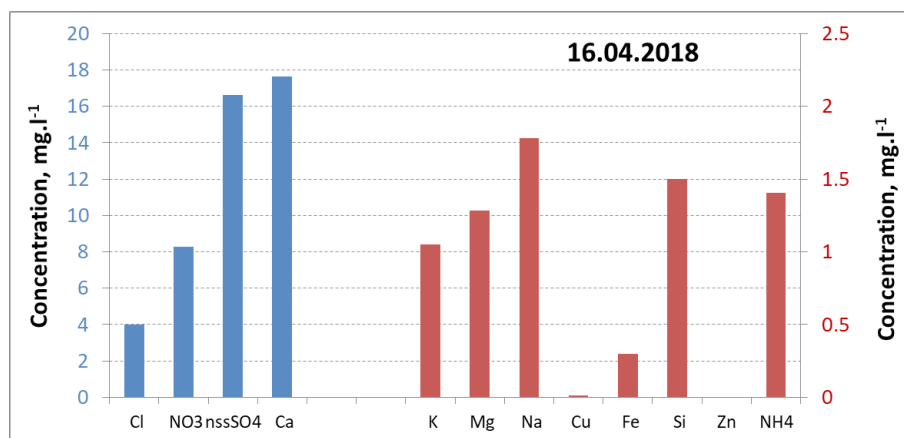
Figure 3. Concentrations of elements in the precipitation
sample from Sofia on 16 April 2018

For the first case the total ionic concentration (TIC) in the precipitation sample is 54.1 mg.l^{-1}, and consisted in 79% of elements: nssSO$_4^{2-}$, NO$_3^-$ and Ca. The pH and EC values of this sample are very high (7.4 and 132.7µS.cm^{-1}). The most abundant element is Ca followed by nssSO$_4^{2-}$ and NO$_3^-$. The concentrations of Si, K and Mg are also high with contribution to the TIC of 3%, 2% and 2%, respectively. The contribution of NH$_4^+$ is 3%.

The second case (30.06.2018) was characterised by more complex synoptic situation some days before. The models suggest that dust might has been transported the preceding days towards the Black Sea. Satellite data are limited in Eastern Europe due to cloudiness, Fig. 4.

a)

b)

c)

d)

Figure 4. Case 30.06.2018 (type B) – a) Dust AOD from NMMB/BSC-Dust model; b) Dust AOD from CAMS-ECMWF model on 29.06.18 at 18h; c) HYSPLIT frequency of back trajectories (22-30.06.18), and d) Dust AOD from IASI instrument on MetOpA on 30.06.2018

The chemical analysis of the precipitation sample in this case shows high concentrations of $nssSO_4^{2-}$, Ca, K and NH_4^+. The measured pH and EC are 4.9 and $50\mu S.cm^{-1}$. The TIC is 48.5 $mg.l^{-1}$ composed in 84% of elements: $nssSO_4^{2-}$, NO_3^- and Ca. The contribution of NH_4^+ is 5% and Si is only 1%.

Figure 5. Concentrations of elements in precipitation sample
from Cherni Vrah on 30 June 2018
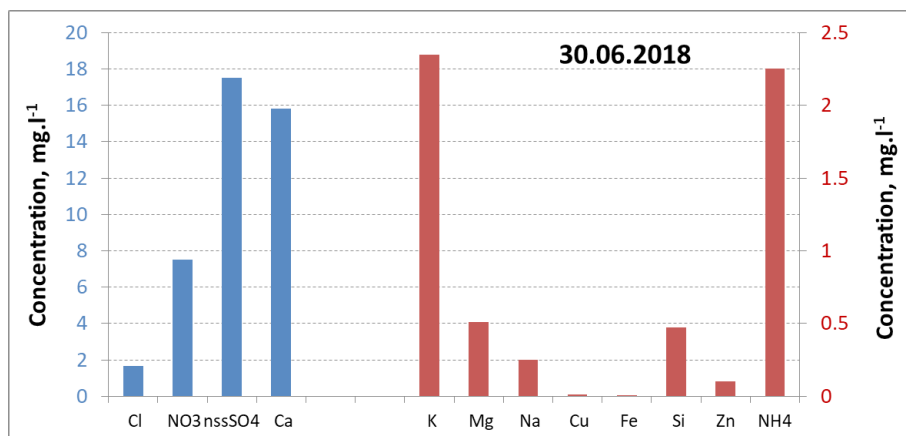
Precipitation chemistry analysis
We present here some statistical parameters for pH and EC, precipitation chemistry elements and TIC, for samples defined as A and B (Table 2).

Table 2. Statistics (mean, standard deviation, minimum and maximum)
for the samples in A (N=16) and B (N=10)

Element mg.l⁻¹	Mean A	SD A	Min A	Max A	Mean B	SD B	Min B	Max B
pH [-]	5.5	0.9	4.1	7.4	5.5	0.5	4.7	6.2
EC [uS/cm]	38.7	34.1	16.4	132.7	29.8	22.5	7.4	76.0
Cl	4.55	7.04	0.44	26.94	1.67	1.93	0.11	6.41
NO3	3.09	3.96	0.17	15.83	4.52	4.84	0.88	15.75
SO4	5.91	5.54	1.67	20.28	5.93	5.45	0.41	17.55
nssSO4	5.64	5.40	1.59	19.70	5.88	5.44	0.41	17.52
Ca	3.89	4.66	1.07	17.66	4.59	5.03	0.75	15.83
K	1.20	2.37	0.08	8.87	0.79	0.74	0.23	2.35
Mg	0.46	0.42	0.14	1.40	0.34	0.24	0.06	0.86
Na	2.40	4.27	0.11	15.64	0.48	0.86	0.10	2.60
Cu	0.02	0.02	0.01	0.05	0.01	0.00	0.01	0.01
Fe	0.06	0.09	0.01	0.30	0.02	0.02	0.00	0.05
Si	0.28	0.36	0.06	1.50	0.24	0.16	0.07	0.55
Zn	0.11	0.24	0.01	0.81	0.05	0.04	0.01	0.11
NH4	0.90	1.00	0.13	3.90	0.92	0.80	0.06	2.33
TIC	22.28	22.28	6.58	68.87	18.72	16.95	2.53	48.50

The pH values ranged from 4.1 to 7.4. The analysis of the distribution of the relative pH frequency for both categories (A and B) showed that 40% of the precipitation samples in A are in the acidity range (pH < 5.0), 6.7% are in the slightly acidic range (5.0 – 5.5) and 6.7% are in the alkaline range (> 7.0). The pH frequency analysis for B samples showed that in 30% pH was in the range 4.5-5.0, 10% were in the slightly acidic range, and 20% were in slightly alkaline range. pH value higher than 6.2 were not observed for B samples. pH values in the neutral range are observed in 40% for B samples, and in 33% for A samples. The mean pH value for both groups of samples from Sofia is 6.05 and is higher than the average multiyear pH (5.12) estimated from the precipitation chemistry network for the period 2002-2019. The same is observed for the samples from Ahtopol – mean for both groups pH is 5.34, while the multiyear one is 5.16.

The contribution of different elements in both A and B samples to the total ionic concentration is presented in Fig. 6. The most abundant ionic species for samples in both categories was $nssSO_4^{2-}$, followed by Cl and Ca for A category, and Ca and NO_3^- for B category.
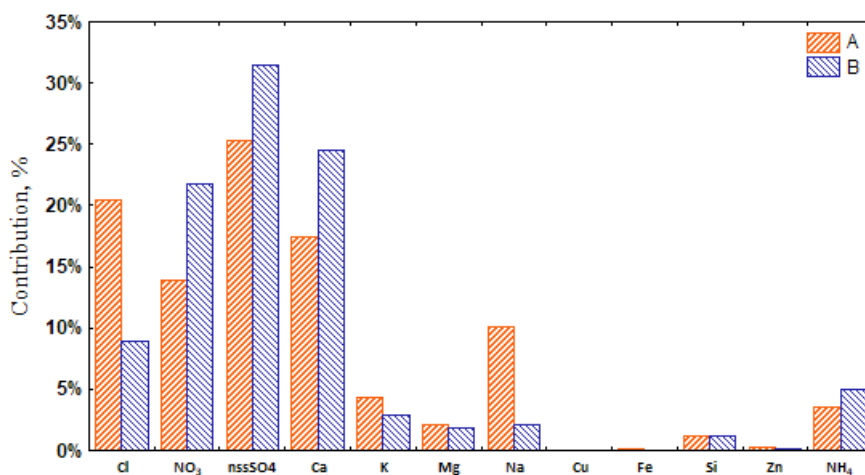

Figure 6. Contribution of different elements in precipitation samples for both categories (A and B)

The total ionic concentration in both A and B samples consist mainly of $nssSO_4^{2-}$, NO_3^- NH_4^+ (A - 44% and B - 58%). For A (flow mainly from south-west) the air masses passing over the Mediterranean Sea are enriched with sea salt aerosol. The evident high correlation of the elements Cl and Na (0.99) conferred this. 31% of the

TIC consist of Cl and Na. The percentage of terrigenous elements (Ca, K, Mg and Si) of the TIC in the A samples is 23.3%. High correlation is obtained also for Ca/Si (0.90) and Ca/Fe (0.84).

The higher contribution of sulphates, nitrates and ammonium ions in B samples can be explained by the enrichment of air masses with substances of anthropogenic origin. Very high correlations were found for $nssSO_4^{2-}$ and Ca (0.91) and Ca/K (0.95), indicating that the main source of those ions are from terrigenous origin (e.g. gypsum - CaSO4) (Conradie et al., 2019). 30.4% of the TIC consist of Ca, K, Ma and Si.

The t-test performed for the mean elemental contributions in the two groups returned a value of 0.035 for the two-tailed p- value, indicating, thus, to statistically significant differences between the two groups. Having in mind that the samples are low in number, we recognize that more robust statistical results could be obtained after collecting and analyzing more precipitations samples in different synoptic situations.

The chemical analysis of all samples confirms that the precipitation associated with dust intrusions is characterized by higher concentrations of terrigenous elements. In both types of intrusions the correlation between $nssSO_4^{2-}$ and Ca is relatively high, indicating similar source of origin. For B samples this correlation ($nssSO_4^{2-}$/Ca) is lower, but correlations between $nssSO_4^{2-}$ and NH_4^+ (0.7) , and NO_3^- and NH_4^+ (0.9) indicate contribution from secondary formed aerosols (($NH_4)_2SO_4$ and NH_4NO_3).

CONCLUSIONS

We have analysed the influence of Saharan dust events on the chemical composition of 26 rain samples collected at three sites in Bulgaria during 2017-2018. The samples were divided into two groups with respect to the direction of the approaching dust loaded masses: A (direct influence) and B (indirect influence). Common features for all samples were elevated values of pH (max to 7.4), EC (max to 202 $\mu S.cm^{-1}$) and Si, Ca, Fe, Mg concentrations. The concentrations of Si and Ca were significantly higher (up to 1.5 and 25 mg.l^{-1}) for A samples. In B samples higher concentrations of sulphates, nitrates and ammonium ions suggest enrichment of air masses with anthropogenic pollutants. The preliminary results, presented here, show that the trajectory of the air masses is an important factor for the chemical composition of precipitations in Bulgaria. Additional data from samples are needed to extend the analysis and perform more robust statistical estimates.

REFERENCES

Basart, S., Pérez, C., Nickovic, S., Cuevas, E. & Baldasano, J.M. (2012). Development and evaluation of the BSC-DREAM8b dust regional model over Northern Africa, the Mediterranean and the Middle East. *Tellus B*, 64, 1-23.

Benedetti A., J.-J. Morcrette, O. Boucher, A. Dethof, R. J. Engelen, M. Fisher, H. Flentjes, N. Huneeus, L. Jones, J. W. Kaiser, S. Kinne, A. Mangold, M. Razinger, A. J. Simmons, M. Suttie, and the GEMS-AER team, (2009). Aerosol analysis and forecast in the ECMWF Integrated Forecast System. Part II: Data assimilation, *J. Geophys. Res.*, 114, D13205

Conradie E.H., P.G. Van Zyl, J.J. Pienaar, J.P. Beukes, C. Galy-Lacaux, A.D. Venter, G.V. Mkhatshwa (2016), The chemical composition and fluxes of atmospheric wet deposition at four sites in South Africa, Atmospheric Environment 146, 113-131.

Dimitrova M., Trenchev Pl., Georgieva E., Neykova N., Neykova R., Nedkov R., Gochev D., Syrakov D., Veleva B., Atanassov D. & Spassova T. (2019). Seasonal changes of aerosol pollutants over Bulgaria, *Proceedings of the 15th Intern. Sci. Conf. Space, Ecology, Safety, SES 2019*, SRTI-BAS, Sofia, ISSN 2603-3321, 241-252.

Goudie, A.S. & Middleton, N.J. (2006). Desert Dust in the Global System. Springer. 287 pp.

Hristova E., Chemical composition of precipitation in urban area, (2017), Bulgarian Journal of Meteorology and Hydrology, 22, 1-2, 41-49.

Hristova E., Veleva B., Georgieva E. &Velchev K. (2020). Cloud and rain water chemical composition at peak Cherni Vrah, Bulgaria (these Proceedings)

Klein, H., Nickovic, S., Haunold, W., Bundke, U., Nillius, B., Ebert, M., Weinbruch, S., Schuetz, L., Levin, Z., Barrie, L.A., &, H. (2010). Saharan dust and ice nuclei over Central Europe. *Atmos. Chem. Phys.*, 10, 10211–10221.

Maher, B.A., Prospero, J.M., Mackie, D., Gaiero, D., Hesse, P.P., & Balkanski, Y. (2010). Global connections between aeolian dust, climate and ocean biogeochemistry at the present day and at the last glacial maximum, *Earth-Science Reviews*, 99, 61–97.

Marécal, V., V.-H. Peuch, C. Andersson, S. Andersson, J. Arteta, M. Beekmann, A. Benedictow, R. Bergström, B. Bessagnet, A. Cansado, F. Chéroux, A. Colette, A. Coman, R. L. Curier, H. A. C. Denier van der Gon, A. Drouin, H. Elbern, E. Emili, R. J. Engelen, H. J. Eskes, G. Foret, E. Friese, M. Gauss, et al., (2015). A regional air quality forecasting system over Europe: the MACC-II daily ensemble production, *Geosci. Model Dev.,* 8, 2777-2813.

Middleton, N., Tozer, P. &Tozer, B. (2019). Sand and dust storms: underrated natural hazards. *Disasters*, 43, 390-409.

Pérez, C., Haustein, K., Janjic, Z., Jorba, O., Huneeus, N., Baldasano, J.M., Black, T., Basart, S., Nickovic, S., Miller, R.L., Perlwitz, J., Schulz, M. &Thomson, M. (2011). An online mineral dust aerosol model for meso to global scales: Model description, annual simulations and evaluation, *Atmos. Chem. Phys.*, 11, 13001-13027.

Pey, J., Querol, X., Alastuey, A., Forastiere, F., and Stafoggia, M. (2013). African dust outbreaks over the Mediterranean Basin during 2001–2011: PM10 concentrations, phenomenology and trends, and its relation with synoptic and mesoscale meteorology, *Atmos. Chem. Phys.*, 1395–1410.

Prospero, J.M., Ginoux, P.M., Torres, O., Nicholson, S.E., Gill, T.E. (2002). Environmental characterization of global sources of atmospheric soil dust identified with the Nimbus-7 Total Ozone Mapping Spectrometer (TOMS) absorbing aerosol product. *Reviews of Geophysics*, 40, (31 pp.)

Rogora, M., Mosello, R., & Marchetto, A. (2004). Long-term trends in the chemistry of atmospheric deposition in northwestern Italy: the role of increasing Saharan dust deposition, *Tellus B*, 56, 426–434.

Rolph, G., Stein, A. &Stunder, B. (2017). Real-time Environmental Applications and Display sYstem: READY. *Environmental Modelling & Software*, 95, 210-228.

Stein, A.F., Draxler, R.R, Rolph, G.D., Stunder, B.J.B., Cohen, M.D. & Ngan, F. (2015) NOAA's HYSPLIT atmospheric transport and dispersion modeling system, *Bull. Amer. Meteor. Soc.*, 96, 2059-2077.

Stuut, J.-B.W., Smalley, I., O'Hara-Dhand, K. (2009). Aeolian dust in Europe: African sources and European deposits. *Quaternary International,* 198, 234–245.

Varga Gy, Kovács J. & Újvári G. (2013). Analysis of Saharan dust intrusions into the Carpathian Basin (Central Europe) over the period of 1979–2011, *Global Planet.*, 100, 333–342.

Xian, P., Reid, J.S., Hyer, E.J. et al. (2019) Current state of the global operational aerosol multi-model ensemble: An update from the

International Cooperative for Aerosol Prediction (ICAP). *Q J R Meteorol Soc*.,145, 176– 209.

✉ **Emilia Georgieva**
https://orcid.org/0000-0002-8466-4976
National Institute of Meteorology and Hydrology
Sofia, Bulgaria
E-mail: emilia.georgieva@meteo.bg

✉ **Elena Hristova**
https://orcid.org/0000-0002-5681-4375
National Institute of Meteorology and Hydrology
Sofia, Bulgaria
E-mail: elena.hristova@meteo.bg

✉ **Blagorodka Veleva**
https://orcid.org/0000-0003-2848-5559
National Institute of Meteorology and Hydrology
Sofia, Bulgaria
E-mail: blagorodka.veleva@meteo.bg

PBL VERTICAL STRUCTURE DURING EXTREME WIND EVENTS AT SEASIDE REGION OF SOUTHERN BULGARIA

Damyan Barantiev[1], Ekaterina Batchvarova[1], Hristina Kirova[2], Orlin Gueorguiev[2]

[1]*Climate, Atmosphere and Water Research Institute – Bulgarian Academy of Sciences (CAWRI – BAS)*
[2] *National Institute of Meteorology and Hydrology (NIMH)*

Abstract: Ground-based remote sensing (*GBRS*) data collection with Scintec Sodar MFAS was performed in southern Bulgarian Black Sea side from August 2008 until October 2016. These high spatial (10 m) and temporal (10 minutes with averaging time of 20 minutes) resolution measurements of wind and turbulent parameters have been used to explore the vertical structure of the coastal boundary layer during extreme wind events. For this purpose, the ninety-percentile of the two-parameter Weibull distribution of the wind speed at every sodar measurement level from 30 up to 600 m is used as a criterion to define the "rare" values within their statistical distributions and to identify a theoretical extreme wind speed profile (reference profile). On this basis, the extreme profiles during the reviewed period have been determined and their multiple time series have been then used to derive averaged profiles of twelve sodar output parameters under extreme winds conditions.

Keywords: extreme wind events; coastal boundary layer; wind and turbulent profiles; remote sensing; sodar

INTRODUCTION

During the last years, numerous public authorities have put resources into elaboration of variable efficient observations and forecast systems of dangerous meteorological events for improved risk management and reduction of socio-economic lost. The extreme weather events could be harmful to human health, infrastructure, economy and even cause loss of human life (IPCC, 2012) Currently, more accurate spatial, qualitative and quantitative assessments of the processes within the Planetary Boundary Layer (*PBL*) have been possible through *GBRS* measurements (Prasad, 2015). Various innovative studies of fundamental meteorological parameters and turbulence in the *PBL* have been based on such type

of equipment (Bradley et al., 2005; Cimini, Marzano, & Visconti, 2011; Coulter & Kallistratova, 2004; Emeis, 2010; Engelbart, Monna, Nash, & Mätzler, 2009; Illingworth et al., 2013; Peña et al., 2016). Measurements in flat coastal terrain within the frame of SafeWind project (Sathe, Courtney, Mann, & R, 2011) have shown the capabilities of *GBRS* instruments to detect extreme wind events using two different types of lidars (continuous wave and a pulsed lidar) and a reference 116.5-metre tall meteorological mast. Monthly (April 2001) remote sensing data from Doppler sodar with high spatial and temporal resolution have been handled to describe the wind speed values in an extensive plateau (horizontal homogeneous area) in North of Spain at the Low Atmosphere Research Centre (Pérez, García, Sánchez, & de Torre, 2004). Over the past decade through research and collaboration within several COST Actions an integration of a number of *GBRS* devices within a uniform European network for observations has been initialized and continues to be upgraded (Engelbart et al., 2009; Illingworth et al., 2015; Illingworth et al., 2013; Illingworth et al., 2017)

Experimental site and measurements

The GBRS methods are not employed in operation in Bulgaria, though such data are needed for better weather forecasts, evaluation of meteorological models, registration of extreme wind events and fundamental research. Data collection with Scintec MFAS Sodar (ScintecAG, 2011) was performed in south Bulgarian Black Sea coast from 1 August 2008 until 31 October 2016 at the Meteorological Observatory (MO) Ahtopol (Fig. 1). The terrain of MO Ahtopol is mostly flat and grassy at about 400 meters inland at 30 m height above sea level and steep about 10 meters high coast with an approximate direction of the coastline from NNW to SSE (Fig. 1). The monostatic multibeam Doppler system is installed at an approximate height of 4.5 m above the ground level (*AGL*) on the administrative building roof (Fig. 1). The soundings have been performed with high spatial (10 m) and temporal (10 minutes with averaging time of 20 minutes) resolution and have laid the basis of coastal *PBL* studies in Bulgaria (Barantiev, Batchvarova, & Novitsky, 2013; Barantiev, Novitsky, & Batchvarova, 2011; Batchvarova, Barantiev, & Novitsky, 2012; Novitsky et al., 2012). During the study period of 3014 days, the sodar has made 341971 measurements, which corresponds to 78.8% coverage. No measurements were allowed during night hours of summers 2008 and 2009 and frequent accidents of the main power supply have been the main reasons for missing observations. The vertical range of the sodar is from 150 m to 1000 m with vertical resolution of 10 m starting from 30 m, but the effective range depends on the atmospheric turbulent inhomogeneity, on the operation setup and software updates. Profiles up to 600 m were taken into account in this study due to the low data availability above this height.

Figure 1. Location of MO Ahtopol in Bulgaria on Google Earth (42° 5'3.37"N, 27°57'4.49"E) with views of the terrene (right) and sodar system on the roof of the administrative building of MO Ahtopol (left)

Methodology

The definition of the Intergovernmental Panel on Climate Change (IPCC, 2001, 2007) for extreme events (exceedance over a relatively low threshold) is employed through determination of the 90th percentile of the performed statistical distribution for all heights and thus "reference" values, at which the wind speed is considered as extreme, are defined. In this study we have performed statistical analysis at each measurement level using the probability density function (pdf) also known as the two parameter Weibull distribution (Papoulis & Pillai, 2002) described in equation (1) based of the method of maximal likelihood (Indhumathy, Seshaiah, & Sukkiramathi, 2014) for all wind speed profiles measured at MO Ahtopol. The two distribution parameters are given in the equations: (2) and (3) (Sornette, 2004), respectively, for a shape parameter $\hat{k}$, which has a non-dimensional value defining the shape of the probability density distribution curve and the scale parameter $\hat{c}$ assuming the dimensionality of the variable wind speed and representing the 63.2th percentile of the distribution (Papanchev, 2013).

$$f(u; c, k) = f(x) = \begin{cases} \dfrac{k}{c}\left(\dfrac{u}{c}\right)^{k-1} e^{-(u/c)^k} & , u \geq 0 \\ 0 & , u < 0 \end{cases} \tag{1}$$

$$\hat{k}^{-1} = \frac{\sum_{i=1}^{N}\left(u_i^k \ln u_i - u_N^k \ln u_N\right)}{\sum_{i=1}^{N}\left(u_i^k - u_N^k\right)} - \frac{1}{N}\sum_{i=1}^{N} \ln u_i \qquad (2)$$

$$\hat{c}^k = \frac{1}{N}\sum_{i=1}^{N}\left(u_i^k - u_N^k\right) \qquad (3)$$

In this way, "reference" wind profile is derived and extreme wind events are determined by comparing it with the actual profiles during the study period. Only profiles with at least ten points with values equal to or greater than those of the reference profile are used. Finally, an "extreme wind "data set based on sodar data is created containing 10854 extreme wind profiles representing about 3.2% of the soundings performed.

Results

In Figure 2 histograms of the wind speed are shown with applied Weibull distributions, certain 90th percentile and statistical data for different measurement levels.
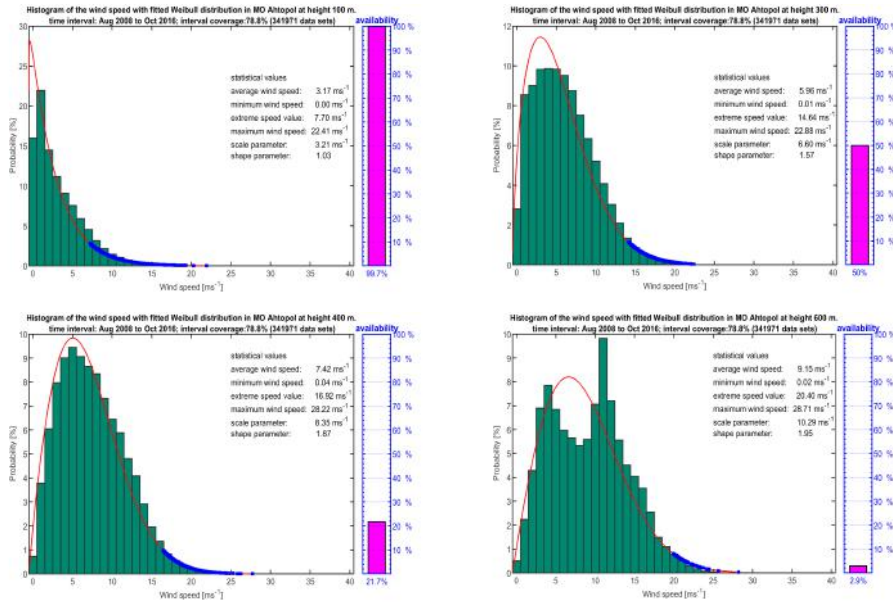

Figure 2. Histograms of wind speed (green bars), two-parameter Weibull distributions (red curves), certain values equal to or exceeding the 90th percentile of the probability density of Weibull distributions (blue squares), availability of data (pink bar) and derived statistical data. Top left – level 100 m, top right - 300 m, bottom left – 400 m, bottom right – 600 m

The pink bar, on the side of each histogram, is indicator for data availability at each of the displayed levels. A characteristic change with height of the wind speed histograms is observed, which is expressed by the typical shift of the maximum to higher wind speed values. Due to the larger variability of wind speed with height, a "dissolution" of the graphs in the Weibull distributions applied to the respective histograms (Figure 2 – red curves) and in the histograms themselves is observed (Figure 2 – green bars). For each statistical distribution of Weibull, actual measured values equal to or greater than its 90th percentile (blue squares on the red curve) are presented, which according to the IPCC definition are defined as extreme values of wind speed (IPCC, 2001, 2007). In addition to each of the graphs in Figure 2 statistical values for the respective heights are derived, such as minimum, maximum and average values of wind speed, extreme value determined by the 90th percentile, as well as values of the two parameters of the respective Weibull distribution.

The changes in the probability distributions of wind speed in height with the attached "reference" profile of extreme values of wind speed for the whole considered period are presented at Figure 3. The color bar shows the probability distribution values changes in height, as its color range is limited to 10% in order to achieve
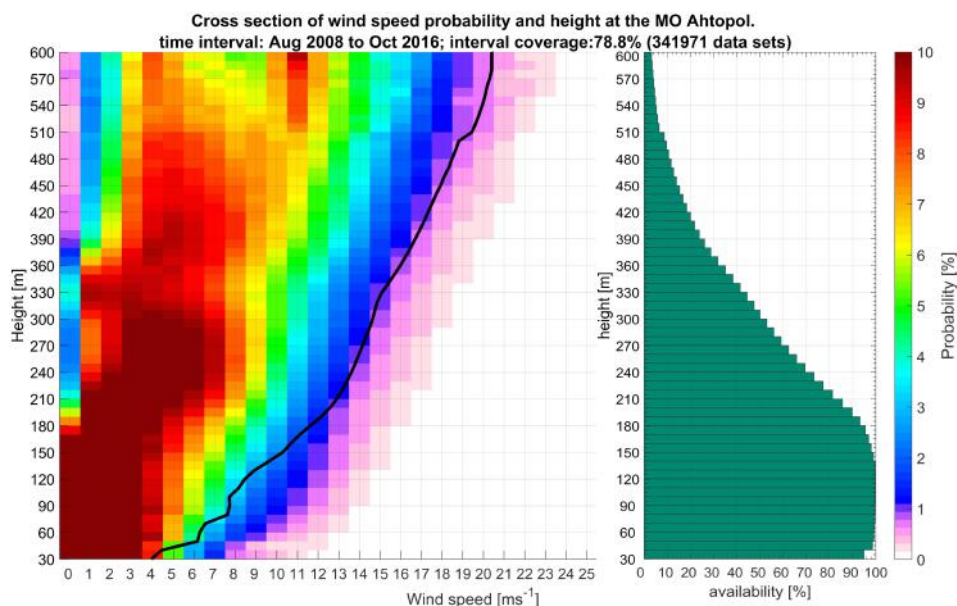

Figure 3. Changes in the probability distributions of wind speed in height (color cross section of altitude and speed intervals) with available data (green bars) and applied reference profile for extreme values of wind speed (black profile), determined by the 90th percentile of the statistical distributions in height

better visualization of the results (values of probability distributions above 10% are colored as 10 %). The area with maximum values of the probability distribution of wind speed in height is clearly observed at the presented graph, as up to 170 m the probability is highest for wind speed up to 3 ms^{-1}. At 300 m, high probability is observed in winds of 3 to 6 ms^{-1}. At 600 m the probability is highest for winds speeds 4 – 5 ms^{-1} and 10 – 12 ms^{-1}. From the green bars showing the change in the number of profiles reaching a certain height, it can be seen that their availability begins to decrease sharply after 180 m *AGL*, with a maximum of data observed in the layer from 90 to 140 m. The values of the reference extreme wind speed profile (*REWSP*) (Figure 3 – black profile) increase almost parabolic with height, as the extreme values at 30 m *AGL* are about 4 ms^{-1}, and at 600 m – about 20 ms^{-1}. *REWSP* is located in the area with a probability distribution of wind speed between 1% and 4% up to 200 m and between 1% and 2% higher up.

The vertical structure of the coastal *PBL* in the study area during extreme winds phenomena is presented in Figure 4 by averaged profiles and their dispersions of 12 output parameters from the sodar measurements - from left to right and from top to bottom: wind direction (*WD*), extreme wind speed profile (*WS*), extreme speed profile dispersion (*sigWS*), vertical wind speed (*W*), vertical wind speed dispersion (*sigW*), horizontal (western) component of the extreme profile (*U*), dispersion of the western component (*sigU*) , horizontal (southern) component of the extreme profile (*V*), dispersion of southern component (*sigV*), eddy dissipation rate (*EDR*), turbulent intensity (*TI*) and turbulent kinetic energy (*TKE*). The *WD* profile graph (Figure 4) shows NNW direction in the registered extreme winds up to 130 m (where most of the profiles are concentrated), which is related to wind blowing parallel to the coastline. Gradual change to west direction is observed between 130 and 200 m. Higher up, the *WD* is in the southwesterly. The greatest dispersion of this profile is observed in first 130 m, after which it decreases gradually. The averaged extreme wind speed profile (*EWSP)* is characterized by a relatively constant dispersion in height, and an almost linear increase in values. Velocities close to 8 ms^{-1} up to 130 m, and their rapid increase in height reaching 24 ms^{-1} at 600 m are observed. In the profile of *W*, positive values up to 160 m altitude are observed, after which negative values are recorded decreasing to -1.3 ms^{-1} at 600 m. In almost all presented averaged profiles, changes in the profiles shape in the layer 40 – 60 m are observed. In the *EDR* profile a sharp decrease of the values up to 90 m is observed. Also of interest is the *sigW* profile with slight peak at a height of 150 – 160 m (where a sharper change of *WD* and faster decrease of the *W* values are observed), followed by almost constant values up to 300 m, and an increase up to the second main peak between 440 m and 490 m. At this height *sigW* has reached maximum values. These peaks are also reflected in the shape of the other averaged turbulent profiles. Following Illingworth et al. (2013) the *PBL* height at Ahtopol during extreme wind situations is between 440 m and 490 m. The height

with peculiarities in the profiles in Figure 4 of 40 – 60 m, 90 m and 150 m can be related to Internal Boundary Layer (*IBL*) and surface layer (*SL*) heights, or very low nocturnal *PBL* height in cold seasons.

The number of extreme wind speed profiles during the different years of the study period by month and hour of the day is shown in Figure 5. The number of *EWSP* for the period is 10854 or 3.2 % of all profiles included in the statistics. It can be noted that 2012 was the windiest year. In 2010 only 13 *EWSP* were registered in December around 8 a.m. *EWSP* are observed in all months and hours, but biggest number (>2500) is recorded in January. Calmest are the months of June and July. Calm and windy periods at Ahtopol can be also identified, namely July 2009 – August 2011 was a calm period, while September 2011 – June 2014 and April 2015 – October 2016 were windy periods. Insight in the atmospheric dynamics gives the statistic of *EWSP* by hour of the day. Calmer periods are revealed at 6 – 7 a.m. and 5-6 p.m., which are related to the start and end of the day during cold seasons and calm periods in the beginning and end of sea breeze during warm seasons. Most windy are the periods 10 p.m. – 1 a.m. and 11 a.m. – 1 p.m., which can be related to the maximal development of the local circulation in both directions.
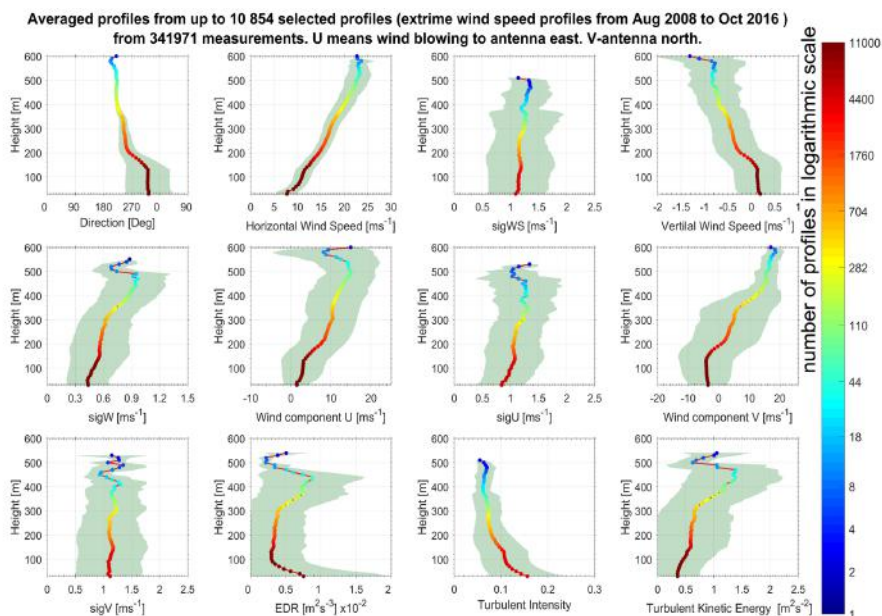

Figure 4. Averaged profiles and their dispersions from a sample with a maximum of 10 854 selected extreme wind speed profiles
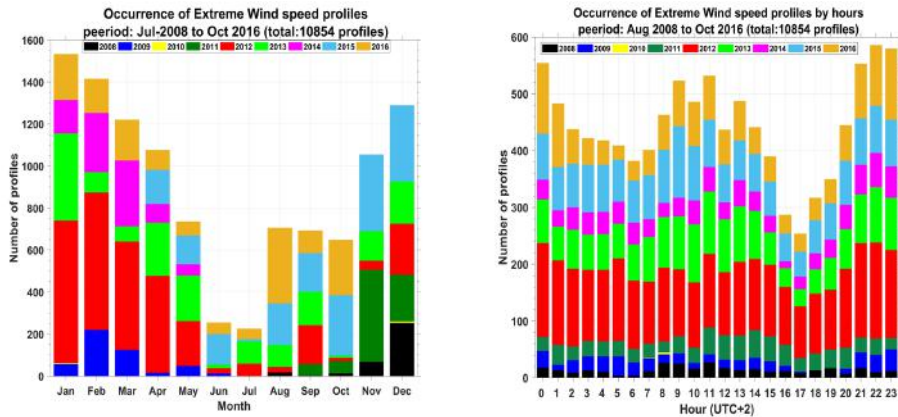
Figure 5. Number of extreme wind speed profiles reported during the different years of the study period in MO Ahtopol by months (left) and hours of the day (right)

CONCLUSIONS

The derived averaged characteristics of the coastal *PBL* in extreme winds conditions are pioneering result based on unique set of GBRS observation data at a Bulgarian Black Sea coastal site. In this paper a super position of different types of air masses is considered which allows to assess the vertical structure and hight of the *PBL* (determined between 440 m and 490 m by the main peaks at graphs of *sigW*, *EDR* and *TKE* in Figure 4), the *IBL* height of 40 - 60 m at high winds and *SL* height or very low nocturnal *PBL* height in cold seasons of 90 or 150 m. This climatic study reveals that quiet and windy periods can be of different length, which is likely related to different types of prevailing weather structures. The observed winter highs and summer lows of extreme winds are likely due to the presence of local coastal circulation. The distinct morning and evening lows in the average distribution by hour are related to transition from night to day and vice versa. The distribution of *EWSP* by year, month and hour of the day is important climatological feature, which is of great use for economic activities (such as construction of buildings, wind energy potential, air quality, climate comfort for citizens and tourists, etc.) and municipal emergency plans and actions in cases of meteorological extreme phenomena.

REFERENCES

Barantiev, D., Batchvarova, E., & Novitsky, M. (2013). *Exploration of the Coastal Boundary Layer in Ahtopol through Remote Acoustic Sounding of the Atmosphere*. Paper presented at the 2nd Nacional Congress on Physical Sciences and 41st National Conference on Physics Education Matters, Sofia, Bulgaria. https://www.researchgate.net/publication/271428857_Exploration_of_the_Coastal_Boundary_Layer_in_Ahtopol_through_Remote_Acoustic_Sounding_of_the_Atmosphere

Barantiev, D., Novitsky, M., & Batchvarova, E. (2011). Meteorological observations of the coastal boundary layer structure at the Bulgarian Black Sea coast. *Advances in Science and Research (ASR)*(6), 251-259. doi:https://doi.org/10.5194/asr-6-251-2011

Batchvarova, E., Barantiev, D., & Novitsky, M. (2012). *Costal Boundary layer wind profile based on SODAR data – Bulgarian contribution to COST Acton ES0702*. Paper presented at the The 16th International Symposium for the Advancement of Boundary-Layer Remote Sensing – ISARS Boulder, Colorado, USA. https://psl.noaa.gov/events/2012/isars/pdf/isars2012-abstractVolume.pdf

Bradley, Stuart, Antoniou, Ioannis, Hünerbein, Sabine von, Kindler, Detlef, Noord, Manuel de, & Jørgensen, Hans. (2005). *SODAR calibration procedure (final reporting on WP3, EU WISE project NNE5-2001-297)* (0-9541649-1-1). Retrieved from Salford, Greater Manchester, UK: http://usir.salford.ac.uk/id/eprint/9590/

Cimini, Domenico, Marzano, Frank S., & Visconti, Guido. (2011). *Integrated Ground-Based Observing Systems* (Domenico Cimini, Frank S. Marzano, & Guido Visconti Eds.): Springer-Verlag Berlin Heidelberg.

Coulter, R. L. , & Kallistratova, M. A. . (2004). Two decades of progress in SODAR techniques: a review of 11 ISARS proceedings. *Meteorology and Atmospheric Physics, 85*, 3 – 19. doi:https://doi.org/10.1007/s00703-003-0030-2

Emeis, S. (2010). *Surface-based remote sensing of the atmospheric boundary layer* (1st ed.). New York: Springer Berlin Heidelberg.

Engelbart, D., Monna, W., Nash, J., & Mätzler, C. (2009). *Integrated Ground-Based Remote-Sensing Stations for Atmospheric Profiling: COST Action 720: Final Report* (978-92-898-0050-1). Retrieved from Luxembourg https://www.cost.eu/wp-content/uploads/2018/07/53632.pdf

Illingworth, A., Cimini, D., Gaffard, C., Haeffelin, M., Lehmann, V., Löhnert, U., . . . Ruffieux, D. (2015). Exploiting Existing Ground-Based Remote Sensing Networks to Improve High-Resolution Weather Forecasts. *Bulletin of the American Meteorological Society, 96*(12), pp. 2107-2125. doi:https://doi.org/10.1175/BAMS-D-13-00283.1

Illingworth, A., Ruffieux, D., Cimini, D., Lohnert, U., Haeffelin, M., & Lehmann, V. (2013). *COST Action ES0702 Final Report: European Ground-Based*

Observations of Essential Variables for Climate and Operational Meteorology. Retrieved from COST Office, PUB1062: http://cfa.aquila.infn.it/wiki.eg-climet. org/Final_Report_EG_CLIMET.pdf

Illingworth, A., Ruffieux, D., Haeffelin, M., O'Connor, E., Cimini, D., & Potthast, R. (2017). *COST Action Final Achievement Report ES1303: Towards operational ground based profiling with ceilometers, doppler lidars and microwave radiometers for improving weather forecasts (TOPROF)*. Retrieved from Brussels, Belgium: http://www.toprof.imaa.cnr.it/images/toprof/pubs/ES1303_ FADataentryReport_2018-03-05_submitted.pdf

Indhumathy, D., Seshaiah, C.V., & Sukkiramathi, K. . (2014). Estimation of Weibull parameters for wind speed calculation at Kanyakumari in India. *Journal of Innovative Research in Science, Engineering and Technology, 3*(1).

IPCC. (2001). *Climate Change 2001: The Scientific Basis. Contribution of Working Group I to the Third Assessment Report of the Intergovernmental Panel on Climate Change* (0521 01495 6). Retrieved from United Kingdom and New York, NY, USA,: https://www.ipcc.ch/site/assets/uploads/2018/03/WGI_TAR_full_report.pdf

IPCC. (2007). *Climate Change 2007: Synthesis Report. Contribution of Working Groups I, II and III to the Fourth Assessment Report of the Intergovernmental Panel on Climate Change* (92-9169-122-4). Retrieved from Printed in Sweden: https://www.ipcc.ch/site/assets/uploads/2018/02/ar4_syr_full_report.pdf

IPCC. (2012). *Managing the Risks of Extreme Events and Disasters to Advance Climate Change Adaptation. A Special Report of Working Groups I and II of the Intergovernmental Panel on Climate Change*. Retrieved from Cambridge, UK, and New York, NY, USA, : https://www.ipcc.ch/site/assets/uploads/2018/03/ SREX_Full_Report-1.pdf

Novitsky , M., Kulizhnikova, L., Kalinicheva, O., Gaitandjiev, D., Batchvarova, E., Barantiev, D., & Krasteva, K. (2012). Characteristics of speed and wind direction in atmospheric boundary layer at southern coast of Bulgaria. *Russian Meteorology and Hydrology, 37*(3), 159 – 164. doi:https://doi.org/10.3103/ S1068373912030028

Papanchev, Toncho. (2013). Модифициран подход за оценка на параметрите на разпределението на Вейбул при изпитвания с нула или единични откази и интервални данни. *Journal of Notices of the Union of Scientists - Varna, Technical Sciences Series, 1*, 53 – 57. http://www.su-varna.org/izdanij/ Tehnauk-1-013/pp53_57.pdf

Papoulis, A., & Pillai, S.U. (2002). *Probability, Random Variables, and Stochastic Processes (4th ed.)*: McGraw-Hill Europe;.

Peña, Alfredo, Floors, R. R., Sathe, A., Gryning, S-E., Wagner, R., Courtney, M., . . . Hasager, C.B. (2016). Ten Years of Boundary-Layer and Wind-Power Meteorology at Høvsøre, Denmark. *Boundary-Layer Meteorology, 158*(1), 1 – 26. doi:https://doi.org/10.1007/s10546-015-0079-8

Pérez, I.A. , García, M.A. , Sánchez, M.L., & de Torre, B. (2004). Analysis of height variations of sodar-derived wind speeds in Northern Spain. *Journal of Wind Engineering and Industrial Aerodynamics, 92*(10), pp. 875 – 894. doi:https://doi.org/10.1016/j.jweia.2004.05.002

Prasad, S. Thenkabail. (2015). *Remotely Sensed Data Characterization, Classification, and Accuracies* CRC Press.

Sathe, A., Courtney, M., Mann, J., & R, Wagner. (2011). *How good are remote sensors at measuring extreme winds?*. Paper presented at the EWEA Conference, Brussels, Belgium. https://repository.tudelft.nl/islandora/object/uuid:9e935a86-2279-4699-919e-cadd37704090/datastream/OBJ/download

ScintecAG. (2011). *Scintec Flat Array Sodars - Hardware Manual (SFAS, MFAS, XFAS) including RASS RAE1 and windRASS* (Software Manual Ed. Version 1.03 ed.). Germany: Scintec AG,.

Sornette, D. (2004). *Critical phenomena in natural sciences : chaos, fractals selforganization and disorder : concepts and tools*. Berlin: Springer.

✉ **Damyan Barantiev**
https://orcid.org/0000-0001-9908-9014
Climate, Atmosphere and Water Research Institute
Bulgarian Academy of Sciences
Sofia, Bulgaria
E-mail: dbarantiev@cawri.bas.bg

✉ **Ekaterina Batchvarova**
https://orcid.org/0000-0002-1293-9440
Climate, Atmosphere and Water Research Institute
Bulgarian Academy of Sciences
Sofia, Bulgaria
E-mail: ekbatch@cawri.bas.bg

✉ **Hristina Kirova**
National Institute of Meteorology and Hydrology
Sofia, Bulgaria
E-mail: hristina.kirova@meteo.bg

✉ **Orlin Gueorguiev**
National Institute of Meteorology and Hydrology
Sofia, Bulgaria
E-mail: orlin.gueorguiev@meteo.bg

BLACK SEA HOLOCENE ENVIRONMENTAL SETTING IN RESPECT OF *OSTREA EDULIS* APPEARANCE AND LOSS

**Ivan Genov[1], Krasimira Slavova[1],
Tzvetana Nonova[2], Elena Koleva-Rekalova[3]**

[1]*Institute of Oceanology - Bulgarian Academy of Sciences (IO-BAS)*
[2]*Institute for Nuclear Research and Nuclear Energy –
Bulgarian Academy of Sciences (INRNE-BAS)*
[3]*Geological institute - Bulgarian Academy of Sciences (GI-BAS)*

Abstract: Geological and palaeoclimatic Holocene setting in the Black Sea has been traced. This research suggests that the appearance of *Ostrea edulis* in the Black Sea during the Middle Holocene, not immediately after the invasion of Mediterranean waters, is due to the dynamics of interconnected climate and abiotic parameters of the basin. Although the reasons for the decrease in abundance of the Black Sea population of flat oysters are still uncertain, we attempts, through a comparative analysis of key abiotic factors in the past and today, to suggest that it is quite possible marine ecosystems to respond to modern changes of key climate-related drivers and pollution by changing their habitat and/or extinction. Geological approaches were used to study the abiotic factors of the environment (salinity and temperature) back in time.

Keywords: Black Sea, Holocene, palaeoenvironment, Ostrea edulis, pollution

INTRODUCTION

This article summarizes the results of a study conducted in the first year of the National Science Program "Environmental Protection and Reduction of Risks of Adverse Events and Natural Disasters" (NSP), WP I.4. The change of abiotic factors (salinity and temperature of sea water) was traced on the basis of palaeogeological and palaeoclimatic studies in the Black Sea from the Early Holocene to date. It was made a speculation that climate changes as well as pollution are possible environmental stressors contributed to Ostrea loss.

In recent years, various authors, in addition to studies of the Black Sea deep-sea sediments - Unit III (lutite), Unit II (sapropel), Unit I (coccolithic ooze) have carried out a detailed study to reconstruct certain palaeoecological and palaeoenvironmental conditions and differentiate the lithological boundaries

from the boundaries of the Black Sea ecozones (Giunta et al., 2007, Mudie, Aksu & Yašar, 2001).

The natural geographic range of *Ostrea edulis* extends from the western Mediterranean and the Black Sea, along the coast of western Europe and the British Isles until 65 degrees north in Norway, where it is generally found in estuarine areas on sheltered, hard substrate (Maathuis et al., 2020) and tolerates salinities of up to 23‰. (Uyan & Aral, 2000). The appearance of *Ostrea edulis* in the Black Sea from different marine environments was estimated by radiocarbon ages (^{14}C) between 5.14±0.27 (Filipova-Marinova & Christova, 2001) and 0.29±0.09 ^{14}C ka BP (Krastev, Parunin & Switoch, 1990). Todorova, Micu & Klisurov (2009) reported that during the 1970s live oysters were still abundant on the reefs and proved that the decline of oyster populations took place between the 1980s and 2000s as proposed some hypotheses about the possible causes for their loss. However, the causes of the significant decrease in abundance of the Black Sea population of the flat oysters are still uncertain (Yakhontova & Piyanova, 2010).

MATERIAL AND METHODOLOGY

Collection of the cores EUXRo03-3 and EUXRo01-1 were done during the implementation of the project MARINEGEOHAZARD. Core 18 was collected in the
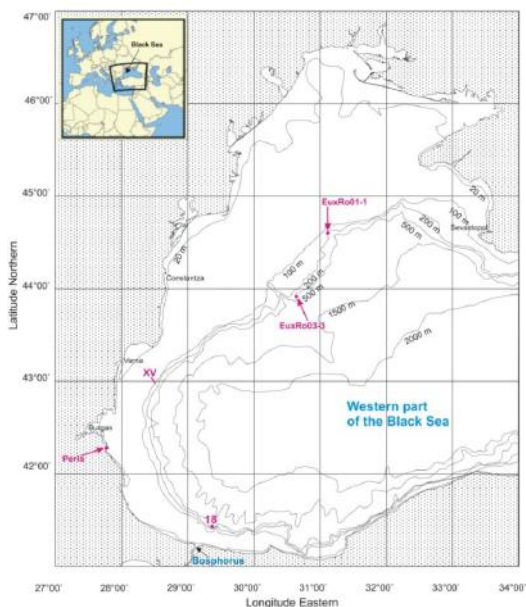

Figure 1. Area of investigations: Cores EuxRo01-1, EuxRo03-3 and 18; seismic profile XV; sediment and water sampling in front of the Perla beach.

frame of IAEA/TC RER/2/003 project. Water and sediment samples in front of Perla beach (Primorsko) were taken by divers in 2019 under the NSP, WP I.4. The profile (XV) was obtained by continuous seismic profiling with a single-channel equipment and a sparker emitter (1000 J) according to project PP 2, IOC BSRC (archive of the IO-BAS) (Fig. 1). It has been transformed into a profile with real depths using sound wave velocities of 1500 m/s and 1800 m/s in seawater and sediments, respectively.

Lithological description and sampling of cores were done in the IO-BAS. Petrographical analyses of aragonite were done in the GI-BAS using light microscope "Zeiss Axioscope 40" with built-in digital photo-camera. The g spectrometry measurements of sediment and water samples were carried out in the INRNE-BAS using HPGe – GMX 50P4 coaxial detector with a Beryllium window (Ortec type) with 50 % counting efficiency and energy resolution 2.3 KeV at 1332 KeV (^{60}Co). Climate change from the Early Holocene to date has been studied using literature and own data on sequential stratigraphy, mineralogical and petrographic analysis, pollen analysis, calcareous nannoplankton studies, satellite data on the temperature in the Black Sea basin for 30 years period of time.

RESULTS AND DISCUSSION

Currently the Black Sea level during the Early Holocene stage and the character of the lake to sea shift are discussed yet. The seismostratigraphic studies in the western Black Sea confirm the curve of the Black Sea level for the last 20 ^{14}C ka BP (Fig. 2). The recognized genetic units in the two youngest sequences on seismic

Figure 2. Black Sea level, climatic events and seismic units by Genov (2018) with addition by Koleva-Rekalova, Genov & Slavova (2018): World ocean – solid sky blue line; Southern Bosphorus sill – dashed curve; formation of the rice-like aragonite - dashed dark green line; formation of acicular aragonite – green line; Last glacial maximum (LGM); Younger Drays (YD); Melt water pulse (MWP). Genetic units are shown on fig.3.
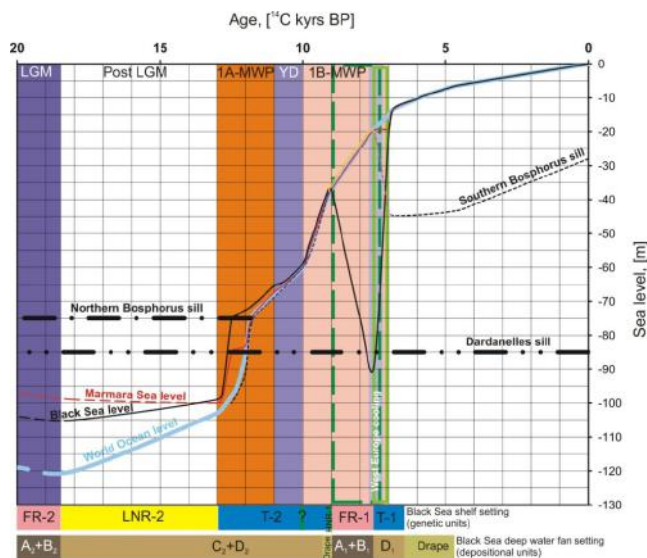
profile (XV) correspond to the respective changes at the baseline level. The profile has been turned into a seismic-geological profile with real depths (Fig. 3).
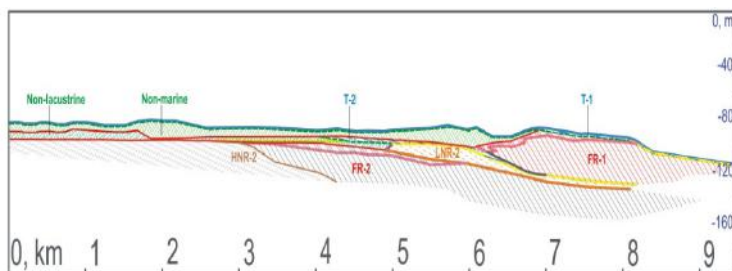

Figure 3. Seismo-geological section – XV (after Genov, 2016). Genetic units: highstand normal regressive (HNR), forced regressive (FR), lowstand normal regressive (LNR), transgressive (T). Surfaces: subaerial unconformity (SU) – red line; basal surface of forced regression (BSFR) – brown line; correlative conformity (CC) – orange line; regressive surface of marine erosion (RSME) – pink line; maximum regressive surface (MRS) – yellow line; transgressive ravinement surface (TRS) – dashed green line; maximum flooding surface (MFS) – blue line and gray line; shoreline trajectory – violet line.

The deposition of Unit II (sapropel) is a consequence of the salt Mediterranean inflow. Therefore, the invasion of Ostrea in the Black Sea is possible only after the beginning of the transgressive phase of the basin ~ 7.5 ^{14}C ka BP (Fig. 2, 4). The lack of suitable abiotic factors (S ‰ and T° C) for the spread of Ostrea in the Black Sea before the marine transgresion ~ 7.5 ^{14}C ka BP is evident from Fig.4.

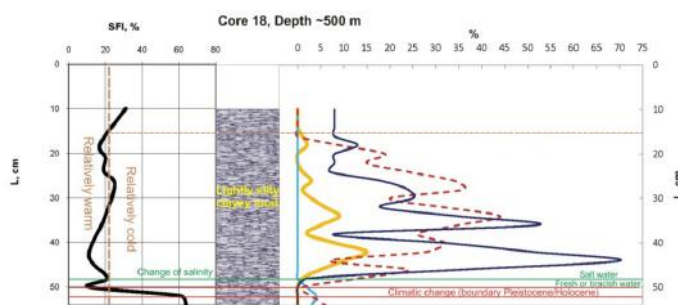**Figure 4.** Pollen-cist diagrams (Genov, 2009 with modifications). SFI - Steppe-forest index; Lingulodinium machaerophorum – dark blue line, Spiniferites ramosus – yellow line, Tectatodium psilatum – blue line, Cymatiosphaera sp. – dashed red line.

Evidence of the above is the redeposition of aragonite rice-like crystals at the base of sapropel mud in cores EUXRo01-1 and EUXRo03-3 (Fig. 5). White aragonite laminae at the base of sapropel mud are composed mainly of aragonite with rice-like morphology and spheroidal aggregates (spherulites). Coccoliths are not observed in the studied aragonite laminae. Chemical aragonite was formed during the Early Holocene lake-brackish stage of the basin in a shallow shelf setting under arid conditions (Slavova et al., 2016; Koleva-Rekalova, Genov & Slavova, 2018).
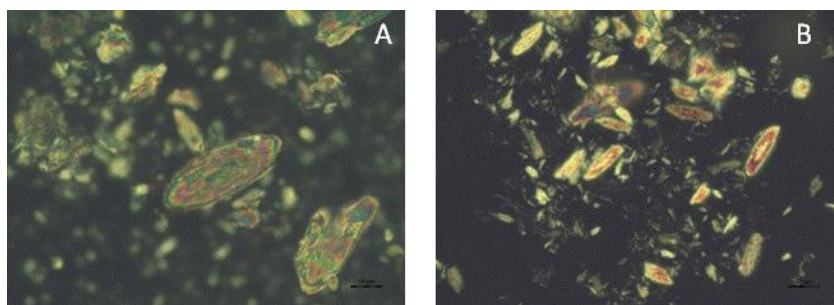

Figure 5. Petrographic (cross-polarized light) microphotographs of smear slides in the studied aragonite laminae. A – Large aragonite crystals with rice-like morphology and many aragonite fragments (Core 01-1_sample 5, 160803_05) ; B – Predominantly aragonite crystals with rice-like shape as well as single fan-like fragments (Core 03-3_sample 6, Ar_029-6). The scale bar is 10 μm.

Reported radiocarbon dates (^{14}C ka BP) of *Ostrea edulis* in the Black Sea (without claiming to be exhaustive) are as follows: 5.14±0.27 (Filipova-Marinova & Christova, 2001); 4.59±0.07 (Switoch, Taldenkova & Yanina, 1986); 4.4 (Porotov, 2007)**;** 3.12±0.05 and 0.29±0.09 (Krastev, Parunin & Switoch, 1990). The first appearance in the Bosphorus is dated of 5.3 ^{14}C ka BP (Algan et al., 2001), i.e. the mass appearance of Ostrea in the Black Sea does not correlate with the transition from lake to sea phase of the basin ~ 7.5 ^{14}C ka BP.

Various authors have carried out a detailed study to reconstruct certain Black Sea paleoecological conditions. Giunta et al. (2007) described three ecozones, recognizable in whole basin. Age of the boundary between Ecozone 3/2 in different cores varies between 6621 and 5808 ^{14}C a BP. The boundary between Ecozone 3/2 is a consequence of the geological events archived by the lithological boundary Unit III/II (~ 7.3 ^{14}C ka BP on the base of published ^{14}C data). Giunta et al. (2007) studying species *B. bigelowii* suggested gradual salinity increase in Ecozone 2, not lower than 17 ‰. Mudie, Aksu & Yašar (2001) estimated salinity range for Zone B1b (7.1- ~3 ka) from 15 - 18‰. Filipova-Marinova et al. (2013) suggested high temperatures and salinity of surface waters during the Holocene climate optimum

(7635-4085 cal. a BP). Paleogenetic data of Coolen et al., (2009) indicated a gradual cooling from 19° C to ~ 15° C in Unit II sediments from ~5.25 ka BP onward to the top of the record (~ 0.45 ka BP) with the exception of a colder interval (~12° C) at around 1.95 ka BP.

The period of temperature measurement shown on Figure 6 covers part of the period of Ostrea's disappearance by Todorova, Micu & Klisurov (2009). Rachev & Kraychev (2017), summarized that for the period 1906-2006 the trend of the increasing of sea water temperature for the Yalta station is 0.09° C for decade. For the period 1986-2006 it is ~ 1° C for decade. Published temperature values for the period ~ 5.0 - ~ 0.45 ka BP (Coolen et al., 2009) differ from the average annual temperature values for the period 1984-2013 (Fig. 6).
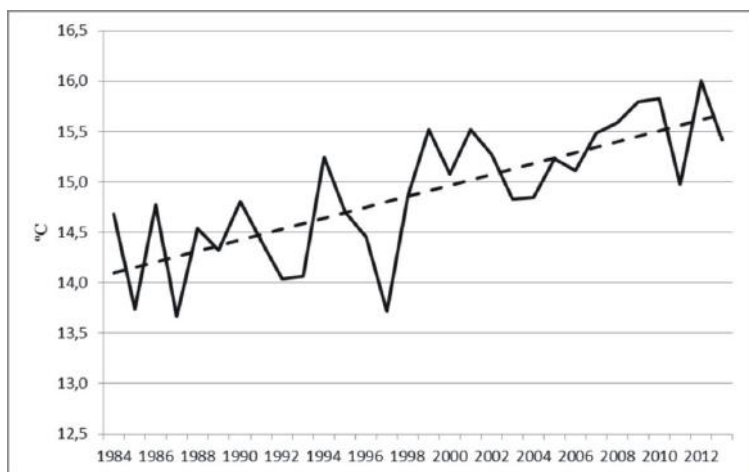

Figure 6. Trend in the average annual surface temperature of Black sea water according to satellite data for the period 1984-2013)[1].

A fluctuations in the temperature can lead to a change in the tolerance of organisms to other abiotic environmental factors. Study of Yakhontova & Piyanova (2010) shows that the mollusks *Ostrea edulis* and other mussels in the Black Sea from wild populations testify to the effect of indeterminable environmental stressors as a cause of satisfactory physiological status. Histological examination did not reveal the presence of Bonamia-like parasite in all studied mollusks.

Content of radionuclides is another very important factor in the marine environment. In many cases radioactive contamination of the water phase can lead to a decrease in species number or total mass in the aquatic ecosystem and can cause irreversible changes in the biological structure of the entire Black Sea. The increase in anthropogenic impacts as well as the change in the radiation situation in the

Black Sea after the Chernobyl accident (1986) are the reasons for us to start some initial measurements of the gamma radionuclides content in sediments collected from the studied area. Two sediment samples (sample 1 - hydrated detritus sand and sample 2 - hydrated detritus sand with whole Ostrea shells) were taken from 14 and 20 m depth at Perla beach area (Primorsko) during the summer in 2019 and were measured by low level gamma spectrometry (Table 1).

Table 1. Gamma radionuclide content (Bq/kg ± SE; SE - measurement uncertainty) in sediments from Perla beach (Primorsko); measurement time – 200000 sec

Sample code	^{137}Cs	^{232}Th	^{234}Th	^{226}Ra	^{40}K
Sample 1	6.22 ± 0.24	8.19± 0.37	< 13	< 1	152 ± 6
Sample 2	5.09 ± 0.24	ND	< 13	< 1	189 ± 7

The data show that the measured values are low and close to the background level. All values are comparable to those obtained in the INRNE-BAS in previous studies of sediments collected at the same region in Primorsko only a few years after the Chernobyl accident - in the period 1992-1996. Strezov et al. (2001, 2002) reported that the data vary in the interval 4.1 and 5.6 Bq.kg^{-1} for ^{137}Cs, between 4.4 – 8.0 Bq.kg^{-1} for ^{232}Th, in the interval 5.7 to 7.6 Bq.kg^{-1} for ^{234}Th and from 4.6 to 5.7 for ^{226}Ra. Higher concentrations (400 - 560 Bq.kg^{-1}) compared to those obtained from us were measured only for ^{40}K. The obtained results are not enough to draw concrete conclusions about the influence of the radionuclides we measured on the behavior of the *Ostrea edulis* species. It is necessary to make additional studies of the mechanisms of absorption, the biokinetics of radionuclides in mussels as well as to monitor the influence of many other factors related to the specificity of the species. Moreover, the oysters of the genera *Ostrea (e.g.O. edulis)* are proven cosmopolitan bio-monitors (Rainbow, 1995).

CONCLUSIONS

Although that there is a need to combine multidisciplinary research of the palaeo and recent climatic and oceanographic environmental conditions, the following conclusions can be drawn: As a result of freshwater basin evolution till ~7.5 ka BP oysters were absent in the Early Holocene Black Sea records, appearing at the midle of the Middle Holocene as a result of salting of the basin and sea temperature fluctuation. It is concluded that *Ostrea edulis* settlead in the Black Sea after ~ 5.0 ka BP, considering the later genesis of the ecozones. Although in published literature the causes of a significant decrease in the abundance of the Black Sea population of flat oysters are still uncertain, the various hypotheses should not be neglected. We draw attention to the fact that the probable cause of the disappearance of *Ostrea edulis* is rather the change of abiotic environmental factors and pollution.

ACKNOWLEDGMENTS

NOTES

1. http://www.iber.bas.bg/sites/default/files/2017/IPU_Kaliakra/IPU-Kaliakra-draft-26-06-2017.pdf

REFERENCES

Algan, O., Çağatay, N., Tchepalyga, A., Ongan, D., Eastoe, C. & Gökaşan, E. (2001) Stratigraphy of the sediment infill in Bosphorus Strait: water exchange between the Black and Mediterranean Seas during the last glacial Holocene. *Geo-Marine Letters,* 20, 209–218.

Coolen, M.J.L., Saenz, J.P., Giosan, L., Trowbridge, N.Y., Dimitrov, P., Dimitrov, D. & Eglinton, T.I. (2009) DNA and lipid molecular stratigraphic records of haptophyte succession in the Black Sea during the Holocene. *Earth and Planetary Science Letters* 284, 610-621.

Filipova-Marinova, M. & Christova, R. (2001) Sea Level Fluctuations in the Western Part of the Black Sea during the Holocene. *Comptes Rendus de l'Academie Bulgare des Sciences*, 54, 5, 59-64

Filipova-Marinova M., Pavlov, D., Coolen M. & Giosan L. (2013) First high-resolution marinopalynological stratigraphy of Late Quaternary sediments from the central part of the Bulgarian Black Sea area. *Quaternary International*, 293, 170–183.

Genov I. (2009). Model of Palaeoenvironmental Evolution of the Black Sea Region during the Last Glacial Maximum-Holocene. *Oceanology* 49 (4), 540–557. DOI:10.1134/S0001437009040122

Genov I. (2016). The Black Sea level from the Last Glacial Maximum to the present time. *Geologica Balcanica*, 45, 3–19.

Genov I. (2018). Correlation of upper Pleistocene-holocene sediments from the deep-water Danube fan and the shelf of the Black Sea. *Comptes rendus de l'Acad´emie bulgare des Sciences*. 71(12), 1665-1671. DOI:10.7546/CRABS.2018.12.11

Giunta, S., Morigi, C., Negri, A., Guichard, F. & Lericolais, G. (2007). Holocene biostratigraphy and paleoenvironmental changes in the Black

Sea based on calcareous nannoplankton. *Marine Micropaleontology*, 63 (1–2), 91–110.

Koleva-Rekalova E., Genov I. & Slavova K. (2018). Aragonite in the Holocene sediments of cores EUXRO01-1 and EUXRO03-3 from the NW Black Sea slope. *Comptes rendus de l'Acade'mie bulgare des Sciences*, 71(7), 930-936. DOI:10.7546/CRABS.2018.07.09

Krastev, T., Parunin, O. & Switoch, A. (1990) Radiocarbon chronology of the latest coastal and shelf deposits in the Bulgarian Black Sea sector, 211-216. *In: Geological evolution of the western part of the Black Sea basin in Neogene-Quaternary time.* Sofia: Publishing house of the Bulgarian Academy of Sciences. (in Russian)

Maathuis, M., Coolen, J., Van der Have, T. & Kamermans, P. (2020). Factors determining the timing of swarming of European flat oyster (Ostrea edulis L.) larvae in the Dutch Delta area: Implications for flat oyster restoration. *Journal of Sea Research,* 156, p.1-11 DOI:org/10.1016/j.seares.2019.101828

Mudie, P.J., Aksu, A.E., & Yašar, D. (2001). Late Quaternary dinoflagellate cysts from the Black, Marmara and Aegean seas: Variations in assemblages, morphology and paleosalinity. *Marine Micropalaeontology*, 43, 155-178.

Porotov, A. (2007). Relative sea-level changes and submersion of archaeological sites along the northern shoreline of the Black Sea. *Journal of Mediterannean geography*, 108, 29-36, DOI:org/10.4000/mediterranee.160

Rachev, N. & Kraichev P. (2017). Changes in the sea surface temperature along the western Black Sea coast for the period 2000–2015, *Annual of Sofia University „St. Kliment Ohridski"*, 110, 1-18. (in Bulgarian)

Rainbow, P. (1995). Biomonitoring of Heavy Metal Availability in the Marine Environment, *Marine Pollution Bulletin,* 31 (4-12), pp. 183-192.

Slavova, K., Genov, I., Koleva-Rekalova, E. & Dobrev, N. (2016). Redeposition of chemical aragonite at the Black Sea sapropel base – proof for early Holocene Black Sea regression, *Comptes Rendus de l'Academie Bulgare des Sciences*. 69(5), 607–614.

Strezov A., Nonova Tz., Ayranov M., Stoilova T. & Mitev K. (2001). Assessment of Radionuclide and Heavy Metal Pollution in Black Sea Sediments and Algae, *In: Proc. 3rd Black Sea Int. Conf. "Environmental protection technologies for Coastal Areas",* Varna, Bulgaria, June 2001, 44-55.

Strezov A., Nonova Tz., Stoilova T. & Petkov P. (2002). Radionuclide and Heavy Metal Content in Marine Ecosystems at the Bulgarian Black Sea Coast*, CIEMS Series ISSN 1563-2727*, 97 – 99

Switoch, A., Taldenkova, E. & Yanina, T. *Marine Holocene along the coast of continents and the island ocean*. Moscow, Science, 1986, 143. (in Russian)

Todorova, V., Micu, D. & Klisurov, L. (2009). Unique oyster reefs discovered in the bulgarian Black Sea. *Comptes Rendus de l'Academie Bulgare des Sciences*. 62(7), 871-874.

Uyan, O. & Aral, O. (2000). A Study on the Possibilities of Obtaining Larva From Native Flat Oysters (Ostrea edulis L.) Living in the Black Sea and Larval Metamorphosis Stage. *Turkish Journal of Zoology*. 24, 343-350.

Yakhontova, I. & Piyanova, S. (2010). Histological investigation of the Black Sea mollusks for the integrated assessment of their population condition. *International Council for the Exploration of the Sea, Session F: Monitoring biological effects and contaminants in the marine environment: where do we go from here?,* ICES CM 2010/ F:45, 7

✉ **Ivan Genov**
https://orcid.org/0000-0002-7528-543X
Institute of Oceanology
Bulgarian Academy of Sciences
Varna, Bulgaria
E-mail: idgenov@io-bas.bg

✉ **Krasimira Slavova**
https://orcid.org/0000-0002-0622-8490
Institute of Oceanology
Bulgarian Academy of Sciences
Varna, Bulgaria
E-mail: slavova@io-bas.bg,

✉ **Tzvetana Nonova**
https://orcid.org/0000-0002-5780-9471
Institute for Nuclear Research and Nuclear Energy
Bulgarian Academy of Sciences
Sofia, Bulgaria
E-mail: nonova@inrne.bas.bg

✉ **Elena Koleva-Rekalova**
https://orcid.org/0000-0003-3066-9015
Geological Institute
Bulgarian Academy of Sciences
Sofia, Bulgaria
E-mail: e_koleva@geology.bas.bg

EFFECT OF ORGANIC MATTER LOADING ON NUTRIENT AND OXYGEN FLUXES AT THE SEDIMENT-WATER INTERFACE IN DIFFERENT SEDIMENTARY HABITATS IN SOZOPOL BAY (SW BLACK SEA): A LABORATORY EXPERIMENT

Stefania Klayn, Dimitar Berov, Ventzislav Karamfilov
*Institute of Biodiversity and Ecosystem Research –
Bulgarian Academy of Sciences (IBER-BAS)*

Abstract. Coastal benthic sediments play an important role in regulating water column nutrient concentrations and primary production via nutrient regeneration and exchanges at the sediment-water interface. This study aimed to characterize the diffusive benthic fluxes of NH_4^+, NO_3^-, PO_4^{-3}, and O_2 in some of the most common shallow sedimentary habitats (fine and coarse sands, seagrass beds, and unvegetated patches within the seagrass beds) along the Bulgarian coast, and their changes under organic loading, through a laboratory experiment. Nutrient fluxes were dominated by a release of NH_4^+ to the water column in all sediment types, and a parallel uptake of NO_3^- by the sediments; both fluxes increased under organic loading, possibly indicating stimulation of nitrate reduction within the sediments. The PO_4^{-3} fluxes were smaller, and the sediments mostly acted as a source for phosphorus under organic loading. O_2 was taken up from the overlying water in all treatments and sediment types, and this flux increased under organic loading, probably in relation to the decomposition of the organic matter and spontaneous chemical oxidation of sulphide ions, released during sulphate reduction within the sediments. The study contributes towards the understanding of nutrient cycling and the role of the benthic compartment in Black Sea coastal soft-bottom habitats.

Keywords: benthic fluxes, sediment-water interface, pore waters, nutrient recycling, coastal zone, Black Sea

INTRODUCTION

Coastal ecosystems, located at the interface of land and sea, and home to a large and continuously growing proportion of the global human population (World Ocean Review, 2017), are subjected to various natural and anthropogenic pressures. Yet, these are some of the most diverse ecosystems, with a wide

variety of habitats, and an important part of global biogeochemical cycles, acting as a buffer for the open ocean from anthropogenic nutrient inputs (Marchant et al., 2014). Eutrophication resulting from increased nutrient inputs to the coastal zone, and consequent deterioration in water quality, continue to be reported worldwide, despite legislative and management measures taken in recent years to reduce loads (Paerl, 1999, Kelly, 2008). Particulate nutrients deposited in coastal sediments may either recycle back into the water column or become retained or transformed in the seabed, depending on physicochemical and biological factors, and particularly the oxygen concentration in the bottom water and advective transport (Ekeroth et al., 2016, Pearce et al., 2017). The benthic compartment can thus act as either a source or a sink for nutrients, and can exert control on the nutrient levels in the overlying water column, especially in shallow environments. The release of nutrients can sometimes lead to secondary benthic-driven eutrophication (Pitkänen et al., 2001). Nutrient fluxes at sediment-water interface, linking the benthic with the pelagic compartment, are a crucial factor affecting nutrient balance and primary productivity in the water column, and from there - a potentially strong determinant of coastal water quality (DiDonato et al., 2006). While many benthic flux studies have focused on compact, non-permeable silts, the sandy sediments, with varying topography and sometimes deep pore water penetration, can provide conditions for efficient remineralization of organic matter and nutrient exchange. They are also some of the most common and widely distributed benthic substrate types, and therefore likely play a significant role in biogeochemical processes (Huettel et al., 2003, Santos et al., 2012). Along the Bulgarian Black Sea coast, Doncheva & Shtereva (2000) registered the highest nutrient fluxes in front of Kamchia River, attributable to the riverine inputs. Doncheva (2010) also found very high sediment-water fluxes in Varna Lake and Varna Bay, especially in summer, which were enough to support hypereutrophic conditions in the lake, and eutrophic - in the bay. However, there are few studies on these processes in the southern Black Sea, where Burgas Bay - the other large bay along the Bulgarian coast, with potentially high water residence times, and which acts as a source of nutrients to the neighbouring coastal waters - is located (Hiebaum, 1990, Hiebaum & Karamfilov, 2005, Berov et al., 2012, Miladinova et al., 2015). This study aims to quantify the interfacial nutrient fluxes in different sedimentary habitat types in Sozopol Bay, and their changes under experimental organic loading, through a laboratory experiment simulating an extreme eutrophication event.

METHODS
Study area and field sampling
Sozopol Bay is a semi-enclosed bay located in the southern part of the Bulgarian Black Sea, and is part of the larger Burgas Bay. The bay is part of the

NATURA 2000 protected area BG0000146 "Plazh Gradina-Zlatna Ribka". The majority of the area is marine, and includes three seagrass meadows, different soft bottom biotopes, and reefs with macroalgae and black mussels. The area is strongly influenced by different anthropogenic pressures from the town of Sozopol, extensive tourism, and fisheries industries in the area. Sampling was carried out during the summer of 2019. 3 replicate core samples (internal diameter 10.5 cm, sampling depth ~20 cm) were collected by Scuba divers from 4 different sedimentary habitats in Sozopol Bay, representing the most common substrates in the area (Figure 1).
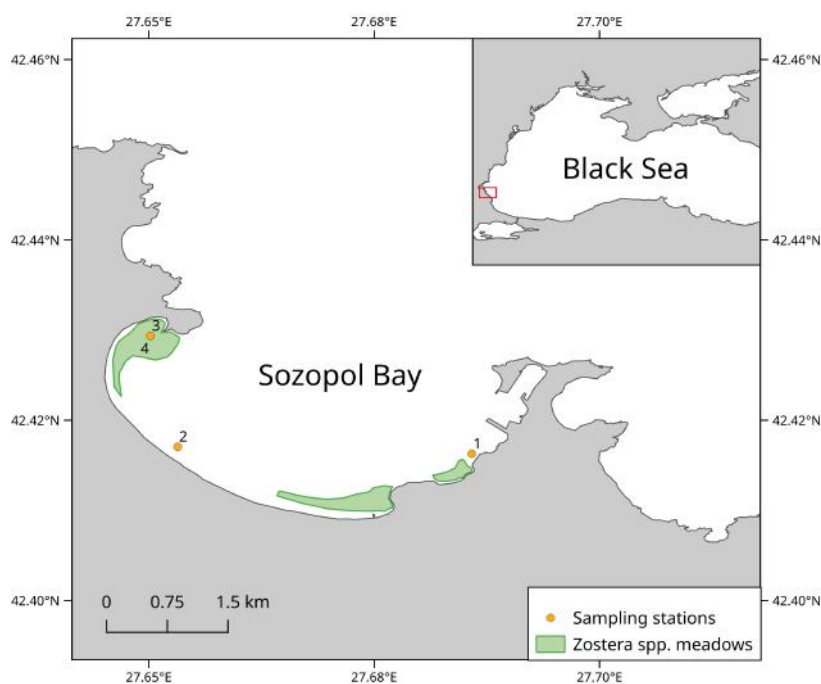

Figure 1. Study area and sampling stations. 1 - coarse sand, 2 - fine sand, 3 - seagrass meadow (Zostera), 4 - unvegetated patch within seagrass meadow (no Zostera). Stations 3 and 4 are adjacent, located within several metres of each other, and so share the same coordinates.

Station 1 has coarse sandy substrate (mean grain size 0.5-1 mm according to the Folk and Ward classification (Folk & Ward, 1957); station 2 - fine sand (mean grain size 0.125-0.25 mm), station 3 - seagrass meadow (*Zostera marina* and *Zostera noltei*), with predominantly fine sandy substrate mixed

with a little silt; and station 4 - an adjacent unvegetated patch within the seagrass meadow ("no Zostera"), with similar substrate, occasionally mixed with mollusk shells and fragments. All stations are located at 4-4.5 m depth. The main characteristics of the sampling sites are presented in Table 1. One of the coarse sand samples was disturbed during handling and transportation, leaving only 2 for that habitat type.

Table 1. Surface sediment characteristics (top 1 cm) at the sampling stations, with the average values for each sample shown in brackets. %TOM - % total organic matter content. Bulk density is derived from dry sediment weight.

Station	Habitat type	%TOM	Porosity $(mL.cm^{-3})$	Bulk density $(g.cm^{-3})$	Water content (%)
1	coarse sand	1.38 (1.35)	0.34 (0.34)	1.09 (1.17)	23.73 (22.60)
2	fine sand	1.28 (1.36)	0.33 (0.19)	1.13 (0.65)	22.33 (22.34)
3	Zostera	1.47 (1.45)	0.58 (0.41)	1.55 (1.13)	27.17 (26.66)
4	no Zostera	1.17 (1.33)	0.46 (0.37)	1.56 (1.24)	22.52 (22.91)

Laboratory experiment

In the laboratory, samples were placed in a gently aerated aquarium, and left to acclimate in near-natural conditions for 1 month. Distilled water was added weekly to maintain water level and salinity. After this period, one replicate per habitat type was used to measure sediment parameters (water content, porosity) and organic matter content. Nutrient ($N-NH_4$, $N-NO_3$, $P-PO_4$) and oxygen concentrations were measured in the water layer immediately overlying the sediment surface, and in the pore waters within the sediments in each of the remaining cores. Pore waters were sampled each cm to 10 cm depth, and oxygen was measured each cm until the detection of persistent anoxic conditions. The nutrient concentrations were measured according to Grasshoff (1976). The oxygen concentrations were measured with a microelectrode (MC100 Microcell O2 meter). Organic matter was determined as weight loss on ignition at 520°C.

One of the two replicates per habitat type was loaded with 6 g dried and finely ground green algae deposited on the sediment surface, or 0.069 $g.cm^{-2}$ - about double the normal surface organic matter content in a typical seagrass bed in the study area (0.03-0.04 $g.cm^{-2}$) (Klayn, 2019). Effectively, this simulates organic loading from an extreme eutrophication event. The other replicate served as control. The sole remaining coarse sand sample was loaded with organic matter. The experiment continued for 39 days, after which the pore water nutrients and oxygen, and the sediment parameters in each sample were measured again according to the same protocol.

Flux calculations

Diffusive fluxes at the sediment-water interface were calculated according to Fick's first law, corrected with the porosity and tortuosity for the particular sedimentary matrix, and expressed in mmol.m^{-2}.day^{-1} (nutrients) and mg.m^{-2}.day^{-1} (oxygen), with positive values representing uptake by the sediments, and negative - release to the water column:

$$F = -\frac{\phi D_0}{\theta^2}\frac{dC}{dx}t$$

ϕ - sediment porosity at the interface; calculated from the sediment samples D_0 - diffusion coefficient of the solute in seawater without the presence of the sediment matrix, corrected for average temperature (25°C for the start and 21°C for the end of the experiment) and salinity (16.5) at the study site and during the experiment (Boudreau, 1997) (Table 2).

Table 2. Specific diffusion coefficients for the solutes in seawater at 21°C (D21) and 25°C (D25).

Solute	D21	D25
O2	0.195	0.216
NH4	0.176	0.191
NO3	0.170	0.185
PO4	0.054	0.060

θ - sediment tortuosity (dimensionless), expressing the influence of the sediment matrix on the diffusion, and calculated based on the porosity as $\theta^2 = 1 - 2ln(\phi)$.
dC - difference in concentration of the solute between the pore water at a particular depth and in the seawater immediately overlying the sediment surface
dx - distance (cm) which the ion has to migrate from that depth to the sediment surface
t - time, as number of seconds in a day (86400).

RESULTS

All sediment types acted as a source of NH_4^+ throughout the experiment, and the magnitude of the flux increased under organic loading - sometimes as much as tenfold, e.g.in the fine sand (Table 3). By contrast, all were a sink of NO_3^-; in most cases the uptake also increased under organic loading (with the exception of the sediments from the unvegetated patch in the seagrass bed). The PO_4^{-3} fluxes were the smallest in magnitude; three of the sediment types subjected to organic loading

had started releasing them to the overlying water at the end of the experiment, and only the coarse sands were taking them up.

Table 3. Diffusive fluxes at the sediment-water interface of oxygen (O2), ammonium (NH4), nitrate (NO3), and phosphate (PO4) in different sediment types from Sozopol Bay at the start of the experiment and 39 days after extreme organic loading. Fluxes are in $mmol.m^{-2}.d^{-1}$ for the nutrients, and in $mg.m^{-2}.d^{-1}$ for the oxygen. Positive values indicate solute uptake by the sediments, and negative - release to the water column.

Habitat type	Solute	Start		End	
		Control	Organic loading	Control	Organic loading
coarse sand	O2	-	13.22	-	50.42
	NH4	-	-34.82	-	-208.13
	NO3	-	126.16	-	180.62
	PO4	-	0.00	-	1.33
fine sand	O2	12.12	12.03	28.17	91.12
	NH4	-197.71	-125.54	-535.98	-1357.14
	NO3	113.51	115.31	145.61	453.99
	PO4	-0.70	0.00	0.00	-9.18
Zostera	O2	35.18	28.66	30.54	40.99
	NH4	-161.48	-20.97	-161.17	-100.00
	NO3	246.18	40.21	243.11	283.45
	PO4	0.98	4.69	-0.79	-1.18
no Zostera	O2	20.57	22.23	20.72	14.32
	NH4	-239.90	-235.93	-44.51	-392.96
	NO3	73.06	111.18	101.48	94.62
	PO4	0.00	0.00	0.53	-1.43

DISCUSSION

The exchange of nutrients between sediments and water is a complex phenomenon which depends on several physical, chemical and biological factors, such as temperature, dissolved oxygen, redox potential, organism activities and organic matter. Our results are comparable to other experimental studies that

found that benthic nutrient regeneration generally increases with organic loading (Kelly et al., 1985). High organic loading also tended to decrease denitrification rates (Sloth et al., 1995). The observed release of ammonium by the sediments and consumption of nitrates could be related to stimulated reduction of nitrates to ammonium within, in anoxic conditions, since by the end of the experiment, most sediment types had become anoxic below 2 cm depth. These results seem to indicate that NH_4^+ dominated the exchange of nitrogen between the sediment and the water column (Chowdhury & Bakri, 2006). The greatest differences in nutrient fluxes induced by the organic loading were observed in the fine sands, although all sediment types exhibited them. There were also differences between the start and the end of the experiment in the controls.

The consumption of O_2 by the sediments was increased in the organic loading treatment at the end of the experiment, likely due to the decomposition of the organic matter and sulphide ions oxidation. It was especially high in the fine sands, which also exhibited the largest differences in N fluxes under organic loading. The PO_4^{-3} fluxes in all sediment types and conditions during our experiment are much smaller than those observed in Varna Lake during the summer, where significant stratification and bottom hypoxia induce a release from the sediments (Doncheva, 2010). No hypoxic conditions were observed in the water layer overlying the sediments during our experiment, but by the end most sediments had become reduced at depths > 2 cm, and a release of PO_4^{-3} to the water column was present. Higher nitrate concentrations in the overlying water have been linked to slower phosphate release from reduced sediments (Gao et al., 2008), which could explain the smaller P fluxes observed.

The amount and quality of organic matter reaching the sediments are known to influence the spatial variability and seasonal differences in sediment nutrient fluxes (Cowan & Boynton, 1996). The algal organic matter used in this experiment is relatively refractory; an eutrophication-induced bloom is more likely to result in accumulation of phytoplankton-derived organic matter, which is more easily decomposed.

This study made apparent the high variability typical for coastal sediments, even at very small scales. The fluxes at the start of the experiment, before any treatment was applied, sometimes differed greatly between replicates of the same sediment type (e.g. Zostera). More replication should be considered in future studies.

The 2-point study design also could be improved by including more intermediary measurements, which would allow tracing the immediate effects of the organic loading on the benthic solute fluxes in the different sedimentary habitats. The macrofaunal communities were not considered in this study, but should be in the future. Benthic faunal activities and behaviour may strongly influence nutrient cycling and fluxes by redistributing organic material, modifying sediment redox conditions, and creating chemical gradients and interfaces for solute exchange. Dense benthic macrophyte cover such as seagrass beds could also alter the fluxes

by capturing nutrients from the water column or from the sediments, and by increasing oxygen penetration in the sediments through the root systems (Renz et al., 2018, Glud et al., 2016).

This study also only considered diffusive fluxes across the sediment-water interface. In natural conditions, and especially for permeable sandy sediments, advection (e.g. through sediment resuspension) can also be an important mechanism, sometimes exceeding diffusive fluxes, and should therefore also be taken into account (Ospina-Alvarez et al., 2014, Pearce et al., 2017).

CONCLUSIONS

Nutrient cycling in coastal marine sediments represents an important ecosystem function, regenerating nutrients for primary producers, and regulating the ability to remove excess (natural or anthropogenic) nitrogen and phosphorus. These processes confer resilience to coastal zones through mitigating eutrophication. Although limited in scope, this study adds to the current knowledge of the influence of sediment type on the nutrient cycling in the coastal Bulgarian Black Sea, and could contribute towards our understanding of the role of coastal benthic habitats in water quality regulation.

REFERENCES

Berov, D., Deyanova, D., Georgieva, I., Gyosheva, B., & Hiebaum, G. (2012). Cystoseira sp.-Dominated macroalgal communities in the SW Black Sea (Burgas Bay, Bulgaria). Current state and possible long-term effects of eutrophication. *Comptes Rendus de L'Académie Bulgare Des Sciences*, *65*(6), 821–830.

Boudreau, B. P. (1997). *Diagenetic models and their implementation: Modelling transport and reactions in aquatic sediments*. Springer Berlin Heidelberg.

Chowdhury, M., & Bakri, D. A. (2006). Diffusive nutrient flux at the sediment-water interface in Suma Park Reservoir, Australia. *Hydrological Sciences Journal*, *51*(1), 144–156. https://doi.org/10.1623/hysj.51.1.144

Cowan, J. L. W., & Boynton, W. R. (1996). Sediment-water oxygen and nutrient exchanges along the longitudinal axis of Chesapeake Bay:

Seasonal patterns, controlling factors and ecological significance. *Estuaries*, *19*(3), 562–580. https://doi.org/10.2307/1352518

DiDonato, G. T., Lores, E. M., Murrell, M. C., Smith, L. M., & Caffrey, J. M. (2006). Benthic nutrient flux in a small estuary in Northwestern Florida (USA). *Gulf and Caribbean Research*, *18*. https://doi.org/10.18785/gcr.1801.02

Doncheva, V. (2010). Nutrients in pore water from surface sediment layer along the eutrophication gradient (Varna Lake - Varna Bay case study). *Comptes Rendus de L'Académie Bulgare Des Sciences*, *63*(4), 547–554.

Doncheva, V., & Shtereva, G. (2000). Preliminary studies of chemical composition of pore waters from sediments along the Bulgarian Black Sea shelf. *Fifth International Conference on Marine Sciences and Technologies - BLACKSEA2000*, 85–87.

Ekeroth, N., Blomqvist, S., & Hall, P. O. J. (2016). Nutrient fluxes from reduced Baltic Sea sediment: Effects of oxygenation and macrobenthos. *Marine Ecology Progress Series*, *544*, 77–92. https://doi.org/10.3354/meps11592

Folk, R. L., & Ward, W. C. (1957). Brazos River bar: A study in the significance of grain size parameters. *Journal of Sedimentary Petrology*, *27*(1), 3–26.

Gao, Z., Zheng, X.-L., Li, W., & Song, H. (2008). Determination of nutrient fluxes across the sediment-water interface in a nitrate-rich reservoir. *2008 2nd International Conference on Bioinformatics and Biomedical Engineering*, 3319–3322. https://doi.org/10.1109/ICBBE.2008.1159

Glud, R. N., Berg, P., Stahl, H., Hume, A., Larsen, M., Eyre, B. D., & Cook, P. L. M. (2016). Benthic carbon mineralization and nutrient turnover in a Scottish sea loch: An integrative in situ study. *Aquatic Geochemistry*, *22*(5), 443–467. https://doi.org/10.1007/s10498-016-9300-8

Grasshoff, K. (Ed.). (1976). *Methods of seawater analysis* (1st ed.). Verlag Chemie.

Hiebaum, G. (1990). *Transformation of carbon in the phytoplankton and bacterioplankton communities of the Burgas bay (in Bulgarian)* [PhD Thesis]. Institute of Ecology.

Hiebaum, G., & Karamfilov, V. (2005). Regime shifts in the annual dynamics of primary production and chlorophyll-a concentrations in the coastal zone of the Bourgas Bay (Western Black Sea). *Large-Scale Disturbances (Regime Shifts) and Recovery in Aquatic Ecosystems: Challenges for Management Towards Sustainability*, 143–158.

Huettel, M., Røy, H., Precht, E., & Ehrenhauss, S. (2003). Hydrodynamical impact on biogeochemical processes in aquatic sediments. *Hydrobiologia*, *494*, 231–236.

Kelly, J., Berounsky, V., Nixon, S., & Oviatt, C. (1985). Benthic-pelagic coupling and nutrient cycling across an experimental eutrophication gradient. *Marine Ecology Progress Series*, *26*, 207–219. https://doi.org/10.3354/meps026207

Kelly, J. R. (2008). Nitrogen effects on coastal marine ecosystems. In J. L. Hatfield & R. F. Follett (Eds.), *Nitrogen in the Environment (Second Edition)* (Second, pp. 271–332). Academic Press. https://doi.org/10.1016/B978-0-12-374347-3.00010-X

Marchant, H. K., Lavik, G., Holtappels, M., & Kuypers, M. M. M. (2014). The fate of nitrate in intertidal permeable sediments. *PLOS ONE*, *9*(8), e104517. https://doi.org/10.1371/journal.pone.0104517

Miladinova, S., Marinov, D., Krastev, V., & Marinski, J. (2015). Multi-compartment water quality assessment of Port Burgas and Burgas Bay. In C. Stylios, T. Floqi, J. Marinski, & L. Damiani (Eds.), *Sustainable development of sea-corridors and coastal waters* (pp. 95–102). Springer International Publishing.

Ospina-Alvarez, N., Caetano, M., Vale, C., Santos-Echeandía, J., Bernárdez, P., & Prego, R. (2014). Exchange of nutrients across the sedimentWater interface in intertidal ria systems (SW Europe). *Journal of Sea Research*, *85*, 349–358. https://doi.org/10.1016/j.seares.2013.07.002

Paerl, H. W. (1999). Cultural eutrophication of shallow coastal waters: Coupling changing anthropogenic nutrient inputs to regional management approaches. *Limnologica - Ecology and Management of Inland Waters*, *29*(3), 249–254. https://doi.org/10.1016/S0075-9511(99)80009-7

Pearce, A. R., Chambers, L. G., & Hasenmueller, E. A. (2017). Characterizing nutrient distributions and fluxes in a eutrophic reservoir, Midwestern United States. *Science of the Total Environment*, *581-582*, 589–600. https://doi.org/10.1016/j.scitotenv.2016.12.168

Pitkänen, H., Lehtoranta, J., & Räike, A. (2001). Internal nutrient fluxes counteract decreases in external load: The case of the estuarial Eastern Gulf of Finland, Baltic Sea. *AMBIO: A Journal of the Human Environment*, *30*(4), 195–201. https://doi.org/10.1579/0044-7447-30.4.195

Renz, J. R., Powilleit, M., Gogina, M., Zettler, M. L., Morys, C., & Forster, S. (2018). Community bioirrigation potential (BIPc), an index to quantify the potential for solute exchange at the sediment-water interface. *Marine Environmental Research*, *141*, 214–224. https://doi.org/10.1016/j.marenvres.2018.09.013

Santos, I. R., Eyre, B. D., & Huettel, M. (2012). The driving forces of porewater and groundwater flow in permeable coastal sediments: A review. *Estuarine, Coastal and Shelf Science*, *98*, 1–15. https://doi.org/10.1016/j.ecss.2011.10.024

Sloth, N. P., Blackburn, H., Hansen, L. S., Risgaard-Petersen, N., & Lomstein, B. A. (1995). Nitrogen cycling in sediments with different organic loading. *Marine Ecology Progress Series*, *116*(1/3), 163–170.

World Ocean Review (2017). *Coasts – a vital habitat under pressure* (WOR5). Maribus. https://worldoceanreview.com/wp-content/downloads/wor5/WOR5_en.pdf

✉ **Stefania Klayn**
https://orcid.org/0000-0003-3610-8155
Institute of Biodiversity and Ecosystem Research
Bulgarian Academy of Sciences
Sofia, Bulgaria
E-mail: stefaniaklayn@yahoo.com

✉ **Dimitar Berov**
https://orcid.org/0000-0001-5235-7800
Institute of Biodiversity and Ecosystem Research
Bulgarian Academy of Sciences
Sofia, Bulgaria
E-mail: dimitar.berov@gmail.com

✉ **Ventzislav Karamfilov**
https://orcid.org/0000-0002-8343-3906
Institute of Biodiversity and Ecosystem Research
Bulgarian Academy of Sciences
Sofia, Bulgaria
E-mail: ventzi.karamfilov@gmail.com

ASSESSMENT OF THE NATURAL LANDSCAPES AS A PREREQUISITE FOR ENVIRONMENTAL RISK ASSESSMENT AND PREPARATION OF MANAGEMENT PLANS

Petja Ivanova-Radovanova

Climate, Atmosphere and Water Research Institute –
Bulgarian Academy of Sciences (CAWRI-BAS)

Abstract. The article discusses a method for assessment of the quality of the natural landscapes in one of the Nature parks in Bulgaria – Rila Monastery Nature Park – as a good practice for the evaluation of the quality of natural resources. The methodology for Rapid Landscape Assessment presented, had been initially developed for the purpose of the development of the management plan of Rila Monastery Nature Park. Significant amount of information from the field have been generated and analyzed by multi-disciplinary team in a relatively short period of time.

It was proved that the approach of rapid assessment is a good practice for cost-effective, rapid and efficient assessment of natural resources. Thus, the methodology can be used in environmental risk assessment of different sites of natural and cultural interest because such sites are normally not only underestimated and also under pressure from different kinds of developments and time constrains.

Keywords: landscape quality; environmental risk assessment; evaluation of natural resources

1. INTRODUCTION

Even though there is a long history of evaluating environmental and ecosystem impacts, the concept of ecological risk has only recently emerged as a distinct field of risk assessment. Assessment of natural resources and risk assessment do not fall exclusively within the domain of any single profession and therefore collection of solid knowledge and further collaboration between all professionals within a multidisciplinary team is essential.

Over last decades there considerable attempt for formulation of conservation policies in landscape protection, such as some international institutions initiated studies for clarification of the terminology in the field of landscape as a basis for harmonizing the criteria and methods for its assessment (Conseil de l'Europe.

2000). In science and practice, different definitions of the basic term landscape were used and most of which are usually formulated on the basis of narrow professional needs (geographical, biological, etc.).There is also reasonable experience resulted multi-disciplinary studies on the diverse issues related to the nature, biodiversity and landscape's place in the environment, economy, recreation and improving the quality of life of people (Coles, Radovanova, 2000), (Dolgov, 2002). Very often the definition does not distinguish between landscape and environment and some authors have accepted that the term "landscape" denotes the appearance of the earth (the earth's surface), emphasizing the possibility of man to design the landscape in an aesthetic way (Giorgis, 1995). According to Convention on the Landscape, adopted in 2000, the landscape is perceived by humans as an area or an area whose appearance and character are the result of the action of natural and cultural (i.e human) factors (Conseil de l'Europe. 2000). The definition, on the one hand, reflects the idea of the evolution of the natural landscape over time under the influence of natural forces and human activity and on the other hand emphasizes that landscape is a whole where the natural and anthropological elements of which are inextricably linked.

The article work in support of the notion that "landscape is a space for experiencing natural beauty" and that is why have to be studied and preserved (Robev,1977). In the last years of development of densely populated urban areas and extensive utilization of natural sites and development of new infrastructure there is an urgent need of regular assessment of the qualities of the landscape (Ulrich, 1986) and development of a local system for evaluation and monitoring and risk assessment of the natural resources, natural, sub-urban and urban landscapes (Radovanova, 2000).

2. METHODOLOGY.

The methodology for Rapid Landscape Assessment (Radovanova, P., Samardjieva,M., 2003) and results presented was developed in support of poorly studied impact of the landscape on the human psyche. This assessment was initiated as a part of the Biodiversity Conservation and Economic Growth project for preparing a management plan for the territory being declared a Nature Par, supported by the USAID (Peev, 2003). The multi-dimensional approach was adopted for enhancement the notion that risk assessment and preservation of the natural resources requires gathering of valuable scientific information for the resources and preliminary evaluation of these existing resources according to the needs and purposely developed criteria. Conservation of nature, biodiversity, landscape and cultural heritage is seen as a holistic process that could be successful only by application of co-creative approach. Number of specific indicators for evaluation of the landscape resources has been identified preliminary to the field work and observations.

After a preliminary discussions and workshops within a interdisciplinary team of experts from natural and social science, and representatives of central government, local institutions, Bulgarian Orthodox Church, small business and NGOs. In case of natural landscape evaluation, these indicators characterized particular features of the surface such as: interesting rock formations, vegetation, rare plant and animal species, the presence of tourist attractions and presence of human interactions and infrastructure. The questionnaires had been developed about quality of the landscape with questions including factors for natural landscapes' quality based on basic concepts and principles of landscape planning and valorisation of the territory. This approach is presented here as a solid base for collection of valuable information which can be used for both risk assessment and management plan development purposes.

The group of experts acting as respondents in the process of assessment of the natural resources on the terrain has been carefully selected as respondents in terms of their experience and knowledge. Additional factor for their selection was the test made for evaluation of the equal understanding of the terms used. Thus, the landscape quality indicators proposed by the author in the questionnaires had been presented to the core group of experts in the area of landscape architecture, forestry, nature conservation, urban planning and design, environmental experts at local authority, environmental non-for government organization and university. Interdisciplinary group of experts also made a ranking list of the indicators proposed according to their importance for the quality of the natural landscapes.

The overall assessment had been implemented in two stages, as followed:

Stage A. Analyses of the existing natural resources

This was the initial stage, which started with the selection of landscape quality indicators, such as interesting rock formations; vegetation; rare plant and animal species; presence of tourist attractions; presence of human interactions and infrastructure.

Stage B. Diagnosis of the existing landscape resources

The stage is related to assessment of the landscape quality on the terrain walking along carefully selected tourist routes and sectors with respect of possibilities different landscape and natural characteristics to be observed. The implementation of the terrain assessment of the landscape resources had been carried out during three site visits with purposely designed examination routes. This part of the landscape assessment had been fulfilled by a small group of experts – landscape architect, forest engineer and sociologist.

3. RESULTS AND ANALYSES

The landscape assessment of the territory was planned for pre-defined purposes of the development of management plan of Rila Monastery Nature Park. The stage

is related to assessment of the landscape quality on the terrain along particularly tracked routes and sectors with possibilities different landscape and natural characteristics to be observed. Overall assessment and evaluation of landscapes had been fulfilled in three parts:

Part A. Analyses of the anasises of the landscape as natural resources

Assessment of landscape elements as a natural resource – rocks and rock formations, forests and shrubs, open spaces (meadows), aquatic elements, plant and animal species, cultural and historical landmarks, infrastructural sites and harmonious sounds;

Part B. Analysed of the assessment of the quality of landscapes

Assessment of the quality of landscapes – the landscapes and their individual elements had been evaluated towards following indicators – picturesque, natural, stable, unique, landscape diversity, typicality, vulnerability, accessibility.

Part C: Ranking of the quality indicators and complex landscape assessment.

Taking into account the information collected, a ranking of the landscape quality indicators by their importance had been made by the experts.

The assessment of the landscape as a natural resource, provide evidence for a rich variety of perspectives, natural elements, flora and fauna presented, sound and touristic sites presented, as follows:

1) Almost all surveyed landscapes – 87.5% – have a rich diversity of perspectives - near, medium and far and were evaluated as very attractive;

2) Water elements existed – lakes, rivers, waterfalls, streams – such as essential part of the natural landscape were present in 62.5% of cases evaluated;

3) Rocks and rock formations – peaks, hills , rocky springs and rivers – are another important element of the landscape value. They were observed in different perspective plans in 62.5% of the studied landscapes;

4) There is a rich variety of flora - vegetation, forest and shrub cover in 68.8% of the studied landscapes;

5) Open spaces, meadows and flower meadows are an element of the landscape in 65.6% of cases;

6) In the majority of the studied landscapes of Rila Monastery Nature Park – 81,25% – there are rare and beautiful plant species;

7) Fauna has also valuable place such as, animal species were detected in 65.6% of the studied landscapes;

8) Natural and harmonic sounds (birdsong, roaring, river, waterfall, insect humming) are heard everywhere in the Nature park in 93.7% of cases;

9) There were also enough tourist infrastructure developed in the area - road, path, hut, shelter, marking – such as it was observed in 84.4% of the studied landscapes;

10) Availability of cultural sites which are specific for the territory has been observed in 9.3% of cases explored.

Assessment of the quality of natural landscape of Rila Monastery Nature Park is indicative for of the high quality of the landscape of Rila Monastery Nature Park:

1) Almost all the studied landscapes – 84, 8% – are highly picturesque and expressive;

2) Almost all landscapes – 90, 62% – are of high stability and durability;

3) Most of the surveyed landscapes in all the surveyed categories – 84, 37% – are evaluated as highly natural and well preserved;

4) Most of the landscapes – 81.5% – have a high degree of originality and uniqueness.

Taking into account the opinion and **ranking made by the interdisciplinary team of experts**, the most important factor for the quality of the landscape, according to experts was factor expressiveness. Second place according to its importance is factor of naturalness (conservation). The third factor is stability, the fourth place is for the factor of uniqueness (rare, exotic), and fifth place is for factor of diversity. The sixth place according to its importance is given to the factor of vulnerability of the landscape and the seventh place is for the accessibility of the given landscape. Last place is given for the typical nature of the landscape on the territory considered. Thus, the complex landscape assessment of the quality of the landscapes investigated had been made and presented (Fig.1). Based on the ranking of the quality of the landscapes, a proposal for planning of the territory of the nature park by zones had been made as a prerequisite for further recommendations for risk assessment, different type of use and development (Fig.2).
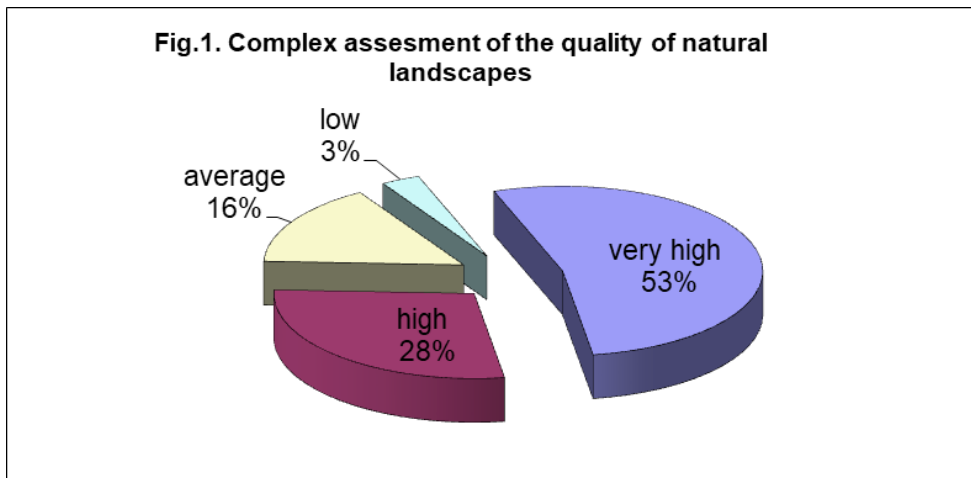

Figure 1. Complex assessment of the quality
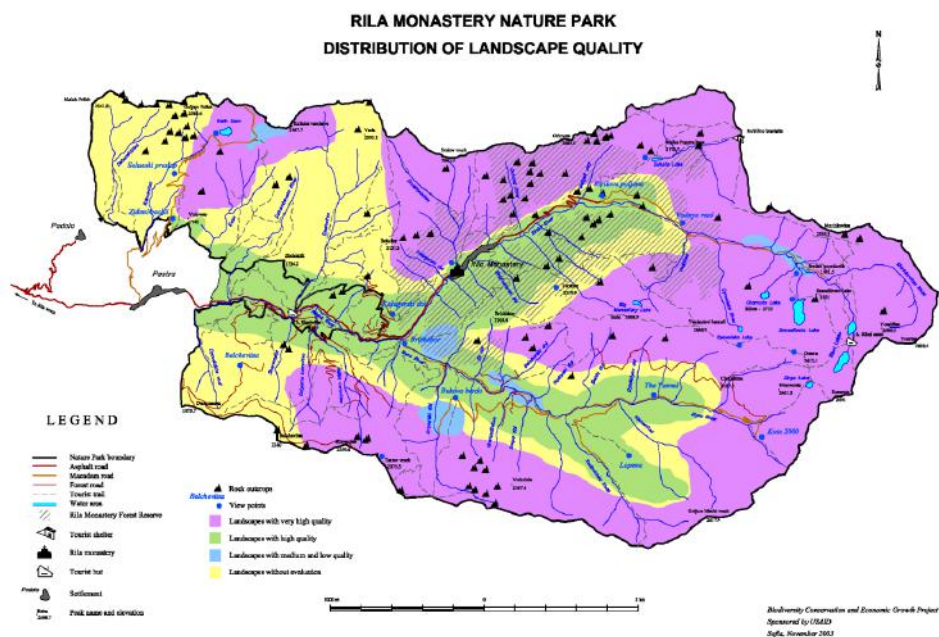of natural landscapes

Figure 2. Zoning of the territory of Rila Monastery Nature Park according to assessment of the landscape quality

4. CONCLUSIONS

It became clear that only healthy ecosystems with preserved nature and rich bio-diversity can provide renewable resources for both nature preservation and local community development. Risk assessment of natural resources and landscapes, based on solid knowledge and understanding for quality of resources available, have been made in accordance with pre-defined indicators.

The method and results presented are good practice for collaboration between professionals within a multidisciplinary team as a way for collection of valuable scientific information about quality of natural amenities as necessary support of zoning, risk assessment and development of management plan for the purpose of both conservation and use of a high quality natural land. This multi-tasked approach is also an excellent example for a tool designed to be applied in relatively short time, by testing specific criteria, according not only to the physical characteristics of the landscapes in nature, but also by assessing quality of landscapes according to socio-psychological impact of the landscapes on the respondents. This methodology could be further replicated and used for rapid evaluation a vast territory and following

risk assessment of any other sites of natural heritage and for further management and valorization of such sites. The method is very useful for environmental risk assessment of different sites of natural and cultural interest also because such sites are normally not only underestimated and also under pressure from different kinds of developments and time constrains.

REFERENCES

Giorgis, S. (1995). Les paysages rureau européens: principes de creation et de gestion. Counseil de l'Europe.

Dolgov K. M. (2002). "Estetika prirodoj". http://philosophy.ru/iphras/;ibrary/estpri.html.

Conseil de l'Europe. (2000). Convention Européenne du Paysage, STE 176. Strasbourg.

Coles, R., Radovanova, P. (2000). Urban open space provision in Sofia and possibility for application of urban and community forest. Proceedings from jubilee international "75 years forest technical education in Bulgaria", Section Landscape architecture and Economic management, 92 – 98.

Peev, D. 2003. Rapid Ecological Assessment of Rila Monastery Nature Park. Report published by the USAID. Sofia: Ministry of Environment and Waters of Republic of Bulgaria.

Radovanova P. and M. Samardjieva. (2003). Rapid Landscape Assessment of Rila Monatery Natura Park. Report for the project of the ARD – Bulgaria No LAG-I-00-99-00013-00, USAID.

Robev, R. (1977). Views and arrangements in landscape management and planning, National Center for Scientific Information. Sofia, Bulgaria.

Ulrich, R.S. (1986). Human responses to vegetation and landscapes .Landscape and urban planning, 13, 29 – 44, Elsevier Science Publishers. The Netherlands.

✉ **Petja Ivanova-Radovanova**
https://orcid.org/0000-0003-2697-333X
Climate, Atmosphere and Water Research Institute
Bulgarian Academy of Sciences
Sofia, Bulgaria
E-mail: p.radovanova@gmail.com

SEISMICITY ON THE TERRITORY OF BULGARIA AND SURROUNDINGS RECORDED BY NOTSSI FOR THE PERIOD 2017-2019

**Dragomir Dragomirov, Emil Oynakov,
Valentin Buchakchiev, Yordan Milkov**
*National Institute of Geophysics, Geodesy and Geography –
Bulgarian Academy of Sciences (NIGGG-BAS)*

Abstract: A map of epicenters of 411 earthquakes with magnitude Mw >= 2.5 that occurred from 2017 to 2019 in Bulgaria and surroundings (sector outlined by latitude = 41°- 44.5^o N and longitude = 22°- 29° E) registered by NOTSSI is presented. Analysis is done on the distribution of the events through time and space, magnitude and depth. The events frequency progression is analyzed for the whole studied period and then compared with each year separately. Generalized analysis is proposed as to what can contribute to variations in the data for the studied period. Catalog of earthquakes with magnitude Mw >= 3.5 is applied.
Keywords: Bulgaria, seismic network, seismicity

INTRODUCTION

The Balkan peninsula is one of the active regions in the Alpine-Himalayan seismic belt. High activity is observed in Western Turkey, Greece, Vrancha region – Romania, Bulgaria, Northern Macedonia, Albania, Serbia. The depth distribution is very characteristic. There are two highly active levels in the range of 20-40 km and 90-110 km and a less active one in 50-70 km.

Bulgaria is an earthquake prone country. Over the past centuries, Bulgaria has experienced strong earthquakes. Some of the European strongest earthquakes during the 20th century have been occurred in Bulgaria. At the beginning of the 20th century, from 1901 to 1928, five strong earthquakes with magnitude larger than or equal to 7.0 occurred on the territory of Bulgaria – 31.03.1901 Ms = 7.2 Shabla earthquake; 04.04.1904 Kresna two earthquakes with Ms magnitudes 7.1 and 7.8; 14.6.1913 Ms = 7.0 G.Orjahovitsa earthquake and two earthquakes near the city of Plovdiv in 1928 - 14.04 with magnitude Ms = 6.8 and 18.04 with magnitude Ms = 7.0.

Strong seismic impact on the territory of Northern Bulgaria have the intermediate earthquakes in Vrancha – Romania region. The strongest being the one in 1944 with

magnitude of 7.7 and some may remember the one in 1977 with magnitude of 7.4 caused a lot of deaths and destructions.

The present study contains generalized information and analysis of the data about the seismic events recorded by the National Operative Telemetric System for Seismological Information (NOTSSI) from 2017 to 2019. Seismic data is gathered in real time by 26 Bulgarian stations and a number of stations from neighbouring countries which increases the accuracy of hypocentral locations. Between 2005 and 2010 almost all stations are modernized and equipped with broadband seismometers. A number of stations also are equipped with accelerometers of type RefTek 131A-02/3 of the company "Refraction Technology". The data from the digitizers DAS 130-01 are collected through the RTPD (Real time protocol demon) module and the data from foreign stations and from Quanterra digital systems are collected with the sl2rptd module.

Data are transferred to the National seismological center in the Geophysical Institute, BAS in real time. Then they are archived in PASSCAL format and additionally in the widely used miniSEED format. The data are processed automatically (relevant signals are recognized and the main parameters of the earthquake are evaluated) by the program Seismic Network Data Processor (SNDP) (Christoskov et al., 2011b). The data are later processed manually by an on-duty seismologist and corrections are made if required. At present the body P-wave magnitude Mp is evaluated by:

$$M_p = log\left(\frac{A}{T}\right)_{max} + \sigma_{BB}(\Delta) + s_j \tag{1}$$

where $\left(\frac{A}{T}\right)_{max} = \frac{V_{max}}{2\pi}$, A is the amplitude in μm, T is a period in s, and V_{max} is the peak ground velocity in μm/s of P-phase recorded on the broadband seismograph vertical-component at epicentral distances less than 10°; $\sigma_{BB}(\Delta)$ is the calibration function; and s_j is the j station magnitude correction.

In the present study Mp is transformed into the more reliable and more widely used Mw magnitude, which would allow the creation of a uniform catalogue for earthquakes, needed for reliable evaluation of the seismic hazard on the territory of the country and surroundings. Mp is transformed into Mw through the formula (D.Solakov et al, 2018):

$$M_w = 0.93 * M_p + 0.31 \tag{2}$$

The high sensitivity of the seismographs allows recording and processing of a great number of local and regional earthquakes. Different magnitude's lower thresholds for reliable determination of local and regional earthquakes are established: Mw=2.5 for the territory of Bulgaria, Mw=3.0 for the central part of the Balkans, Mw=5.0 for regional events. The accuracy of the epicenter location is different; except on the distance it depends also on the epicenter position with respect to the recording network. The parameters of seismic events occurring

at a distance more than 100-150 km outside the territory of Bulgaria should be accepted only informatively and cannot be used for reliable seismotectonic investigation.

After comprehensive analysis of the digital records and application of the above mentioned calculation procedures it is established that 411 of all registered earthquakes for the three-year period are on the territory of Bulgaria and surroundings outlined by space window 41º – 44.5º N and 22º – 29º E. In 2017 the registered earthquakes were 114, in 2018 – 168 and in 2019 – 129. In the Fig. 1 are plotted the earthquake epicenters using different magnitude levels.
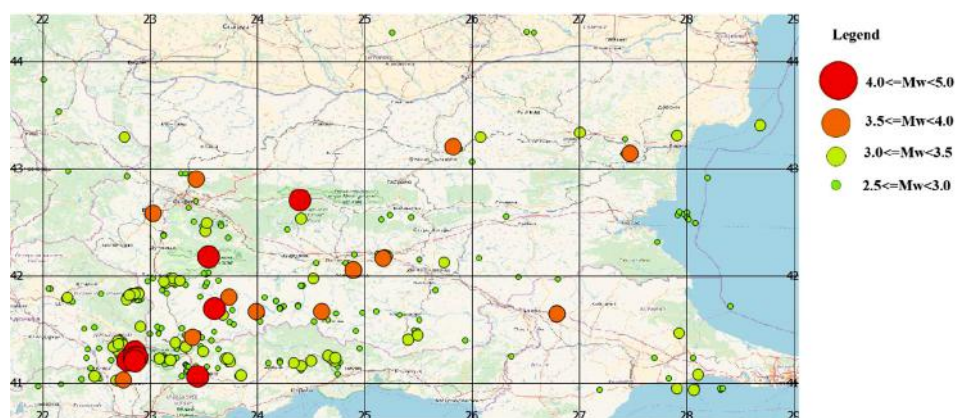
Figure 1. Map with the epicenters of the recorded events.

The number of the events in the magnitude interval Mw=2.5-3 is 305, in Mw=3.1-3.5 - 72, in Mw=3.6-4 - 22, in Mw=4.1-4.5 – 10, Mw=4.6-5 is 2 earthquakes (as shown in Fig.2). This distribution shows that the number of events increases with the decrease of magnitude and that is true for every year (as shown in Fig.3). Fig.3 shows a higher number of earthquakes in every magnitude range for the year of 2018 compared to 2017 and 2019, however that can be contributed to the overall higher number of earthquakes for the whole year of 2018 and the characteristic distribution of number of earthquakes in the different magnitude ranges is preserved. Fig.4 shows that the data fit well with theoretical expectations, meaning that all incoming earthquakes have been detected by the network.

Throughout the studied period 63 earthquakes in total were felt on the territory of Bulgaria from local and regional sources. The strongest event outside Bulgaria during the studied period occurred in the region of Tirana (Albania) with magnitude Mw=6.4. Throughout the studied period and region three earthquakes occurred, generated in seismogenic zones on the teritory of Bulgaria with maximum intensity

in the epicentral zone – V (MSK-64): 11.11.2017, 42.91°N, 23.37°E, Mw=3.9, depth=10km; 26.11.2017, 42.69°N, 24.42°E, Mw=4.2, depth=17km; 21.02.2018, 42.05°N, 24.94°E, Mw=4.3, depth=14km.
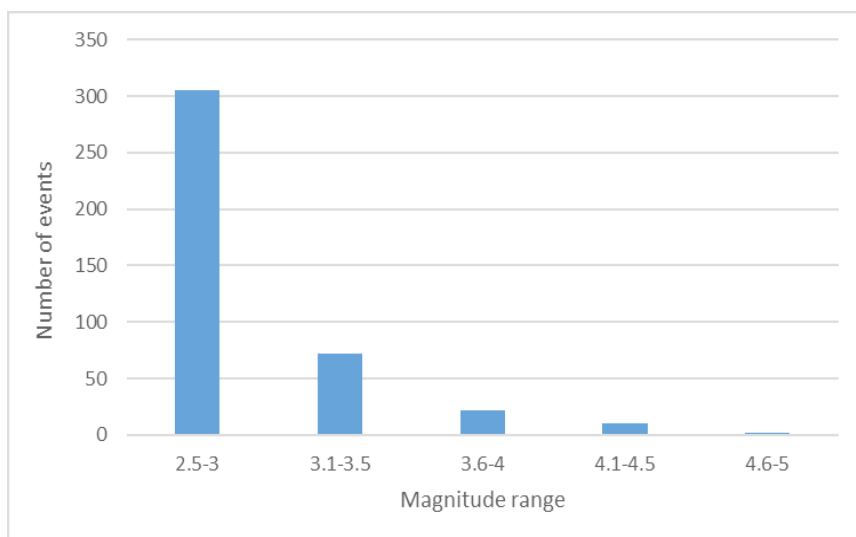

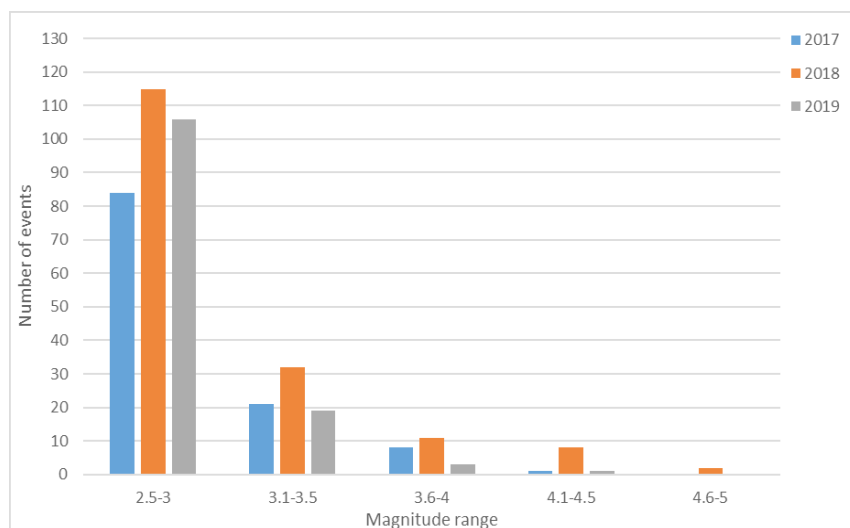**Figure 2.** Magnitude frequency distribution

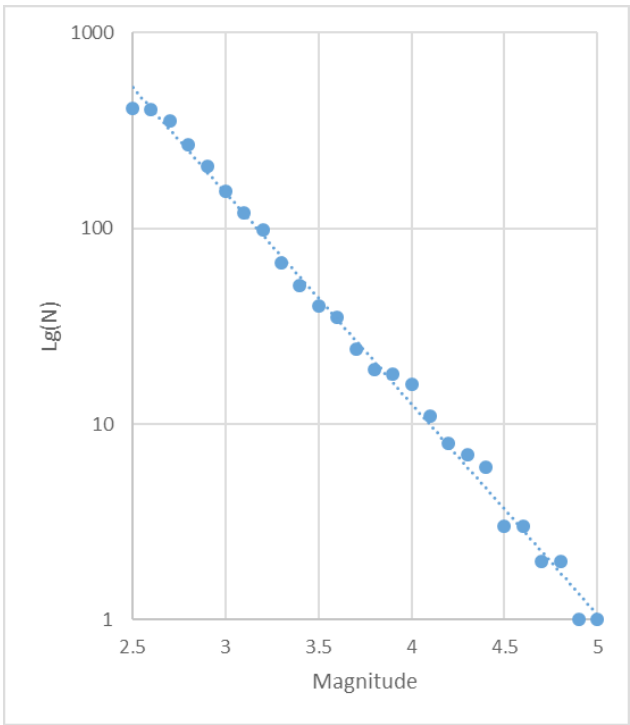**Figure 3.** Magnitude frequency distribution for each separate year

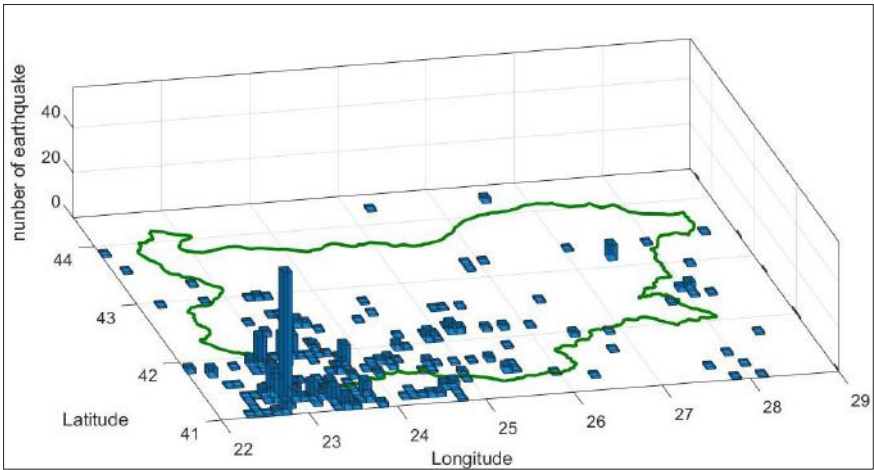**Figure 4.** Cumulative LogN-magnitude distributions of the earthquakes

Figure 5. Number of events according to coordinates

Table 1. List of earthquakes with M w>= 3.5 in Bulgaria
and surroundings during 2017-2019

Date	Time	Latitude [N°]	Longitude [E°]	Depth [km]	Magnitude [Mw]
3.1.2017	22:02:32	43.2	25.83	16	3.8
29.7.2017	3:31:39	41.02	22.75	18	3.7
14.9.2017	1:53:18	42.58	23.03	13	3.6
4.10.2017	12:53:24	41.83	22.83	10	3.5
11.11.2017	4:54:05	42.9	23.43	17	3.9
24.11.2017	17:26:50	41.66	24.6	13	3.6
26.11.2017	19:01:31	42.7	24.4	14	4.1
8.12.2017	4:05:57	41.42	23.4	15	3.9
18.12.2017	17:51:11	41.66	23.99	20	3.6
1.1.2018	22:13:51	41.23	22.85	11	4.3
1.1.2018	22:16:12	41.23	22.87	12	4.0
1.1.2018	22:19:12	41.22	22.86	11	3.7
1.1.2018	23:00:46	41.24	22.86	12	4.0
2.1.2018	4:24:16	41.20	22.85	11	5.0
2.1.2018	4:28:41	41.20	22.79	9	4.0
2.1.2018	17:36:33	41.20	22.86	13	4.5
5.1.2018	3:06:13	41.29	22.86	7	4.0
5.1.2018	9:50:54	41.23	22.87	20	3.5
7.1.2018	22:57:08	41.23	22.87	12	3.5
5.2.2018	9:13:07	41.23	22.88	13	4.4
21.2.2018	23:41:58	42.07	24.91	14	4.7
22.2.2018	23:15:04	42.05	24.89	14	3.8
7.3.2018	22:13:38	43.14	27.48	9	3.7
25.3.2018	15:01:59	41.64	26.79	16	3.7
26.4.2018	0:45:02	42.75	29.88	20	3.6
10.4.2018	9:49:19	42.07	29.35	17	3.6
12.5.2018	6:30:51	42.16	25.17	15	3.5
18.6.2018	9:00:29	41.79	23.74	18	3.5
2.8.2018	14:17:37	41.69	23.60	19	4.3
17.11.2018	12:09:27	41.05	23.44	11	4.1
27.2.2019	16:41:20	41.21	23.74	13	3.9
6.3.2019	06:65:62	42.76	29.22	15	3.5
19.3.2019	03:30:33	41.13	23.34	11	3.6
30.4.2019	18:22:35	43.16	27.47	5	3.6

2.6.2019	13:09:09	41.95	29.2	7	3.7
10.8.2019	06:39:39	41.95	26.43	20	3.6
22.9.2019	12:13:21	41.63	25.34	13	3.6
29.12.2019	17:36:53	41.96	23.47	17	3.8
30.12.2019	18:01:40	42.17	23.55	12	4.3

As usual, the largest concentration of the epicenters in the other regions of Bulgarian territory during the studied period is marked in the southwestern part of the investigated region (presented in Fig.1 and Table 1). The strongest influence on the teritory of Bulgaria from a seismic source, outside of the teritory of the country, in the studied region, was registered on tje 02.01.2018 with epicentral coordinates 41.2°N , 22.85°E and Mw=5.0. The observed maximum intensity in the south-western part of the country was V (MSK-64). From 2017 to 2019 13 events of Mw≥4.0 occurred in this region and almost all of them occurred in 2018. That spike of activity is consistent with the aforementioned earthquake and its foreshocks and aftershocks.

A detailed analysis of seismicity in the individual seismic zones is hard to be fulfilled because of the insufficient quantity of events and the narrow magnitude range of the earthquakes. The joint statistics of all the events in Fig.1 characterize predominantly the seismicity parameters of the southwestern part of the territory under investigation.
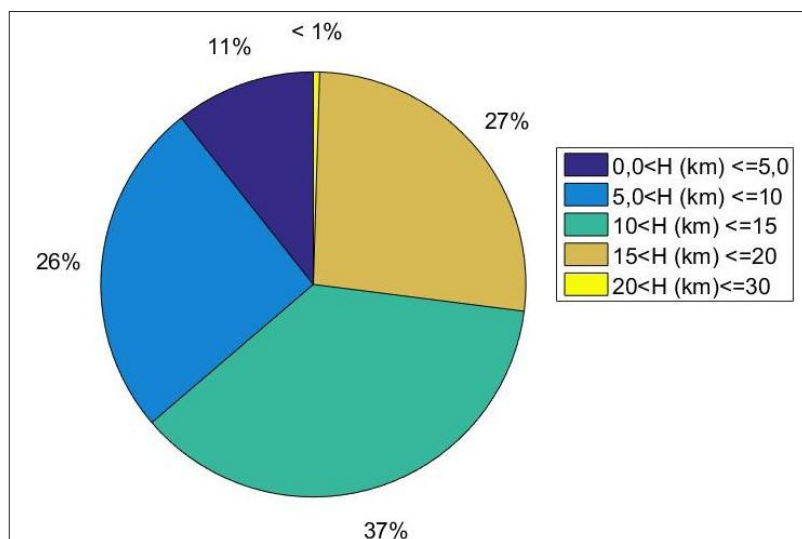

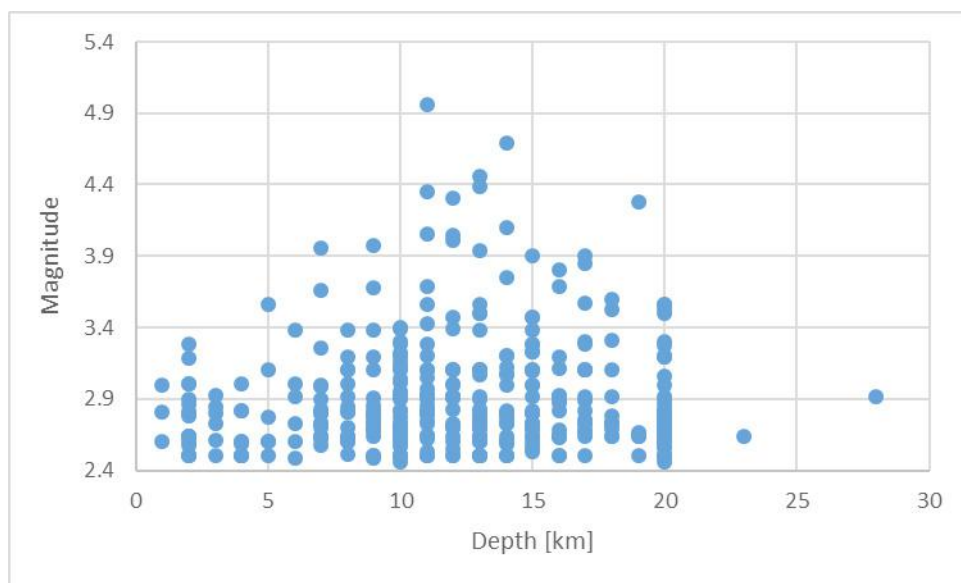**Figure 6.** Depth distribution

Figure 7. Magnitude-depth distribution

The graphs of the depth distribution in Fig.6 and Fig.7 show that the majority of events occur in range 5-20 km depth. Fig.7 does not show correlation between magnitude and depth, as the majority of the events occurred in the 5-20 km depth range. The number of events does not decrease smoothly with increase of the depth. In the same time the number of events in the interval 10-15 km is the largest. The magnitude distribution of the events in depth (Fig.7) permits to note some differentiation of depth "floors" with the increase of magnitude - the maximums can be traced out for the depth interval from 5 to 20 km. The stronger events with magnitude Mw>= 4 have depth in the range10-20 km. The magnitude – depth distribution for the studied period of three years in Fig.7 is consistent with the magnitude – depth distribution for each year.

Fig.7,8 illustrates the distribution of seismicity in time according to the number of events per months. From June to November of 2017 there is a steady increase in activity which can be contributed to the increase in activity in the southwestern region on the territory, however for that period the magnitude of the earthquakes is in the range Mw=2.5-4.1. The highest amount of earthquakes for the studied period is displayed in January and February of 2018, when 43 and 32 earthquakes respectively occurred, and it is associated with seismic activity in South-Western Bulgaria, more specifically foreshocks and aftershocks to an
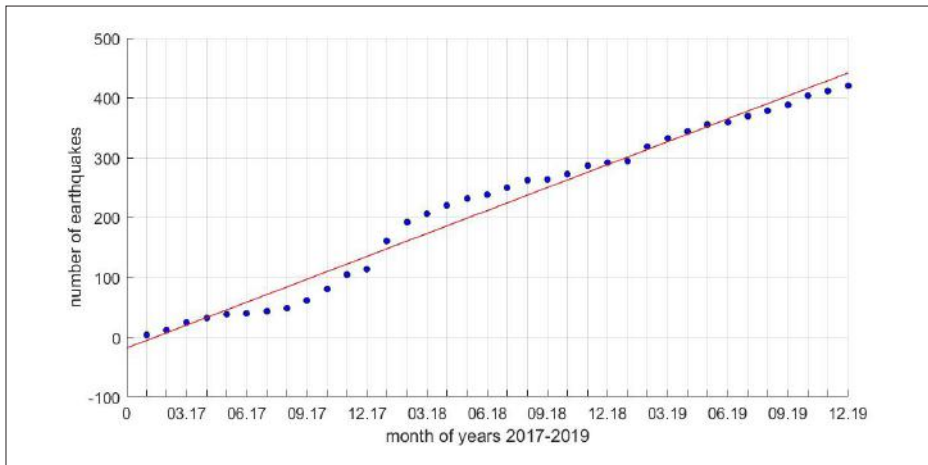
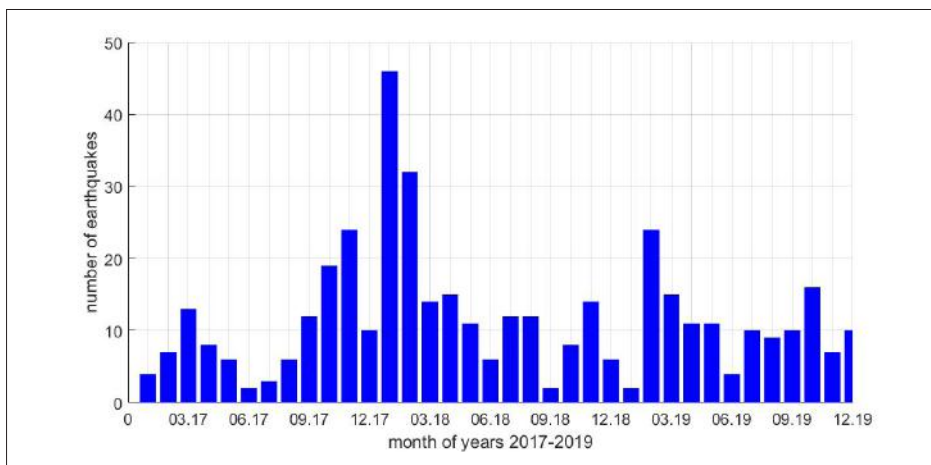**Figure 8.** Number of earthquakes for every month of the considered period

Figure 9. Increase of the number of earthquakes through the months

earthquake with magnitude Mw=5.0 near the Bulgaria-Greece-North Macedonia border. Another spike in activity comes in February of 2019 and it can be contributed to southwestern Bulgarian region and eastern Black Sea, just off the coast of the Burgas region. Fig.8 shows that there is no definite distribution of the earthquakes throughout the months. However, Fig.9 shows a steady increase in the number of earthquakes for the studied period.

REFERENCES

Christoskov L., L. Dimitrova, D. Solakov, 2011b. Digital broadband seismometers of NOTSSI for practical magnitude determinations of P waves. *Bulgarian Geophysical Journal.* v.XXXVIII, N1-4/2011, ISSN 1311-753X, 62-72.

D. Solakov, S. Simeonova, P. Raykova, I. Aleksandrova, 2018. Empirical relations converting Md and Mp magnitudes applied in Bulgarian seismological routine practice to moment and magnitude. Comptes rendus *de l'Acad´emie bulgare des Sciences,* 71, 8, , DOI:DOI:10.7546/ CRABS.2018.08.09, 1076-1085. SJR:0.21, ISI IF:0.27

✉ **Dragomir Dragomirov**
National Institute of Geophysics, Geodesy and Geography
Bulgarian Academy of Sciences
Sofia, Bulgaria
E-mail: drago.n.dragomirov@gmail.com

✉ **Emil Oynakov**
National Institute of Geophysics, Geodesy and Geography
Bulgarian Academy of Sciences
Sofia, Bulgaria
E-mail: emil.ilievmg@gmail.com

✉ **Valentin Buchakchiev**
National Institute of Geophysics, Geodesy and Geography
Bulgarian Academy of Sciences
Sofia, Bulgaria
E-mail: valioka12@gmail.com

✉ **Yordan Milkov**
National Institute of Geophysics, Geodesy and Geography
Bulgarian Academy of Sciences
Sofia, Bulgaria
E-mail: jori@abv.bg

INTRINSIC OSCILLATIONS OF RIVER STREAMFLOWS DETERMINED BY ARIST METHOD

Yavor Chapanov

*Climate, Atmosphere and Water Research Institute –
Bulgarian Academy of Sciences (CAWRI-BAS)*

Abstract. The river streamflows analyses can be successfully used in water resource planning and management, depending on the needs of the wide range users. It is possible to use these applications in several general directions: as informal, qualitative guidance for water managers, stakeholders and decision makers and prediction about long-term drought variability; for quantitative assessments of long-term hydrologic variability and assessment the severity and duration of drought cycles; as direct inputs into hydrologic models of a water system, etc. The long-term oscillations of the river streamflows are influenced mainly by the solar activity and climate interaction, whose variations often consist of synchronous cycles. The intrinsic oscillations of Danube and Don streamflows are determined by the recently created autoregressive method ARIST. These oscillations are compared with the intrinsic oscillations of solar and climate indices and mean Black Sea level variations. Conclusions about the use of intrinsic oscillations in floods or drought prediction are made.

Keywords: river streamflow; ARIST; climate; mean sea level

INTRODUCTION

The global warming, accelerated after 1980, leads to glaciers melting, sea levels rising, large fields areas drying and significant changes in all ecosystems, weather and climate. The main reason of global warming is human activity and releasing heat-trapping gases. The greenhouse gases grout explains the major part of the observed increase of the mean air temperature, but other sources of significant climate variations are solar cycles and connected with them changes of the total solar irradiance, solar wind, interplanetary magnetic field, cosmic rays, space dust, ionospherical effects and etc. The recent anthropogenic effects of global climate change are reviling by a stabile linear increase of the mean temperature, while the solar influence on climate is characterized by significant oscillations with periods of about 11, 22, 45 years and their harmonics. The periodical climate variations, due to solar activity, are connected with oscillations of precipitations and corresponding

river streamflows. The change of river streamflows and water balances are connect-ed with ecological flow and protection of aquatic ecosystems and wetlands. The proper knowledge and forecast of river streamflow cycles is important in manage-ment of effective water regime and environment (Kolcheva, 2016, 2020; Kolcheva and Ilcheva, 2016). Strong correlation in narrow frequency bands between decadal cycles of solar activity, Mean Sea Level (MSL), river streamflow, precipitation and temperature are determined in number of publications. These results are based on known decadal and centennial solar oscillations and their harmonics. Nevertheless, there are several significant spectral peaks outside the solar frequency bands and their properties are important in precise analyzes of climate change and forecasts. The parameter of these intrinsic oscillations will be determined here by the recently created autoregressive method ARIST.

DATA

The used data consist of centennial time series of river Danube and Don stream-flow, MSL variations at Black Sea stations Poti and Batumi, the Palmer Drought Severity Index over South-East Europe and Total Solar Irradiance (TSI) variations. The annual discharge data of 2 large European rivers (Fig. 1) from the following river stations are used (http://www.sage.wisc.edu/riverdata):

– River Danube, station Drobeta – Turnu Severin, country Romania, latitude 44.7°N; longitude 22.42°E, basin area 576232km^2;

– River Don, country Russia, station Razdorskaya, latitude 47.50°E; longitude 40.67°N, basin area 378000km^2.
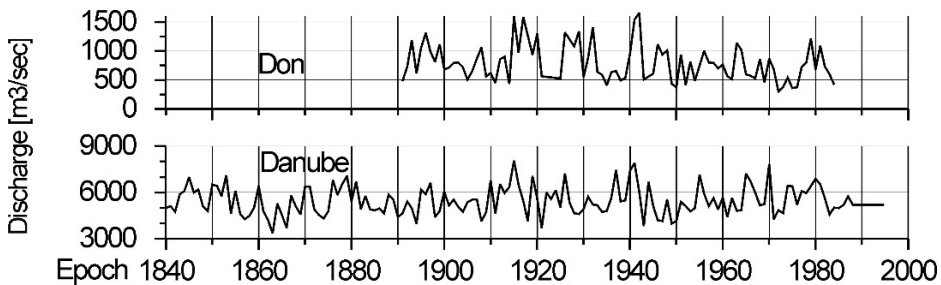

Figure 1. Annual discharge of rivers Don and Danube

The Palmer Drought Severity Index (PDSI) (Palmer, 1965) represents the severity of dry and wet spells. It is based on monthly temperature, precipitation and soil-water holding capacity data. The global PDSI data (Dai et al., 1998; 2004) consist of the monthly surface air temperature (Jones and Moberg 2003) and precipitation (Dai et al., 1998; Chen et al., 2002) over global land areas from 1870 to 2006. These data is represented as PDSI values in global grids 2°.5′2°.5. The

Palmer classification of drought conditions is in terms of minus numbers: between 0.49 and -0.49 – near normal conditions; -0.5 to -0.99 – incipient dry spell; -1.0 to -1.99 - mild drought; -2.0 to -2.99 – moderate drought; -3.0 to -3.99 – severe drought; and -4.0 or less - extreme drought. The positive values are similar about the wet conditions. The PDSI variations over the South-East Europe are determined for area between longitude $10° – 30°$ E and latitude $32°.5 – 50°$ N. This area consists of 44 grids of the global PDSI data and the individual values of PDSI variations are calculated by means of robust Danish Method (Kubik, 1982; Juhl, 1984; Kegel, 1987). This method allows to detect and isolate outliers and to obtain accurate and reliable solution for the mean values. The calculated values of the PDSI variations over South-East Europe by the Danish Method are shown in Fig. 2
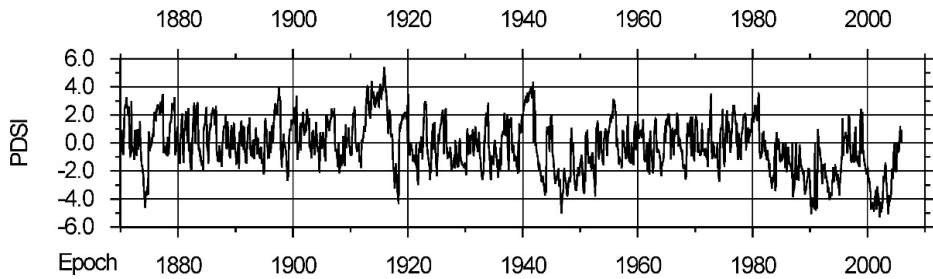

Figure 2. Variations of the PDSI over South-East Europe

The estimated TSI for the last 400 years (Fig. 3) is based on the NRLTSI2 historical TSI reconstruction model (Kopp et al., 2016; Lean, 2010; Coddington at al., 2016).
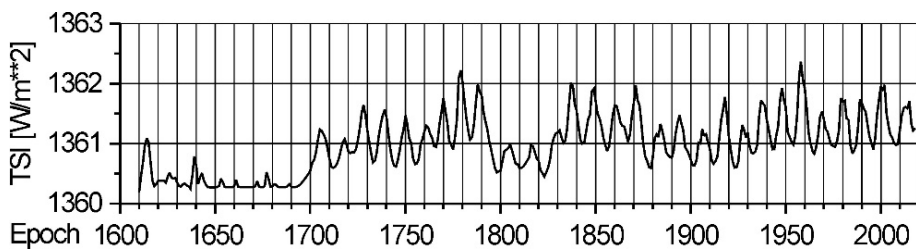

Figure 3. TSI variations

The provided by the Permanent Service for Mean Sea Level data of monthly variations of the mean level of Black sea consist of several mareograph stations, where the data from stations Poti and Batumi, cover time span larger than a century (Fig. 4).
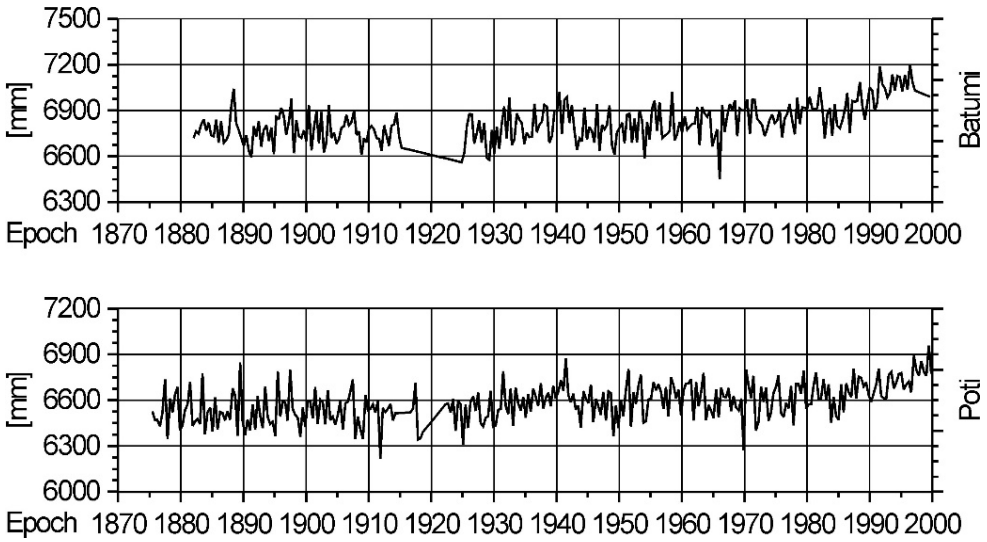
Figure 4. MSL variations at stations Batumi and Poti. The linear trends are removed

METHODS

The iterative regression method (ARIST) is used to determine amplitudes, phases and periods of unknown oscillations in the time series connected with some problems of astrometry, Earth rotation and geodynamics. The properties of the method are investigated by means of simulated time series and real data.

The iterative regression method ARIST (Wolberg, 1967; Rigozo and Nordemann 1998; Rigozo et al., (2005) is an iterative least square method for determination the amplitudes, phases and periods of unknown oscillations in the observational and time series.

Let the observations in n epochs t_i are $Y_i^{(0)}$ and the unknown parameters of k-th oscillations are the amplitude $A^{(k)}$, frequency $w^{(k)}$ and phase $j^{(k)}$. The so-called conditional function $F_i^{(k)}$ is

$$F_i^{(k)} = Y^{(k)} \quad A^{(k)} ù \left(\omega^{(k)} t \quad \varphi^{(k)} \right), \, i=1,\ldots,n, \, k=1,\ldots,m, \qquad (1)$$

where $Y_i^{(k)}$ is the conditional function for the k-1-th oscillation

$$Y_i^{(k)} = F_i^{(k-1)}. \qquad (2)$$

The corrective terms $X_1^{(k)}$, $X_2^{(k)}$, $X_3^{(k)}$ are calculated for every iteration by means of the Least Squares Method.

$$X = N^{-1}W,\tag{3}$$

where

$$X = (X_1^{(k)}, X_2^{(k)}, X_3^{(k)})^{\mathrm{T}},$$

$$N_{pq} = \sum_{i=1}^{n} \frac{\dfrac{\partial F_i^{(k)}}{\partial X_p^{(k)}} \dfrac{\partial F_i^{(k)}}{\partial X_q^{(k)}}}{P_i^{(k)}}, \quad p=1,\ldots,3, \; q=1,\ldots,3,\tag{4}$$

$$W_p = \sum_{i=1}^{n} \frac{\dfrac{\partial F_i^{(k)}}{\partial X_p^{(k)}} F_i^{(k)}}{P_i^{(k)}}, \quad p=1,\ldots,3.$$

The weighing coefficients $P_i^{(k)}$ are

$$P_i^{(k)} = D_Y^{(k)} + \left(\frac{\partial F_i^{(k)}}{\partial t} \right)^2 D_t^{(k)},\tag{5}$$

where $D_Y^{(k)}$ and $D_t^{(k)}$ are dispersions associated to $Y^{(k)}$ and t, respectively. The corrective terms are applied to the unknown parameters as follows:

$$A^{(k)} = A_0^{(k)} - X_1^{(k)},$$
$$w^{(k)} = w_0^{(k)} - X_2^{(k)},\tag{6}$$
$$j^{(k)} = j_0^{(k)} - X_3^{(k)},$$

where $A_0^{(k)}, w_0^{(k)}, j_0^{(k)}$ denote values from the previous iteration.

RESULTS
FFT spectra

The time series spectra are calculated by the Fast Fourier Transform (FFT), shown in Fig. 5. The Danube streamflow spectrum is coherent with the spectrum of PDSI variations over SE Europe, while the spectrum of Don streamflow is coherent with Danube and PDSI variations for 22-year oscillations only. The FFT spectrum of the PDSI variations over the South-East Europe (Fig.5) consists of several significant peaks below 10a and three greatest peaks, closed to the periods of the solar activity – 11a, 22a and 45a. This spectrum points out that the long-term of PDSI variations over the South-East Europe are dominated by decadal oscillations whose frequencies are close to solar cycles. The MSL station spectra have individual decadal peaks.
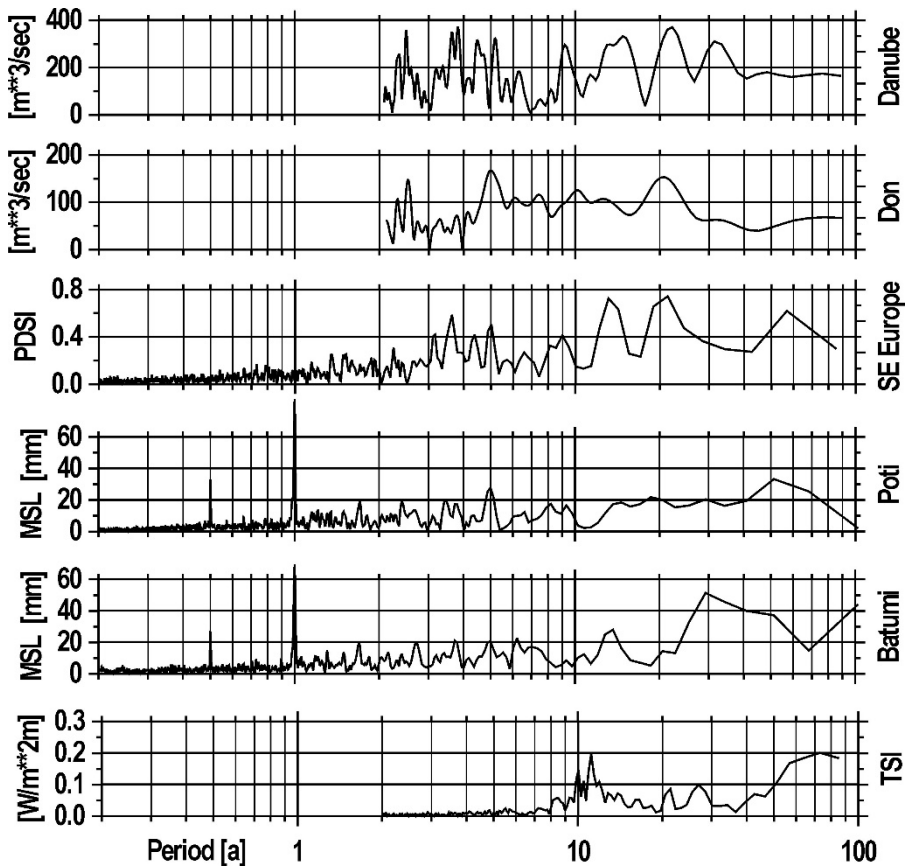
Figure 5. FFT spectra of the time series

Intrinsic periods of the time series

The ARIST Method determines a lot of oscillations of the chosen time series. Some of the obtained values of the intrinsic periods are grouped around of the most significant oscillations. The results are shown in Table 1. All time series have oscillations with periods below 10 years, and some of them are connected with the harmonics of the solar cycles. The Method ARIST does not discover long-term oscillations of station Poti, probably due to the high-level noise in the data. Some oscillations with periods between 10 and 20 years are close to the 11-year sunspot cycles and harmonics of bicentennial solar oscillations. One of determined oscillations with periodicity between 20 and 30 years corresponds to solar magnetic cycle, and other – to solar harmonics. The oscillations with periods above 22 years play important role in long-term analyses and their estimates may improve forecasts.

Table 1. Periods in years of intrinsic oscillations determined by ARIST Method

Time series	Below 10yr	10-20yr	20-30yr	30-40yr	40-60yr	Above 60yr
Danube	2.3; 3.4; 7.9; 8.4; 9.4; 9.8	11.5; 13.8; 17.1; 19.6	23.3; 24.9	33.0; 38.2	51.6	77.4; 109.5
Don	3.6; 5,3; 5.7; 6.2; 7.7; 9.3	12.4; 15.4	23.2; 25.2	31.0	46.5	64.6; 93.0
PDSI	5.6; 6.9; 8.3; 9.5	10.0; 10.7; 12.2; 13.0; 15.1; 16.2	21.5; 29.8	34.6; 36.6	-	125.5
Poti	1.5; 1.7; 2.0; 2.5; 2.7; 3.2; 6.5; 8.6; 9.2	-	-	-	-	-
Batumi	2.0; 2.5; 2.9; 4.8; 7.3; 9.5	13.8; 15.5	-	35.4	-	-
TSI	2.4; 3.3; 5.1; 7.5; 8.7; 9.5; 9.7	10.0; 10.5; 10.7; 11.0; 11.3; 12.7; 13.1; 14.6; 15.1; 15.7; 18.2	21.5; 22.7; 26.5; 27.2;	31.4; 34.0	40.8; 45.3; 51.0; 58.3	68.0; 81.6; 136.0; 204.0

CONCLUSIONS

The iterative regression method ARIST determines amplitudes, phases and periods of unknown oscillations in the time series. The knowledge of precise values of the periods of intrinsic oscillations of climate and water time series may significantly improve the long term forecasts. These oscillations should be used together with the known response of climate indices to the solar cycles and their harmonics.

REFERENCES

Chen, M., P. Xie, J.E. Janowiak, and P.A. Arkin (2002). Global land precipitation: a 50-yr monthly analysis based on gauge observations. J. Hydrometeorol., 3, 249 – 266.

Coddington, O., Lean, J.L., Pilewskie, P., Snow, M., Lindholm, D. (2015). A solar irradiance climate data record. *Bull. American Meteorological Soc*. 97(7), 1265-1282, doi:10.1175/BAMS-D-14-00265.1.

Dai, A., I. Fung, and A. D. Del Genio (1997). Surface observed global land precipitation variations during 1900 – 1988. J. Climate, 10, 2943 – 2962.

Dai, A., K. E. Trenberth, and T. Karl, (1998). Global variations in droughts and wet spells: 1900 – 1995. Geophys. Res. Lett., 25, 3367 – 3370.

Dai, A., K. E. Trenberth, and T. Qian (2004). A global data set of Palmer Drought Severity Index for 1870 – 2002: Relationship with soil moisture and effects of surface warming. J. Hydrometeorology, 5, 1117 – 1130.

Jones, P.D., and A. Moberg (2003). Hemispheric and large-scale surface air temperature variations: An extensive revision and an update to 2001. J. Climate, 16, 206 – 223.

Juhl, J. (1984). The "Danish Method" of weight reduction for gross error detection, *XV ISP Congress proc., Comm. III*, Rio de Janeiro.

Kegel, J. (1987). Zur Lokalizierung grober Datenfehler mit Hilfe robuster Ausgleichsfervahren, *Vermessungstechnik*, 35, №10, Berlin.

Kolcheva, K. (2016). Experimental research on the effective water abstraction permitting regime, *BJMH*, Vol. 21, No 1 – 2.

Kolcheva, K. (2020). Adapting the public water supply to climate change, *Journal of Environmental Protection and Ecology* Vol. 21, Iss. 1, 280 – 292.

Kolcheva, K., Ilcheva, I. (2016). Water abstraction management and environment, *Journal of International Scientific Publications*, Vol. 10, page 145 – 165.

Kopp, G., Krivova, N., Lean, J., and Wu, C.J. (2016). The Impact of the Revised Sunspot Record on Solar Irradiance Reconstructions, *Solar Physics*. doi: 10.1007/s11207-016-0853-x

Kubik, K. (1982). An error theory for the Danish method, *ISP Symposium, Comm. III*, Helsinki.

Lean, J.L. (2010). Cycles and Trends in Solar Irradiance and Climate, Wiley Interdisciplinary Reviews, *Climate Change* 1. doi: 10.1002/wcc.018.

Palmer, W. C. (1965). Meteorological Drought. Res. Paper No.45, U.S. Weather Bureau, Washington, 58pp.

Rigozo, N.R., Nordemann, D.J.R. (1998). Analise por iterative regression de periodicities em series temporais de registros geofisicos, *Revista Brasileira de Geofisica* v.16 (2/3), 149 – 158.

Rigozo, N.R., Echer, E., Nordemann, D.J.R., Vieira, L.E.A., de Faria, H.H. (2005). Comparative study between four classical spectral analysis methods, *Applied Mathematics and Computation* v.168, 411 – 430.

Wolberg, J.R. (1967). *Prediction Analysis*, D. Van Nostrand, 291 pp.

✉ **Yavor Chapanov**
http://orcid.org/0000-0002-6159-3554
Climate, Atmosphere and Water Research Institute
Bulgarian Academy of Sciences
Sofia, Bulgaria
E-mail: yavor.chapanov@gmail.com

INITIAL ASSESSMENT OF COMPOSITION, ABUNDANCE, SPATIAL DISTRIBUTION AND HOTSPOTS IDENTIFICATION OF FLOATING MACRO-LITTER IN THE BULGARIAN BLACK SEA WATERS

Violeta Slabakova, Ivelina Zlateva, Krasimira Slavova
Institute of Oceanology – Bulgarian Academy of Sciences (IO-BAS)

Abstract: The present research is focused on composition, density, distribution and identification of accumulative areas of floating marine litter (FML) in the Bulgarian Black Sea coastal, shelf and offshore waters. Macro-debris abundances were determined in compliance with MSFD protocol for visual observations based on fixed-width strip transect method. Six floating litter monitoring surveys were carried out between 2017 and 2019. Over 144 hours of visual observations were performed in a total of 288 transects, covering an overall survey area of 7.52 km^2. 1320 litter items were identified and classified during the campaigns of which 90% were detected as plastic materials. The presence of floating debris was observed throughout the entire study area with density ranging from 0 to 1750 items km^{-2} and average density of 170 items km^{-2}. Unexpectedly marine litter concentration patterns were evenly distributed among the studied regions with some specifics at certain sites.
Keywords: Black Sea, floating marine litter, monitoring, MSFD

INTRODUCTION

The litter is present across the entire marine environment due to anthropogenic activities. Large quantities of debris have been observed and documented on beaches (Galgani et al., 2015), the seafloor (Maes et al., 2018) and floating at the surface (Galgani et al., 2015) of the European seas. Some of the highest densities of marine litter have been recorded in marginal seas such as Mediterranean and Black Sea (Galgani et al., 1996; Ioakeimidis et al., 2014; Suaria & Aliani, 2014). In the Black Sea, plastics are recognized as the dominant category in all domains – beaches (Muresan et al., 2018; Simeonova & Chuturkova, 2019), sea surface (Suaria et al., 2015), and the sea floor (Moncheva et al., 2016, Raykov et al., 2020),

however comprehensive data for floating litter is still absence for the Bulgarian Black sea waters. The present study aims to investigate the current state as well as to draw an initial assessment of composition, abundance, spatial distribution and hotspots identification of FML in the Bulgarian Black Sea waters.

The Marine Strategy Framework Directive (MSFD, 2008/56/EC) has forced Member States to achieve or maintain Good Environmental Status (GES) by 2020[1]. MSFD is based on the monitoring of 11 Descriptors, of which Descriptor 10 is corresponding to marine litter. In compliance with these priorities and for proper implementation of MSFD, in 2017 Bulgaria has started regular observations of marine litter. The present study is based on data collected within the period 2017-2019, aiming to present the assessment outcome and to further conduct activities, related to identified hotspots and to draw recommendations for improved monitoring.

MATERIAL AND METHODS

Three distinct regions – coastal, shelf and open sea at area specific depths (0 – 30 m, 30 - 200 m and > 200 m), were selected to investigate the spatial distribution, abundance and composition of FML (Fig. 1), according to the requirements of National Marine Litter Monitoring Program[2] and delineation of pelagic habitat of the Bulgarian Black Sea waters (Moncheva, Todorova, et al., 2012; Peneva, Slabakova & Moncheva, 2013).
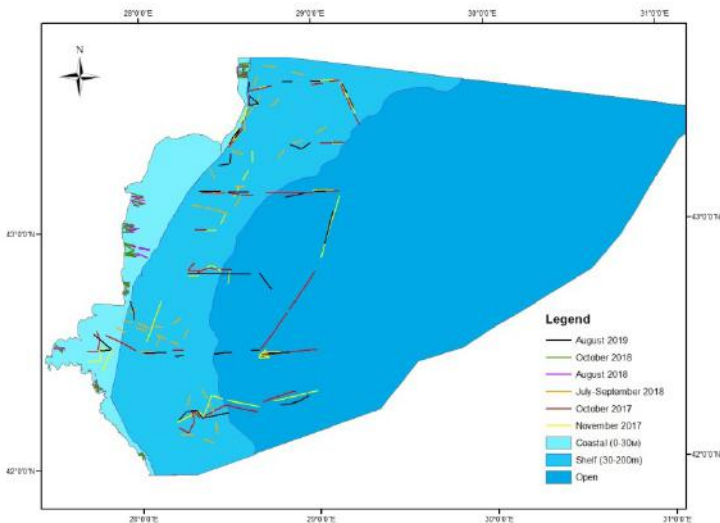

Figure 1. Study area (coastal, shelf and open regions) with total transects and yearly surveys performed during 2017-2019 in standard effort conditions (≤5 m/s).

Six FML monitoring surveys were carried out between 2017 and 2019 in the Bulgarian Black Sea waters (Fig. 1). Three of them were carried out onboard R/V "Akademik" in the shelf and offshore regions in the autumn of 2017 and in the summer of 2019; one campaign in the shelf waters with fishing vessel during July-September 2018 and two surveys were conducted by rigid-hull inflatable boat in the coastal area during the summer and autumn in 2018. Visual observations for FML (> 2.5 cm) were performed following the protocol proposed by the MSFD TG10 Guidance on Monitoring of Marine Litter in European Seas (Galgani et al., 2013). The surface litter was assessed based on fixed-width strip transect method (Thiel et al., 2003). Observations were carried out at speed around 5.5 (± 0.5) knots, approximately 3 m above sea level for the shelf and offshore areas and 1m for coastal region. FML was recorded from the bow of the vessels/boat by skilled observer, covering each side of the ship within 3 m observation corridor at each side of the vessels or 2 m for the inflatable boat. The length of each transect was measured according to start-end geographic coordinates recorded by portable GPS connected to computer. In order to standardize the survey effort, the duration of observations was fixed to 30 min, corresponding to the mean transect length of 4.75±0.7 km. All transects were observed under low wind speed conditions recorded with a portable anemometer (≤ 5 m/s) and good visibility.

Over the entire sampling period, a total of 288 transects were performed as 67 out of which were free of litter. A distance of 1367 km was covered corresponding to 144 h of observations. Detailed information regarding the survey area and number of transect and density per region is presented in Table 1.

Table 1. Survey effort data: number of transects, transect lengths, surveyed area and total number and density of FML.

Region	Number of transect (N)	Number of litter free transect (N)	Total survey length (km)	Total surveyed area (km²)	Litter items (N)	Avg. Density (item km⁻²)	Min Density (item km⁻²)	Max Density (item km⁻²)
Coastal	80	31	344	1.38	206	146	0	1750
Shelf	144	28	709	4.26	624	146	0	907
Open sea	64	8	314	1.88	490	252	0	857

Litter items were identified according to type and size. The FML items were classified in 7 categories according to the type of the material (Artificial polymer materials, Rubber, Cloth/Textile, Paper/Cardboard, Processed wood, Metal and Unidentified) and their relevant subcategories (in total 48 subcategories)[2]; additionally, six size classes were recorded (2.5-5 cm; 5-10 cm; 10-20 cm; 20-30 cm; 30-50 cm; > 50 cm).

FML density, expressed in number of items km^{-2} was calculated using the formula (Hinojosa & Thiel, 2009):

$$D = N/(W/1000) \times L \qquad (1)$$

where: N is the number of observed floating litter items, W is a distance perpendicular to the transect in m and L is the length of the transect in km. No specific correction (Ryan, 2013) or methodology (Buckland et al., 1993) regarding the effective strip width was applied.

The ESRI software ArcMap 10.2 was used to visualize the survey transects and to calculate the length and area covered by each visual observation as well as to produce the Kernel density map showing the geographical presentation of regions with higher probability of floating litter occurrence (Sá et al., 2016).

K-means cluster analysis was applied to detect groups of transects per area (coastal, shelf and open sea), aiming identification of hotspots for further investigation and improved monitoring, as well as areas with lower litter densities. Analysis of similarities (ANOSIM) and nonmetric multidimensional scaling (NMDS) were implemented additionally to provide an overview of litter distribution patterns and data similarities per area and categories. All statistical analyses and graphic representations were performed using the statistical and programming software R 3.6.2 (R Core Team, 2019), packages 'vegan' and 'ggplot2' (Jari Oksanen et al. 2019), available through the CRAN repository (www.r-pro ject.org).

RESULTS AND DISCUSSION

Percentage shares of FML major categories in the entire survey is presented in Fig. 2, the most abundant category is Plastics representing 90% of the overall litter quantities detected in the studied regions, followed by 5.63% share of Paper/Cardboards category and 1.22% accounted for Processed wood category.

Plastics subcategories by percentage share for a) coastal, b) shelf and c) open sea regions are presented in Fig. 3. The most abundant plastic subcategories in the entire study region were G124 (Another plastic items) – 35% and G79 (Plastic items) – 25%. The top 3 subcategories of the plastic materials identified in coastal area were G124 – 35%, G79 – 18% and G82 (styrofoam pieces) – 11%. Identical trend is observed in the shelf and offshore regions for subgroups G124 (38% and 32%, correspondingly) and G79 (28% and 25% respectively) with exception of group G82. The lowest percentages shares of plastic litter items observed below 1 % (in the shelf area) were: G63 (buoys) – 0.2%; in the open sea area; G67 (industrial packaging and plastic plots) – 0.2%; G94 (plastic covers and oilskin) – 0.2%.

Distribution FML size classes per study regions is presented in Fig. 4. The dominant class registered in the three studied domains is Class A with size ranging from 2.5 to 5 cm and Class B (5-10 cm), size classes C and F denoted equal shares
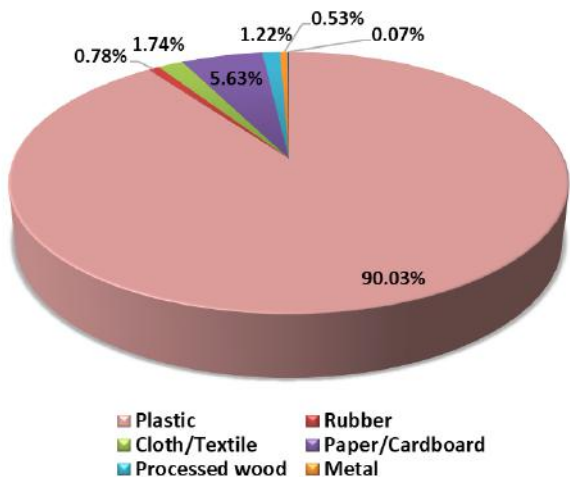
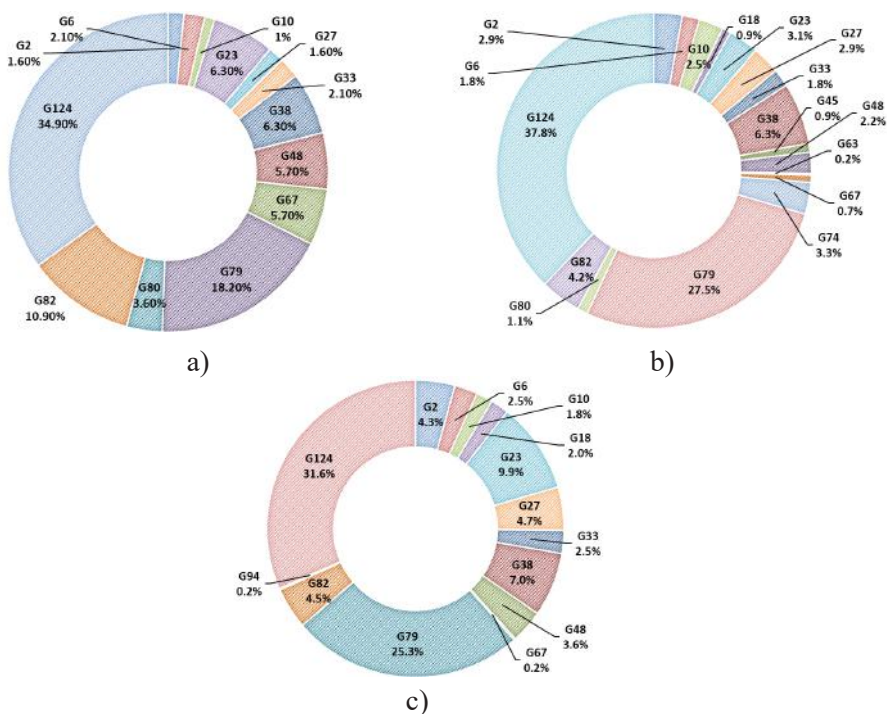**Figure 2.** Percentage share of major litter items categories

Figure 3. Plastics subcategories by percentage share for
a) coastal, b) shelf and c) open sea regions.

within the regions. All size classes were evident on the sea surface, covering the entire survey area. The overall pattern showed evenly distributed size classes for all sites (Fig. 4).
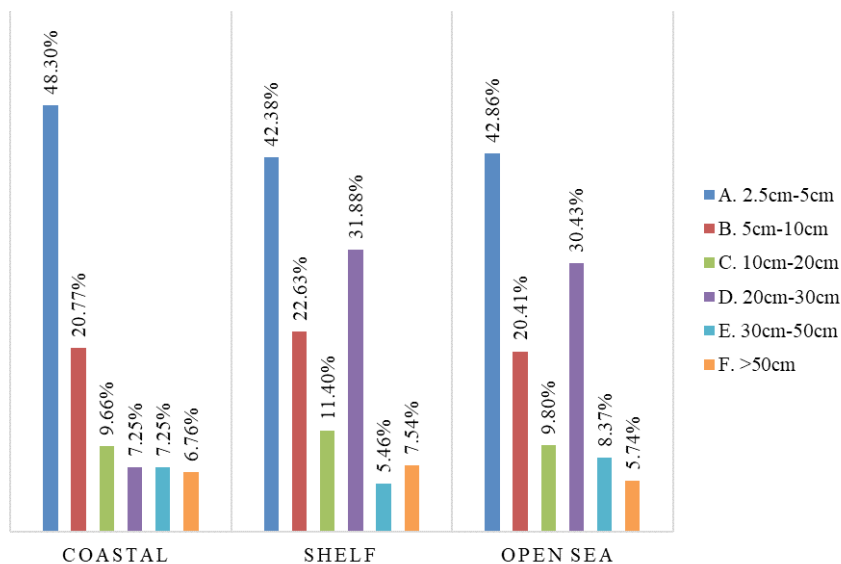

Figure 4. Size classes of FML observed in the coastal, shelf and open sea regions in the period 2017-2019

The average litter density estimated for the entire study area was 170 items km^{-2}, with average densities in coastal and shelf regions calculated approximately of the same magnitude (146 items km^{-2}), while the concentration of FML in open sea was nearly two times higher than other regions (Table 1).

K-means cluster analysis applied to coastal, shelf and open sea dataset (only for most abundant categories) suggested 2 contrast groups for each studied area with clustering vectors and means values, calculated as presented in Table 2.

Table 2. K-means cluster analysis results.

Studied area	Cluster means					No of transects detected in the highest litter densities group	Geographical area (hotspots/ polygons)
	Cluster	**Plastic (items km^{-2})**	**Textile (items km^{-2})**	**Cardboard (items km^{-2})**	**Wood (items km^{-2})**		
Coastal	C1	144.23	0.00	8.63	-	76	-
	C2	1089.20	13.16	31.25	-	4	*Sozopol-Alepu, Burgas bay*

Shelf	C1	114.38	2.79	13.19	-	93	-
	C2	489.67	8.89	15.39	-	15	*Durankulak-Kaliakra, Burgas*
Open sea	C1	152.63	0.00	7.25	4.32	45	-
	C2	477.45	18.59	16.48	12.09	19	Northern, Central and South open sea regions

The transects identified in each 2nd cluster (C2) per region (Table 2), differentiated 7 distinct geographical polygons considered as hotspots, recommended for close monitoring as follows: coastal area - Sozopol-Alepu and Burgas bay, shelf area: Durankulak-Kaliakra and Burgas and 3 open sea polygons conditionally denoted Northern, Central and Southern. Kernel density spatial distribution was applied to indicate FML hotspots/polygons (Fig.5). The highest densities of marine debris were found in south coastal area (Sozopol –Alepu polygon) and open sea North
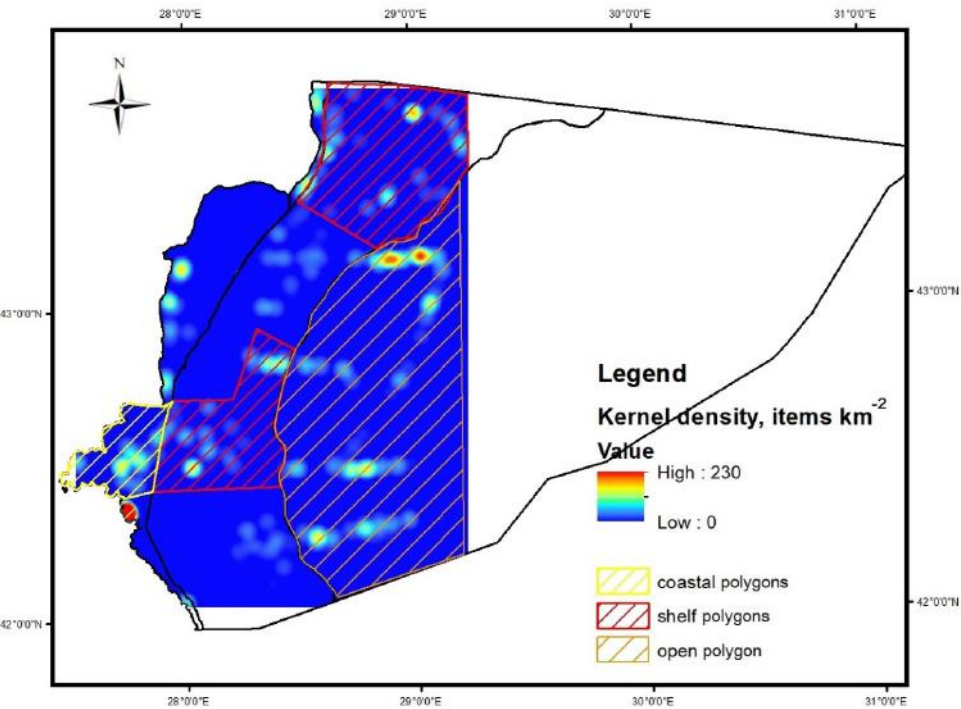

Figure 5. FML distribution Kernel density map.

polygon. Signfficantly high values of FML items were also observed in open sea (Central and South regions) and shelf surface waters (Durankulak-Kaliakra and Burgas polygons).

Analysis of similarities in data within and between the regions (coastal, shelf and open sea) was applied in 2 stages, at first place NMDS of data based on dissimilarity matrix was performed (not shown) - stress value 0.09086181, followed by ANOSIM in order to determine if statistically significant differences between the clustered groups of transects exist. Calculated ANOSIM statistic R value was 0.02219 and the respective significance value was 0.1528, showing that there was no evident difference between the three groups and the distribution of high and low ranks within and between groups was even. Specifically, the distribution pattern of FML (in terms of density) was similar in the coastal, shelf and open sea regions.

FML presence and distribution in the Black sea region is poorly known and before the present study only limited data have been reported. The preliminary results from a ship-based survey in 2016 in the Romanian waters were published by Suaria et al., (2015). The highest litter density found in the study area was estimated to 136 items km^{-2}, which is comparatively low than that, registered by the present research. The plastic items were undoubtedly the most abundant litter category representing 89% of the anthropogenic induced litter, which fully correspond to the major category distribution characteristics in the Bulgarian Black sea waters. On a global scale the reported statistics on FML density distributions (Galgani, Hanke & Maes, 2015) leads to conclusion that the densities identified with the present study are extremely higher, compared to Baltic and North seas (resp. 11-52 and 25-38 items km^{-2}). The higher FML concentrations, observed in the Black sea can be possibly explained with the fact that the latter is a marginal sea and catchment drains rivers of 23 European and Asian countries is highly populated (160 million people) (Freund, Abbaspour & Lehmann, 2017); with intense dynamic eddy-driven circulation system, allowing cross-border transportation of marine debris (Topçu & Öztürk, 2010). Further study of environmental drivers which are possibly causing a serious impact on marine litter such as transportation, accumulation and eventual assemblages (hotspots) are critically needed to be investigated, moreover the suspected sources of marine debris must be clearly identified and monitored.

NOTES

1. https://ec.europa.eu/info/research-and-innovation/research-area/oceans-and-seas/eu-marine-strategy-framework-directive_en

2. https://www.bsbd.org/msfd/2016/BLKBG-D10_Marine%20Litter_revised.pdf

REFERENCES

Buckland, S., Anderson, D., Burnham, K. & Laake, J. (1993). *Distance Sampling: Estimating Abundance of Biological Populations*. Chapman & Hall, London.

Freund, E., Abbaspour, K. & Lehmann, A. (2017). A. Water Resources of the Black Sea Catchment under Future Climate and Landuse Change Projections. **Water**, **9**, 8, 598, https://doi.org/10.3390/w9080598.

Galgani, F., Souplet, A. & Cadiou, Y. (1996). Accumulation of debris on the deep sea floor off the French Mediterranean coast. *Marine Ecology Progress Series*, 142, 225–234. https://doi.org/10.3354/meps142225.

Galgani, F., Hanke, G., Werner, S., Oosterbaan, L., Nilsson, P., Fleet, D., Kinsey, S., Thompson, R.C., Van Franeker, J., Vlachogianni, T., Scoullos, M., Mira Veiga, J., Palatinus, A., Matiddi, M., Maes, T., Korpinen, S., Budziak, A., Leslie, H., Gago, J., & Liebezeit, G. (2013). *Guidance on Monitoring of Marine Litter in European Seas. Scientific and Technical Research series*, Report EUR 26113 EN.

Galgani, F., Hanke, G. & Maes, T. (2015). Global distribution, composition and abundance of marine litter. In: *Marine Anthropogenic Litter*, Springer, 29–56.

Hinojosa,I.&Thiel, M. (2009).Floating marine debris in fjords, gulfs and channels of southern Chile. *Marine Pollution Bulletin*, 58, 341-350.

Ioakeimidis, C., Zeri, C., Kaberi, H., Galatchi, M., Antoniadis, K., Streftaris, N., Galgani, F., Papathanassiou, E. & Papatheodorou, G. (2014). A comparative study of marine litter on the seafloor of coastal areas in the Eastern Mediterranean and Black Seas. *Marine Pollution Bulletin*, 89, 1-2, 296–304. https://doi.org/10.1016/j.marpolbul.2014.09.044.

Maes, T., Barry, J., Leslie, H., Vethaak, A., Nicolaus, E., Law, R., Lyons, B., Martinez, R., Harley, B., Thain, J. (2018). Below the surface: twenty-five years of seafloor litter monitoring in coastal seas of North West Europe (1992–2017). *Science of the Total Environment*, 630, 790–798. https://doi.org/10.1016/J.SCITOTENV.2018.02.245.

Muresan, M., Begun, T., Voicaru, C., Vasile, D. & Teacă, A. (2018). Beach litter occurrence in sandy littoral: case study-the Romanian Black Sea coast. *Geo-Eco-Marina*, 23, 205–213.

Moncheva, S., Todorova, V., et al. (2012). Initial Assessment and GES of the Bulgaraian Black SeaWatersReport, http://www.bsbd.org/v2/bg/page_1722859.ht.

Moncheva, S., Stefanova, K., Krastev, A., Apostolov, A., Bat, L., Sezgin, M., Sahin, F. & Timofte, F. (2016). Marine litter quantification in the Black Sea: a pilot assessment. *Turkish Journal of Fisheries and Aquatic Sciences*, 16, 1, 213–218. https://doi.org/10.4194/1303-2712-v16_1_22.

Oksanen, J., Guillaume Blanchet, F., Friendly, M., Kindt, R., Legendre, P., McGlinn. D., Minchin, P., O'Hara, R., Simpson, G., Solymos, P., Henry, M., Stevens, Szoecs, E. & Wagner, H. (2019). Vegan: Community Ecology Package. *R package version 2.5-6.* https://CRAN.R-project.org/package=vegan

Peneva, E., Slabakova, V. & Moncheva, S. (2013). Identification of similarities in the Black Sea using EOF analysis of remote sensing data and relevance to MSFD implementation. *International Conference, MARES2020,* Varna, Bulgaria, Book of abstracts, 169.

Raykov, V., Zlateva, I., Ivanova, P., Dimitrov, D. & Golumbeanu, M. (2020). Stratified Seafloor Marine Litter Assessment. Bulgarian Black Sea Waters Case. *Journal of Environmental Protection and Ecology,* 21, 2, 463-471.

Ryan, P.G. (2013). A simple technique for counting marine debris at sea reveals steep litter gradients between the Straits of Malacca and the Bay of Bengal. *Marine Pollution Bulletin*, 69, 128–136.

Sá, S., Bastos-Santos, J., Araújo, H., Ferreira, M., Duro, V., Alves, F., Panta-Ferreira, B., Nicolau, L., Eira, C. & Vingada, J. (2016). Spatial distribution of floating marine debris in offshore continental Portuguese waters. *Marine Pollution Bulletin*, http://dx.doi.org/10.1016/j.marpolbul.2016.01.011.

Simeonova, A. & Chuturkova, R. (2019). Marine litter accumulation along the Bulgarian Black Sea coast: categories and predominance. *Waste Management*, 84, 182–193. https://doi.org/10.1016/j.wasman.2018.11.001.

Suaria, G. & Aliani, S. (2014). Floating debris in the Mediterranean Sea. Marine Pollution Bulletin, 86, 1–2, 494–504.

Suaria, G., Melinte-Dobrinescu, M., Ion, G. & Aliani, S. (2015). First observations on the abundance and composition of floating debris in the North-western Black Sea. *Marine Environmental Research*, 107, 45–49. https://doi.org/10.1016/j.marenvres.2015.03.011.

Thiel, M., Hinojosa, I., Vásquez, N. & Macaya, E. (2003). Floating marine debris in coastal waters of the SE-Pacific (Chile*). Marine Pollution Bulletin*, 46, 2, 224–231.

Topçu, E. & Öztürk, B. (2010). Abundance and composition of solid waste materials on the western part of the Turkish Black Sea seabed. *Aquatic Ecosystem Health & Management*, 13, 3, 301-306. doi: 10.1080/14634988.2010.503684.

✉ **Violeta Slabakova**
https://orcid.org/0000-0002-3089-0126
Institute of Oceanology
Bulgarian Academy of Sciences
Varna, Bulgaria
E-mail: v.slabakova@io-bas.bg

✉ **Ivelina Zlateva**
https://orcid.org/0000-0003-4133-5627
Institute of Oceanology
Bulgarian Academy of Sciences
Varna, Bulgaria
E-mail: izlateva@io-bas.bg

✉ **Krasimira Slavova**
https://orcid.org/0000-0002-0622-8490
Institute of Oceanology
Bulgarian Academy of Sciences
Varna, Bulgaria
E-mail: slavova@io-bas.bg

ENDEMIC FORESTS IN DANGER: LAND USE SHIFTS AND ACCOMPANYING IMPACTS UPON THE NATURAL FLOOD STORAGE RESERVOIRS ALONG THE NORTH BULGARIAN BLACK SEA COAST

Iliyan Kotsev, Bogdan Prodanov
Institute of Oceanology – Bulgarian Academy of Sciences (IO-BAS)

Abstract: Longozes represent endemic forests native to the East Balkans. Key factors for their existence are the humid subtropical climate with mild winters and the river inundations occurring twice-yearly. These hygrophilous forests play an essential regulatory role in the runoff peaks by ensuring a crucial ecosystem service as flood storage reservoirs. Nowadays, because of highly decreased and fragmented areals, longozes are red-listed as critically endangered. Hence, they are subject to preservation in compliance with the EU Habitats Directive and Annex 1 of Bulgaria's Biodiversity Act. Aim and objectives of the study herein are: to investigate the spatio-temporal changes in the longoz forests' areals along the North Bulgarian coast; to analyze the consequences of the anthropogenic impacts upon the river runoff; to provide a generalized assessment of the longozes' contemporary flood retention capabilities. Topographic maps from the late 19th century were integrated in GIS to reconstruct the longozes' historical extents by on-screen digitizing of the areas of interest. Analogous procedures were applied to such from the mid-1970s, a time frame correlating with the Socialist extensive development of Bulgaria's coast. The areas' historical land cover as in the late 1980s was further refined using Landsat imagery. These historic data sets were chronologically compared to the longozes' contemporary extents, available as up-to-date cadastral data. The comparisons were executed using GIS crosstabulation techniques. The analyses demonstrate the ubiquitous decrease of the longozes due to overexploitation of the wood resources, land use shifts, resort construction, decreased river runoff, etc. These findings imply for a deteriorated environmental status, impaired flood storage capacity and the inability of the woods to act as a regulator of the peak ourflows nowadays, well correlating with the recent extreme coastal floods with fluvial origin.

Keywords: longoz forests, natural flood retention, Batova and Kamchia Rivers, landscape transformation, change detection.

INTRODUCTION

Longoz forests represent hygrophilous (primarily riparian) intrazonal vegetation with high levels of endemism, native to the eastern part of the Balkan Peninsula, i.e., eastern Bulgaria, northern Greece and European Turkey (Dimitrov, 1992; Dimitrov & Tzonev, 2015). They used to be widely distributed on the Bulgarian Black Sea coast in the past, particularly, along the slow-flowing river downstream sectors and river mouths of estuarine type. Their formation and existence of these forests is related to the humid, transitional to Mediterranean climate with strong influence by the Black Sea basin, which some scholars classify as belonging to the humid subtropical type (Kotteck et al., 2006; Peel et al., 2007; Rubel & Kottek, 2010). Falls and winters along the Bulgarian coast are mild, characterized by periodic river inundations occurring twice yearly, during the high waters in late winter-early spring and again in late fall (Dimitrov & Tzonev, 2015). Hence, longozes, alongside riparian wetlands, which were likewise largely present in the past, used to play an important environmental role on the landscape scale by ensuring the crucial ecosystem service as peak runoff regulators and natural flood storage reservoirs. However, because of their highly decreased and fragmented areals, longozes are nowadays red-listed in Bulgaria as a critically endangered habitat type (Dimitrov & Tzonev, 2012). Accordingly, theses hygrophilous forests are subject to preservation and restoration in compliance with the EU Habitats Directive and Annex 1 of the country's National Biodiversity Act (2002).

AIM AND OBJECTIVES

The goals of the study herein can be summarized in the following:

– To investigate the spatio-temporal alterations of the longoz forests' areals along the North Bulgarian coast by applying a comparative-historical analysis;

– To lay the fundament for an assessment of the longoz forests' impaired flood retention capabilities;

– To mark out future research and management topics on this environmental issue, namely with focus on the anthropogenic impact on the natural river runoff regulators and the resulting fluvial flood hazard on the Bulgarian Black Sea coast.

PILOT STUDY SITES

Two representative sites along the North Bulgarian coast were selected as pilot case studies for the survey discussed herein, namely Baltata Locality bordering the Albena Maritime Resort, and Longoza Locality contiguous to Kamchia Recreational Area (Fig. 1).

Baltata Locality, a protected area since 1962 established pursuant to the national Protected Areas Act (1999), as well as a constituent part of a NATURA 2000 protected site since 2008 that has been designated in compliance with Council Directive 92/43/EEC (i.e., BG0000102 Dolinata na reka Batova/Batova River Val-

Figure 1. Location of the two pilot study sites:
a. Baltata Locality; b. Longoza Locality

ley site of community importance), presently holds the nature conservation status of a managed reserve. The reserve's buffer zone is nowadays a separate nationally designated protected area called "Blatno kokiche" (Summer snowflake), having the status of a protected locality (*zashtitena mestnost* in Bulgarian). Both protected areas preserve the remnants of the once vast longoz forest formed in the flood plain of the Batova River (Register of the protected territories and NATURA 2000 sites in Bulgaria, 2014).

Longoza Locality, a protected area since 1951 established pursuant to the Protected Areas Act of the Republic of Bulgaria (1999), as well as a constituent part of a NATURA 2000 protected site since 2008 that has been designated in compliance with the EU's Habitats Directive (i.e., BG0000116 Kamchia site of community importance), is currently with the status as a strict biosphere reserve called Kamchia. Its buffer zone, similar to Baltata Locality, also represents a separate protected locality nowadays called Longoza, named after the area itself (Register of the protected territories and NATURA 2000 sites in Bulgaria, 2014). Both protected areas are located in the floodplain of the Kamchia River, which is the longest Bulgarian Black Sea tributary (Ivanov et al., 1961; Hristova, 2012; Kotsev, 2017). An intriguing fact is that probably Longoza is among the oldest protected areas in present-day Bulgaria. It used to have the status of a protected forest from the 16th century onwards, while the country was a constituent part of the Ottoman Empire, until the declaration of the semi-independent Principality of Bulgaria in 1878, when, unfortunately, the forest lost its preservation status and became subject to an extensive exploitation for timber by national and foreign companies (Dimitrov, 1992).

DATA AND METHODS

GIS data sets on historical land cover of the two pilot study sites were created by on-screen digitizing of the areas of interests from archive topographic maps, compiled at different scales and dating from four different periods: the late 19th century and the 1930s of the 20th century; 1970s and 1980s of the 20th century. In addition, Landsat imagery was used for further cross-check and data refinement of the 1980s land cover data set.

Crosstabulations in GIS represent the core technique of the change detection analyses carried out in relation to the study discussed herein. Accordingly, the resultant three historical GIS data sets were cross-tabulated versus up-to-date cadastral layers – one for each of the selected pilot study sites.

RESULTS
Baltata Locality

The first pilot study site spreads over a territory of roughly 528 ha. As of the late 19th century, 97.7 % of it used to be covered by longozes, with the remainder 2.3 % being the beach-dune complex developed at the land-sea interface in front of the forest and stretching between the river mouths of Batova to the north and Kranevska to the south (Fig. 2).
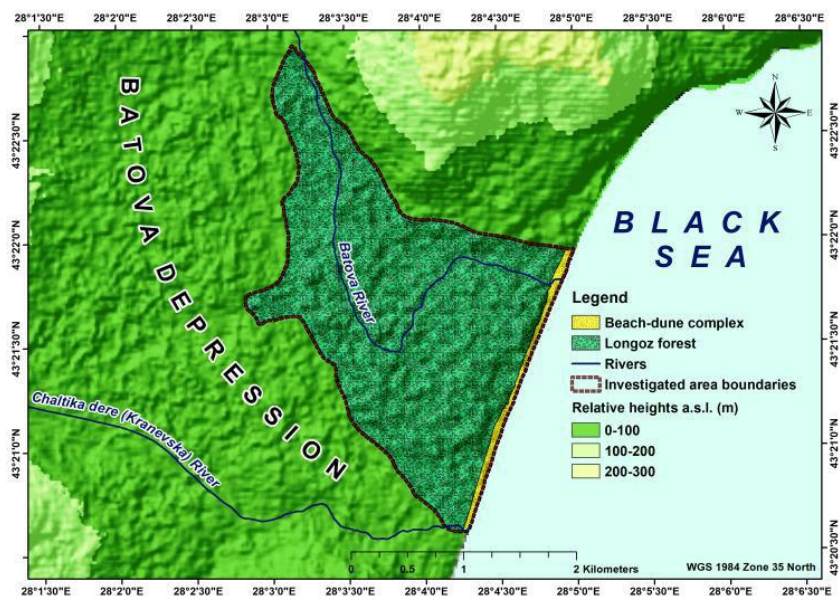

Figure 2. Map of Baltata Locality as of the late 19th century, reconstructed from archive topographic maps compiled at scale 1: 126,000

As of the late 1970s – early 1980s, the extent of the longoz forests has decreased from 97.7 % to barely 46.4 % due to land clearing for agricultural and resort-building demands (Fig. 3). In this period, the river mouth of Batova was artificially trans-located to the south via a system of water canals. Subsequently, Albena Maritime Resort was built on the former marshy terrain, meanwhile becoming one of the greatest coastal consumers of fresh water, supplied by the karst streams feeding Batova River and which the longoz ecosystems at Baltata Locality highly depend on. The aggregate landscape transformation at the case study site (late 19 century vs. late 1970s – early 1980s) adds up to 52.4 %, while the transformed area of the longoz forests is 53.6 %.
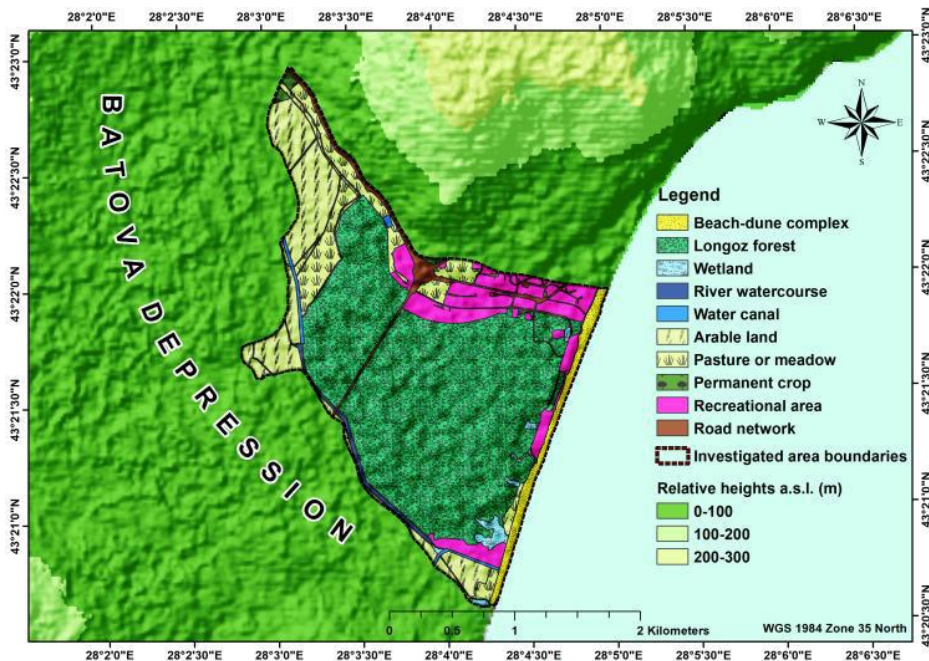

Figure 3. Map of Baltata Locality as of the late 1970s – early 1980s of the 20th century, reconstructed from archive topographic maps compiled at scale 1: 5,000 and 1: 50,000, refined using Landsat imagery

The final time frame subject to analysis is the period early 1980s – 2019 (Fig. 4). Overall, the landscape transformation at Baltata Locality as of 2019 in comparison to the early 1980s is much lower – 5.8 %. Further transformation of the longoz forests (around 0.1 %) are demonstrated by the crosstabulation results, which however fall within the statistical error. There is an overall increase of the longoz forests ex-

tent at Baltata Locality, which is attributed to the abandonment of the former camp site near the southeastern tip of the pilot study site.

Longoza Locality

The second pilot study site has an area of approximately 2,500 ha. As of the late 19th century, 88.9 % of it used to be covered by longoz forests, while the contiguous beach-dune complex, known as Kamchia-Shkorpilovtsi beach, comprised 2.3 % of the site's aggregate area (Fig. 5). The remainder used to be wetlands (so-called azmatsi, representing old river beds of the Kamchia) – 7.2 %, and the river water-course – 1.6 %.
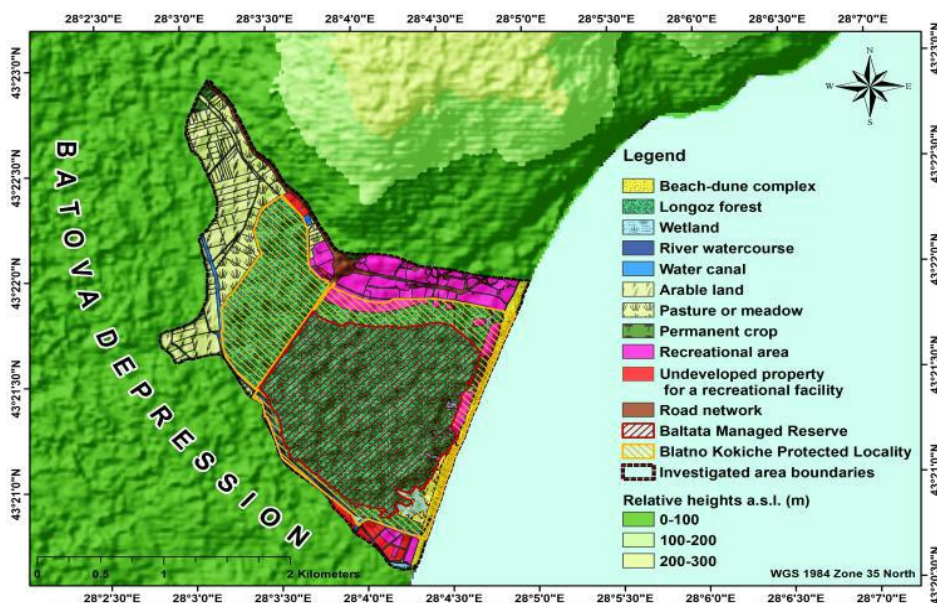

Figure 4. Map of Baltata Locality as of 2019

As of the late 1970s – early 1980s, the relative area of the longoz forests at the case study site dropped drastically, from almost 89 % to barely 49.1 %. Among the greatest anthropogenic alterations of the Kamchia River's hydrologic regime was the construction of four large reservoirs in its catchment basin, as well as the conversion of the Oryahovo Wetlands into agricultural land. As of comparably smaller environmental impact, but nevertheless incompatible with the nature conservation purpose of the area, may be assessed the establishment of the Kamchia Recreational Area. The total landscape transformation in comparison to the late 19th century is 46.7 % while the transformed area of the longoz forests is 47.6 % (Fig. 6).
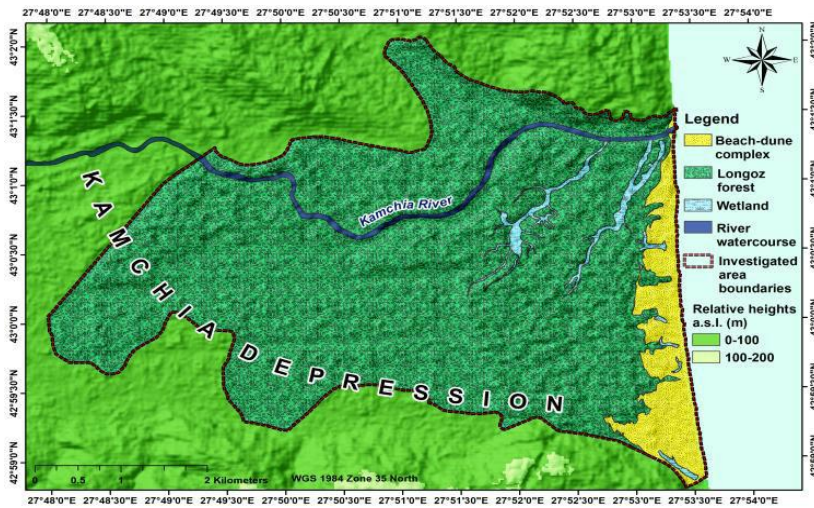
Figure 5. Map of Longoza Locality as of the late 19th century, reconstructed from archive topographic maps compiled at scale 1: 126,000
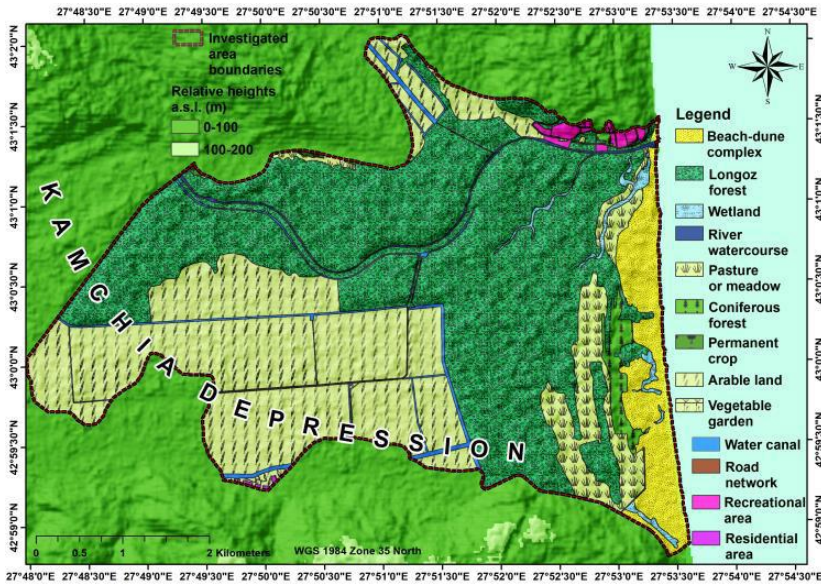

Figure 6. Map of Longoza Locality as of the late 1970s – early 1980s of the 20th century, reconstructed from archive topographic maps compiled at scale 1: 5,000 and 1: 50,000, refined using Landsat imagery

The last compared period (early 1980s – 2019) reveals further moderate landscape transformations at Longoza Locality, estimated at 0.9 %. The relative area of the longoz forests is estimated at 49%, which demonstrates an insignificant decrease in comparison to the precedent period (Fig. 7).
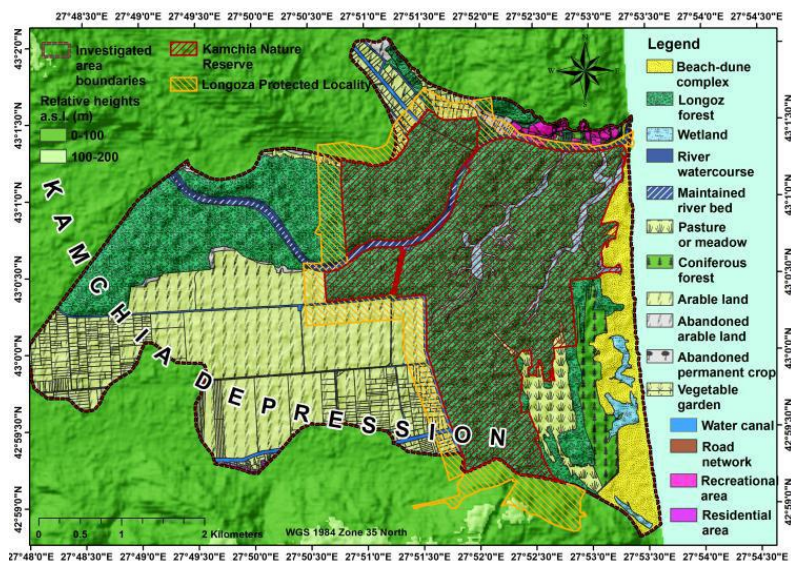

Figure 7. Map of Longoza Locality as of 2019

DISCUSSION

The analyses of the crosstabulation results reveal that the aggregate landscape transformation at Baltata Locality is approximately 37 %, while at Longoza Locality these values are even higher – nearly 46 % when comparing the late 19th century versus the contemporary states of the two pilot study sites. Most impacted by these anthropogenic-driven landscape-scale alterations are indeed the longoz forest ecosystems. The areas deprived of vegetation cover are definitely flood-prone and often subject to resort construction nowadays, with all implications resulting from it.

CONCLUSIONS

The present GIS-based study confirms that both pilot study sites have undergone significant levels of human-driven landscape transformation. The longoz forests at both investigated locations are of severely decreased spatial extents. The most significant landscape transformations occurred during the Socialist period in Bulgaria, marked by extensive recreational and agricultural development. Nevertheless, present-day alterations of the landscape pattern (i.e., construction of residential, recre-

ational facilities and tourist infrastructure) take place mainly on former agricutural land. These transformations, along with the decreased areals of the longoz forests imply for their impaired flood storage capabilities nowadays. The findings of the present study are in a good correlation with the recent extreme floods of non-marine (particularly fluvial) origin along the North Bulgarian Black Sea coast during periods of peak river ouflow.

REFERENCES

Biodiversity Act of the Republic of Bulgaria (2002). Available at https://lex.bg/laws/ldoc/2135456926 (in Bulgarian, last accessed on September 10th, 2020)

Council Directive 92/43/EEC of 21 May 1992 on the conservation of natural habitats and of wild fauna and flora (Habitats Directive) (1992). Available at http://eur-lex.europa.eu

Dimitrov, B. (1992). The influence of River Kamchia overflows on the longoz ecosystems. *Yearbook of Sofia University "St. Kliment Ohridski",* Book No2 (Geography), 84, 55-63 (in Bulgarian)

Dimitrov, M. & Tzonev, R. (2015). Riparian and lowland mixed woodlands and longoses. In Biserkov, V. et al. (Eds.) *Red Data Book of the Republic of Bulgaria, Vol. III (Natural Habitats)*, 281-284. BAS & MoEW, Sofia

Hristova, N. (2012). Black Sea catchment basin. In *Rivers of Bulgaria*, pp. 153-193. Sofia: Tip-Top Press (in Bulgarian)

Ivanov, K., Marinov, Iv., Panayotov, T., Petkov, Al. (1961). Hydrographic characteristic of the rivers. Black Sea (drainage) basin. In *Hydrology of Bulgaria*, pp 72-85. Sofia: Nauka i Izkustvo State Press (in Bulgarian)

Kottek, M., Grieser, J., Beck, Ch., Rudolf, Br., Rubel, Fr. (2006). World Map of the Köppen-Geiger climate classification updated. *Meteorologische Zeitschrift*, **15(3):** 259-263

Kotsev, I. (2017). Hydrographic structure of the Bulgarian Black Sea coast. In Kotsev, I. & Stanchev, Hr. (Eds.) Sensitivity mapping and analysis of the Bulgarian Black Sea coastal zone, 38-43. Sofia: Pulsio Press

Peel, M. C., Finlayson, B. L., McMahon, T.A. (2007). Updated map of the Köppen-Geiger climate classification. *Hydrology and Earth system Sciences*, 11: 1633-1644

Protected Areas Act of the Republic of Bulgaria (1999). Available at https://www.lex.bg/laws/ldoc/2134445060 (in Bulgarian, last accessed on September 10th, 2020)

Register of the protected territories and NATURA 2000 sites in Bulgaria, Executive Environment Agency, 2014 (available at http://eea.government.bg/zpo/en/index.jsp, last accessed on September 10th, 2020)

Rubel, Fr., Kottek, M. (2010). Observed and projected climate shifts 1901-2100 depicted by world maps of the Köppen-Geiger climate classification. *Meteorologische Zeitschrift*, **19(2):** 135-141

✉ **Iliyan Kotsev**
https://publons.com/researcher/AAG-1484-2019/
Institute of Oceanology
Bulgarian Academy of Sciences
Varna, Republic of Bulgaria
E-mail: xarz@mail.bg

✉ **Bogdan Prodanov**
http://orcid.org/0000-0002-8118-3034
Institute of Oceanology
Bulgarian Academy of Sciences
Varna, Republic of Bulgaria
E-mail: bogdanprodanov@gmail.com

ECOLOGICAL ASSESSMENT OF STRUMA RIVER IN PERNIK REGION, BULGARIA IN DECEMBER 2019

Antonina Kovacheva[1], Diana Rabadjieva[1], Radost Ilieva[1], Rumiana Gergulova[1], Veselin Nanev[2], Ivelin Vladov[2]

[1] *Institute of General and Inorganic Chemistry – Bulgarian Academy of Sciences*
[2] *Institute of Experimental Morphology, Pathology and Anthropology with Museum – Bulgarian Academy of Sciences*

Abstract: The hydrological characteristics of water basins in Pernik region, Bulgaria have been badly worsened since the summer of 2019. This study was performed in the low-flow period of December 2019 and covered eight sampling stations along the Struma River between Studena dam and Pchelina dam, region of the town of Pernik. The analytical data obtained and the calculated threshold pollution indices of the single nutrients PO_4^{3-}, NO_2^-, NO_3^- and NH_4^+ and their integrated threshold pollution indices showed water pollution in respect of PO_4^{3-} and NH_4^+. The concentrations of PO_4^{3-} at all stations, of NH_4^+ ions in the waters after Pernik city, and of NO_3^- and NO_2^- before Pchelina dam exceeded the respective maximum allowed concentrations (MAC) according to the Bulgarian legislation. The waters were pure in respect of the trace metals Al, Fe, Co, Ni, Cu, Zn, Cd, and Pb; only Mn exceeded its MAC. The chemical species of the trace metals were calculated by thermodynamic modeling and discussed on the base of the "*Hard and Soft Acids and Bases*" (HSAB) principle.

Keywords: water pollution, chemical species, nutrients pollution, Struma River

INTRODUCTION

Struma River is a medium-sized cross-border river in southwestern Bulgaria, whose total length is 360 km, of which 242 are located on the territory of Bulgaria and 118 km on the territory of Greece.

It springs from the Vitosha Mountain, passes through Pernik, Radomir, Kyustendil, Dupnitsa and Blagoevgrad valleys and then leaves the Bulgaria borders. Owing to its importance for the region through which it flows, the Struma River is subject to monitoring by the Bulgarian National Monitoring System of the environment (NSMOS) which provides timely information about the state of the environmental elements and the factors having an impact on it. According to the "National Report on the State and Protection of the Environment in the

Republic of Bulgaria" from 2017, in recent years there has been a trend to improve the water quality in the Struma River in terms of dissolved oxygen, biologically required oxygen, ammonium nitrate nitrogen and phosphates while according to the "biotic index" the condition of its waters has deteriorated after the town of Pernik. The public interest in the river has also increased and especially in 2019 non-governmental organizations have repeatedly informed about problems related to the hydrological characteristics and living conditions in the river.

It was of interest to us to trace the ecological condition of the river as it passes through one of the most polluted regions of Bulgaria - the region of Pernik, characterized by developed coal mining, coal processing and machine building industries. Our goal was, through field research in the section of the river between the dams Studena and Pchelina, to determine the physicochemical and chemical characteristics of the river in certain areas, to determine the potential pollutants and to calculate their chemical species by applying thermodynamic models, which will allow us to perform a complex assessment of its ecological condition. The study was conducted during the shallow-water period in December 2019.

EXPERIMENTS
Sampling, preservation and analyses
Surface water samples of Struma River were taken in December, 2019. Eight sampling stations (Fig. 1) were selected, located as follows: 1 – after Studena dam, the main source of drinking water for the town of Pernik; 2 - before the town of Pernik; 3, 4 and 5 - in the town of Pernik, item 4 being in close proximity to an industrial zone and a railway station; 6 - after the town of Pernik; 7 – close to the town of Radomir; and 8 - before Pchelina dam, used for irrigation of agricultural areas.
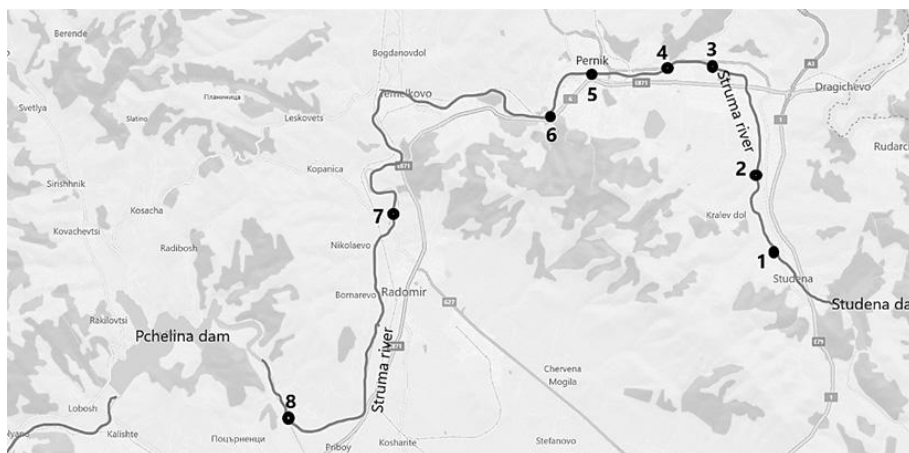

Figure 1. Locations of sampling stations (1-8)

Water samples (approximate volume of 1.5 L) were collected from the upper surface layer (0 – 20 cm) of the river. Each sample consisted of 3 sub-samples collected at a distance of 3-5 m from each other. They were filtered through 0.45 µm Millipore (Millipore, Bedford, MA, USA) membrane filters. Filtrates for inductively coupled plasma optical emission spectrometry (ICP OES) analysis were acidified with 65% HNO3 p.a. (Merck, Darmstadt, Germany) to pH<2.0.

Physicochemical characteristics (temperature, pH, conductivity, dissolved oxygen and salinity) of the water samples were measured *in situ* by a portable Multi 340i-WTW equipment (WTW, Weilheim, Germany) using a series of calibrated temperature–compensated electrodes.

Alkalinity and nutrients (PO_4^{3-}, NO_2^-, NO_3^- and NH_4^+), measured *in situ*, as well as Cl^- and SO_4^{2-} ions were determined spectrophotometrically on a portable NOVA instrument (Merck, NJ, USA). CO_3^{2-} content was calculated from the alkalinity value. Metals (K, Ca, Mg, Al, Fe, Mn, Co, Ni, Cu, Zn, Cd and Pb) were determined by ICP OES on a PRODIGY 7 spectrometer (Teledyne Leeman Labs, USA). The Na content was calculated as the difference between ion equivalents of anions and cations.

Thermodynamic modeling

A thermodynamic ion-association model (Grenthe *et al*. 1997), Visual Minteq computer program version 3.1 (Gustafsson 2001), was utilized for simulating the soluble inorganic species of trace elements. The experimental chemical data for the total concentrations of elements and pH were used as input data. In cases when the analytic results for a given element were below its detection limit, the latter was used.

The following additional assumptions were made in order to calculate the species concentrations and their ratios: (i) the activity coefficients of all possible simple and complex species were calculated using the extended Debye-Hückel theory; (ii) Mn^{6+} and Mn^{7+} ions were not considered in the calculations, since they are not stable in natural waters (ATSDR 2012); (iii) redox processes were evaluated with the inclusion of all the redox pairs that may exist in the systems studied, namely O^0/O^{2-}, N^{3+}/N^{5+}, N^{3-}/N^{5+}, Co^{3+}/Co^{2+}, Cu^+/Cu^{2+}, Fe^{2+}/Fe^{3+}. The results showed domination of the O^0/O^{2-} couple. In all cases insignificant amounts of Cu^+, Fe^{2+} and Mn^{3+} were detected. For this reason, only the ions Cu^{2+}, Fe^{3+} and Mn^{2+} were taken into consideration; (iv) in the ion-association model a thermodynamic equilibrium was assumed only for the complex formation processes.

RESULTS AND DISCUSSION
Physicochemical and chemical assessment

The results for the physicochemical characteristics and chemical parameters of the Struma River waters are shown in Table 1. The waters at all studied stations are characterized by a weakly alkaline pH value (7.75 - 8.44), which is characteristic of surface river waters.

Table 1. Physicochemical characteristics and chemical parameters
of the river waters

Parameters	MAC	Sampling stations							
		1	2	3	4	5	6	7	8
Physicochemical characteristics									
T, ºC		5.9	6.0	6.0	6.4	6.0	9.3	8.9	7.7
pH	6.5-8.7 [a]	7.96	8.44	7.95	8.16	8.12	7.75	8.04	8.31
Eh, mV		-49	-77	-50	-57	-58	-34	-60	-67
Conductivity µS cm^{-1}	750 [a]	708	590	590	1059	1319	1237	1068	1018
Dissolved O_2, mg L^{-1}	7.00-6.00 [a]	3.14	4.08	3.57	3.67	3.64	3.26	3.11	3.81
Alcalinity, mg L^{-1}		193	150	137	190	197	198.3	230	239
Macrocomponents (C, mg L^{-1})									
Na calc		0.78	1.69	24.15	72.1	81.1	36.8	54.7	61.7
K		4.04	3.61	5.74	8.4	11.4	11.2	10.7	8.8
Mg		27.5	24.4	16.1	29.7	33.2	31.9	29.2	29.2
Ca		61	56	53	78	147	144	108	98
Cl	300 [a]	32	43	42	34	32	85	31	30
SO_4^{2-}	300 [a]	33	36.5	60	237	**435.2**	257.1	239.1	220
CO_3^{2-}		115.8	90	82.2	114	118	119	138	143.4
Nutrients (C, mg L^{-1})									
$P-PO_4^{3-}$	0.025-0.06 [a]	0.24	0.22	0.19	0.49	0.30	0.13	0.37	0.39
$N-NO_2^-$	0.03-0.06 [a]	0.03	0.021	0.04	**0.07**	**0.06**	**0.07**	**0.14**	**0.12**
$N-NO_3^-$	0.8 - 2 [a]	1.4	0.6	0.8	0.6	0.9	0.2	**2.3**	**2.5**
$N-NH_4^+$	0.1-0.3 [a]	0.12	0.08	**0.94**	**2.3**	**1.01**	**0.56**	**0.98**	**0.94**
Trace metals (C, mg L-1)									
Al	0.025 [a]	<0.001	<0.001	<0.001	<0.001	<0.001	<0.001	<0.001	<0.001
Fe	0.1 [c]	<0.03	<0.03	<0.03	<0.03	<0.03	<0.03	<0.03	<0.03
Mn	0.05 [c]	<0.002	<0.002	0.339	0.195	0.155	0.197	0.046	<0.002
Co	0.1 [c]	<0.002	<0.002	<0.002	<0.002	<0.002	<0.002	<0.002	<0.002
Ni	0.034 [b]	<0.004	<0.004	<0.004	<0.004	<0.004	<0.004	<0.004	<0.004
Cu	0.01 [cc]	<0.002	<0.002	<0.002	<0.002	<0.002	<0.002	<0.002	<0.002
Zn	0.04 [cc]	<0.003	<0.003	<0.003	<0.003	<0.003	<0.003	<0.003	<0.003
Cd	0.0015 [b]	<0.002	<0.002	<0.002	<0.002	<0.002	<0.002	<0.002	<0.002
Pb	0.014 [b]	<0.003	<0.003	<0.003	<0.003	<0.003	<0.003	<0.003	<0.003

Notes: MAC - maximum allowed concentration;
([a]) Bulgarian regulation 4/2012- "quality II good water" for rivers in the plains;
([b]) European Parliament Directive 2013/39/EC on inland surface waters;
([c]) Bulgarian regulation 4/2012- annual average;
([cc]) Bulgarian regulation 4/2012- annual average, at $CaCO_3$ content in the water 100 – 250 mg L^{-1}.

The electrical conductivity varies in a wide range from 590 to 1319 $\mu S\ cm^{-1}$, in stations 1 - 3 being below the permissible value for river waters, and in stations 4 - 8 exceeding the maximum allowed value, which is an indication of increased salt content at the latter stations. Dissolved oxygen is below the limit for surface water. A probable reason for this is the low turbulence of the water in this section of the river, but it is also a signal for a probable inflow of unregulated polluted sewage waters (Kannel *et al.* 2007).

As regards the macrocomponents Mg (16.1 - 33.2 mg L^{-1}), Cl^- (30 - 43 mg L^{-1} with the exception of station 6 with 85 mg L^{-1}) and CO_3^{2-} (82.2 - 143.4 mg L^{-1}), their concentrations vary within relatively narrow limits. In contrast, for SO_4^{2-} (33 - 435.2 mg L^{-1}), K (3.61 - 11.4 mg L^{-1}), Na (0.78 - 81.1 mg L^{-1}) and Ca (53 - 147 mg L^{-1}) we found that their concentrations vary in a much wider range, the concentration of SO_4^{2-} ions in station 6 exceeding the maximum allowable concentration (Bulgarian regulation 4 / 2012- "quality II good water" for rivers in the plains). There is a general trend of increasing concentrations of SO_4^{2-}, K, Na and Ca along the river from station 1 to station 6, followed by a slight decrease to station 8. These results point to pollution as a result of coal mining in the region.

The waters studied were heavily polluted with regard to nutrients, except the waters of stations 1 and 2, where only PO_4^{3-} ions exceeded the MAC values (Table 1, Fig. 2). To assess the pollution, threshold pollution indices of the single elements (C_f) were calculated by the formula $C_f = C/C_{MAC}$, where C is the concentration of the element, and C_{MAC} is the maximum allowed concentration (when MAC is given within a concentration range, then the maximum value was used). Integrated threshold pollution indices in respect of nutrients were calculated as well, using the formula $P_w = \Sigma C_f^i/n$), where n is the number of nutrients (Yan *et al.* 2015; Weissmannova and Pavlovsky 2017).

The waters from all studied stations are polluted with phosphate ions, and their values exceed the maximum allowable concentration (C_{fP} varies between 2.17 at station 6 and 8.17 at station 4). $N-NH_4^+$ contamination follows the trend of $P-PO_4^{3-}$, only stations 1 and 2 being pure from NH_4^+ (Table 1, Fig. 2). NH_4^+ concentrations in the waters of stations 3 - 8 exceed the MAC value, reaching a maximum ($C_{fNH4+} = 7.67$) at station 4. The peak in the pollution (Fig. 2) with $P-PO_4^{3-}$ and $N-NH_4^+$ is at station 4 and is a clear indication of household pollution in the area of Pernik. The concentrations of $N-NO_2^-$ and $N-NO_3^-$ increase along the river from station 1 to station 7, marking their maxima at station 7 ($C_{fNO2-} = 2.33$) and station 8 ($C_{fNO3}^- = 1.25$), respectively, together with a second maximum in the values for C_{fP} and C_{fNH4+}. These results point to pollution as a result of agricultural activities. According to the calculated integrated threshold pollution indices, most polluted are the waters of station 4 in the industrial zone of Pernik ($P_{w4} = 4.33$), followed by stations 7 and 8 in the region of the town of Radomir ($P_{w4} = 3.23$).
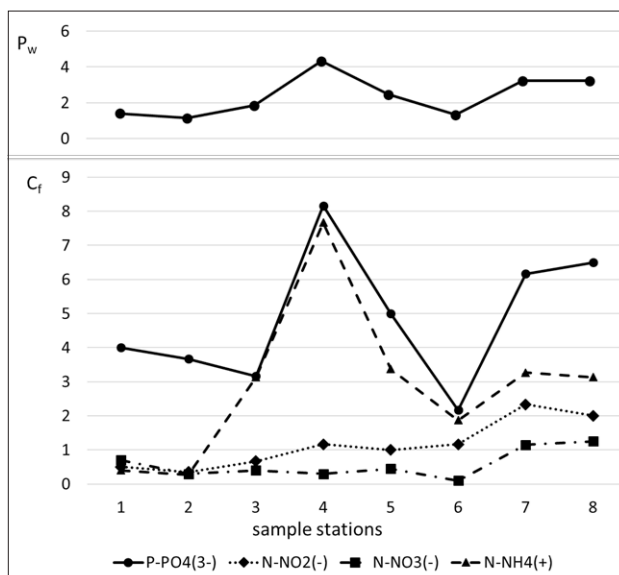
Figure 2. Threshold pollution indices of single nutrients (C_f) and integrated threshold pollution indices (P_w) of waters studied

The calculated ratio of total N/P concentrations in the studied area is presented in Figure 3. The average ratio is 7.04, ranging from 3.18 to 9.36. This means that the values of the N/P ratio are lower than the optimal ratio for the development of aquatic ecosystems (about 16) (Hibaum 2010) (Fig. 3).
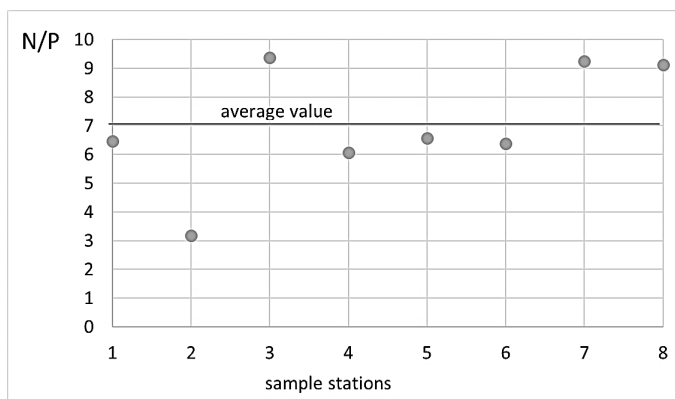

Figure 3. N/P ratio in the waters of Struma River in Pernik region in December 2019.

The waters were pure in regard of the trace metals Al, Fe, Co, Ni, Cu, Zn, Cd, and Pb; only Mn exceeded its MAC value at stations 3-6.

Thermodynamic modeling

In aqueous solutions the chemical elements are present as free ions or complex forms. The changes in the environment – natural or anthropogenic – lead to changes in the chemical species of the pollutants in the natural basins, and hence, in their toxicity. Trace metals include elements of key interest in terms of biogeochemical cyclic processes, owing to their specific properties, reactivity and significance as pollutants. Therefore, object of thermodynamic calculations was the species distribution of the trace metals under study. A thermodynamic ion-association, Visual Minteq computer program version 3.1, was applied for simulating the soluble inorganic species of trace elements in the waters studied. The calculations were done for the waters of station 1 (with minimal pollution), station 3 (with maximum value of Mn, the major trace metal pollutant), station 5 (with maximum value of SO_4^{2-} ion), station 6 (with minimum pH) and station 7 (with maximum nutrient pollution).

The results show that according to the predominant soluble inorganic forms (Fig. 4) the transition metals can be divided into 3 groups as follows:

Group A (Fig. 4a) - Al and Fe, for which the dominant soluble inorganic species are the hydroxy complexes $Me(OH)_n^{3-n}$ (Me = Al, Fe; n = 2,3,4). The $Al(OH)_4^-$ species (95.8 - 98.9%) is dominant in all waters studied. Small amounts (1.2-3.5%) of $Al(OH)_3^0$ were also calculated. In contrast to Al, $Fe(OH)_2^+$ species (93.8 - 98.5%) are dominant in all studied waters followed by $Fe(OH)_3^0$ (1.1 - 3.7%) and $Fe(OH)_4^-$ (0.2 - 2.4%).

Group B (Fig. 4b) - Cu and Pb, for which the carbonate species $MeCO_3^0$ (Me = Cu, Pb) dominate. In addition to $CuCO_3^0$ (84.6 - 89.0%), also Cu^{2+} (1.9 - 8.0%), $CuOH^+$ (3.6 - 5.5%), $Cu(CO_3)_2^{2-}$ (1 - 4.7%) and insignificant amounts of $CuSO_4^0$ (0.1 - 1.1%) were calculated for copper. For Pb, in addition to $PbCO_3^0$ (69 - 82.4%), the presence of two other carbonate species $PbHCO_3^+$ (2.3 - 7%) and $Pb(CO_3)_2^{2-}$ (0.8 - 4.2%), Pb^{2+} (3 - 11.4%)), $PbOH^+$ (6.2 - 9%) and $PbSO_4^0$ (0.5 - 4.3%) was calculated.

Group C (Fig. 4c) - Co, Ni, Mn, Zn and Cd, dominated by free Me^{2+} ions ranging from 49.7% (Zn^{2+}, station 7) to 87.1% (Co^{2+}, station 3). $MeCO_3^0$ (2.7 - 25.9%) and $MeSO_4^0$ (1.6 - 16.4%) were calculated as concomitant forms, the content of which is comparable for the different elements and varies in a similar way in the waters of the different stations, depending on the pH and the concentration of SO_4^{2-} and CO_3^{2-} ions. There is a general trend according to which the lowest values of free Me^{2+} ions are registered in the waters of stations 5 and 7, characterized by a higher pH (8.12 and 8.04, respectively) compared to station 1 (pH 7.96), station 3 (pH 7.95) and station 6 (pH 7.75). The highest content of $MeSO_4^0$ complexes was calculated

in the waters of station 5 (with maximum concentration of SO_4^{2-}) and of $MeCO_3^0$ in the waters of station 7 (with maximum concentration of SO_4^{2-}). The presence of $MeHCO_3^+$ (Me = Co, Ni, Mn, Zn and Cd) in the range of 1.3 - 7.4%, $MeOH^+$ (Me = Co, Zn) in the range of 1.1 - 2.1% and $CdCl^+$ (3.4 - 9.8%) was also calculated.
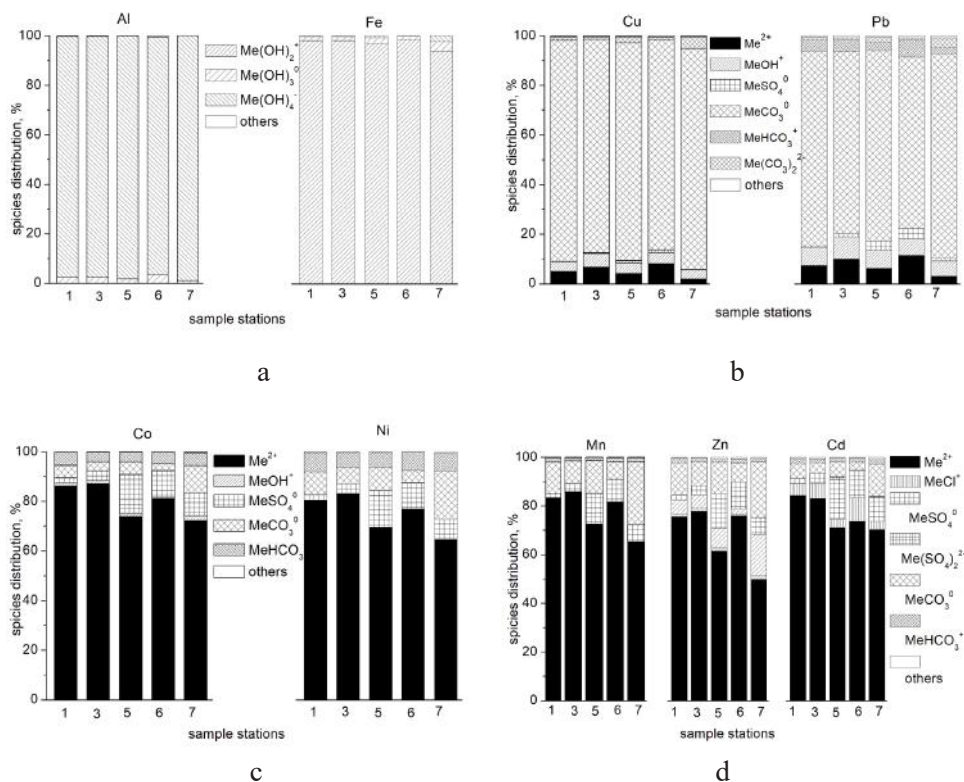

a

b

c

d

Figure 4. Distribution of Al and Fe (a), Cu and Pb (b),
Co, Ni, Mn, Zn and Cd (c) chemical species in the waters
of the selected stations 1, 3, 5, 6 and 7 of the studied area.

The chemical behavior of the trace metals and their chemical forms in water systems are determined by the redox potential, pH, chemical composition of the waters, as well as by the ability of the metals to coordinate preferentially with some of the anions and the stability of the respective forms derived. The theoretical bases which could be applied for explaining the metal-ligand interactions are the "*Hard and Soft Acids and Bases*" (HSAB) principle (Pearson 1968; Parr *et al*. 1983), as well as the crystal field stabilization energy (CFSE). The Pearson concept (Pearson

1968) for *hard* and *soft Lewis acids* (metal ions) and *Lewis bases* (ligands), and the Klopman scale (Klopman 1968) for *hardness* and *softness* determine the type of the ligands that form metal complexes in the water systems under consideration. According to these, *soft Lewis acids* preferably coordinate with *soft Lewis bases* and *hard Lewis acids* – with *hard Lewis bases*. When the ligand concentration is sufficient to form complexes with the metal ions, the stability of which exceeds that of all other possible complexes, these are the dominant ones. The *hardness* of the trace metals examined in this study decreases in the order $Al^{3+}> Fe^{3+}>Mn^{2+}> Co^{2+}>Ni^{2+}>Cu^{2+}>Zn^{2+}> Pb^{2+}>Cd^{2+}$, while the *hardness* of the main ligands present in waters decreases in the order $OH^->H_2O > SO_4^{2-}> CO_3^{2-}> Cl^-$ (Klopman 1968, Pearson 1968, Parr *et al*. 1983). Al and Fe can be considered as *hard Lewis acids* preferring to coordinate with OH^- ions forming hydroxy complexes, which were actually calculated in our modeling (Fig. 4a). Cd^{2+} can be considered as the *softest Lewis acid* among the metals studied, preferring to coordinate with *soft* inorganic ligands as Cl^- if they are in a sufficient amount. The other elements can be considered as *borderline* cases. Although Zn is a rather *soft Lewis acid* and Mn is a rather *hard Lewis acid*, both metals have analogous behavior, since they possess CFSE=0 (Mn^{2+} d^5, high spin; Zn^{2+} d^{10}) so free Me^{2+} ions were calculated as dominant for them (Fig. 4d). The dominance of the carbonate complexes of Cu and Pb (Fig. 4b) is a result of the high stability of their $MeCO_3^0$ complexes and is in accordance with the Irving-Williams rule according to which stability constants follow the sequence $Mn^{2+} < Co^{2+} < Ni^{2+}< Cu^{2+} \approx Pb^{2+}> Zn^{2+}$ (Turner *et al.* 1981). Thus, the low stability of Co and Ni complexes determines the calculation of free Me^{2+} ions as dominant (Fig. 4d).

REFERENCES

National Report on the State of Environment in Bulgaria (2017) http://eea. government.bg/en

Grenthe, I., Puigdomenech, I., Hummel, W. (1997) *Chemical background for the modelling of reactions in aqueous systems*, In: Modelling in aquatic chemistry, OECD Publications.

Gustafsson, J.P. (2001) Modeling the acid–base properties and metal complexation of humic substances with the Stockholm Humic Model. *J Colloid Interf Sci*, 244, 102–112.

ATSDR (Agency for Toxic Substances and Diseases Registry) (2012) *Toxicological profile for manganese*. US Department of Health and Human Services, Public Health.

Kannel, P.R., Lee, S., Lee, Y., Kanel S.R., Khan, S.P. (2007) Application of Water Quality Indices and Dissolved Oxygen as Indicators for River Water Classification and Urban Impact Assessment. *Environ Monit Assess,* 132, 93–110.

Yan, C.-A., Zhang, W., Zhang Z., Liu, Y., Deng, N. N. (2015) Assessment of water quality and identification of polluted risky regions based on field observations & GIS in the Honghe River watershed, China, *PLoS ONE*. 10(3), e0119130.

Weissmannova, H, Pavlovsky, J. (2017) Indices of soil contamination by heavy metals – methodology of calculation for pollution assessment (minireview), *Environ Monit Assess,* 189, 616-620.

Hibaum, G. (2010) *Collection of reports on the Integrated Management Plan of the Pomorie Lake Protected Area BG0000152 and the Pomorie Protected Area BG000062*, 32-47.

Pearson, R.G. (1968) Hard and soft acids and bases, HSAB. I. Fundamental principles. *J Chem Educ*, 45, 581–587.

Parr, R.G., Pearson, R.G. (1983) Absolute hardness: companion parameter to absolute electronegativity. *J Am Chem Soc*, 105, 7512–7516.

Klopman, G. (1968) Chemical reactivity and the concept of charge- and frontier-controlled reactions, *J Amer Chem Soc,* 90, 223-234.

Turner D. R., Whitfield M., Dickson A. G. (1981) The equilibrium speciation of dissolved components in freshwater and seawater at 25°C and 1 atm pressure, *Geochim Cosmochim Acta*, 45, 855-881.

✉ **Antonina Kovacheva**
Institute of General and Inorganic Chemistry
Bulgarian Academy of Sciences
Sofia, Bulgaria
E-mail: antonina1975@abv.bg

✉ **Diana Rabadjieva**
Institute of General and Inorganic Chemistry
Bulgarian Academy of Sciences
Sofia, Bulgaria

✉ **Radost Ilieva**
Institute of General and Inorganic Chemistry
Bulgarian Academy of Sciences
Sofia, Bulgaria

✉ **Rumiana Gergulova**
Institute of General and Inorganic Chemistry
Bulgarian Academy of Sciences
Sofia, Bulgaria

✉ **Veselin Nanev**
Institute of Experimental Morphology
Pathology and Anthropology with Museum
Bulgarian Academy of Sciences
Sofia, Bulgaria

✉ **Ivelin Vladov**
Institute of Experimental Morphology
Pathology and Anthropology with Museum
Bulgarian Academy of Sciences
Sofia, Bulgaria

ECO-INNOVATION AS A BASIS FOR CLEAN PRODUCTION MODEL IN THE FOOD INDUSTRY: AN INSIGHT FROM BULGARIA

Silviya Topleva, Tsvetko Prokopovp Donka Taneva
University of Food Technologies – Plovdiv, Bulgaria

Abstract. In this paper we propose a model for implementation of eco-innovations of clean production in the SMEs of the food industry in Bulgaria. The clean production is a preventative approach to managing environmental aspects. The paper presents the essence of clean production, the methods for its achievement and outlining the possible options and barriers for SMEs from the food industry in Bulgaria to implement the relevant eco-innovations. The ecological footprint of the food industry makes the need for an integrated implementation of clean production practices from raw material extraction to packaging and waste disposal of final consumer.

Keywords: clean production; eco-innovation; ecodesign; food industry

INTRODUCTION

The clean production is a preventative approach to managing environmental aspects. More broadly, the clean production concerns the technological and technical aspects of product manufacturing (Boye, Arcand, 2013). In the practice of clean production, ecodesign innovations occupy a leading position. In the food industry in Bulgaria, the clean producton is not yet widespread.

The food industry could be seen as the cross-point of the relationship between nature and respect attributed to the human race. In this sense, the clean production of food products expresses simultaneously the preservation of nature and the improvement of the quality of life of the people. The priority for clean production of food products is the reduction of the consumption of energy and water resources and the establishment of a waste management system at each phase of the life cycle. The clean productin achievement is not a one-dimensional business activity, but an integrated, complex process of management and redesign of the environmental aspects of the company's production, distribution, and consumer functions. The eco-innovation project management and the ecodesign of process and products are at the basis of this complex practice.

The food industry is characterized by cumulative growing environmental aspects throughout all the life-cycle phases of the product. The production stage requires a high consumption of water and energy resources. The high quantity of wastes marks every preserved product from the raw material procurement to the disposal of the packaging by the final consumer.

The structure of the food industry traditionally builds by a number of small and medium-sized enterprises (SMEs) operating in conditions of monopolistic competition. According to the National Statistical Insitute, for 2018 in Bulgaria has a total of 31 272 enterprises in the manufacturing sector, as SMEs among them are 30 985. The added value that generate these enterprises amounted to 3 655 355 thousand Euros, as for the entire sector is 7 767 101 thousand Euros (NSI, 2019).

The SMEs in food industry are often family businesses that combine tradition and innovation. Moreover, the enhancement of the competitiveness of small and medium enterprises faces them to the challenge to develop innovative production solutions. Clean production offers to the small and medium enterprises incentive to be both innovative, competitive and profitable (Birkin et al., 2009).

The implementation of clean production practice in food industry SMEs goes beyond the scope of their innovation and investment activity. SMEs often do not have the methodology and resources to implement the practices of clean production in their technology and business processes. They face the challenge to optimize resource use in the production process, to meet regulatory and consumer demands for environmentally-friendly products and, at the same time – the inability to achieve them.

The purpose of the paper is to propose a model for implementation of eco-innovations of clean production in the SMEs of the food industry in Bulgaria. The achievement of this objective requires presentation of the essence of clean production, the methods for its achievement and outlining the possible options and barriers for SMEs from the food industry in Bulgaria to implement the relevant eco-innovations.

CLEAN PRODUCTION MODEL TOOLS METHODOLOGY

The resource-based view, dynamic capabilities view, and strategic entrepreneurship are the main drivers of innovative sustainable business models innovations (Schneider and Spieth, 2013). The resource-based view is associated with the effective management of the company's resources. The dynamic capabilities view relies on the company's potential to create value added through eco-innovation. The strategic entrepreneurship involves the company's capabilities to combine its strengths with the favorable opportunities of the external environment. Thus, the unity of the company's resources, competencies and capabilities becomes the source of innovative green business modeling of corporate sustainability through implementation of clean production.

To achieve sustainable business growth through clean production is necessary the correct application of appropriate methods. The clean production methodology typically affects the technological processes and technical characteristics of the products and environment.

The basis of clean production is reuse and recycling of by-products and waste, the use of renewable energy sources, optimization of the consumption of energy and water resources. Thus, the clean production is becoming an expression of the essence of the bio-based economy. The clean production means that the by-products and the waste from the production of one product become a raw material for other products and production processes. The recycling and reuse of resources and raw materials as a basis for clean production are a new area for eco-innovation in the food industry (Dalhammar, 2016). The recycled food content is a sensitive issue for both producers and consumers. The studies in the field are still experimental and at the sensory analysis level (Prokopov et al. 2018). In light of this idea, the clean production of food products helps to relieve the raw material dependence of the sector and contributes to enhancing the food security of mankind.

Cradle-to-Cradle certification is applied for products, which are result of clean production, recycling and reuse of waste products with a high content of the biologically active substances. The adequate transformation of conventional technological processes into clean production requires a careful analysis of the environmental aspects of the product life cycle phases.

LCA is a product-oriented tool for analyzing and quantifying the products'environmental impact of cradle-to-grave (Boye and Arcand, 2013, p. 3). LCA is an internationally recognized tool whose application is regulated by ISO standards.

The Life Cycle Assessment supports the definition and calculation of the cumulative impact of the product or process on the environment, the formulation of alternatives for improving the environmental aspects of products and processes, development of company and sector analysis, quantitative substantiation of the change in the ecological footprint of a product or process (Williams, 2009, p. 2). Thus, LCA is often perceived as a source of clean production.

The Life Cycle Assessment and accompanying methods diagnose, summarize and indicate where are the most prominent environmental aspects of the food product (Calderón et al., 2010). They do not provide strategies for the environmental development, innovations, redesign of the product or process and clean production. This requires the application of the MET Matrix method.

The MET Matrix method allows to investigate and to operationalize the specific environmental aspects of the product through input materials, energy and the level of emitted toxicity (Ostad-Ahmad-Ghorabi and Pamminger, 2007). The method combines qualitative and quantitative analysis. Based on the results of the MET Matrix analysis, the products are grouped into five groups:

➢ Type A: Raw material intensive product
➢ Type B: Manufacture intensive product
➢ Type C: Transportation intensive product
➢ Type D: Use intensive product
➢ Type E: Disposal intensive product

The application of the MET Matrix method guides manufacturers in choosing a specific strategy to improve the environmental aspects of the product and the implementation of clean production.

The efforts to reduce resource consumption and the emissions, as well as the processing and secondary use of materials and raw materials through ecodesign and clean production, help reduce operating costs. The responsible business conduct goes beyond the imperatives of business efficiency and increasingly focuses on eco-efficiency and eco-balances. The clean production is increasingly recognized a guiding principle in manifacture development strategies, especially in the food industry.

RESULTS AND DISCUSSION

The clean production of food products determines the prevention and reduction of environmental aspects of food throughout all phases of the life cycle. The clean production also affects the engineering characteristics of the technological processes (Dewberry and Goggin, 1996; Graedel and Allenby, 1995). The strategic green resource management is at the core of clean production. The eco-efficient products have reduced energy and resource consumption and minimal waste. It stimulates the development of innovations.

The clean production is an incremental green innovation that allows simultaneous cost and resource input optimization, improvement of quality and of applied resources and technologies.

The innovation model of clean production is among the basic business case for sustainability. The innovative business models for sustainability can be summarized in three aspects: 1) business case for sustainability generates corporate sustainability and sustainable development (Dyllick and Hockerts, 2002); 2) eco-innovation is the result of the company's economic rationality (Eden, 1994); and 3) eco-innovation is encouraged if it brings value for the company (van Marrewijk, 2003). The business model for implementation of clean production is a proactive eco-innovation, according to the Wilson's classification (Wilson, 1975).

The food industry is very resource intensive. According to Eurostat data, electricity consumption by industry, transport activities and households / services (GWh) in Bulgaria varies between 7818 – 8910 GWh for the period 2010 – 2016, which is above the electricity consumption of comparable countries such as Estonia (2095 – 2152 GWh), Croatia (3478 – 3291), Latvia (1590 – 1667 GWh), Slovenia (5487 – 6057 GWh).

Drying and packaging are also resource intensive. The packaging of food products is related to food quality and safety. At the same time, it is also a communication tool between manufacturers and consumers. The possibilities of digital marketing contribute to the implementation of clean production at the stage of market presentation and advertising of food products (Kulova and Mihailov, 2018).

The nature of production technology in the food industry is also characterized by high waste intensity. Animal and vegetal wastes, according to Eurostat data in Bulgaria, vary between 731091 – 972685 tonne for the period 2010 – 2016. For comparison, these wastes for Estonia are 280338– 151405 T, Croatia – 119502 – 614474 T, Latvia – 166304 – 143395 T, Hungary – 808058 – 734568 T, Slovenia – 264045 – 267438 T (Eurostat). The majority of countries are trying to reduce the amount of generated animal and vegetable waste. The trend in Bulgaria is the opposite, which also calls for more intensive measures for the implementation of clean production. A positive trend in Bulgaria is the increase in the share of recyclable wastes – 1708337 – 2049372 tonne (Eurostat). The trend in other European countries in the region is similar. But, the waste generated by the Bulgarian industry for the period 2010 – 2016 is characterized by sustainability and even slight growth: 3306468 – 3469171 tonne (Eurostat). In the other European countries in the region, the trend is similar. The optimization of waste management in the production processes is supported by the project management of the corresponding innovations (Teneva et al., 2018). Significantly the achievement of sector sustainability is a function of waste reduction. On this background, Environmental protection expediturre in Bulgaria for the period 2010 – 2013 is 0.37 – 0.66% of GDP (Eurostat), bringing the country closer to other European countries. The share of Total environmental investments for 2010-2013 in Bulgaria is 0.46-0.34% of GDP (Eurostat), whereby the country also does not differ from other European countries.

In terms of content, the ecoindustrial synergy of clean production is based on recycling design, design for recovered production, and design for release (Madu, 2003, pp. 156 – 157). The idea is to incorporate recyclable materials with extended life and multiple uses into the production process and to design the waste-free end of product life cycle.

The achievement of clean production is a function of the use in the manufacturing process of materials and components with extended life, which can be recovered and reused, the use of recycled materials and / or raw materials that are recyclable, designing waste-free end of product life cycle, i.e. the transformation of waste materials (by-products) into production raw materials.

The scarcity of resources, the need for energy efficiency, the optimization of waste production intensity and the rising food quality and safety requirements determine the need for the implementation of clean production in SMEs

in food industry. In addition to improving the environmental aspects of the product, clean production could also be motivated by the striving to reduce costs, increase confidence, open up new market segments, increase fairness and responsibility. Thus, environmental, economic and social factors intertwine with the application of clean production. The functional innovations for clean production implementation help to achieve eco-efficiency. In the light of this analysis, clean production is becoming the main source for the food industry sustainability.

The implementation of eco-innovations often encounters a number of constraints and barriers, including inertia in companies (Chesbrough, 2010; Doz and Kosonen, 2010). The business model for the clean production implementation is generally applicable to all interested small and medium-sized enterprises in food industry, but it still requires some limitations. They are primarily related to the innovative nature of the model and hence the need for investment. Often, it is difficult for SMEs to allocate funds for green innovation, even if they are not so complex. Furthermore, the production volume of SMEs usually does not allow the negotiation of lower prices for ecological raw materials. Thus, the risk of unprofitable manufacture increases. The consumer prices would also be uncompetitive, threatening the market realization of the product. Therefore, the eco-innovative business model of clean production is better suited to implementation in innovative food start-ups, SMEs that are a part of green cluster networks and eco-oriented companies with previous green innovations.

The dimensions and application of clean production in the Bulgarian food industry at this stage are hampered by the immaturity of the economic forms in the country, the lack of free capital in the enterprises for voluntary investments in environmental projects (rather it meets regulatory requirements), the lack of experience and insufficient methodological knowledge.

The benefits and contributions of clean production in SMEs can help to overcome these difficulties.

CONCLUSION

The clean production is an integral part of efforts to achieve high quality and food safety from raw material extraction to end-user consumption. The clean production is not solely a technological innovation, but a holistic business model that involves integrating environmental requirements into corporate strategy, indicators, tools and process and industrial design.

The ecological footprint of the food industry makes the need for an integrated implementation of clean production practices from raw material extraction to packaging and waste disposal of final consumer. Thus, functional food products can be created to combine the requirements of high quality, safety, eco-efficiency and health.

REFERENCES

Birkin, F., Cashman, A., Koh, S. C. L., & Liu, Z. (2009). New sustainable business models in China. Business Strategy and the Environment, 18(1), pp. 64 – 77.

– Boye, J., Arcand, Y. (2013) Current Trends in Green Technologies in Food Production and Processing. Food Ingineering Reviews, vol. 5, Issue 1, pp. 1 – 17.

Calderón, L.A., Iglesias, L., Laca, A. et al., (2010) The utility of Life Cycle Assessment in the ready meal food industry, Resources, Conservation and Recycling 54, pp. 1196 – 1207.

Chesbrough, H. (2010) Business model innovation: opportunities and barriers, Long Range Planning, Vol. 43, Nos. 2/3, pp. 354 – 363.

Dalhammar, C. (2016) Industry attitudes towards ecodesign standards for improved resource efficiency. Journal of Cleaner Production 123, pp. 155 – 166.

Dewberry, E., Goggin, P. (1996) Spaceship Ecodesign. Co-Design, p. 12 – 17.

Doz, Y. and Kosonen, M. (2010) Embedding strategic agility: a leadership agenda for accelerating business model renewal, Long Range Planning, Vol. 43, Nos. 2/3, pp.370 – 382.

Dyllick, T. and Hockerts, K. (2002) Beyond the business case for corporate sustainability, Business Strategy and the Environment, Vol. 11, No. 2, pp.130 – 141.

Eden, S. (1994) Using sustainable development: the business case, Global Environmental Change, Vol. 4, No. 2, pp.160 – 167.

Eurostat, https://ec.europa.eu/eurostat

Graedel, T.E., Allenby, B.R. (1995) Industrial Ecology. New Jersy: Prentice Hill.

International Organization of Standardization, www.iso.org

Kulova, I. and Mihailov, M. (2018) Digital Marketing – the Key to Successful Electronic Business, Scientific Works of University of Food Technologies, Proceedings of the 65th Anniversary Scientific Conference with International Participation "Food Science, Engineering and Technology – 2018", Organized in cooperation with the Foundation "Scientific Research", pp. 205 – 210.

Madu, C. (2003) Competing on Quality and Environment. Chi Publishers.

National Statistical Institute, http://www.nsi.bg

Ostad-Ahmad-Ghorabi, H., Pamminger, R. (2007a) Ecodesign for Sustainable Development. Education and Culture Lifelong Learning Progrmme Erasmus.

Prokopov, Ts, Chonova, V., Slavov, et al. (2018), Effects on the Quality and Health-enchancing Properties of Industrial Onion Waste Pow-

der on Bread, Journal of Food Science and Technology, 55 (12), pp. 5091 – 5097.

Schneider, S., and Spieth, P. (2013). Business model innovation: Towards an integrated future research agenda. International Journal of Innovation Management, 17(01), 134000.

Teneva A.,Nikolova-Alexieva V., Tuntova A., (2018), Maintaining Steady Cost Projection on Wastewater Engineering Projects in Bulgaria, International Conference on High Technology for Sustainable Development (HiTech), doi.org/10.1109/hitech.2018.8566388

Van Marrewijk, M. (2003) Concepts and definitions of CSR and corporate sustainability, between agency and communion, Journal of Business Ethics, Vol. 44, Nos. 2/3, pp.95 – 105.

Williams, A. (2009) Life Cycle Analysis: A Step by Step Approach. Illinois Sustainable Technology Center.

Wilson, I. (1975) What one company is doing about today's demands on business, in Steiner, G.A. (Ed.): Changing Business-society Interrelationships, Los Angeles Graduate School of Management, UCLA.

✉ **Silviya Topleva**
https://orcid.org/0000-0002-3598-8587
University of Food Technologies
Plovdiv, Bulgaria
E-mail: silviyatopleva@gmail.com

✉ **Tsvetko Prokopov**
https://orcid.org/0000-0002-3054-6958
University of Food Technologies
Plovdiv, Bulgaria
E-mail: tsvetko_prokopov@abv.bg

✉ **Donka Taneva**
https://orcid.org/0000-0001-6036-8702
University of Food Technologies
Plovdiv, Bulgaria
E-mail: don_taneva@abv.bg

ASSESSMENT OF THE CHANGES IN THE GROUNDWATER RECHARGE TO PRECIPITATION RATIO IN THE RECENT YEARS INFLUENCED BY THE AIR TEMPERATURE AND RAIN INTENSITY INCREASE IN THE WEST AEGEAN REGION OF BULGARIA

Olga Nitcheva[1,2], Polya Dobreva[1,2],
Nelly Hristova[3], Vesselin Koutev[4], Donka Shopova[2],
Albena Vatralova[2], Emil Bournazki[2]

[1] *Institute of Mechanics – Bulgarian Academy of Sciences (IMech – BAS)*
[2] *Institute for Climate, Atmosphere and Water Research –*
Bulgarian Academy of Sciences (CAWRI – BAS)
[3] *"St. Kliment Ohridski" University of Sofia*
[4] *University of Forestry "Sveti Kliment Ohridski"*

Abstract. The topic of this report concerns the expected changes of the important part of the water resources of Bulgaria caused by the moving of the main precipitation to the warm seasons. The study examines the influence of the air temperature and rain intensity as main factors for the change in the potential groundwater recharge / precipitation ratio in the summer months of three recent years on the territory of Southwest Bulgaria (Basins of Struma and Mesta rivers).

The assessment has been performed by application of a precipitation-runoff hydrological model, which is a sub-model of NASA's climate model.

Keywords: groundwater recharge; R/P; rainfall-runoff model (CLM)

INTRODUCTION

The climate changes lead to frequency and intensity of extreme rainfalls and storms, can lead to less groundwater recharging, as much of the rainfall is lost as runoff[1]. In this case, the intensity of precipitation reaching the earth's surface exceeds the capacity for infiltration of the soil, runoff occurs and thus limits the part of precipitation that can contribute to recharging (Tashie, Mirus & Pavelsky, 2016).

The generation of runoff by exceeding the infiltration depends not only on the precipitation characteristics, but also on complex conditions such as soil stratigraphy, hydraulic properties, topography, vegetation and preconditions (Mirus & Loague, 2013).

Extreme rainfalls become more frequent. This trend will continue as the planet continues to warm. Warmer air can hold more water vapor. For each degree of warming, the capacity of the air for water vapor increases by about 7 percent. An atmosphere with more humidity can lead to more intense rainfall events, which we have seen in the recent years[2)].

In Bulgaria since 2014 the annual rainfalls have increased moving the intensive precipitations to the warm seasons. Although the rainfall in the recent years is above the annual average, the country's runoff is decreasing, as is the runoff / precipitation ratio from 30% to 16%[5]. The reason for this is the high temperature during the greater part of the rainfalls, which leads to increased evapotranspiration and less surface runoff and subsurface recharge. Intensive rainfalls also lead to increased flood runoff[6] (Perrou; Garioud & Parcharidis, 2018). All this leads to reduced soil infiltration, insufficient groundwater resources and disturbed balance in the soil-air-crop-water system.

This report presents a calculation of the groundwater (GW) recharge/precipitation ratio in the summer months May, June and July of the years 2013, 2018 and 2019 with increasing air temperature and rain intensity. They are selected for investigation because of the significant rainfalls occurred at that time of the year. The study is done by simulating the water and energy cycle on the territory of West Aegean region in Bulgaria.

This region is characterized as very fertile land, with best soil and climatic conditions for growing agricultural products. A Bulletin of the Ministry of Environment and Water[5] for the total runoff of the region, obtained from hydrometric measurements and assessment by hydro-geological methods, estimates the average annual runoff values as amounting up to 3412.10^6 m^3, 326.10^6 m^3 of which are groundwater recharge, ie. 9.5% of the total outflow. The forecasts are for decrease in this percentage. The current hydrological study simulates the water balance and monitors the effectiveness of soil infiltration to the groundwater in conditions of extreme summer rainfall, which is more than half the annual rainfall (Gartsiyanova, 2019), (Vasileva, 2019), (Kolcheva, 2019).

The purpose of the study is to compare the average monthly temperatures, GW recharge and its ratio to the rainfall during the summer months of the selected years in order to assess the degree of the impact of climatic condition changes that will increase in the future.

Carried out is mapping of the calculation results to visualize the distribution of GW recharge/rainfall ratio over the basin territory.

METHODOLOGY AND STUDY AREA

The study is performed by simulating the water, energy and phenology cycle on the territory of West Aegean region using the mathematical model – CLM (Community Land Model, NASA) has been undertaken (Oleson at al., 2004). Meteorological,

soil texture and phenology input needed by the model in this study is gathered from NASA atmosphere NCEP/NCAR Reanalysis data and the International Geosphere – Biosphere Programme (IGBP) data base (Kalney at al., 1996). The surface runoff is calculated as a function of the soil moisture. The dynamics of the water flow through the soil profile is physically represented by the Richards equation (1) presenting the soil water retention functions by the Clapp and Hornberger dependences.

$$\frac{\partial \theta}{\partial t} = - \frac{\partial q}{\partial z} - e \qquad (1)$$

where θ is the volumetric soil water content (mm³ of water mm⁻³ of soil), t is the time (s), z is the soil profile depth (mm), positive upwards, q is the soil infiltration (mm s⁻¹), e is the evapotranspiration (s⁻¹). The equation (1) is solved numerically by dividing the soil column into ten horizontal layers with boundary condition of the infiltration flux into the top soil layer and gravitational drainage at the bottom of the soil column (specified here as the hydraulic conductivity K of the tenth soil layer – 3.43 m). In case of high rainfall when the soil profile gets saturated and the surface excess water doesn't run off the flux boundary condition switches to a pressure head boundary condition.

The initial conditions for temperature and mositure distribution in the soil profile can be set by the user or be accepted the CLM model default initialization – uniform soil temperature of 283 K and volumetric water content 0.3 mm³/mm³ in all ten soil layers with no snow and canopy water.

The model calculated GW recharge can be considered as a potential one as the further moving of the infiltrated water to GW body is conditioned by the hydrogeological properties of the area. Nevertheless this is the amount of the atmosphere water that will feed in one or other way the GW resources.

The terrain surface grid in the present study is built with resolution (cells) 5 x 5 km, employing the model built-in water transport and transformation properties data according to the topography, land cover, soil profile and vegetation (this resolution can be reduced to 1 x 1 km in case of available data). The atmospheric forcing data are distributed in computational grid nodes with cells 200 x 200 km. The large-scale network with such grid resolution was accepted because of the availability of the climatic data in its nodes, such as air temperature, air pressure, specific humidity, solar radiation, wind speed, precipitation with several hours time step, something which is the most problematic issue with such investigations. The network mostly influences the precision of the rainfalls distribution when they have more local character. Furthermore the study has a comparative purpose and some deviations in the results absolute values are not of importance in the particular case.

The model veracity is investigated in model inter-comparison studies – Project for Intercomparison of Land Surface Parametrization Schemes (PILPS) and Global Soil Wetness Project (GSWP) (Dirmeyer, Dolman & Sato, 1999). For adaptation and cali-

bration of the model suiting the Bulgarian climatic and soil conditions a number of studies have been carried out in the recent years, showing sufficiently good approach to measurement or calculated by other methods data (Nitcheva, 2018).

The West Aegean region is one of the four river basin management regions of Bulgaria with an area of 20 700 km[2]). It covers the catchment areas of the Struma, Mesta and Dospat rivers. This region is the most water-yielding zone of the country, the relief is highly mountainous, the climate is temperate-continental and Mediterranean in its southern part. The Struma River springs from Vitosha Mountain at 2246 m above sea level, the average altitude of the catchment is 900 m. The Mesta River springs from Rila Mountain at 2240 m above sea level, the average altitude of the catchment is 1318 m. The Dospat River springs from the Western Rhodopes at 1643 m above sea level, the average altitude of the catchment is 1200 m above sea level. These are the three rivers characteristics on the Bulgarian territory. They continue into Greek territory and flow into the Aegean Sea[6].

RESULTS AND DISCUSSION

The average monthly temperatures, monthly groundwater recharge, monthly rainfall and GW recharge/rainfall ratios for the summer months - May, June and July during the three years (normal – 2013, and wet summers- 2018, 2019), calculated with the Community Land Model (CLM), are shown in Table 1.

Table 1. Model calculated watershed parameters –
Precipitation, T, Recharge and R/P ratios

Summer months	Average air T (ºC)	GW recharge (mm)	Precipitation (mm)	GW recharge/ precipitation	Annual precipitation (mm)	Average annual air T (ºC)
May 2013	14,3	16	97	0,16		
June 2013	16,6	95	230	0,41	813	9,9
July 2013	18,4	3	98	0,00		
May 2018	15,4	53	194	0,27		
June 2018	17,6	107	299	0,35	1283	11,3
July 2018	18,5	102	295	0,35		
May 2019	12,5	55	176	0,31		
June 2019	18,6	111	300	0,34	918	10,3
July 2019	19,6	5	150	0,03		

The average annual temperature in 2018 and 2019 has increased to the one in 2013. In the three years under review it is noticeable that in June the summer precipitation is of the highest values. So we will comment on the results of that month in the three years. The average monthly air temperature in June 2013 is 16.6º C, in June 2018 – 17.6º C, and in June 2019 it is 18.6º C, ie. the increase is significant.

The monthly precipitation respectively is 230 mm, 299 mm and 300 mm. The total precipitation has also increased in the last two years. The groundwater recharge in June 2013 – 95 mm (813 mm annual rainfall), June 2018 – 107 mm (1283 mm annual rainfall), June 2019 – 103 mm (918 mm annual rainfall). The GW recharge/rainfall ratio is respectively 0.41, 0.35 and 0.34, i.e. in the last two years, when the summer rainfall intensity grows, the efficiency of groundwater feeding goes down with 6%.

Figures 1, 2 and 3 show the model calculated GW recharge/rainfall ratio distribution over the West Aegean region.

Figure 1. GW recharge/rain ratio distribution in June 2013

Figure 2 shows that the most vulnerable to the climate changes impact is the eastern part of the region (in red).

Figure 2. GW recharge/rain ratio distribution in June 2018

Figure 3. GW recharge/rain ratio distribution in June 2019

In 2018 and 2019, the catchment area of the Dospat River is the region with the lowest rainfall efficiency in terms of groundwater recharge. The reason for this is the high altitude – from 1200 mm to 1610 mm. Another reason is the partly eroded rocky terrain surface. Main soil types are Chromic Luvisols and Albic and Humic Cambisols. Soil profiles are usually less than 25 cm, due to the intensive erosion. The reduction of infiltration capacity and the increased runoff in turn increases flooding risk (Ungaro, Calzolari, Pistocchi, & Malucelli, 2014) among the other effects on the soil feature itself. It is advisable the building of simple dikes for runoff velocity and intensity decrease. Also, new practices and technologies techniques should be applied such as building rain harvesting wells for improvement of the subsoil infiltration, thus collecting more precipitable rain water in the groundwater that will create favourable soil-water-crop-air environment.

CONCLUSIONS

Climate change and increasing pressure on farmland to satisfy the growing demand require an increasing capacity of water and land management. Understanding the climate change impact on basic groundwater-precipitation relations is key to management.

The study of the change in GW recharge/rainfall in recent years shows that rainfall is increasing but runoff is decreasing. The reason for it is the change in the seasonal distribution of the rainfalls - intense rainfall during the warm season with developed leaf cover on the ground and increased evaporation. This leads to reduced groundwater resources and disturbed equilibrium in the soil zone. The practical implementation of the engineering solutions mentioned herein would improve soil functionality and ecosystem services thus contributing to adaptive water and land management.

NOTES

1. Mohammad, A. (2020, May 24). Climate Change. An-Najah National University. Retrieved from http://www.hwe.org.ps/Projects/Training/Sustainable%20 Management/presentations/Climate%20Change%20-%20General%20Overview.pdf

2. Center for Climate and Energy Solutions (2020, June 2). Extreme Precipitation and Climate Change. Retrieved from https://www.c2es.org/content/extreme-precipitation-and-climate-change/

3. Executive Environment Agency (ExEA) (2020, May 20), Национален доклад за състоянието и опазването на околната среда в РБългария 2017. Retrieved from http://eea.government.bg/bg/soer/2017/water/water2

4. Hellenic International Development Cooperation Department (2020, April 4). Use of modern technology for the protection and management of water resources in Strymonas/Struma River basin. Retrieved from https://www.researchgate. net/profile/Charalampos_Doulgeris/publication/290597480_Use_of_modern_ technology_for_the_protection_and_management_of_water_resources_ in_StrymonasStruma_River_basin/links/569a403008aea1476948f8aa/ Use-of-modern-technology-for-the-protection-and-management-of-water-resources-in-Strymonas-Struma-River-basin.pdf

5. Ministry of Environment and Water (MOEW) (2020 April 2). Пресни водни ресурси на България. Retrieved from https://www.moew.government.bg/bg/vodi/ byuletin-za-sustoyanieto-na-vodnite-resursi/presni-vodni-resursi-na-bulgariya/

6. Ministry of Environment and Water, (2020 May 20). Descriptions of the charatceriscs of the Показаните резултати са за Descriptions of the characteristics of the West Aegean River Basin Directorate. Retrived from https://wabd.bg/docs/plans/purb1621/01_Razdel_1_Harakteristiki_ZBR.pdf

REFERENCES

Tashie, A., Mirus, B.& Pavelsky, T. (2016). Identifying long-term empirical relationships between storm characteristics and episodic groundwater recharge. *Water Resources Research*, *52(1), 21 – 35.*

Mirus, B. & Loague, K. (2013). How runoff begins (and ends): Characterizing hydrologic response at the catchment scale. *Water Resources Research, 49(5), 2987 – 3006.*

Perrou, T.; Garioud, A. & Parcharidis, I. (2018). Use of Sentinel-1 imagery for flood management reservoir-regulated river basin. *Front. Earth Sci., 12, 506 – 520.*

Gartsiyanova, K. (2018). Groundwater studies in Bulgaria. *Prob-lems of Geography, 3/4, 56 – 74.*

Vasileva, T. (2019). An assessment of potential groundwater recharge zones in Bulgaria. *Geologica balcanika, 48(1), 43 – 61.*

Kolcheva, K. (2019). Water Allocation climate change – character. *Water Affairs Journal, ½, 2 – 10.*

Oleson, K., Dai, Y., Bonan, G., Bosilovich, M., Dickinson, R., Dirmeyer, P., Hoffman, F., Houser, P., Levis, S., Niu, G., Thornton, P., Vertenstein, M., Yang, Z. & Zeng, X. (2004). Technical Description of the Community Land Model (CLM), Colorado NCEP/NCAR press.

Kalnay, E., Kanamitsu, M., Kistler, R., Collins, W., Deaven, D., Gandin, L., Iredell, M., Saha, S., White, G., Woollen, J., Zhu, Y., Chelliah, M., Ebisuzaki, W., Higgins, W., Janowiak, J., Mo, K.C., Ropelewski, C., Wang, J., Lectmaa, A., Reynolds, R., Jenne, R. & Joseph, D. (1996). The NCEP/NCAR 40-year reanalysis project. *Bull. Amer. Meteorol. Soc., 77, 437 – 471.*

Dirmeyer, P., Dolman, A., Sato, N. (1999). The Global Soil Wetness Project: A pilot project for global land surface modeling and validation. *Bulletin of the American Meteorological Society 80, 851 – 878.*

Nitcheva, O. (2018). Hydrology models approach to estimation of the groundwater recharge. Case study in the Bulgarian Danube Watershed. *Environ Earth Sci 77, 464.*

Ungaro, F., Calzolari, C., Pistocchi, A., Malucelli, F. (2014). Modelling the impact of increasing soil sealing on runoff coefficients at re-gional scale: a hydropedological approach. J. Hydrol. Hydromech., 62 (1), 33 – 42.

✉ **Olga Nitcheva**
Institute of Mechanics
Institute for Climate, Atmosphere and Water Research
Bulgarian Academy of Sciences
Sofia, Bulgaria
E-mail: olganitcheva@yahoo.com

✉ **Polya Dobreva,**
Institute of Mechanics
Institute for Climate, Atmosphere and Water Research
Bulgarian Academy of Sciences
Sofia, Bulgaria
E-mail: polya2006@yahoo.com

✉ **Nelly Hristova**
"St. Kliment Ohridski" University of Sofia
Sofia, Bulgaria
E-mail: hristovaneli@abv.bg

✉ **Vesselin Koutev**
University of Forestry "Sveti Kliment Ohridski"
Sofia, Bulgaria
E-mail: koutev@yahoo.com

✉ **Donka Shopova**
Institute for Climate, Atmosphere and Water Research
Bulgarian Academy of Sciences
Sofia, Bulgaria
E-mail: dshopova@gmail.com

✉ **Albena Vatralova**
Institute for Climate, Atmosphere and Water Research
Bulgarian Academy of Sciences
Sofia, Bulgaria
E-mail: albenav@mail.bg

✉ **Emil Bournazki**
Institute for Climate, Atmosphere and Water Research
Bulgarian Academy of Sciences
Sofia, Bulgaria
E-mail: bournaski@aim.com

RAPANA VENOSA RAPA WHELK RESPONSIBLE FOR RAPID DESTRUCTION OF BLACK SEA COASTAL *MYTILUS GALLOPROVINCIALIS* LITTORAL REEF COMMUNITIES - RESULTS FROM A PRELIMINARY STUDY IN SW BLACK SEA (SOZOPOL BAY, BULGARIA)

Dimitar Berov, Stefania Klayn, Ventsislav Karamfilov
Marine Ecology Laboratory, Institute for Biodiversity and Ecosystem Research – Bulgarian Academy of Sciences

Abstract: The dynamics of predator-prey interaction between the invasive Rapa whelk *R. venosa* and the black mussel *M. galloprovincialis* in the coastal zone of the Black Sea shapes the structure of the benthic hard rock ecosystems in the littoral area of the basin. Applying a combination of observational methods (transects, photo surveys) and exclusion 'cage' experiments we tracked the rapid increase in Rapa whelks population density (from 1.1 ind.m^2 up to 13 ind.m^{-2}) and the destruction of infralittoral mussel communities by the Rapa whelks in the study area (from up to 2469.95±1184.82 g.m^{-2} wet biomass and 1054.66±228.19 ind.m^{-2} to practically none). A rapid recovery was noted just 6 months later in caged experimental plots where *R. venosa* could not reach the newly settled mussels, in contrast to open plots where no new mussel colonies developed. The importance of harvesting of Rapa whelks by divers as means of local control of their populations, and of the preservation of natural circalittoral *M. galloprovincialis* populations as sources of larvae for the resettlement of coastal habitats is also discussed.

Keywords: Black Sea, exclusion experiment, Rapana venosa, Mytilus galloprovincialis, invasive species

INTRODUCTION

Coastal marine ecosystems are a hotspot of biodiversity and productivity, and provide essential resources and ecosystem services to humans inhabiting the coastal zone. (Pan et al., 2013) Located at the interface between land and the open seas, they serve as buffers between coastal human activities and open seas, and are impacted by transport, industry, agriculture, fisheries and tourism. The Black Sea is one of the marine basins that is most severely impacted by human activities in

recent decades. Being a semi enclosed sea receiving outflows from some of the largest European rivers, it accumulates nutrient inputs and pollution from large parts of the European continent. This, in combination with severe overexploitation of local natural resources, and impacts from invasive species, led to a severe decline and degradation of local benthic and pelagic ecosystems (Daskalov, 2002; Mee, 1992; Zaitsev, 1992).

The black mussel *Mytilus galloprovincialis* (Lamarck, 1819) thrives in the nutrient-rich coastal waters of the Western Black Sea where it forms some of the most abundant and productive benthic ecosystems – circalittoral soft-bottom biogenic reefs and infralittoral rocky bottom communities (Zaitsev, 2008). These ecosystems were significantly affected by the deterioration of environmental conditions in the 1980s, especially in the NW Black Sea shelf, where eutrophication, bottom hypoxia and predation from the invasive Rapa whelk *Rapana venosa* (Valenciennes, 1846) led to the destruction of more than 90% of the circalittoral mussel reefs (Konsulova, 1992; Marinov, 1990; Zaitsev, 1992).

Rapana venosa, a native species to the NW Pacific, was introduced in the Black Sea in the 1940s and quickly spread throughout the whole basin, reaching the Bulgarian coast by the mid-1950s (Bondarev, 2014; Zolotarev, 1996). Having no natural predators in the Black Sea and having access to abundant food sources - mussels, clams and other soft- and hard bottom crustaceans , the Rapa whelk population developed rapidly, turning it into an invasive species that severely impacted local benthic ecosystems. A classical 'predator-prey 'interaction cascade has developed between the Rapa whelk and the black mussels that follows a complex dynamism and has multiannual oscillations (Bondarev, 2014; Snigirov et al., 2013).

In the absence of natural predators, removal of the invasive species by humans is the only possible way to control, at least locally the spread of the invader. *R. venosa* harvesting is an important fisheries activity in Bulgaria. Annually between 3116 and 4835 tons of Rapa whelk are collected (Executive Agency for Fisheries and Aquaculture official data for 2010-2019). Commercial scuba divers collecting *R. venosa* by hand in the shallow coastal rocky reefs and sandy bottoms collect more than 70% of these quantities – between 1754 and 4800 tons per year (EaFA official data 2010-2019). Annual harvests of *R. venosa* with beam trawls from sandy and muddy bottoms in deeper waters are in the range between 1700 and 2400 tons. The harvesting of *R. venosa* by beam trawls usually takes place within the areas where *M. galloprovincialis* reefs on muddy soft bottoms are present in the Bulgarian Black Sea shelf – Varna Bay, offshore areas in front of Cape Kaliakra, Cape Emine and Cape Maslen nos. Even though the removal or Rapa whelks should be beneficial for the mussels, historically, this activity has had significant negative effects on the recovery of these ecosystems (BSBD, 2013; Konsulova, 1992; Todorova et al., 2012). Currently this type of harvesting is regulated – certain areas

of the shelf are open for harvesting in different periods, which in theory should be related to the recovery of mussel populations from this impact. The local harvesting of Rapa whelks by divers could be significant in some coastal areas. In the area of our study – Sozopol bay – annually between 50 and 250 tons or *R. venosa* are collected by divers (EAFA official data 2010-2019). This local removal of *R. venosa* from coastal reefs and sandy bottoms could have a significant local impact on their populations and helps to decrease the predatory pressure on local *M. galloprovincialis* communities.

The goal of the current study was to collect in-situ information on the dynamics of the R*. venosa - M. galloprovincialis* predator-prey interactions in the coastal rocky reef habitats in an area with well-developed and abundant mussel communities. Permanent monitoring quadrants were set up, where the state of the benthic ecosystems was monitored periodically with non-destructive photo methods. Additionally, an exclusion experiment, limiting the access of *R. venosa* to certain areas of the benthal was also set up, allowing us to study the degree of influence of this predator pressure on the state and structure of the studied benthic ecosystem.

MATERIALS AND METHODS

In order to study the effects of the predatory pressure of *R. venosa* on *M. galloprovincialis*-dominated communities, a cage exclusion experiment was set up. The study was carried out in the BG0000146 'Gradina-Zlatna ribka' Natura 2000 SCI area in the vicinity of Sozopol, SW Black Sea (Fig. 1). The site has a diversity of soft- and hard bottom substrates and hosts most of the typical Black Sea benthic and pelagic species and habitats. Two sites were selected in the area – a shallow-water (2 m depth) sheltered rocky reef in an area under local eutrophication pressure, which until recently had a well-developed *M. galloprovincialis* reefs (Site 1), and a deeper coastal rocky (5-6 m depth) reef on an exposed site under no local anthropogenic pressures, with well-developed *M. galloprovincialis* communities (Site 2). The distance between Site 1 and Site 2 is app. 3 km (Fig. 1) At each site, three stainless steel frame cages with 50/50 cm base and 20 cm height were placed with metal anchors mounted with an underwater drill (Nemo Tools Inc.). Initially a 2 cm mesh size plastic net was used for the cages, which was replaced with a 0.5 cm mesh size within the first month of the experiment, as small *R. venosa* (<2 cm) continued entering the exclusion area.

A 50/50 cm control plot was marked adjacent to each cage. Additionally, at each cage a 50/50 'zero' control sample was collected for evaluation of biodiversity and population characteristics of benthic communities at the start of the experiment. Cage mounting was carried out by a team of two scientific scuba divers, and required between 30 and 60 min per cage, depending on rock hardness and time required for drilling. A transect for visual estimation of *R. venosa* population density was
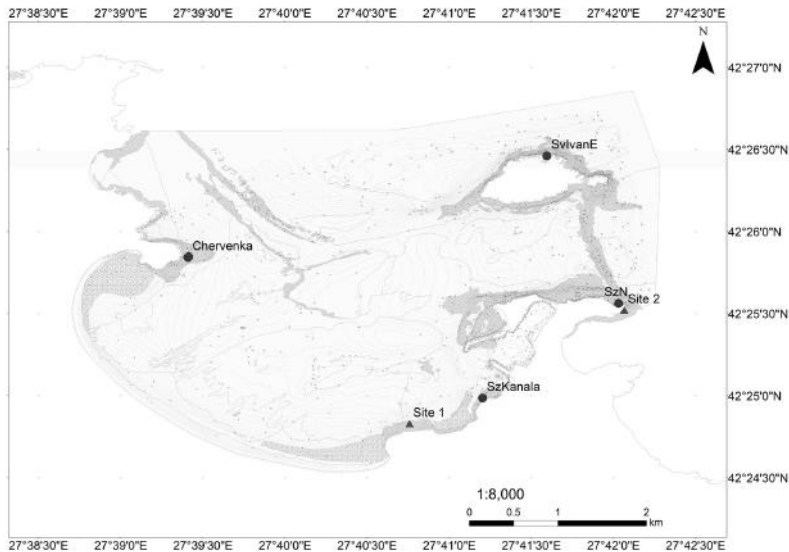
Figure 1. Map of the study area BG0000146 'Gradina-Zlatna ribka' with positions of monitoring sites (circles) and cage experiment sites (triangles). Rocky bottoms (grey-white stripes), soft-bottom types (white) and Zostera seagrasses (textured) and bathymetry (0.5 m isolines) are also marked.

selected and marked at each site, starting from the deep end of the rocky reefs where sandy bottom starts and finishing and the shallow end of the site, following the main vector of Rapa whelk movement (Site 1 – 20 m transect, 5-2 m depth; Site 2 - 20 m transect, 10.5-2.5 m depth) (Bondarev, 2014) Following the severe winter storms in December-February 2020, all three cages at Site 2 and one of the three cages at Site 1 were destroyed – removed from the rocky reefs, thus allowing *R. venosa* to access the exclusion area.

Photos of the benthal within each cage and adjacent control plots were taken periodically (07.2019, 09.2019, 10.2019, 02.2020, 06.2020) with a Canon 5D MIII camera in an Ikelite housing with two Ikelite DS-161 strobes. The % cover of the benthos at each plot by visible zoobenthic and macroalgal species was evaluated with CoralPoint Count 3.6, following a stratified random point distribution for species identification (100 points per photo, details on methodology in (Berov et al., 2016)). For a better visualization and as an attempt to estimate mussel growth, 3D photogrammetry models of each plot were constructed with the photos taken using Agisoft Metashape Professional (Agisoft LLC).

As part of our efforts of developing a citizen-science project (BaklanMed Reconnect Project, https://cs-reconnect.hcmr.gr/) for observation of the changes in

benthic ecosystems in Sozopol Bay, a network of permanently marked quadrants was placed in the study area (Fig. 1). It included 4 sites where two 50/50 cm quadrants with typical infralittoral benthic communities were selected (C. *barbata* and *C. bosphorica*-dominated macroalgal communities, *M. galloprovincialis*-dominated zoobenthic communities) and marked by placing metal anchors with a drill. Photos of each quadrant within the network were taken periodically (06.2019, 10.2019, 06.2020) and the presence and quantities of visible macrobenthic species were determined.

RESULTS
Biodiversity and characteristics of species
At the start of the experiment, the benthic community at Site 1 was dominated by opportunistic green macroalgae – *Cladophora coelothrix, C. albida, Ulva rigida*, intermixed with *Mytilaster lineatus* mussels and other bivalves (*Irus irus*), and other molluscs (Fig. 2). The average length of *M. lineatus* from 'zero control' samples at Site 1 was 7.7±5.8 mm (max size 24.4 mm), with 248±82.1 ind.m^{-2} population density and a wet biomass of 72.21±21.50 g.m^{-2}. The wet biomass of macroalgae within the sampled 'zero controls' was 624.56.08±451.31g.m^{-2} (*Cladophora coelothrix, Cladophora albida, Ulva rigida*). No Rapa whelks were found in the sampling plots. The zoobenthic community identified in 'zero control' samples at Site 1 had 29 taxa overall (Crustacea - 9, Polychaeta - 9, Mollusca - 7, Varia - 4), with total abundance 2316 ind.m^{-2}, and total biomass 11.3 g.m^{-2}. The dominant zoobenthic species was *Bittium reticulatum* with 556 ind.m^{-2} and 3.6 g.m^{-2}.
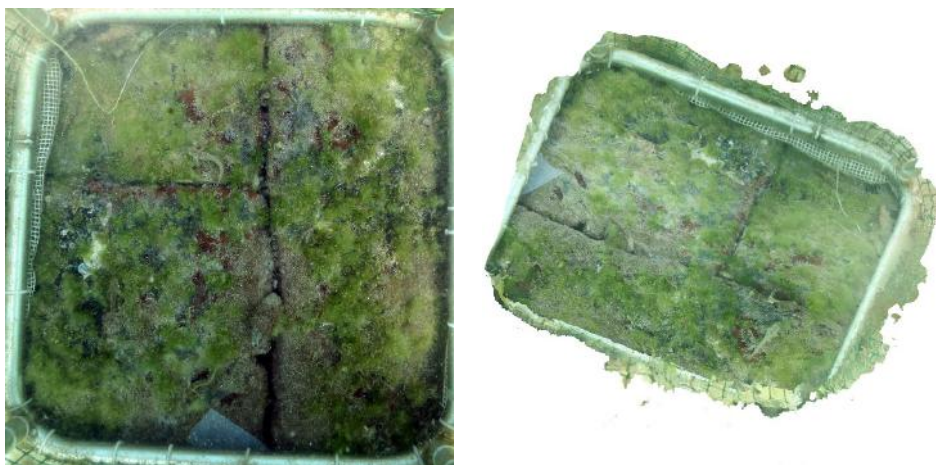
Figure 2. Photo (left) and ortophotomosaic (right) of benthos
in cage 2 at Site 1, 08.2019

The benthic community at Site 2 at the start of the experiment was dominated by the black mussel *M. galloprovincialis,* intermixed with *Mytilaster lineatus,* both overgrown by red macroalgae – *Gelidium spinosum, G. latifolium*, green macroalgae – *Ulva rigida*, and occasional presence of newly settled *Cystoseira barbata* brown macroalgae (Fig. 3). The average length of *M. galloprovincialis* from 'zero control' samples at Site 2 was 19.35 ± 11.3 mm (max size 108.37 mm), with 1054.66 ± 228.19 ind.m^2 population density and a wet biomass of 2469.95 ± 1184.82 g.m^{-2}. The wet biomass of macroalgae within the sampled 'zero controls' was 5.08 ± 5.77 g.m^{-2} (*Gelidium spinosum, G. latifolium, Ulva rigida, Cystoseira barbata*). Small size 0-1 year old *Rapana venosa* were also present in large numbers within the sampled *M. galloprovincialis* community – 56 ind.m^2 with average wet biomass of 1.18 ± 1.05 g.m^{-2} and average length of 17.37 ± 4.26 mm. The zoobenthic community identified in 'zero control' samples at Site 2 had 44 taxa overall (Polychaeta - 15, Crustacea - 14, Mollusca - 12, Varia - 3), with total abundance 4096 ind.m^{-2}, and total biomass 1358.1760 g.m^{-2}.
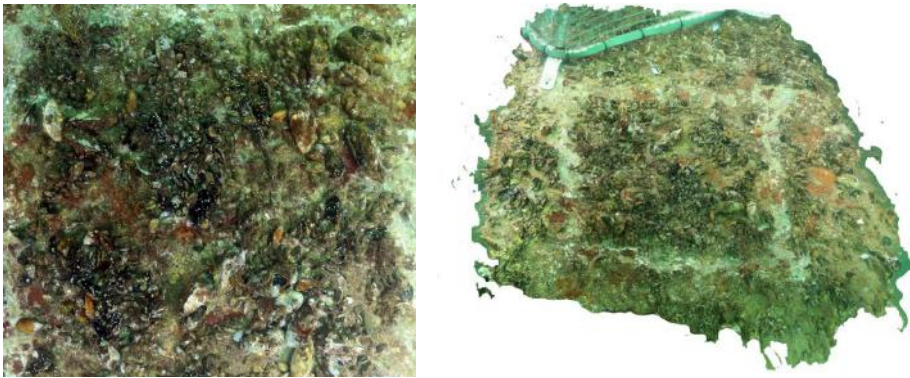
Figure 3. Photo (left) and ortophotomosaic (right) of benthos
in cage 4 at Site 2, 07.2019

Temporal dynamics and predator-prey interactions
In the course of the summer of 2019 a rapid increase in the population density of *R. venosa* was noted at Site 2. Numbers increased from 1.1 ind.m^{-2} to over 10 ind.m^{-2} between early July and late August, reaching a peak of over 13 ind.m^{-2} in October (Fig. 4), when local aggregations of Rapa whelks of up to 544 ind.m^2 were also observed. The predators seem to have moved on the rocky reef from the adjacent sandy bottoms over the course of just a few weeks. They gradually preyed on all available *M. galloprovincialis* colonies, removing them almost completely from the deep end of the reefs up to the water line at 0 m by October 2019. In contrast, at Site 1, which is just 3 km away from Site 2, no such 'explosion' or *R.*

venosa populations was observed (small increase from 1.1 to 1.15 ind.m^{-2} between July and August 2019). Still, in all sampling events at Site 1, Rapa whelks were present in the vicinity of the study site and were 'roaming' the reefs, feeding on available mussels.
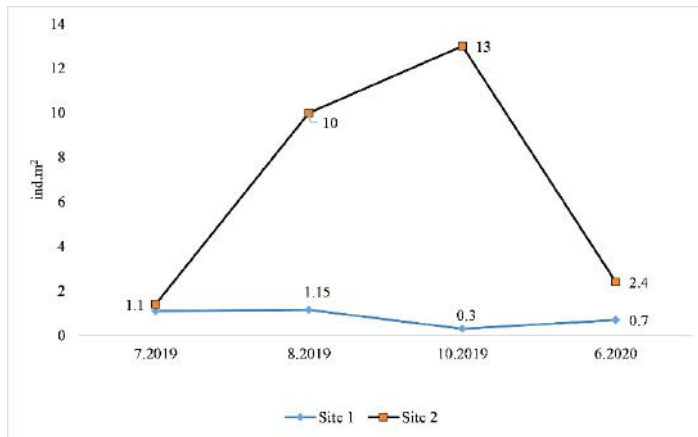

Figure 4. *R. venosa* population density at study sites (visual transects data)

Due to the lack of predatory pressures at site 1, the population density of mussels at control plots remained constant throughout the summer of 2019 (Fig. 5, Fig. 6). A significant change in the cover and number of mussels was observed by June 2020 however – large numbers of newly settled *M. galloprovincialis* and *Mytilaster lineatus* mussels were present within the cages, while their numbers at the control sites decreased even further. This is a clear indication that in the absence of predatory pressure from *R. venosa*, the mussel communities at the study site are capable of resettling and developing. Even the small number of Rapa whelks present at Site 1 were able to completely remove the newly settled mussels outside the cages, and prevent the new development of a mussel-dominated benthic community. Interestingly, within the cages at Site 1, by June 2020 the macroalgal species that were the dominant epibenthic group by 2019, had drastically decreased in cover and biomass. Instead, the substrate within these cages was colonized and overgrown by a large number of Ascidia invertebrate filter feeders. A possible reason for this shift in dominant organisms is the shading effect from the cage mesh, which created a low-light environment unsuitable for the typical green and red seasonal macroalgae.

The 'explosion' of the Rapa whelk population at Site 2 resulted in a rapid removal of mussels from the rocky reefs (Fig. 7). *M. galloprovincialis* seemed to be the preferred prey for *R. venosa*, as their numbers rapidly decreased, and they were completely removed from the unprotected control plots by October 2019. The

number of the smaller *Mytilaster lineatus* decreased more gradually, and they were still present in large numbers by October 2019. By February 2020 however, all mussels were removed from the control plots at the site, as well as from the caged areas (cages missing).

The entry of Rapa whelks < 2 cm through the mesh of the cages prior to its replacement with 0.5 cm mesh a month after the start of the experiment led to a rapid removal of *M. galloprovincialis* from the plots - their numbers dropped tenfold in just 8 weeks (Fig. 7.). Interestingly, this experimental mishap revealed that even small Rapa whelks (<2 cm) are capable of preying on large *M. galloprovincialis* mussels, which were larger in size (20-100+ mm) than their predator. Those that entered the cages started feeding on *M. lineatus* after all large *M. galloprovincialis* mussels were removed from the plots. These observations suggest that *R. venosa* displays a preference for prey with larger size and better nutritional characteristics.
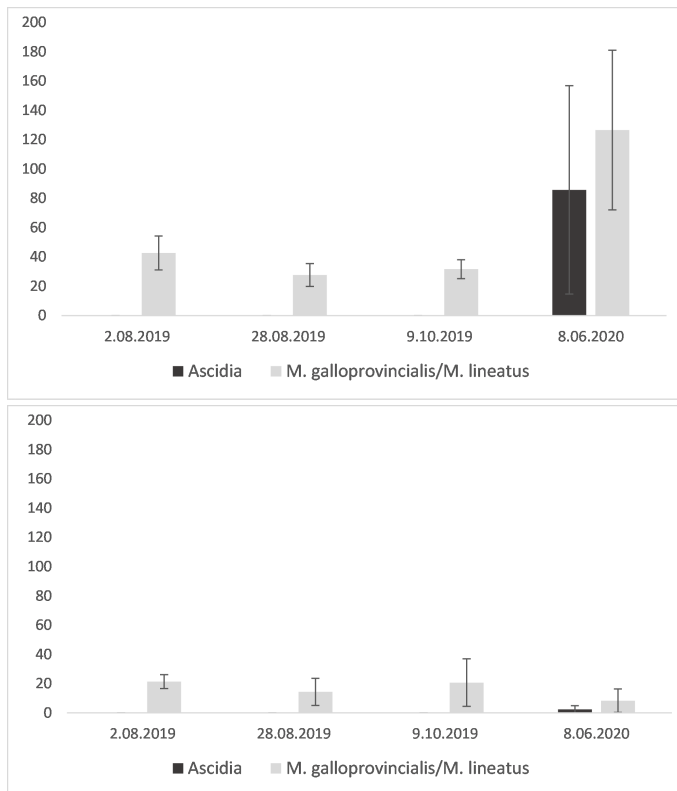
Figure 5. Number of benthic organisms in cages (upper graph) and control plots (lower graph) at Site 1 [ind.50 cm^{-2}]
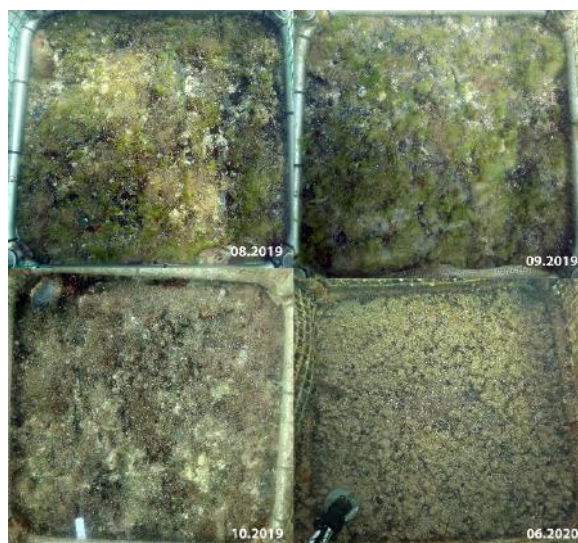
Figure 6. Photos of benthic communities within cage 2
at Site 1in different sampling seasons
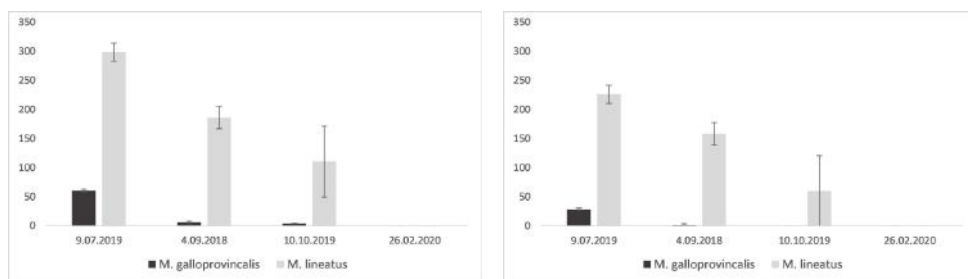
Figure 7. Number of benthic organisms in cages (left graph) and control plots
(right graph) at Site 2 [ind.50 cm^2]

The rapid destruction of mussel beds at the study sites was not limited to just these locations, as similar predatory pressure was observed at all monitoring quadrants throughout the Sozopol Bay area (Fig. 8).

At mussel-dominated sites (SvIvanE, Chervenka), Rapa whelks completely removed all *M. galloprovincialis* by the autumn of 2019, while the relative abundance of *M. lineatus* remained similar (Chervenka), or even increased (SvIvanE). Similarly, at the Cystoseira-dominated sites (SzKanala, SzN), *M. galloprovincialis* was completely removed by October 2019, while the cover by Cystoseira spp. algae remained constant.

By the spring of 2020, the rocky bottom previously occupied by the mussels was overtaken by seasonal green and red macroalgae (*Ceramium virgatum, Ulva rigida, Cladophora albida*), and patches of newly settled *M. galloprovincialis/M. lineatus* were also present. Whether or not these would be able to grow and recover in size and biomass to their previous state is unclear, and depends on the extent of the *R. venosa* predatory pressure in the area in the coming seasons.
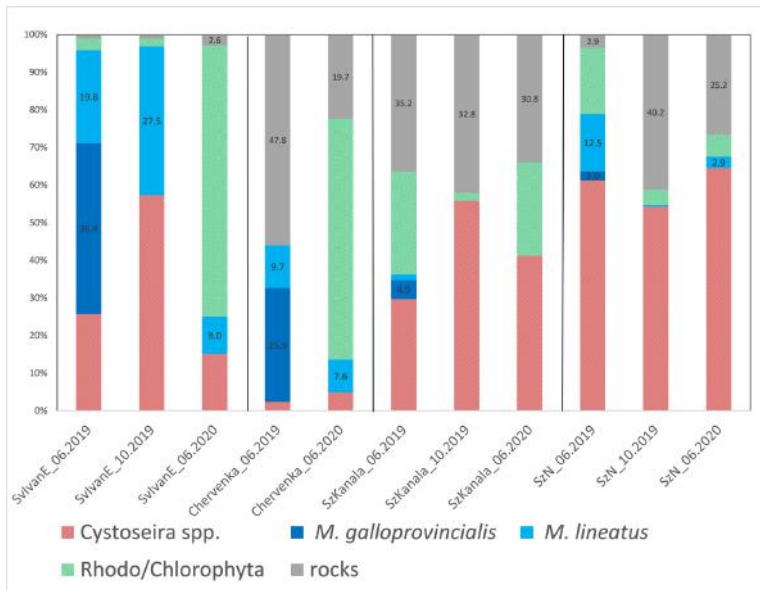
Figure 8. % cover of dominant benthic organisms
at monitoring quadrants throughout the study site

DISCUSSION

Our seasonal observations and experimental results showed that *R. venosa* predatory pressure in the study area is directly responsible for the observed decline of *M. galloprovincialis* and a rapid shift of rocky reefs ecosystems in the study area from mussel-dominated towards algae-dominated communities. This shift is in line with previous observations from rocky reefs along the Bulgarian Black Sea coast (BSBD, 2013; Karamfilov et al., 2018) and the Northern Black Sea coastline (Bondarev, 2014; Snigirov et al., 2013), where at a number of locations various stages of a similar shift were observed.

The rapid disappearance of the dominant habitat-forming mussels from the area corresponds to a loss of vital ecosystem services provided by the black mussels - loss of biodiversity, decrease in the food availability for fish feeding on the

associated benthic organisms and loss of biofiltration and sequestration capacity. Assuming a near complete removal of all adult *M. galloprovincialis* individuals from exposed rocky reefs in the study area (1.05 km^2), and taking into account the estimated biomass of mussels from collected samples, our rough estimates are that the Rapa whelks removed between 1544 and 3971 tons of black mussels from the substrate in the course of just a few months. This corresponds to a total loss of filtering capacity by mussels in the range of $2.6*10^6 - 4.3*10^6$ liters per hour and range of phytoplankton cells removal of $1.3*10^8 - 2.1*10^8$ cells.hour^{-1} (based on *M. galloprovincialis* clearance rates estimations by Denis (1999)). The loss of black mussel communities from the study area resulted in a deterioration of food availability for commercial fish species in the area, such as the anereid polychaetes *Neanthes fucata* and *Platynereis dumerilii*, which were the most important prey items in the diet of horse mackerel along the Bulgarian coast in spring (Georgieva et al., 2019).

Whether or not the shift from mussel-dominated algae to reefs dominated by seasonal green and red algae and perennial Cystoseira spp. brown macroalgae is permanent or temporary depends on the ability of the newly settled *M. galloprovincialis* larvae to continue growing under the predatory pressure from Rapa whelk, and develop into a fully grown mussel biocenosis. The recovery of the local mussel population could be aided by Rapa whelk commercial harvesting by scuba divers that could significantly reduce the predator stress on a local scale. The fact that *M. galloprovincialis* populations thrive in temperatures below 10 ºC beneath the seasonal thermocline (40-45 m), where *R. venosa* cannot reach due to its preferences to higher seawater temperatures (Bondarev, 2014), highlights another important measure for the recovery of the mussel biocenosis. As long as these deeper circalittoral mussel populations exist, a constant flow of larvae would settle available substrates in the coastal shallow-water zones. The local mussel farms, which are protected from *R. venosa* farms (long-lines mussel aquaculture type)*,* are an additional source of *M. galloprovincialis* larvae that could recolonize available substrates and speed up the recovery process. The regulation of bottom trawling in areas with well-developed circalittoral mussel beds below the seasonal thermocline is therefore essential for the recovery of coastal mussel communities. These effects should be acknowledged in future Natura 2000 marine protected areas management plans, and be considered as measures that could aid the recovery and maintenance of 'Good environmental status' of *M. galloprovincialis* infralittoral rocky reef communities.

REFERENCES

Berov, D., Hiebaum, G., Vasilev, V., Karamfilov, V., 2016. An optimized method for scuba digital photography surveys of infralittoral benthic habitats. A case study from the SW Black Sea Cystoseira-dominated macroalgal communities. Underw. Technol. 34, 11–20. doi:https://doi.org/10.3723/ut.34.011

Bondarev, I., 2014. Dynamics of Rapana venosa (VALENCIENNES, 1846) (Gastropoda: Muricidae) Population in the Black Sea. Int. J. Mar. Sci. 4, 46–60. doi:10.5376/ijms.2014.04.0003

BSBD, 2013. Report on Art.8, 9 and 10 on the Marine Strategy Framework 2008/56/EC and the Ordinance for the protection of the marine environemnt. Marine region ' Black Sea. Varna, Bulgaria.

Daskalov, G., 2002. Overfishing drives a trophic cascade in the Black Sea. Mar. Ecol. Prog. Ser. 225, 53–63. doi:10.3354/meps225053

Denis, L., 1999. Clearance rate responses of Mediterranean mussels, Mytilus galloprovincialis, to variations in the flow, water temperature, food quality and quantity. Aquat. Living Resour. 12, 279–288. doi:10.1016/S0990-7440(00)86639-5

Georgieva, Y., Daskalov, G., Klayn, S., Stefanova, K., Stefanova, E., 2019. Seasonal diet and feeding strategy of horse mackerel Trachurus mediterraneus (Steindachner, 1868) (Perciformes: Carangidae) in the south-western Black Sea. Acta Zool. Bulg. 71, 201–210.

Karamfilov, V., Berov, D., Klayn, S., Biserkov, V., Hineva, E., Dencheva, K., 2018. Analysis of the state of the marine environment - 2017. Chapter 2.4 Benthic ecosystems - macrophytobenthos. Varna.

Konsulova, T., 1992. Mussel Mytilus galloprovincialis L a m. (Bivalvia) natural resources along the northern Bulgarian Black sea coast in relation to Rapana thomasiana Grosse (Gastropoda) distribution. Tr. na Instituta po Okeanol. 1, 104–109.

Marinov, T., 1990. The zoobenthos of the Bulgarian section of the Black Sea. Bulgarian Academy of Sciences, Sofia.

Mee, L.D., 1992. The Black-Sea in Crisis - a Need for Concerted International Action. Ambio 21, 278–286.

Pan, J., Macrocal, M., Bazzini, S., Vallina, M., De Marco, S., 2013. Coastal Marine Biodiversity Challenges and Threats, in: Aria, A., Menendez, M. (Eds.), Marine Ecology in a Changing World. CRC Press, p. 270.

Snigirov, S., Medinets, V., Chichkin, V., Sylantyev, S., 2013. Rapa whelk controls demersal community structure off Zmiinyi Island, Black Sea. Aquat. Invasions 8, 289–297. doi:10.3391/ai.2013.8.3.05

Todorova, V., Karamfilov, V., Biserkov, V., Panayotova, M., Ivanova, P., Doncheva, V., Hiebaum, G., Tasev, G., Konsulova, T., Raykov, V., Daskalov, G., Deyanova, D., Gyosheva, B., Trayanova, A., Dencheva, K., Keremedchiev, S., Trifonova, E., Berov, D., Kotsev, I., Slabakova, V., Klayn, S., Vrabcheva, I., Dimov, K., Borisova, E., Stamatova, H., 2012. Report on project "Enlargement of the Natura 2000 ecological network within the Bulgarian Black Sea sector".Contract 7976/04.04.2011 between MoEW and IO-BAS. Sofia.

Zaitsev, Y., 2008. An introduction to the Black Sea ecology. Smil Edition and Publishing Agency Ltd, Odessa.

Zaitsev, Y., 1992. Recent changes in the trophic structure of the Black Sea. Fish. Oceanogr. Vol 1 1, 180–189.

Zolotarev, V., 1996. The Black Sea Ecosystem Changes Related to the Introduction of New Mollusc Species. Mar. Ecol. 17, 227–236. doi:10.1111/j.1439-0485.1996.tb00504.x

✉ **Dimitar Berov**
https://orcid.org/0000-0001-5235-7800
Marine Ecology Laboratory
Institute for Biodiversity and Ecosystem Research
Bulgarian Academy of Sciences
Sofia, Bulgaria
E-mail: dimitar.berov@gmail.com

✉ **Stefania Klayn**
https://orcid.org/0000-0003-3610-8155
Marine Ecology Laboratory
Institute for Biodiversity and Ecosystem Research
Bulgarian Academy of Sciences
Sofia, Bulgaria

✉ **Ventsislav Karamfilov**
https://orcid.org/0000-0002-8343-3906
Marine Ecology Laboratory
Institute for Biodiversity and Ecosystem Research
Bulgarian Academy of Sciences
Sofia, Bulgaria

REMOTE SENSING OF OIL POLLUTION IN THE BLACK SEA – THE MOPANG CASE

Irina Gancheva, Elisaveta Peneva
Faculty of Physics, "St. Kliment Ohridski" University of Sofia,

Abstract. This study focuses on the case of the underwater oil leak form the ship Mopang, sunk in 1921 near the city Sozopol on the Bulgarian coast. In the summer of 2018, some of its engine fuel was released and reached the coast, gaining significant public and media attention. The available Sentinel-1 radar images for the affected region for the years 2017 and 2018 are processed and the results show that oil leaks were visible as early as February 2017. Significant amount of oily discharge was detected during the summer months of both years. During the rest of the year there were occasional discharges, without accumulation during particular periods.

The sunken ship Mopang is used as a verified case to demonstrate the capability of remote sensing techniques for reliable detection of oil pollution on the sea surface in small scales close to the shoreline, combining radar and optical data. Sentinel-1 and 2 images, together with drone acquisitions are analysed, discussing the benefits of each method and taking into consideration the particularities of the region of interest.

Based on the availability of radar acquisitions with detected oil slicks twice a day at 4 am and 4 pm for some days, we have investigated the evolution of the detected oil slick on the sea surface, depending on the marine meteorological conditions.

Keywords: oil pollution in Black Sea, SAR, ocean remote sensing

INTRODUCTION

The Black Sea is a semi-enclosed basin and as such oil pollution is a serious threat to the environmental system. Over 80% of the Bulgarian shoreline is protected area by Natura2000 as it provides a nesting area for various protected bird species, which makes it particularly vulnerable to chemical contamination (Sofia, 2011). Even though oil pollution is common in the Bulgarian waters due to accidental spills or routine waste discharges. Another source of oily pollution, which is not always considered as a serious threat for the ecosystem, comes from natural seeps from the sea floor and sunken ships which release their remaining engine fuel.
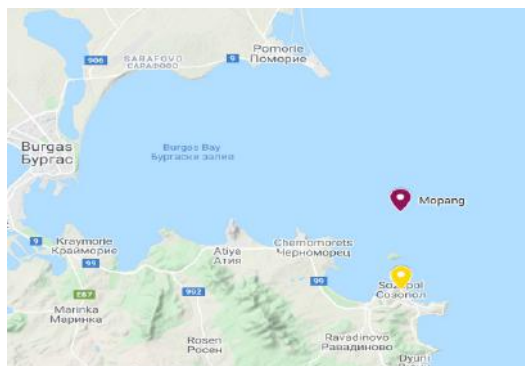
Figure 1. Position of the sunken ship

In the beginning of August 2018 the sunken ship Mopang began releasing some of its engine fuel, which attracted serious public attention, as the ship remains are located in direct vicinity of the island St. Ivan, about 10 km away from the busy tourist city Sozopol, figure 1. The accident was reported by citizens in the Maritime Safety Agency in Bourgas which then initiated cleaning up the tanks and pumping out the remaining fuel. The activity was compleated in the summer of 2019.

Mopang was an US build cargo steamship of the Liberty ships type, build in 1920 and sunk in June 1921 after hitting a mine. The sea depth in the region where the shipwrecks are located is between 20 and 33 m[1]). The capacity of the engine tanks is to hold about 600 tons of fuel and according to some estimations they had about 100 – 150 tons inside[2]).

The potential of the Synthetic Aperture Radar (SAR) as an information source for the automatic detection of oil pollution released in the sea has been acknowledged and investigated years ago and nowadays this method is widely used for the operational monitoring (Brekke & Solberg, 2005; Topouzelis, 2008; Fingas & Brown, 2014). On radar images oil appears as dark formation, as it smoothens the natural sea roughness and thus decreases the backscattering properties of the sea surface. Other natural phenomena, such as local surface currents, eddies or algal blooms, have the same appearance on radar data and might cause false detections in case of an automatisation of the oil detection process.

The implementation of optical remote sensing images for detecting oil on the sea surface is a challenging task. Promising results have been demonstrated, based on the analysis of the spectral reflectance of oil on water (Lu et al., 2013). Marine water absorbs strongly in the near infrared band and appears dark on false colour composites. If an oily component is spread on the sea surface it would change the backscattering characteristics and the reflectance in the area would appear brighter compared to the sea background.

In this study we investigate radar and optical satellite images, collected from ESA's Copernicus programme[3]. The presence of oil in vicinity of Mopang is detected from radar data and optical data is used as complementary source for verification of the radar detections. On optical images, captured with drone, the Mopang leaks were visible as well.

All available acquisitions for the years 2017 and 2018 were analysed in order to understand the extend of the pollution and its intensity. Radar data reveals slicks on most of the summer time images with varying intensity and distribution.

METHODS

The satellite data used in this study comes from the Sentinel missions 1 and 2 and is processed and visualized with the software Sentinel Application Platform – SNAP. The automatic detection of oil leaks from radar imagery is done using an adaptive threshold algorithm (Solberg et al., 2004) and the detected areas are cumulatively plotted according to the month of acquisition (figure 2 and 3). For images, acquired on the same day from ascending and descending pass, the detected oil areas are plotted on a separate figure together with the surface currents of the acquisition time in order to track the development of the slick. The ocean currents data is acquired from the Copernicus Marine Environment Monitoring Service – CMEMS Black Sea physics reanalysis product[4].

The adaptive threshold algorithm calculates the mean backscatter value for pixels in a large window and applies a user defined detection threshold value for estimating each pixel of the area. If the backscatter value of the pixel is below the threshold, it is detected as dark spot. If it is above the threshold, it is estimated as background pixel. Moving the window of averaging and estimating the backscatter for each pixel gives information if a given spot has lower reflectance, which can be caused by oil spreading on the ocean surface, damping the capillary waves. Clustering of the dark spots and defining a minimum cluster size, provides the user with a mask, showing all detected dark spots having larger dimension compared to the defined minimum. (Topouzelis, 2008)

The main drawback of the adaptive threshold is the notable amount of false detection of look-alike objects, caused by other phenomena. These could be minimised by further investigation of the detected areas. A classification according to shape, size and orientation can significantly reduce the amount of false alarms, especially for the areas in direct vicinity of the shoreline (Topouzelis, 2008; Capizzi et al., 2016).

The capability of the SNAP ocean tool for oil spill detection for the Black Sea region has been demonstrated in previous studies and is estimated as good (Gancheva & Peneva, 2019). Some of its major drawbacks is detection in areas close to the shoreline, which underlines the importance of additional analysis and classification of the results in this study. Due to this the initial parameters for

detection were fine-tuned and additional inspection of the surface reflectance and texture of the image in the area where the ship is positioned was done for each acquisition. This procedure gave the confidence to clearly distinguish between oil trace and look-alike objects detected by the algorithm.

The optical data from Sentinel-2 is presented as false colour composite and histogram stretching is used for better visualization.
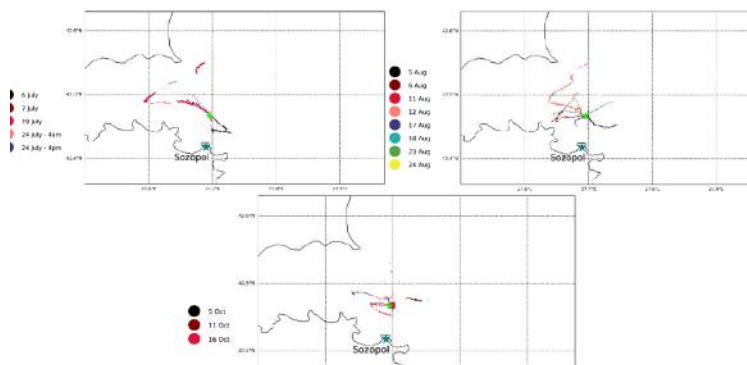
RESULTS AND DISCUSSION

Figure 2. Cumulative plots of all detected oil seeps originating from the sunken ship Mopang for the months July, August and October 2017. Oil seep detections for each day are plotted with different colours, colour map on the left side of the image. The coordinates of the ship are denoted with a green star
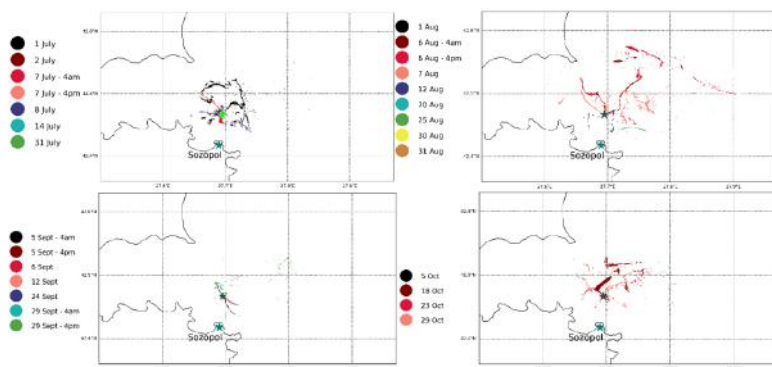
Figure 3. Cumulative plots of all detected oil spills originating from the sunken ship Mopang for the months July – October 2018. Oil seep detections for each day are plotted with different colours, colour map on the left side of the image. The coordinates of the ship are denoted with a grey star.

All available acquisitions from Sentinel-1 from the years 2017 and 2018, which include the region of interest were processed, revealing similar results and conclusions.

The cumulative plots for the months July, August and October 2017 and July, August, September and October 2018 are presented in figure 2 and 3 with each acquisition date on which an oil slick was detected, being indicated with a different colour. The plot for September 2017 is not included, as there were no detections, which could be referred to Mopang.

Acquisitions from the rest of the year were processed as well. Occasional surface features, which could be referred to Mopang, were visible on limited amount of days spread throughout the year without significant accumulation related to particular month or season. The small coloured areas which are not clustered with the main detection slick are caused by false detections due to the small scale of the event and inaccuracy of the detection algorithm.

The majority of the detections for both 2017 and 2018 are during the summer months. This observation can be explained with the calmer sea conditions being favourable for the oil to remain on the sea surface and not mix with the ambient water after emerging from the ship tanks. During 2018 there are more oil detections compared to 2017. However July and August 2018 show similarly intensive oil releases, which can be related to the Mopang leaks. In the Bulgarian media it was stated, that part of the ship collapsed due to its age and poor state in the beginning of August 2018, leading to the oil leakages, but our investigation disproves it as the leak was evident during most part of the summer during the previous year as well[5].

Every 6 days the Sentinel-1A and B pass over the area of interest, acquiring images at 4 am in descending and 4 pm in ascending orbit. In favourable meteorological conditions, such as low sea waves and moderate winds, the oil slick originating from the sunken ship is visible on both acquisitions, which provides an opportunity to study the evolution of the surface dispersion over time depending on the surface currents, wind speed and direction.

Three selected cases are presented on figure 4, 5 and 6: the position of the oil slick is plotted on the map of the stream lines, indicating the speed and direction of the surface current at acquisition time. The grid resolution of the reanalysis data is ca. 3km (1/36° in zonal and 1/27° in meridional direction), thus the current speed closer to the shoreline cannot be determined.

The plots reveal that the position of the oil slick is in the low current speed area and it disperses mainly along when the speed is higher than 10 cm/s or across the stream lines in the case of weak current.
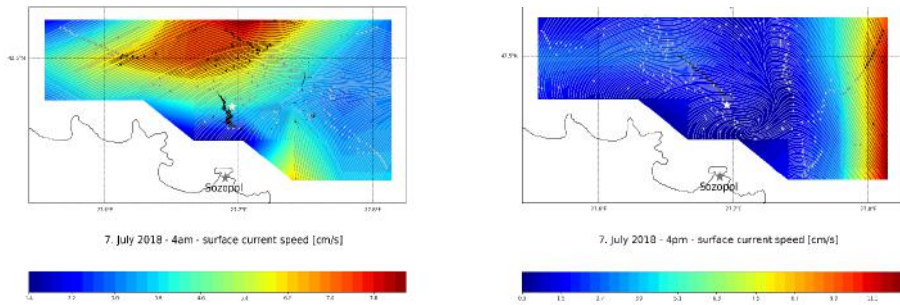
Figure 4. Oil slick detected on 7. July 2018 at 4am and 4pm
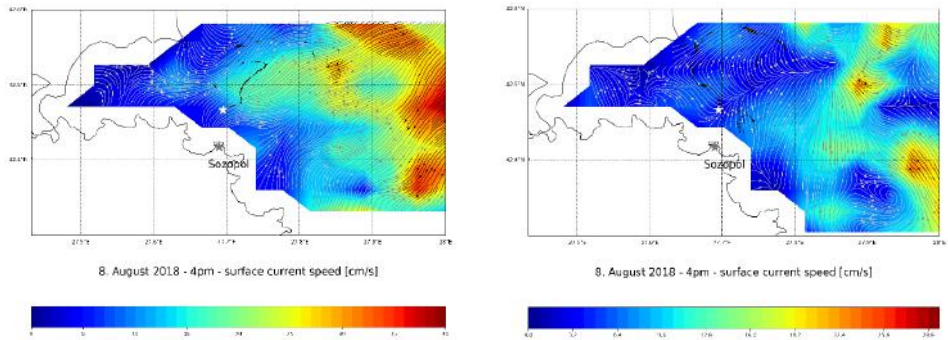with surface current speed and direction at the acquisition time

Figure 5. Oil slick detected on 8. August 2018 at 4am and 4pm with surface
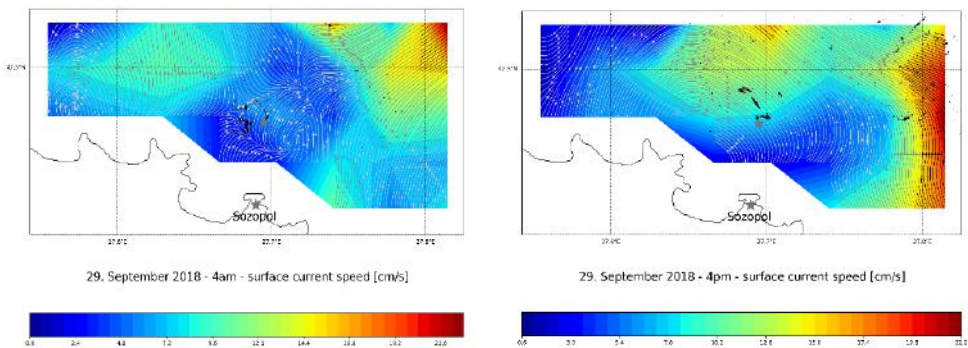current speed and direction at the acquisition time

Figure 6. Oil slick detected on 29. September 2018 at 4am and 4pm
with surface current speed and direction at the acquisition time

The optical data from Sentinel-2 is presented in false colour composite, Red: B8 – 785nm – 899nm; Green: B4 – 650nm – 680nm; Blue: B3 – 543nm – 578nm. The histograms were stretched for better visualisation of the surface features. A snapshot of the drone acquisition is also visualized in figure 9 after histogram stretching for enhancement of the visibility.

The satellite data in the visible spectrum is used as a complementary source aiming to better understand the scale of the pollution during the summer months. The acquisition plan of Sentinel-1 and 2 is such that the optical images are acquired one day before or after the radar information for our area of interest in the middle latitudes. That is why the verification of the oil presence on the sea surface from two data sources, acquired at the same time, is not possible. Moreover many of the Sentinel-2 images are cloudy for the area of interest, that limits the continuity of the observation. Despite this limitation the visibility of the oil slick throughout many days of the analysed period in June – September 2018 indicates significant release of oil near the Mopang location.

The oily trace is difficult to identify, even if the optical image is cloud-free. Because of that the Sentinel-2 data is solely a complementary source of information in this study. Four examples are given in figure 7 and 8: the oil spill is visible and could be definitely related as oil originating from Mopang, but only if preliminary information about the oil presence exists.
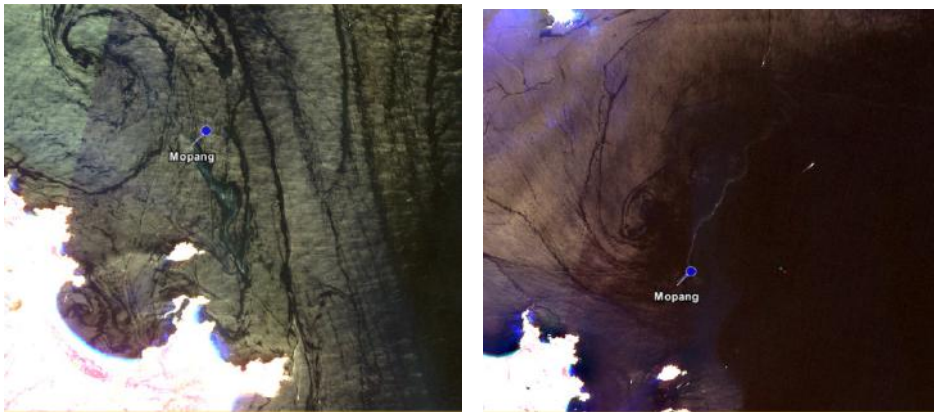

Figure 7. False colour composite of the oil slick detected on 2. July and 6. August 2018 from optical remotely sensed data. The visibility of the oil trace is enhanced through histogram stretching

Figure 8. False colour composite of the oil slick detected on 31. August and 10. September 2018 from optical remotely sensed data. The visibility of the oil trace is enhanced through histogram stretching
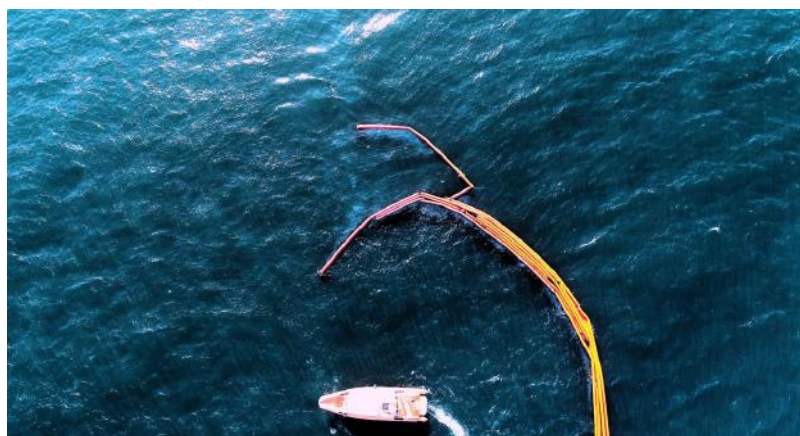

Figure 9. Drone image of the leak area. The oily trace is visible as a brighter trace, damping the capillary waves. The booms are not stopping the dispersion of the pollution, which is propagating from the centre of the picture to the upper end. The visibility is enhanced through histogram stretching. Image curtesy – Institute for Oceanology, Bulgarian Academy of Sciences

CONCLUSIONS

In this study we demonstrated the capacity for reliable detection of small scale oil slicks near the shoreline from radar satellite data, using images from Sentinel-1 processed with an adaptive threshold algorithm. Optical satellite data was used for verification of the

presence of oil on the sea surface and estimating the scale of the release. As a test case was used the particular case of the oil leakage from the sunken ship Mopang, which has been under water since 1921, located in direct vicinity of the Bulgarian coastline.

For the purposes of our research we processed the available Sentinel-1 data-sets from 2017 and 2018 and we demonstrate that oil spills, which could be identified as released from the ship tanks are visible as early as February 2017 and throughout the summer seasons of 2017 and 2018. The oil pollution visible during the summer period of 2017 was of the same order as that in 2018, which leads to the conclusion that the leak started before 2017. Both in July and August 2018 and August 2017 similarly intensive leaks are identified. The spatial extend of the detected oil patches varies between 0.17 and 2.4 km^2.

Regarding the detection of small scale oil pollution using optical data, look-alike objects and the change of the ocean colour are major limitations. They limit the recognisability of the oily trace, so that the slick is not clearly visible on many of the cloud-free Sentinel-2 images analysed in this study. These are well-known constraints for the implementation of satellite data in the visible spectrum for reliable operational monitoring of oil pollution. Nevertheless, as we demonstrate here optical images can be used as complementary information source to radar acquisitions, helping to estimate the scale of the event.

The availability of SAR satellite images with detected oil slick in the morning and afternoon for three dates (7. July, 6. August and 29. September 2018) gives an unique opportunity to investigate the evolution of the spill in terms of shape and extension and to evaluate the surface current impact on dispersion. It is seen that in general the shape and extension doesn't change significantly over the day, however it changes its direction and orientation relative to the surface current. The slicks propagate along or across the surface current stream, away of the areas with large current velocity.

The measures to limit the pollution taken by the responsible authorities have given the possibility to film the spilling with a drone. The image reveals the intensity of the leak, which couldn't be isolated within the area of the booms.

NOTES

1. https://www.wrecksite.eu/wreck.aspx?17360

2. http://www.xinhuanet.com/english/2018-08/13/c_137387725.htm

3. https://www.copernicus.eu/en

4. http://marine.copernicus.eu/documents/PUM/CMEMS-BS-PUM-007-004.pdf

5. https://www.24chasa.bg/novini/article/7023835

REFERENCES

Sofia (2011). National Emergency Plan for Protection of the Black Sea against Oil Spill Pollution *(in Bulgarian)* – Национален авариен план за борба с нефтени разливи в Черно море.

Brekke, C., & Solberg, A. H. (2005). Oil spill detection by satellite remote sensing. *Remote sensing of environment*, *95*(1), 1 – 13.

Topouzelis, K. N. (2008). Oil spill detection by SAR images: dark formation detection, feature extraction and classification algorithms. *Sensors*, *8*(10), 6642 – 6659.

Fingas, M., & Brown, C. (2014). Review of oil spill remote sensing. *Marine pollution bulletin*, *83*(1), 9 – 23.

Lu, Y., Li, X., Tian, Q., Zheng, G., Sun, S., Liu, Y., & Yang, Q. (2013). Progress in marine oil spill optical remote sensing: detected targets, spectral response characteristics, and theories. *Marine Geodesy*, *36*(3), 334 – 346.

Solberg, A. S., Brekke, C., Solberg, R., & Husoy, P. O. (2004, September). Algorithms for oil spill detection in Radarsat and ENVISAT SAR images. In *IGARSS 2004. 2004 IEEE International Geoscience and Remote Sensing Symposium* (Vol. 7, pp. 4909 – 4912). IEEE.

Capizzi, G., Sciuto, G. L., Woźniak, M., & Damaševicius, R. (2016, June). A clustering based system for automated oil spill detection by satellite remote sensing. In *International Conference on Artificial Intelligence and Soft Computing* (pp. 613 – 623). Springer, Cham.

Gancheva, I., & Peneva, E. (2019, February). Verification of the SNAP ocean-tool for oil spill detection for the Bulgarian Black sea region. In *AIP Conference Proceedings* (Vol. 2075, No. 1, p. 120009). AIP Publishing LLC.

✉ **Irina Gancheva**
https://orcid.org/0000-0002-5247-2638
Faculty of Physics
"St. Kliment Ohridski" University of Sofia
Sofia, Bulgaria
E-mail: irina.gancheva@phys.uni-sofia.bg

✉ **Elisaveta Peneva**
https://orcid.org/0000-0003-1325-685X
Faculty of Physics
"St. Kliment Ohridski" University of Sofia
Sofia, Bulgaria
E-mail: elfa@phys.uni-sofia.bg

A STOCHASTIC NUMERICAL APPROACH FOR CONTAMINANT REMOVAL IN CONSTRUCTED WETLANDS UNDER UNCERTAIN-BUT-BOUNDED INPUT PARAMETERS

Konstantinos Liolios[1], Georgios Skodras[2], Krassimir Georgiev[1,3], Ivan Georgiev[1,3]

[1]Institute of Information and Communication Technologies – Bulgarian Academy of Sciences (IICT-BAS)
[2]Department of Mechanical Engineering, University of Western Macedonia – Kozani, Greece
[3]Institute of Mathematics and Informatics – Bulgarian Academy of Sciences (IMI-BAS)

Abstract: The operation problem of Horizontal Subsurface Flow Constructed Wetlands (HSFCW) to remove pollutants under uncertainty is investigated numerically in a stochastic way. Uncertain-but-bounded input-parameters are considered as interval parameters with known upper and lower bounds. This uncertainty is treated by using the Monte Carlo method. A typical pilot case of an HSFCW concerning Biochemical Oxygen Demand (BOD) removal is presented and numerically investigated. The relevant numerical results have a good matching to available experimental ones, and so the effectiveness and the reliability of the proposed stochastic approach is proven.

Keywords: Constructed wetlands; Monte Carlo method; Uncertain-but-bounded input-parameters**.**

1. INTRODUCTION

In the Environmental Engineering praxis, the use of Constructed Wetlands (CWs) for the wastewater treatment has been significantly increased during the last 30 years, see e.g. (Kadlec and Wallace, 2008), (Vymazal, 2014), (Gorgoglione & Torretta, 2018). The reason is the ability of these systems to remove pollutants, to improve the ground water quality and to clean the wastewater before its deposition to the environment. The outlet concentrations of the pollutants, after their "treatment" inside the CWs, are much smaller in comparison to their inlet concentrations. Thus, concerning the ground-water quality, the CWs protect the environment and the public health and they could be an important factor in the wastewater treatment. This holds especially for small

settlements or for urban regions which are far away from big cities, without any other solution for the degradation of dangerous pollutants in ground-water. So, CWs contribute significantly to environmental protection and to reduction of disaster risks.

As concerns the numerical treatment of the above CW problem, significant contributions have been already reported, see e.g. the above mentioned references and moreover (Bear & Cheng, 2010), (Anderson, Woessner & Hunt 2015), (Langergraber,, Giraldi,, Mena, Meyer, Pena, Toscano, Brovelli & Korkusuz, 2009), (Rousseau, Vanrolleghem & De Pauw, 2004), (Zheng & Bennett, 2002). But it must be noted that input parameters concerning the numerical treatment of the above CW problem are rarely known in a safe way, which usually requires detailed in-situ measurements. So, the numerical solution of the above CW problem is usually realized in the Environmental Engineering praxis by using a mean-value estimate of the various uncertain input parameters.

In the present study, the problem of a Horizontal Subsurface Flow Constructed Wetland (HSF CW) operating to remove pollutants is analyzed in a numerical stochastic way. Emphasis is given to the uncertainty concerning the input parameters. For this purpose, the input-parameters are considered as interval parameters with known upper and lower bounds, characterized in Civil Structural Engineering as uncertain-but-bounded parameters, see e.g. (Muscolino & Sofi, 2012, 2013), (Impollonia & Muscolino, 2011), (Papadrakakis, Stefanou & Papadopoulos, 2011). The herein numerical approach is based on Monte Carlo simulation methods (Dimov, 2008). Finally, in a typical HSF CW example, the removal of Biochemical Oxygen Demand (BOD), which is one of the most common essential municipal pollutant, is stochastically investigated.

2. METHOD OF ANALYSIS

The stochastic numerical methodology developed herein is realized in the following steps, see e.g. (Dimov, 2008), (Kottegoda & Rosso, 1997), (Ang & Tang, 1984), (De Marsily, 1986): First the deterministic problem for each set of the random input variables is solved. Next the probabilistic problem is treated by using Monte Carlo simulations. Finally, a statistical analysis of the outputs is realized.

2.1. The deterministic problem

The traditional numerical simulation of CW operation is usually treated as a *deterministic* one, based on the solution of the following system of partial differential equations (1)-(7).

The three-dimensional groundwater flow equation is written, using tensorial notation (i,j = 1,2,3), see (Zheng & Bennett, 2002):

$$\frac{\partial}{\partial x_i}\left(K_{ij}\frac{\partial h}{\partial x_j}\right) + q_s = S_s\frac{\partial h}{\partial t} \qquad (1)$$

Where they are: K_{ij}: component of the hydraulic conductivity tensor, in [m/sec]; h: hydraulic head, in [m]; q_s: volumetric flow rate per unit area of aquifer representing fluid sources (positive) and sinks (negative), in [sec^{-1}]; S_y: specific yield of the porous materials.

The velocity field q_s, in [m/sec], is computed through the Darcy relationship:

$$q_i = -K_{ij}\frac{\partial h}{\partial x_j}$$

(2)

The partial differential equation which describes the fate and transport of a contaminant with adsorption in 3-D, transient groundwater flow systems can be written:

$$\varepsilon R_d\frac{\partial C}{\partial t} = \frac{\partial}{\partial x_i}\left(\varepsilon D_{Sij}\frac{\partial C}{\partial x_j}\right) - \frac{\partial}{\partial x_i}(q_i C) + q_s C_s + \sum_{n=1}^{N}R_n$$

(3)

ε: porosity of the subsurface medium [dimensionless]; R_d: retardation factor [dimensionless]; C: dissolved concentration of solute, in [mg/L]; D_{sij}: solute hydrodynamic dispersion coefficient tensor, in [m^2/sec]; ΣR_n: chemical reaction term, in [mg/L/sec] C_s: concentration of the source or sink flux, in [mg/L]..

As concerns the reaction term ΣR_n in equation (3), this is given by the formula:

$$\Sigma R_n = -\lambda R_d C^\alpha$$

(4)

λ, α: removal coefficients. For $\alpha = 1$, the usual linear reaction case of first-order decay is active, with λ in [day^{-1}].

The solute *hydrodynamic dispersion* coefficient tensor in equation (3) is decomposed (Bear & Cheng, 2010) in the diffusion part and the mechanic dispersion part as follows:

$$D_{ij} = D^0{}_{ij} + D^M{}_{ij}$$

(5)

For the simple case of unidirectional flow with flow velocity u, for the mechanic dispersion part $D^M{}_{sij}$ it holds along the longitutional direction:

$$D_L = a_L|u|$$

(6)

and along the transversal direction:

$$D_T = a_T|u|$$

(7)

a_L: longitutional dispersivity, in [cm]; a_T: transverse dispersivity, in [cm].

The above system of the partial differential equations (1)-(3), combined with appropriate initial and boundary conditions, describe the 3-dimensional flow of groundwater and the transport and removal of contaminants in a heterogeneous

and anisotropic medium. Thus, the unknowns of the problem are the following five space-time functions: The hydraulic head $h = h(x_i;t)$; the three velocity components: $q_i(x_j;t)$; and the concentration $C = C(x_i;t)$.

The numerical solution of the above deterministic problem is here obtained by using the Visual MODFLOW computer code (Waterloo Hydrogeologic Inc., 2006). The input parameters concerning the various coefficients of the above system of equations (1)-(3) are rarely known in a safe way, which usually requires detailed in-situ measurements. Therefore, the numerical treatment of the above deterministic problem is usually realized in the praxis by using a mean-value estimate of the various coefficients.

2.2. The stochastic problem

Next, the various coefficients of the problem governing equations (1)-(7) are considered as random variables. Probability density functions are used, based on lower and upper bounds for reliable estimates known either from praxis or in-situ measurements. For the quantitative estimation of the various uncertainties, a Monte Carlo simulation is applied.

As well-known (Dimov, 2008), (Kottegoda & Rosso, 1997), (Ang & Tang, 1984), Monte Carlo simulation is simply a repeated process of generating deterministic solutions to a given problem. Each solution corresponds to a set of deterministic input values of the underlying random variables. A statistical analysis of the obtained simulated solutions is finally performed. According to the computational methodology, first the above deterministic problem for each set of the random input variables is solved and then a statistical analysis is followed. In the existing literature there are some recent studies concerning the application of stochastic methods in CWs, see e.g. (Freeze, 1975), (Werner & Kadlec, 2000), (Kadlec, 1997).

3. A NUMERICAL EXAMPLE

A numerical example concerning the removal of Biochemical Oxygen Demand (BOD) in a pilot-scale HSF CW tank is presented. This pilot-scale HSF CW was constructed and operated in the frame of a research project realized in the facilities of the Laboratory of Ecological Engineering and Technology, Department of Environmental Engineering, Democritus University of Thrace (DUTh), Xanthi, Greece. More details about these facilities are available in (Liolios,, Moutsopoulos & Tsihrintzis, 2012), (Akratos & Tsihrintzis, 2007).

The dimensions of the investigated tank are: 3 m length, 0.75 m width and 1 m height-see Figure 1. The tank contained the most usual porous media (medium gravel - MG) and was planted with common reed (*Phragmites australis* reed – R). This tank is named as (MG-R). For the herewith numerical investigation, relevant available experimental data from the operation of the above pilot-scale HSF CW are used (Akratos & Tsihrintzis, 2007) The mean value of the inlet BOD concentration

was C_{in} = 361.1 mg/Liter. The remaining BOD concentration was measured at three places in distances from inlet: L/3, 2L/3 and L.

As concerns the uncertain-but-bounded input parameters for the stochastic analysis, these are estimated here by using available upper and lower bounds, denoted as U_B and L_B, respectively. For example, the first-order decay coefficient λ of equation (4) is estimated by the bounds L_B = 0.10 [day⁻¹] and U_B = 0.20 [day⁻¹] reported in (Liolios et al., 2012):

$$0.10 \leq \lambda \leq 0.20 \tag{8}$$

In general, according relevant investigations, the hydraulic conductivity K has a LOGNORMAL probability distribution, whereas porosity ε, and dispersivity α_L have a NORMAL probability distribution (Freeze, 1975). The first-order decay coefficient λ is considered here to have a UNIFORM probability distribution according the results of (Liolios,, Moutsopoulos & Tsihrintzis, 2012). So, for the investigated HSF CW case, in the Table 1 the truncated Probability Density Functions (PDF) are shown. By COV is denoted the Coefficient of Variation. The mean values are estimated as $(U_B + L_B)/2$.
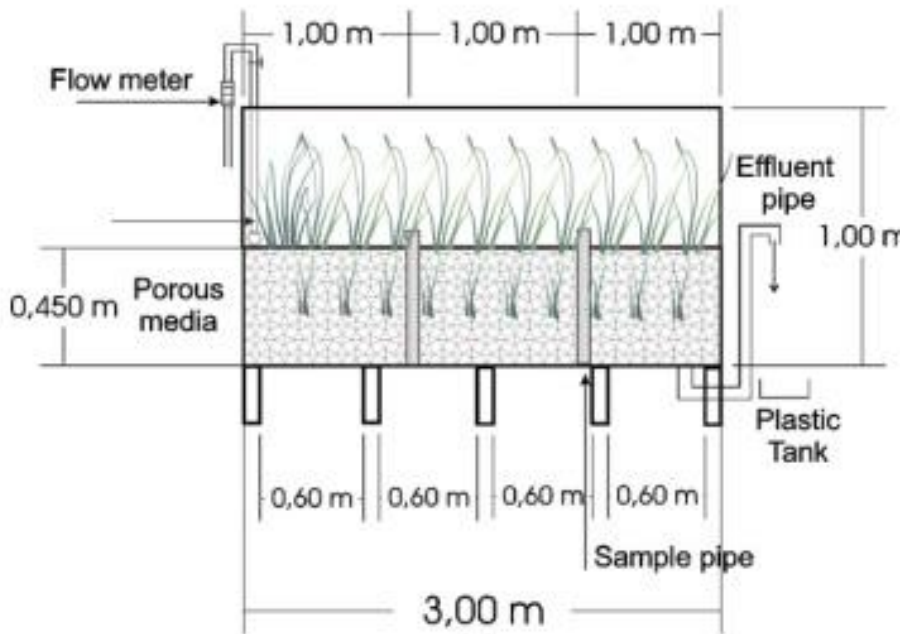
Figure 1. The investigated pilot-scale HSF CW tank: Schematic section along the tank, (Akratos andTsihrintzis, 2007).

Table 1. Distribution properties of uncertain-but-bounded input parameters

Input parameters	Distribution, PDF	Mean value	COV [%]
K [m/sec]	LOGNORMAL	1.538	25
ε in [%]	NORMAL	0.365	15
a_L [cm]	NORMAL	2.70	50
λ [day^{-1}]	UNIFORM	0.15	20

Next, using 200 Monte Carlo samples, obtained representative probabilistic results for the BOD concentration ratios C/C_{in}, in [%], are reported in Table 2 and compared with corresponding experimental ones (Akratos &Tsihrintzis, 2007). As this comparison shows, the proposed stochastic approach provides reliable results.

Table 2. Representative results for the BOD concentration ratios C/C_{in} in [%]

Distance from inlet	Experimental Mean value C/C_{in} [%]	Stochastic Mean value C/C_{in} [%]	COV [%]
[1]	[2]	[3]	[4]
$x_1 = L/3$	37.4	39.18	8.48
$x_2 = 2L/3$	23.5	24.84	12.84
$x_3 = L$	14.9	13.71	19.53

4. CONCLUDING REMARKS

A stochastic approach based on Monte Carlo simulations has been developed for the problem of ground water flow and contaminant removal in constructed wetlands, taking into account uncertain input parameters. In a numerical example concerning BOD removal in a pilot HSF CW tank, the comparison between available experimental results and the computed stochastic ones have shown a very satisfactory agreement. Thus, the effectiveness and the reliability of the proposed stochastic approach is proven and can be used for CWs tanks having similar operation parameters with the investigated in the present study.

REFERENCES

Akratos, C. & Tsihrintzis, V (2007). Effect of Temperature, HRT, Vegetation and Porous Media on Removal Efficiency of Pilot-Scale Horizontal Subsurface Flow Constructed Wetlands. *Ecological Engineering*, 29, 173-191.

Anderson, M.P., Woessner, W.W. & Hunt, R.J. (2015). *Applied Groundwater Modeling: Simulation of Flow and Advective Transport*. San Diego: Academic Press, 2nd Edition.

Ang, A.H.S. & Tang, W.H. (1984). *Probability Concepts in Engineering Planning and Design, vol. 2: Decision, Risk and Reliability*. New York: Wiley.

Bear, J. & Cheng, A.H.D. (2010). *Modeling Groundwater Flow and Contaminant Transport*. Dordrecht: Springer.

De Marsily, G. (1986). *Quantitative Hydrogeology*. London: Academic Press.

Dimov, I. (2008). *Monte Carlo Methods for Applied Scientists*. London: World Scientific.

Freeze, R.A. (1975). A Stochastic-Conceptual Analysis of One-Dimensional Groundwater Flow in Nonuniform Homogeneous Media. *Water Resources Research*, 11(5), 725-741.

Gorgoglione, A. & Torretta, V. (2018). Sustainable Management and Successful Application of Constructed Wetlands: A Critical Review. *Sustainability*, 10(11), 3910.

Impollonia, N. & Muscolino, G. (2011). Interval Analysis of Structures with Uncertain-But-Bounded Axial Stiffness. *Computer Methods in Applied Mechanics and Engineering*, 200, 1945–1962

Kadlec, R.H. & Wallace, S.D. (2008). *Treatment Wetlands*., Boca Raton: CRC Press, 2nd Edition.

Kadlec R.H. (1997) Deterministic and Stochastic Aspects of Constructed Wetland Performance and Design. *Water Science and Technology*, 35(5), 149-156

Kottegoda, N.T. & Rosso, R. (1997). Statistics, Probability and Reliability for Civil and Environmental Engineers. New York: McGraw-Hill,.

Langergraber, G., Giraldi, D., Mena, J., Meyer, D., Pena, M., Toscano, A., Brovelli, A. & Korkusuz, E.A. (2009). Recent Developments in Numerical Modelling of Subsurface Flow Constructed Wetlands. *Science of the Total Environment*, 407(13), 3931-3943

Liolios, K.A., Moutsopoulos, K.N. & Tsihrintzis, V.A. (2012). Modeling of Flow and BOD Fate in Horizontal Subsurface Flow Constructed Wetlands. *Chemical Engineering Journal*, 200-202, 681-693.

Muscolino, G. & Sofi, A. (2012). Stochastic Analysis of Structures with Uncertain-But-Bounded Parameters Via Improved Internal Analysis. *Probabilistic Engineering Mechanics*, 28, 152-163.

Muscolino, G. & Sofi, A. (2013). Bounds for the Stationary Stochastic Response of Truss Structures with Uncertain-But-Bounded Parameters. *Mechanical Systems and Signal Processing*, 37, 163–181.

Papadrakakis, M., Stefanou, G. & Papadopoulos, V. (2011). *Computational Methods in Stochastic Dynamics*. Dordrecht: Springer,

Rousseau, D.P.L., Vanrolleghem, P.A. & De Pauw, N. (2004). Model-Based Design of Horizontal Subsurface Flow Constructed Treatment Wetlands: A Review. *Water Research*, 38(6),1484-1493.

Waterloo Hydrogeologic Inc. (2006). *Visual MODFLOW v. 4.2. User's Manual*. Virginia: U.S. Geological Survey,

Werner, T.M. & Kadlec, R.H. (2000). Stochastic Simulation of Partially-Mixed, Event-Driven Treatment Wetlands. *Ecological Engineering*, 14(3), 253-267.

Vymazal, J. (2014). Constructed Wetlands for Treatment of Industrial Wastewaters: A Review. *Ecological Engineering*, 73, 724-751.

Zheng, C. & Bennett, G.D. (2002). *Applied Contaminant Transport Modelling*. New York: Wiley, 2nd Edition

✉ **Konstantinos Liolios**
https://orcid.org/0000-0002-0937-547X
Institute of Information and Communication Technologies
Bulgarian Academy of Sciences
E-mail: kostisliolios@gmail.com

✉ **Georgios Skodras**
[2]Department of Mechanical Engineering
University of Western Macedonia
Kozani, Greece
E-mail: gskodras@uowm.gr

✉ **Krassimir Georgiev**
https://orcid.org/0000-0001-5277-2887
Institute of Information and Communication Technologies
Institute of Mathematics and Informatics
Bulgarian Academy of Sciences
E-mail: georgiev@parallel.bas.bg

✉ **Ivan Georgiev**
Institute of Information and Communication Technologies
Institute of Mathematics and Informatics
Bulgarian Academy of Sciences
E-mail: ivan.georgiev@parallel.bas.bg